Hydrogenography

A thin film optical combinatorial study of hydrogen storage materials

Robin Gremaud
PhD thesis (2008)
Vrije Universiteit Amsterdam

Cover: Crater in the Haleakalā volcano, Maui, Hawaii. The changing color of the rocks gives us information on their composition and oxidation state. Similarly, we derive the composition and hydrogen content of the thin hydride films studied in this thesis from their optical appearance.

VRIJE UNIVERSITEIT

Hydrogenography, a thin film optical combinatorial study of hydrogen storage materials

ACADEMISCH PROEFSCHRIFT

ter verkrijging van de graad Doctor aan
de Vrije Universiteit Amsterdam,
op gezag van de rector magnificus
prof.dr. L.M. Bouter,
in het openbaar te verdedigen
ten overstaan van de promotiecommissie
van de faculteit der Exacte Wetenschappen
op donderdag 16 oktober 2008 om 13.45 uur
in de aula van de universiteit,
De Boelelaan 1105

door

Robin Florian Arnaud Gremaud

geboren te Marly, Zwitserland

promotor: prof.dr. R.P. Griessen
copromotor: dr. B. Dam

Contents

Chapter 1

Introduction

The search for new lightweight metal hydride storage materials is essentially looking for a needle in a haystack. This thesis addresses this issue by the development of a new thin film optical combinatorial approach, Hydrogenography, that greatly facilitates the identification and characterization of new hydrogen storage materials. The fact that absorption of hydrogen in metals leads to large optical changes[1] is at the basis of the method. With a straightforward optical setup, the hydrogenation of thousands of potential hydrogen storage materials deposited as thin film on a single substrate is monitored and compared simultaneously. In particular, this thesis discusses the following questions:

1. Can we determine the hydrogenation kinetics and thermodynamics, as well as the microstructure of thin hydride films by simply looking at the evolution of their optical properties?

2. In what respect are these three materials properties interdependent?

3. Can we identify by Hydrogenography new alloys/composites with suitable properties for application?

In this chapter, the basic concepts about metal hydrides for hydrogen storage and combinatorial techniques are introduced.

1.1 The Hydrogen cycle

Hydrogen constitutes 75% of the elemental mass of the Universe, occurring mainly in a plasma state (H^+).[2] On Earth, the most stable form of hydrogen gas is the diatomic hydrogen molecule (H_2). It is however rare, because most of the hydrogen is preferably bound in the form of water and hydrocarbons. This means that gaseous hydrogen has to be produced and is therefore a secondary fuel. It can be obtained by electrolysis of water using a primary energy source (solar or geothermal) and combusted back to water in a clean, closed chemical cycle involving no release of carbonaceous pollutants. An energy supply based
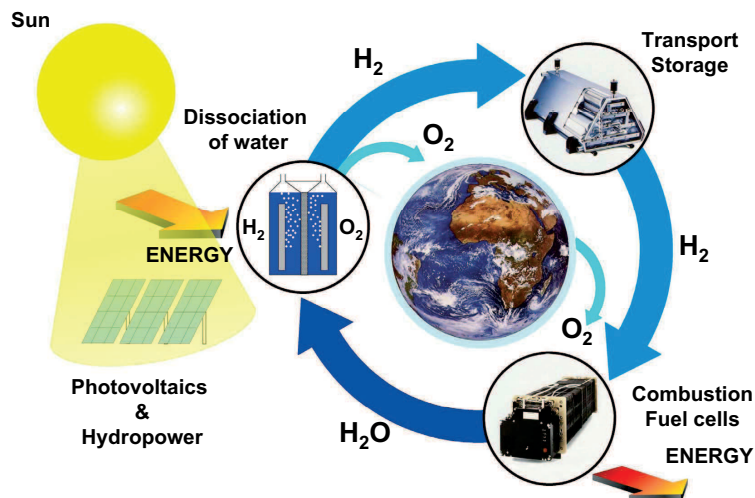
Figure 1.1: The hydrogen cycle is a clean, closed cycle. Using the sun as input energy, water is split by electrolysis, producing O_2 and H_2 which are recombined in a fuel cell to deliver energy. At an intermediate stage, hydrogen must be stored, either as an energy buffer for intermittent renewable energy sources (e.g. solar or wind) or to embark in mobile applications. One of the most promising solution for H storage is to absorb it in metal-hydrides. Image by A. Züttel.[4]

on the hydrogen cycle would provide an alternative to the not everlasting fossil fuels as well as reduce our dependence on the regions extracting them. It would also reduce the amount of greenhouse gases present in the atmosphere and help to slow down global warming.[3]

Primary renewable energy sources are irregular in intensity (solar) or not uniformly distributed (geothermal), and this results in a serious mismatch between energy supply and demand. The advantage of hydrogen in this context is its potential to store energy, either as a buffer in stationary applications to compensate peaks in demand and supply or to replace batteries in mobile applications. A key issue for the large scale use of hydrogen as an energy carrier is therefore the availability of a safe and effective way to store it reversibly. Presently, possibilities to store hydrogen are: as a pressurized gas, liquid, physisorbed on materials with a high surface area or in metal hydrides.[5,6] Metal hydrides provide presently the most attractive option to store hydrogen reversibly.

1.2   Metal hydrides for hydrogen storage

Various type of hydrides exist: ionic (NaH, LiH, MgH_2), polymeric covalent (AlH_3), volatile covalent (NH_3), metallic interstitial hydrides ($PdH_{0.7}$, $LaNi_5H_6$) and complex hydrides (Mg_2NiH_4, $NaAlH_4$). In the complex hy-

drides, two bonding mechanisms occur: n hydrogen are covalently bonded to a metal A, forming a complex ion AH_n^{-m} with valence m.[7] This complex ion forms in turn an ionic bond with an alkaline or alkali-earth element, according to the 18-electrons rule.[8] The boundary between different types of bonding in hydrides is not sharp and depends mainly on the difference in electronegativity between the hydrogen and the metal concerned. This diversity is made possible by the nature of the hydrogen atom: the proton having a single 1s electron, it displays either an alkaline or halogen behavior depending on the electronegativity of his bonding partner.

Many metals and intermetallic compounds absorb hydrogen when exposedto the proper hydrogen pressure and desorb the hydrogen again when their environment is evacuated. This was already recognized by Graham in 1866 for Pd.[9] But it is only one century later that, driven by the sudden need for renewable energy during the oil crisis, the reversible hydrogenation reaction of LaNi$_5$ based intermetallics was considered to store hydrogen.[10] This type of materials was implemented successfully in Ni-MH batteries but not for storing hydrogen for mobile application. That is because these materials contain only 1.4 weight percent (wt%) of hydrogen, making them competitive in term of energy density for batteries but not in term of tank weight for cars.

In fact, a severe list of requirements should be fulfilled by the ideal storage materials for mobile application: The primary requirement is that it must be usable under practical conditions, meaning essentially operation temperatures between 243 up to 393 K at H$_2$ gas pressures p around 10^5 Pa. Under these conditions, the Gibbs free energy of the metal G_M has to be equal to the one of the hydride G$_{MH}$.

$$G_M = G_{MH} \Leftrightarrow \Delta G = \Delta H - \mathcal{T}\Delta S = 0 \qquad (1.1)$$

This can be rewritten in the form of the Van 't Hoff's equation:[11]

$$\ln\left(\frac{p_{eq}}{p_0}\right) = \frac{\Delta H}{R\mathcal{T}} - \frac{\Delta S_0}{R} \qquad (1.2)$$

where p$_{eq}$ is the H$_2$ equilibrium plateau pressure, ΔH the hydride enthalpy of formation in $J(mol\ H_2)^{-1}$, ΔS$_0$ the entropy of formation in $J(K\ mol\ H_2)^{-1}$at p$_0$ =1.013 $\cdot$ 10^5 Pa, R the gas constant and $\mathcal{T}$ the absolute temperature. If in a first approximation, ΔS$_0$ is mainly determined by the loss of entropy when gaseous H$_2$ is absorbed in the solid, i.e. ΔS$_0 \cong$ -ΔS$_{H_2}$ =-130.684 J(K molH$_2$)$^{-1}$ at a pressure of 10^5 Pa and room temperature, a practical hydrogen storage material should have an enthalpy of the order of -40 kJ(mol H$_2$)$^{-1}$. In fact, there is presently a drive for even less negative values, to reduce the heat exchange burden during hydrogen loading. This would increase the operation temperature, or, for the reaction still to happen around normal conditions, the absolute entropy change should be reduced accordingly ($|\Delta S| < |\Delta S_{H_2}|$).

Besides the thermodynamic requirements for the hydrogenation reaction there are a number of crucial other parameters. An important one is the kinetics of hydrogen release and absorption that is determined by the (nano-) structure of the material, the nucleation and growth mechanism, the diffusion and the catalytic properties of the surface. In addition, given the fast charging generally required, a high thermal conductivity of both the metal and the hydride phase is needed. The availability and affordable price of the hydride constituent is also of importance. Sofar, no hydride satisfies all these requirements. Until recently, two families of metal hydride systems seemed promising: so-called Mg-based systems and the light-weight complex hydrides of alkali and alkali earth metals, the alanates and boranate (e.g. $NaAlH_4$, $LiAlH_4$, $LiBH_4$). [12–16]

During the last few years, other ways to store hydrogen have also been proposed. Potential reactions involve lithium amide ($LiNH_2$) and imide (Li_2NH), [17] alane (AlH_3) [18] or different complexes of ammonia. [19] Chemical hydrides, i.e. the hydrolysis of metals (Li, Na, Mg, Al or Zn) [20] or of complex hydrides [21] to produce hydrogen are also actively considered.

1.3   Combinatorial techniques

An essential ingredient for this thesis is the application of an optical combinatorial technique to quickly screen a large number of alloy compositions. After a short review of combinatorial techniques in materials research, we will focus on their application to hydrogen storage research.

Combinatorial research has been very effective in the field of biochemical and pharmaceutical research. Only recently these techniques were rediscovered in the field of materials science and engineering, [22–24] as structure-property relations plays an essential role in materials science and functional materials become increasingly complex. The use of oxides, nitrides, hydrides etc. implies that also processing options increase dramatically. In combinatorial research, a large number of compounds with different compositions are synthesized and characterized in parallel. In this way, a wide range of properties ranging from bio-functional to magnetic or dielectric materials can be efficiently addressed. Due to the wide range of applications and materials, combinatorial materials science techniques have evolved in various ways.

The most obvious way to compare many materials compositions at a time is to produce thin film with chemical compositional gradients that develop across a wafer in a co-deposition process in the absence of substrate rotation. In this case, the local composition need to be carefully measured in order to map the properties. To circumvent this problem Xiang [25] developed a technique based on spatially addressable materials libraries from multilayer thin film precursors. In this case, sites with different multilayer combinations are spatially separated but simultaneously thermally processed. Thermal diffusion and nucleation

determine the phase formation of each site in this process. This technique has been extended to atomic layer epitaxy, in which crystal structures are built layer-by-layer.[26]

The success of a combinatorial approach depends heavily on the availability of a suitable high throughput screening technique. Optical properties are very well suited for this purpose as they allow to measure a large number of samples simultaneously. In chemistry luminescence provides often an excellent means to quickly probe a large number of samples at once.[27] Alternatively, scanning probe techniques are used, although these techniques suffer from a limited scan range. Instead of looking directly at the samples one can also infer some of their properties from their influence on the underlying substrate, for example, by using microelectromechanical systems (MEMS). Recently, microstructured wafers with cantilever arrays were used to identify the strain properties of polymers.[28,29] In general, sensor arrays provide a convenient platform to measure various chemical and physical parameters in parallel.[30]

1.3.1 Combinatorial techniques in hydrogen storage research

As the understanding of hydride materials developed and their limitations for an application in the automotive sector became clear, attention shifted away from simple binary or ternary hydride systems to compounds or composites consisting of multiple elements. However, the number of possible combinations grows factorially, and with all the parameters to be incorporated, a nearly infinite parameter space opens. The search for new hydrogen storage materials is thus necessarily time consuming. Either a lengthy ball-milling procedure or a complicated chemical synthesis is needed to produce the necessary nano-grained materials.

Several groups try to identify new hydrogen storage materials by bulk chemical synthesis. These methods rely mostly on parallel processing of various sample compositions.[31] An interesting approach was introduced by Zhao[24] who uses diffusion-multiples (i.e. phases formed through interdiffusion of several bulk materials in intimate interfacial contact) to study the formation of hydrides.

The use of thin films to explore new metal-hydride storage options is at first sight not obvious, given the fact that practical systems designed to store large quantities of hydrogen will require kilograms of (powdered) materials. However, thin film combinatorial methods are ideally suited for a fast and efficient exploration and a speed of analysis that are out of reach for bulk chemical methods. Moreover, advanced metal-hydrides may also find an application as thin film battery materials.[32] Comparing bulk and thin film properties one has to keep in mind that thin films are influenced by the substrate surface. Due to the lattice expansion resulting from hydrogenation, the films are strained.

To relieve this strain, in epitaxial YHx films a complex twinning and reorientation mechanism occurs.[33,34] If the film remains clamped, this results in an anisotropic expansion at low hydrogen concentrations and to dislocation loops and a complex rearrangement of nanograins at high hydrogen concentrations (typically for hydrogen to metal ratios H/M>0.1). Experiments on MgHx,[35] YH$_x$[36] and NbH$_x$[37] films suggest that the enthalpy of hydrogenation can be 14-16 kJ(mol H$_2$)$^{-1}$less negative than that of bulk material. This is probably not only due to clamping effects but also to the nanocrystalline structure of films. An electrochemical comparison between Mg-Sc-H thin film and bulk material shows, however, a remarkable similarity in the equilibrium potential. [38]

A big advantage of thin films is the minimization of diffusional problems. The grains are small by nature and only very thin layers are needed for the analysis. Moreover, thin films easily allow for a study of the surface structure, which facilitates the investigation of the catalytic mechanisms involved in hydrogen sorption. Olk et al.[39] studied the hydrogenation of thin films using compositional library samples. They used spatially resolved infrared imaging for high-throughput screening. This method is interesting as the generated heat relates in principle to the enthalpy of formation. However, the typical temperature changes of the thin films are small due to the large contact area with the substrate that acts as a heat sink. Moreover, the change in emissivity of the film surface dominates the signal and makes difficult the determination of the temperature change. These difficulties are circumvented by using optical transmission in the visible part of the optical spectrum instead of thermal emissivity. Van der Molen et al.[40] and Van Gogh et al.[41] chose such a method to study the kinetics of hydride formation, in particular the role of the catalytic Pd caplayer and bufferlayers for YH$_x$ and LaH$_x$ switchable mirrors. Without a combinatorial approach, they would not have discovered that an AlO$_x$ buffer layer between the Pd caplayer and the Y switchable mirror has only a beneficial effect on the optical switching and the lifetime of the sample, if its thickness lies within 0.9 and 1.1 nm. Borgschulte et al.[42] showed that Lambert-Beer's law can be used to relate the measured optical transmission of a hydrogenated film to its hydrogen concentration. Basically, they found that in a two-phase mixture of a metal and its hydride, the concentration c of hydrogen increases linearly with the logarithm of the optical transmission T, i.e.:

$$\ln\left(\frac{T}{T_0}\right) \propto c \qquad (1.3)$$

where T_0 is the transmission in absence of hydrogen.

More recently, new techniques based on microsensor arrays were introduced for the high-throughput characterization of combinatorial thin hydride film libraries. Ludwig et al. use an opto-mechanichal method involving micro-

machined cantilevers arrays to follow the effect of volume expansion,[30,30] while
Hayden et al. developed an array of microhotplates MEMS to perform tem-
perature programmed desorption and infrared thermography measurements on
thin hydride films libraries.[43]

1.4 This Thesis

After an introduction on the basics thermodynamics of metal hydrides and a
description of the experimental techniques developed in this thesis (Chapter 2),
we start by considering the thin film PdH_x system (Chapter 3). Although both
Pd metal and its hydride are metallic, we demonstrate that the optical trans-
mission change during hydrogen sorption is high enough to record pressure-
optical transmission-isotherms (PTI). Similarly to what is done with conven-
tional pressure-concentration-isotherms, this allows us to obtain the thermody-
namic parameters (enthalpy and entropy) of the hydrogen sorption reactions.
In thin films, an important difference with bulk hydrides is the clamping to
the substrate. Hydrogen sorption is accompanied with expansion and large
stresses develop in thin films that influence enthalpy, entropy and hysteresis.
We therefore follow the changes in microstructure and residual stress with cy-
cling and correlate them to the isotherm change. This allows us to sort out the
various stress relaxation contributions to the isotherms. The large reduction in
stress observed also explains why optically determined enthalpy and entropy
measured on relaxed PdH_x films are in remarkable agreement with bulk values.

In chapter 4, we expand the PTI acquisition method to $Mg_yNi_{1-y}H_x$ thin
films with a compositional gradient in the Mg fraction y. This system is
particularly interesting, as two stoichiometric semiconducting hydrides, MgH_2
and the complex Mg_2NiH_4, are likely to coexist in the film. Additionally, as
we record the optical transmission of all compositions simultaneously, Mg- or
Ni-doping effects at intermediate compositions and the influence of specific
compositions (phase boundaries, eutectics) on the hydrogenation properties
are easily detected. We focus especially in this chapter on the hydrogenation
kinetics of gradient thin films. The rate of hydrogen absorption for all com-
positions is investigated by following the change in optical transmission upon
an sudden change of the hydrogen pressure. The pressure and temperature
dependence of the rate is then modeled with a two-step approach, and simple
expressions are derived for different rate-limiting step conditions. The model
is then compared with the experimental results on the $Mg_yNi_{1-y}H_x$ thin films.

At the contrary to Mg and Ni, Mg and Ti are immiscible, and no stable
bulk compound is expected at any composition in the metallic phase diagram.
However, one of the most surprising properties of the $Mg_yTi_{1-y}H_x$ films stud-
ied in chapter 5 is their structural stability: the initial high degree of mixing

is maintained upon hydrogen cycling, in contrast to other seemingly very similar Mg-transition metal systems such as Mg-V-H. This property is reflected in the optical isotherms, which show an unusual shape, incompatible with a sequential hydrogenation of Ti and Mg in the film. To understand this unusual hydrogenation, we develop a multi-site lattice gas model for optical isotherms and apply it on PTIs measured by hydrogenography on $Mg_yTi_{1-y}H_x$ sputtered thin films. The model reproduces the measured PTIs well and allows to derive experimental values of the chemical short-range order parameter (CSRO) s which are in good agreement with the local surrounding of Ti and s values determined by EXAFS.[44] Furthermore, the model gives information on the local lattice's departures from the average lattice given by Vegard's law. With Hydrogenography, we can then directly measure the influence of this chemical environment and geometrical changes around Mg-sites on their hydrogenation enthalpy.

We show in chapter 6 that Hydrogenography is also a very valuable method for performing exploratory search of new hydrogen storage materials. The remarkable properties of the $Mg_yTi_{1-y}H_x$ and the $Mg_yNi_{1-y}H_x$ systems in addition to the work of Yang et al.[45] on bulk Mg-Ni-Ti hydride motivated us to explore the $Mg_yNi_zTi_{1-y-z}H_x$ system. As we start from a metallic ternary phase diagram (Mg-Ni-Ti), we use two-dimensional compositional gradients deposited on large three-inch sapphire wafers. The hydrogen content is inferred from the change in optical transmission. The ability to record isotherms, enthalpy and entropy values for all the interesting compositions of the Mg-Ni-Ti phase diagram simultaneously demonstrates the power of Hydrogenography: it allows to quickly identify the range of compositions with favorable thermodynamics and kinetics properties. Furthermore, it provides data of unprecedented quality to study enthalpy-entropy compensation effects.

In chapter 7, we investigate the structural, optical and dc electrical properties of $Mg_yAl_{1-y}H_x$ gradient thin films. Alkali alanates form a promising class of complex hydrides in view of hydrogen storage, and in this chapter we aim at the synthesis of the $Mg(AlH_4)_2$ alanate from the elements. We use Hydrogenography to map simultaneously all the hydride forming compositions and the kinetics thereof in the gradient thin film. Additionally, we combine X-ray diffraction, visible/ultraviolet spectrophotometry, resonant nuclear analysis and Rutherford backscattering spectrometry to identify the metal and hydride phases formed. This complex approach is made necessary by the large-scale hydrogen-induced segregation of MgH_2 and Al that occurs in the Al-rich part of the film. Besides MgH_2, an additional semiconducting phase is found by electrical conductivity measurements around an atomic [Al]/[Mg] ratio of 2 (y = 0.33). This suggests that the film is partially transformed into $Mg(AlH_4)_2$ at around this composition.

Chapter 2

Theoretical and experimental background

2.1 Thermodynamics of metal-hydrides

2.1.1 Introduction

In this section we present the basic thermodynamics of metal hydride systems. We discuss the general thermodynamics of a first and second order phase transition in metal hydrides and we derive the Van 't Hoff equation. In addition, we briefly discuss the simple lattice gas model. Finally we study the phase diagrams and the pressure-composition isotherms of PdH and NbH. These typical systems illustrate the thermodynamics of metal hydrides. In addition, they help to elucidate the entropy contribution of the atomic hydrogen in the metal. This contribution is commonly undervalued by the hydrogen storage community.

2.1.2 First order phase transition between two hydride phases

A metal M can absorb hydrogen when it is exposed to molecular hydrogen gas at a pressure p. The atomic hydrogen absorbed in the metal may form two or more phases. In this subsection we discuss the thermodynamics of a first order phase transition between a low hydrogen concentration α-phase and a high concentration β-phase.

The chemical reaction for the transition from the α- to the β-phase is

$$2\text{MH}_{c_\alpha} + (c_\beta - c_\alpha)\text{H}_2 \Longrightarrow 2\text{MH}_{c_\beta} \qquad (2.1)$$

where c_α and c_β are the hydrogen concentrations in the α- and β-phase respectively. During the phase transition, there is a coexistence between *three* hydrogen phases, namely the molecular hydrogen gas phase and the two metal hydride phases. The condition for equilibrium at a temperature T is expressed in terms of the chemical potential of the gas phase $\mu_{H_2}(p, T)$, the hydride

phases $\mu_H^\alpha(c_\alpha, T)$ and $\mu_H^\beta(c_\beta, T)$, and of the metal host in the two hydride phases $\mu_M^\alpha(c_\alpha, T)$ and $\mu_M^\beta(c_\beta, T)$

$$2\left(c_\alpha \mu_H^\alpha + \mu_M^\alpha\right) + (c_\beta - c_\alpha)\mu_{H_2} = 2\left(c_\beta \mu_H^\beta + \mu_M^\beta\right),\tag{2.2}$$

where we have omitted the dependences on p, T, c_α and c_β. The chemical potential is related to the partial molar enthalpy $\bar{H}$ and the partial molar entropy $\bar{S}$ through the relation

$$\mu = \left(\frac{\partial H}{\partial n}\right)_{p,T} - T\left(\frac{\partial S}{\partial n}\right)_{p,T} = \bar{H} - T\bar{S}.\tag{2.3}$$

Using this relation to express all the chemical potentials in eq. (2.2) in partial molar quantities, we find

$$\Delta H_{\alpha\to\beta} = T\Delta S_{\alpha\to\beta}\tag{2.4}$$

where

$$\Delta H_{\alpha\to\beta} = 2\frac{H_\beta - H_\alpha}{c_\beta - c_\alpha} - \bar{H}_{H_2}\tag{2.5}$$

and

$$\Delta S_{\alpha\to\beta} = 2\frac{S_\beta - S_\alpha}{c_\beta - c_\alpha} - \bar{S}_{H_2}\tag{2.6}$$

are the reaction enthalpy and the entropy change respectively in reaction (2.1), in which we have used the definitions

$$H_\nu = c_\nu \bar{H}_H^\nu + \bar{H}_M^\nu\tag{2.7}$$

$$S_\nu = c_\nu \bar{S}_S^\nu + \bar{S}_M^\nu\tag{2.8}$$

and $\nu = \alpha$ or β. The partial molar entropy of molecular hydrogen gas is given by[46]

$$\bar{S}_{H_2} = -R\ln(p) + \frac{7}{2}R\ln\left(\frac{eT}{9.13}\right).\tag{2.9}$$

The weak temperature dependence is usually neglected. The partial molar entropy may then be written as

$$\bar{S}_{H_2} = -R\ln\left(\frac{p}{p_0}\right) + S_{H_2}^0,\tag{2.10}$$

where R is the gas constant and $S_{H_2}^0 = 131$ J K^{-1}(mol H$_2$)$^{-1}$ is the standard molar entropy (when $p = p_0 = 1.013 \times 10^5$ Pa and $T = 298$ K) of the hydrogen gas. Inserting this expression for the entropy of the molecular hydrogen gas in eq. (2.4) leads directly to the Van 't Hoff equation

$$\ln\left(\frac{p}{p_0}\right) = \frac{\Delta H_{\alpha\to\beta}}{RT} - \frac{1}{R}\left(2\frac{S_\beta - S_\alpha}{c_\beta - c_\alpha} - S_{H_2}^0\right).\tag{2.11}$$

The term between parentheses on the right-hand side is known as ΔS. The first term between these parentheses represents the metal hydride contribution, which we denote as

$$S^\dagger = 2\frac{S_\beta - S_\alpha}{c_\beta - c_\alpha}. \tag{2.12}$$

2.1.3 Second order phase transition in metal hydrides

The simple elemental hydrides often have a critical temperature T_c above which the phase transition becomes second order. In this case we shall refer to the hydride phase, since we cannot distinguish between the α- and the β-phase.
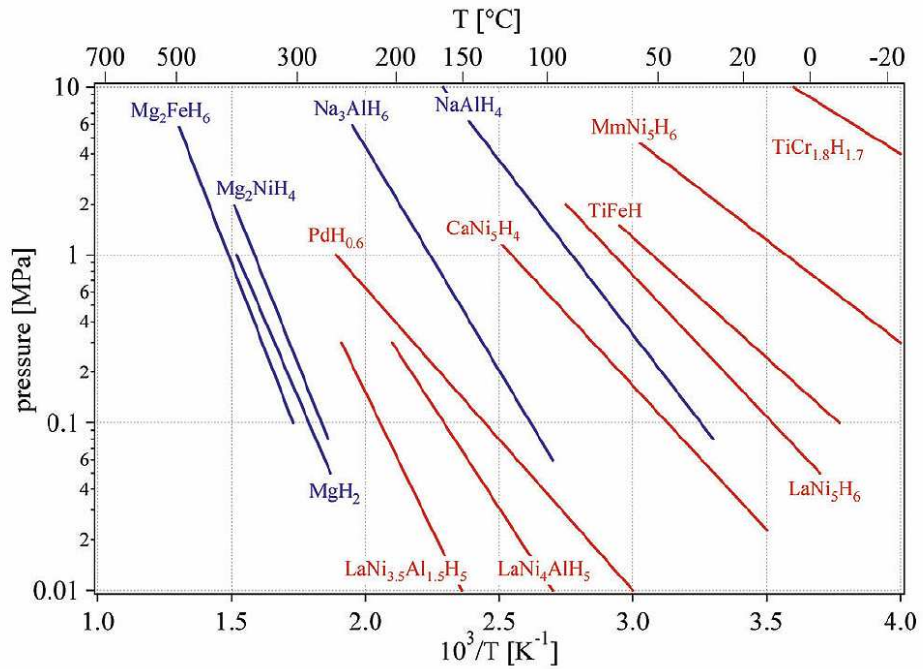
Figure 2.1: Van't Hoff plots of some selected hydrides(Figure from A. Züttel [47]). Complex metal hydrides are indicated by a blue color and interstitial hydrides are indicated with a red color.

The following condition holds when the metal hydride phase is in equilibrium with the gas phase

$$2\mu_H(c_H, T) = \mu_{H_2}(p, T). \tag{2.13}$$

The factor 2 on the left-hand side accounts for the *atomic* nature of the hydrogen in the metal in contrast to the *molecular* hydrogen in the gas phase. This relation can be expressed in terms of the partial molar quantities

$$2\left(\bar{H}_H - T\bar{S}_H\right) = \bar{H}_{H_2} - T\bar{S}_{H_2}. \tag{2.14}$$

Using, once again, the expression for the partial molar entropy of molecular hydrogen gas in eq. (2.10) we find

$$\ln\left(\frac{p}{p_0}\right) = \frac{\Delta H}{RT} - \frac{\Delta S}{R}, \tag{2.15}$$

where

$$\Delta H = 2\bar{H}_H - \bar{H}_{H_2}, \tag{2.16}$$

and

$$\Delta S = 2\bar{S}_H - S_{H_2}^0. \tag{2.17}$$

The first term is the hydride contribution, which we denote as

$$S^\dagger = 2\bar{S}_H. \tag{2.18}$$

In summary, the thermodynamics of the first and second order phase transition is described by the Van 't Hoff equation

$$\ln\left(\frac{p}{p_0}\right) = \frac{\Delta H}{RT} - \frac{\Delta S}{R}, \tag{2.19}$$

where ΔH is the heat of formation of the hydride phase and ΔS is the difference between the partial molar entropy of the hydride phase and the standard entropy of hydrogen gas. We would like to stress the difference of the hydride contributions to this term between the first and second order phase transitions given in eqs. (2.12) and (3.9). Figure 2.1 shows Van 't Hoff plots for various metal hydride systems.

2.1.4   Mean field treatment of the lattice gas model

In this subsection we discuss briefly the lattice gas model, which can be used to describe the thermodynamics of the interstitial hydrides.

When a hydrogen atom is absorbed in the metal it dilutes the lattice, making the environment more favorable for another hydrogen atom. Thus, there is an elastic interaction between the hydrogen atoms, known as the H-H interaction. We include this interaction in the lattice gas model using a mean field approximation. The use of a mean field approximation is justified by the long range of the elastic interaction.

In this model there are N identical lattice sites, which can be occupied by at most one hydrogen atom. When the hydrogen enters a lattice site it gains an energy ϵ_0. A hydrogen atom can interact with z nearest neighbors by the H-H interaction interaction ϵ. The total energy of the system is given by

$$E = N_H\epsilon_0 + \frac{1}{2}z\frac{N_H^2}{N}\epsilon, \tag{2.20}$$

where N_H are the number of hydrogen atoms in the lattice. The second term on the right-hand side describes the interaction between the N_H hydrogen atoms with an averagely occupied surrounding zN_H/N and the factor $\frac{1}{2}$ is included to avoid double counting. The partition function of this system is given by

$$Z = \frac{N!}{N_H!\,(N! - N_H!)}\exp\left(\frac{N_H\epsilon_0 + \frac{1}{2}z\frac{N_H}{N}\epsilon}{k_BT}\right) \tag{2.21}$$

where k_B is Boltzmann's constant. The combinatorial factor incorporates the number of distinguishable configurations of the system. We can determine the chemical potential from the partition function in eq. (2.21) within Sterlings approximation[a]

$$\mu_H = k_BT\ln\left(\frac{c_H}{1 - c_H}\right) + \epsilon_0 + \epsilon z c_H, \tag{2.22}$$

where the hydrogen concentration is given by

$$c_H = \frac{N_H}{N}. \tag{2.23}$$

We can derive the patrial molar quantities $\bar{H}_H$ and $\bar{S}_H$ from the chemical potential

$$\bar{H}_H = \left(\frac{\partial\left(\mu_H\backslash T\right)}{\partial\left(1\backslash T\right)}\right)_{c_H} = \epsilon_0 + \epsilon z c_H \tag{2.24}$$

$$\bar{S}_H = -\left(\frac{\partial\mu_H}{\partial T}\right)_{c_H} = -RT\ln\left(\frac{c_H}{1 - c_H}\right) \tag{2.25}$$

The gas constant R is introduced to express all quantities per mol H. This partial molar entropy accounts for the different configurations of the system and is therefore referred to as the *configurational* entropy. We use this expression in our discussion of the PdH and NbH systems in Sec. 3.3.1.

2.2   Experimental techniques

2.2.1   Chemical gradient deposition by sputtering

Our thin films are prepared by dc/rf argon sputtering.[48] The addition of reactive gases (H_2,O_2) during deposition is also possible. Figure 2.2 shows the inside of the AJA 7-gun ultra-high vacuum dc/rf magnetron co-sputtering system (base pressure of 10^{-7} Pa). The targets are placed off-axis with respect to the circular substrate holder to create a chemical metallic gradient. For the deposition of binary A_yB_{1-y} compositional gradients of element A and B, we use targets facing each other. For ternary $A_yB_{1-y}C_{1-y-z}$ gradients, the elements

---

[a] $\ln(n!) \approx n\ln(n) - n$

A, B and C are positioned every 120°. Homogeneous thickness cap(layers) are obtained by rotating the sample stage during deposition. Two different sample stages are available, with either radiative heating (up to 900 K) and substrate bias or cooling to liquid N_2 temperature. The steepness of the compositional gradients and the relative amount of each deposited element is controlled by the tilt angle and the power applied to the targets. These parameters thus determine the compositional range of the sample. As an unwanted side effect of the deposition technique the thickness of the film generally varies. The deposition rate in the center of the sample is measured with a quartz crystal and calibrated by profilometry.
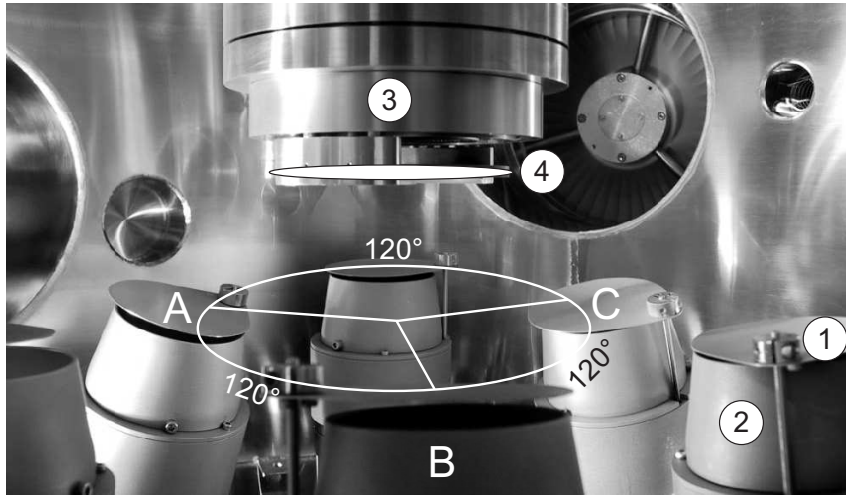
Figure 2.2: Photograph inside the AJA sputtering chamber. Six sputter guns are visible, each of them containing a different element/alloy. Here the geometric configuration to deposit ternary gradients is shown. The guns containing the A, B and C elemental targets are positioned every 120° on a circle. The targets are placed off-axis with respect to the circular substrate to create a chemical metallic gradient with composition $A_yB_{1-y}C_{1-y-z}$ onto the sample. (1) shutter, (2) sputter gun, (3) rotatable sample stage, (4) sample.

After deposition, the exact compositional scale is determined by Rutherford backscattering spectrometry using 2 MeV He^+ ions with a 1 mm^2 spot size on films deposited in parallel on glassy carbon substrates. The carbon substrates do not contribute to the background for energies above approximately 0.5 MeV, and for thicknesses below 200 nm, the metal peaks are generally well separated at higher energies. From RBS the exact (within 1-2%) deposition rate of each element in the layer is determined for every position probed. Figure 2.3(a) shows the depositions rates in Å/s as a function of position on the sample for a binary Mg_yNi_{1-y} gradient. Used powers are 118 W (rf) and 21 W (dc) for Mg, respectively Ni, and a tilt angle of 8 mm. Target are facing each other. The corresponding Mg fraction y dependence on position is shown in

(b). About half of the Mg-Ni phase diagram is deposited at once. The *line* corresponds to a Boltzmann fit and is used to determine the compositional dependence of subsequently measured quantities on the sample, such as the optical transmission, XRD signal, resistivity, etc.
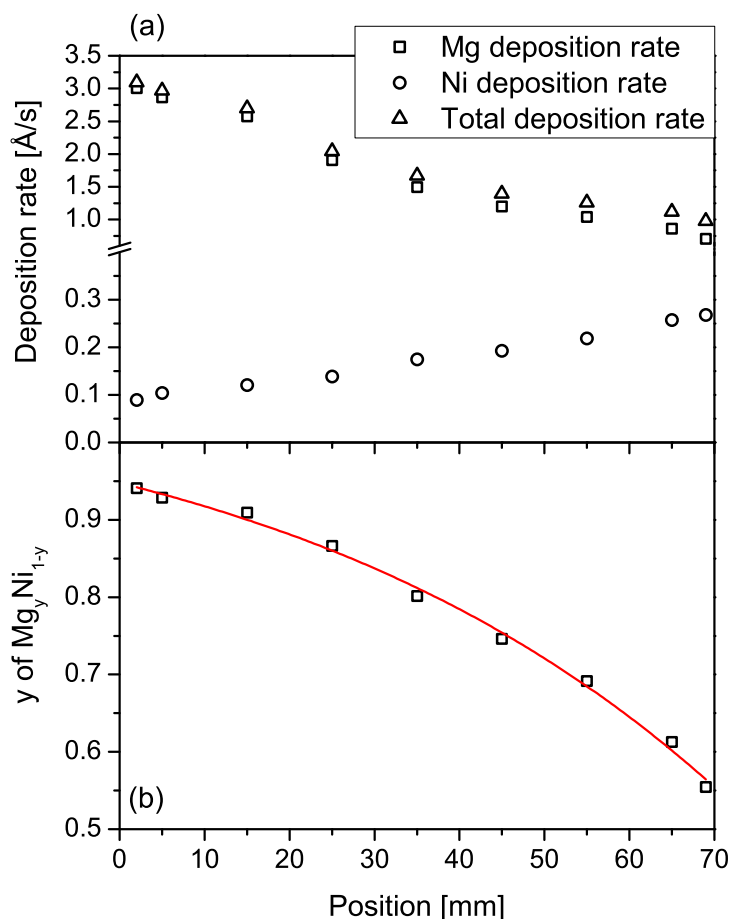
Figure 2.3: (a) Mg (rf 118 W), Ni (dc 21 W) and total deposition rate as function of position for a Mg_yNi_{1-y} compositional gradient. (b) *Symbols*, Corresponding Mg fraction y. *Line*, Boltzmann fit.

As can been seen in Fig. 2.4, samples deposited in subsequent runs still share the same composition scale. This figure also illustrate an alternative method to estimate the compositional gradient: by keeping the same geometry and power applied to the targets, single-element calibration wedge-shaped thin films are independently deposited. Their thickness is then measured by profilometry. Assuming that the bulk molar volume applies, the [A]:[B] ratio

r is determined:

$$r = \frac{t_A V_B}{t_B V_A} \tag{2.26}$$

with $t_{A,\,B}$ the thickness and $V_{A,\,B}$ the molar volume of the elements A and B. The atomic fraction of A is then directly $y = r/(1+r)$.
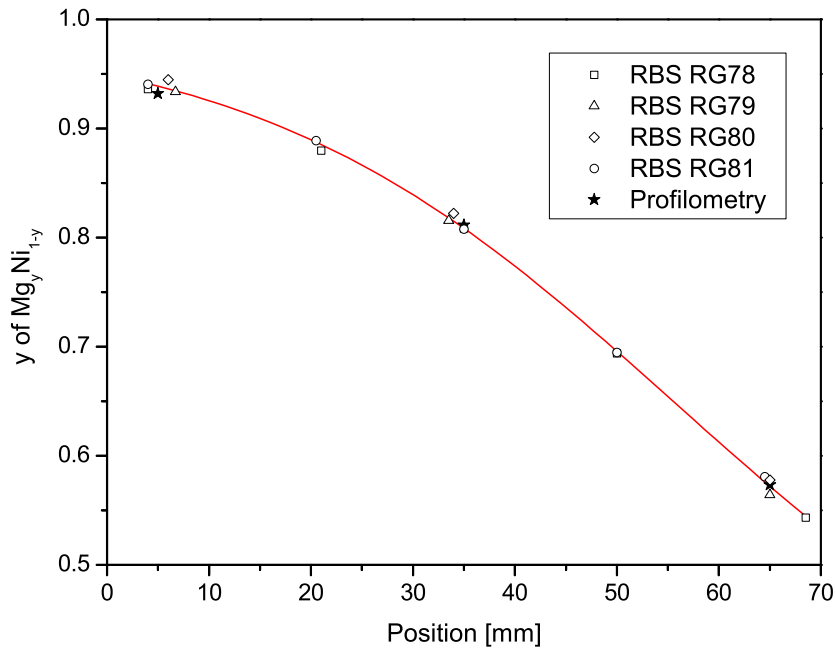
Figure 2.4: Compositional dependence of the Mg atomic fraction y in $Mg_y Ni_{1-y}$ gradients deposited in subsequent runs. Each *open symbol* corresponds to a different sample. The *stars* are compositions determined by profilometry on separately deposited single-element wedge layers.

2.2.2 Hydrogenography setup

The optical transmission as a function time, hydrogen pressure or temperature is recorded in the Hydrogenography setup. The whole cell is placed in an oven, which can control temperature from 305 K to 573 K. A schematic representation of the hydrogenography setup is shown in Fig. 2.5. The complete thermal equilibration of the setup is verified by comparing the output of two PT-100 resistors placed at different locations in the oven, one of them being in contact with the sample holder. A 150 W diffuse white light source (the projector) illuminates the sample from the substrate side, and a 3-channel (RGB) SONY XC-003 Charged-Coupled Device (CCD) camera continuously monitors the transmitted light as a function of hydrogen pressure. The 3-channel transmission intensities are added, resulting in a 1.1 to 3.3 eV photon energy bandwidth. The use of a camera makes possible the recording of the transmission for all compositions y *simultaneously*. The gas pressure increase is controlled by a MKS 248/250 forward Proportional-Integral-Differential (PID) system that regulates both inlet and outlet gas flows using electronic valves and a roughening pump. 0.1 % and 4 % hydrogen in argon gas mixtures and pure H_2 gas are used to achieve hydrogen (partial) pressures between 10^{-1} Pa$< p_{H_2} < 10^6$ Pa. Single crystal sapphire windows with a diameter of 76 mm withstand the large pressure and temperature differences.
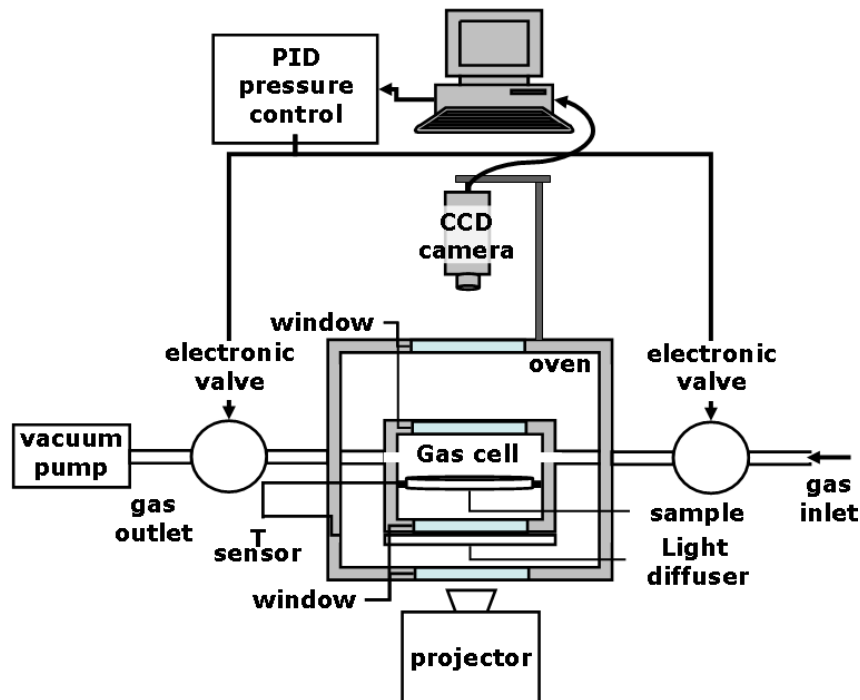
Figure 2.5: Schematic representation of the Hydrogenography setup.

Color neutral filters are used to accommodate the large difference in optical

contrast between metallic and hydrided states and to calibrate the absolute transmission value. To check the linearity of the CCD in position, the transmission T of a wedge-shaped Mg metallic thin film deposited on glass with thickness 30-90 nm is measured. Three different filters are needed to cover the range of transmission shown in Fig. 2.6. According to Lambert-Beer law the logarithm of the transmission varies linearly with the thickness t:

$$\ln(T) = -\alpha t \qquad\qquad (2.27)$$

where α is the Mg absorption coefficient. We find $\alpha = 0.11$ nm^{-1}. This is in fair agreement with the 1.1 to 3.3 eV photon-energy averaged absorption coefficient of 0.12 nm^{-1} calculated from the Mg dielectric function in Palik.[49] This also shows that with these illumination conditions, absolute transmission of 10^{-4} are measurable, two orders of magnitude below the level routinely reached by conventional visible spectrometers.
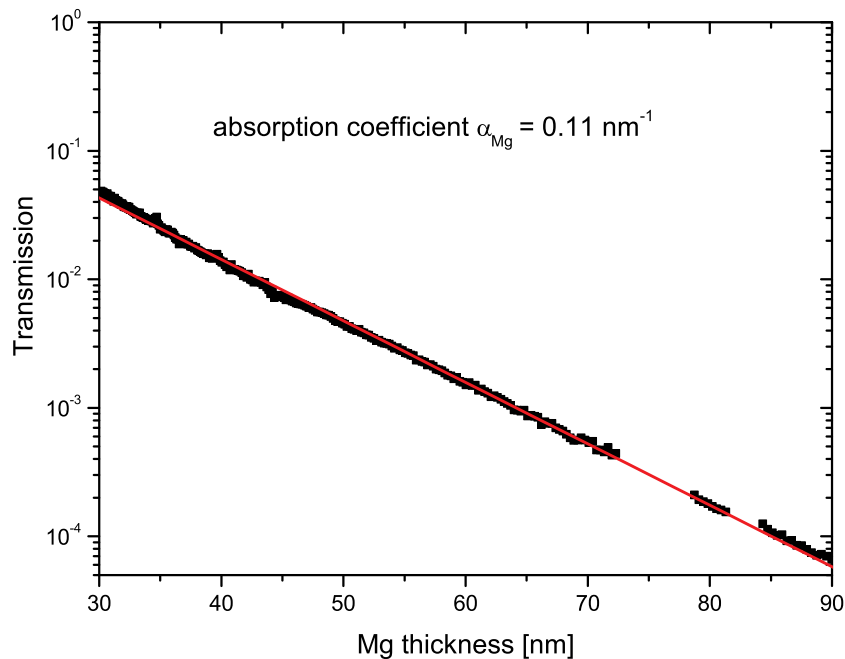
Figure 2.6: *Symbols*: optical transmission of a metallic Mg wedge thin film as a function of film thickness. Data are missing around 75 and 82 nm due to pinholes. The *line* is a linear fit of the logarithm of the transmission.

2.2.3 UHV fiber optics UV/VIS spectrometer

Thin films studied in the Hydrogenography setup have to be transported in air from the deposition setup. While the Pd capping layer provides sufficient protection against oxidation for Mg-transition metal films, this is no longer the case for alkali based films (Na or Li codeposited with Al or B) needed for the study of alkali alanate or boranates hydrogen storage materials. We therefore designed a ultra-high vacuum fiber optic reflection and transmission spectrometer operating in the ultraviolet/visible for fundamental optical characterization of alanate and boranate gradient thin films. The setup is designed to also follow the transmission and/or reflection as a function of time, temperature or H_2 pressure as in the Hydrogenography setup.

Figure 2.7 displays a photograph and scheme of the complete setup, with a 4-gun dc/rf sputter chamber (Ar + H_2) (1), and UHV transfer (7) to the fiber optic spectrometer (3) through the load-lock (2). Dynamic H_2 pressure from 10^{-4} to $2 \cdot 10^2$ Pa and static pressures up to 10^5 Pa can be applied in the spectrometer chamber during the R & T measurements. A separate chamber (4) for pressures up to 10^6 Pa is attached to the spectrometer chamber. It include viewports to monitor the light coming from a He-Ne laser (8) transmitted through the sample.
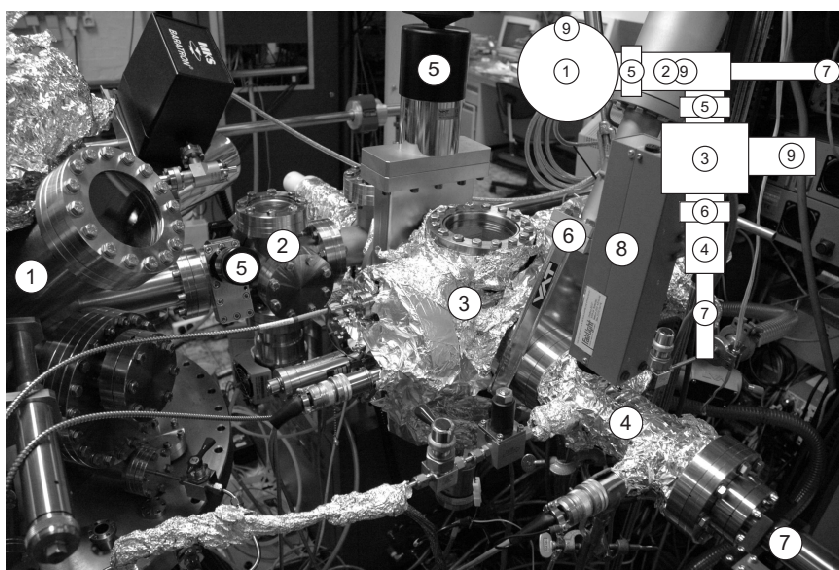
Figure 2.7: Photograph and schematic representation of the UHV UV/VIS fiber optic spectrometer and sputtering setup. (1) 4-gun sputter chamber, (2) load-lock, (3) Fiber optic spectrometer chamber, (4) 10 bar hydrogenation chamber, (5) 10^5 Pa-UHV valve, (6) 10^6 Pa-UHV valve, (7) transfer arm, (8) He-Ne laser, (9) turbomolecular pump.

The optical reflection and transmission spectra in the range 1.1-6.2 eV

photon-energy range (wavelength 1100-200 nm) are recorded with two dispersive OCEAN OPTICS HR4000 spectrometers. A tungsten-halogen light source is used for the visible, and a deuterium source for the UV (wavelength 400-190 nm) ranges. Reflection and transmission are measured by means of two optical fibers facing each other at normal incidence. The 6 radially distributed cores of a 7-core fiber serve for the illumination, while the remaining central core carries the reflected light to the first spectrometer through a light splitter. The light transmitted through the sample is collected by a second, single-core fiber facing the illumination fiber connected to the second spectrometer. Figure 2.8 shows the inside of the spectrometer. The illumination and reflection (1), and transmission (2) fibers are attached to a 100 mm long clap (4) operated from the outside by a manipulator (5) through the UHV flange (6). The light spot size on the 50 x 15 x 0.53 mm^3 substrate (3) is $\approx$ 1 mm^2. The optical clap closes with a 10 mum vertical position repeatability on any spot along the 50 mm long gradient sample. Longitudinal positioning is done with the transfer arm (7). Resistive heating along the clap is implemented.
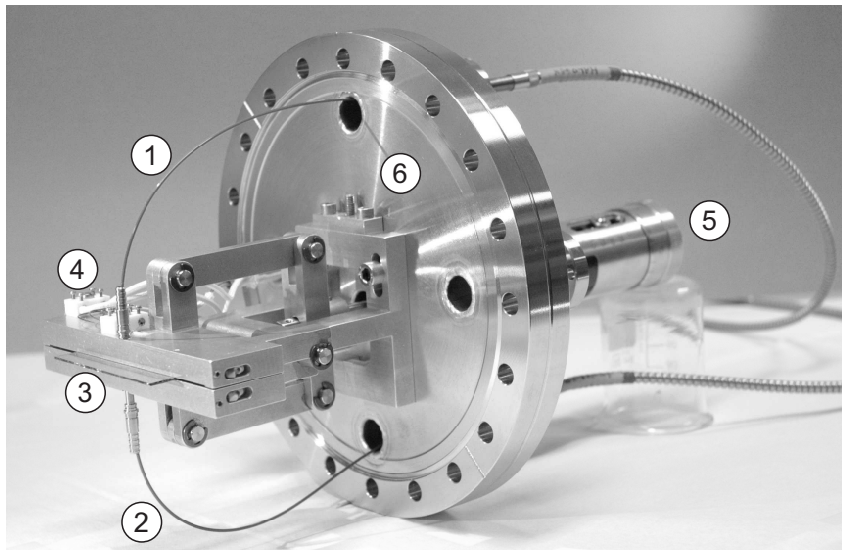
Figure 2.8: Photograph of the reflection and transmission optical clap. (1) Illumination and reflection fiber, (2) transmission fiber, (3) substrate, (4) movable clap with resistive heating, (5) manipulator to open/close the clap, (6) UHV flange.

The sample reflectance R is determined in the following way:

$$R = \frac{I_R(\text{sample}) - I_R(\text{background})}{I_R(\text{Al}) - I_R(\text{background})} \cdot R_{PE}(\text{Al}) \tag{2.28}$$

where $I_R(\text{sample})$, $I_R(\text{background})$ and $I_R(\text{Al})$ denote the intensity reflected in the reflection spectrometer in presence of the sample with light source on, no sample with light source off, and of the reference Al coated sample with light source on, respectively. $R_{PE}(\text{Al})$ is the reflectance of the same Al sample measured independently in a Perkin-Elmer Lambda 900 diffraction grating spectrometer.

The transmittance T is similarly:

$$T = \frac{I_T(\text{sample}) - I_T(\text{background})}{I_T(\text{free beam}) - I_T(\text{background})} \cdot \frac{T_{PE}(\text{substrate})}{T_{FS}(\text{substrate})} \tag{2.29}$$

where $I_T(\text{sample})$, $I_T(\text{background})$ and $I_T(\text{free beam})$ denote the intensity transmitted in the transmission spectrometer in presence of the sample with light source on, no sample with light source off, and of the free beam (no sample or substrate) with light source on, respectively. $T_{PE}(\text{substrate})$ is the transmittance of the bare substrate measured independently in a Perkin Elmer Lambda 900 diffraction grating spectrometer, and

$$T_{FS}(\text{substrate}) = \frac{I_T(\text{substrate}) - I_T(\text{background})}{I_T(\text{free beam}) - I_T(\text{background})} \tag{2.30}$$

the transmission of the substrate measured in the fiber optics spectrometer. The use of the correction factor $T_{PE}(\text{substrate})/T_{FS}(\text{substrate})$ is made necessary by the close proximity of the reflection and transmission fiber probes: Due to the higher index of refraction of the substrate materials, the amount of light that reaches the transmission fiber in presence of a substrate is considerably increased (by about 120% for a sapphire substrate) with respect to the free-beam situation.

The optical spectra of a 10 nm Pd film deposited on a 0.53 mm thick sapphire substrate measured with our fiber optic spectrometer are compared with the Perkin Elmer spectra in Fig. 2.9. They are in good agreement up to a photon-energy of 6 eV, which is capital for the characterization of wide-band gap insulators such as the alakali alanates.[50]
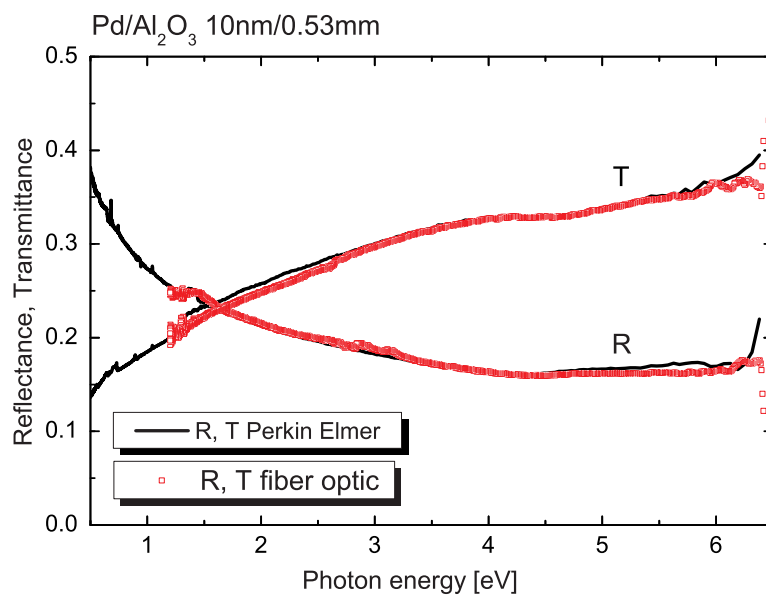
Figure 2.9: Calibration of the fiber optic spectrometer: Reflectance R and transmittance T of a 10 nm Pd thin film on a 0.53 mm sapphire substrate. *Lines*, R & T measured with a commercial Perkin Elmer Lambda 900 diffraction grating spectrometer. *Symbols*, R & T measured with our fiber optic UHV spectrometer.

2.2.4 HI-STAR area X-ray detector

The structural characterization is performed in a Bruker D8 Discover X-ray diffractometer (XRD) (Cu-Kα, λ=1.5418 Å) equipped with an Euler sample goniometer, a HI-STAR area detector and the GADDS software. The 2θ and χ axis denote the two directions of the detector. A beryllium hemispherical dome is mounted on the sample for controlling (hydrogen) pressures between 1 and 10^5 Pa. The residual stress in a film can be measured by XRD with the $\sin^2\psi$ method.[51] The method consists in measuring a given diffraction peak at $2\theta_{hkl}$ as a function of Euler angle ψ. This section presents the geometry of our XRD setup and the relation of the detector angle χ, the sample angle χ_S and the diffraction angle θ with the Euler angle ψ (See Fig. 2.10). ψ denotes the

Figure 2.10: Geometry of the XRD setup, including the 2D HI-STAR detector. The *ellipse* is the locus of points meeting the diffraction condition in a plane normal to the incoming X-ray beam $\vec{S}$. $\vec{D}$ is the diffracted beam for a particular detector angle χ, and $\vec{n}$ the corresponding normal to the diffraction plane. The angle between the normal to the substrate ($\vec{z}$ axis) and $\vec{n}$ is the Euler polar angle ψ used in stress measurements (See Chap. 3.) The *Dashed arrows* meet the diffraction condition in the yz plane, i.e for a 1D detector.

angle between a XRD reflection direction and the normal to the substrate (See Fig. 2.11). The ψ angle is corresponding to the rocking curve angle in a 1D geometry, though ψ does not stays in the same plane when χ is varied. This has implications if the sample is textured. Additionally, the residual stress in a film can be measured with the $\sin^2\psi$ method.[51] The method consists in measuring a given diffraction peak at $2\theta_{hkl}$ as a function of Euler angle ψ (See Sec. 3.2.2). To reach ψ values up to 90°, the sample angle χ_S between the

z-axis and the normal to the substrate has to be also varied in the xz-plane.

If $\mathbf{S}$ and $\mathbf{D}$ are the source and diffracted beam directions, respectively, then $\mathbf{D} \times \mathbf{S}$ is in the diffraction plane and

$$\mathbf{n} = (\mathbf{D} + \mathbf{S}) \times (\mathbf{D} \times \mathbf{S}) \qquad (2.31)$$

is the normal direction to the diffraction plane. For $\chi_S = 0$, ψ is then directly the angle between $\mathbf{n}$ and the z-axis in Fig. 2.10. Figure 2.12 shows the ψ angle as a function of detector angle χ and three sample χ_S angles for a diffraction $\theta = 20°$. Note that within the detector range ($\chi < 30°$), $\psi \geq \chi + \chi_S$.
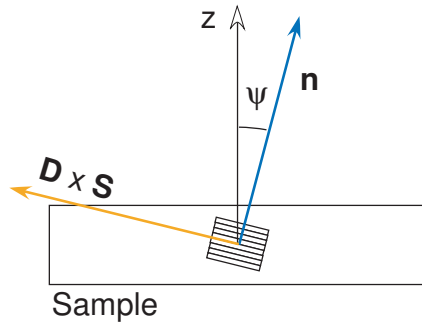
Figure 2.11: Euler angle ψ.
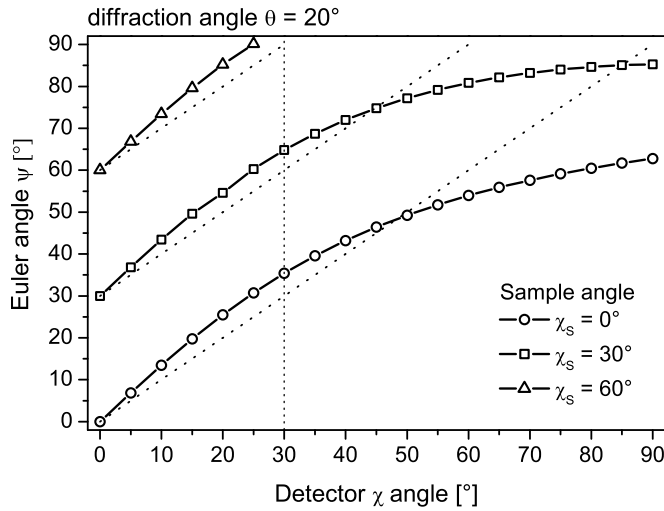
Figure 2.12: polar angle ψ between the diffraction plane and the substrate plane as a function of detector χ angle, for sample angles $\chi_S = 0°$, $30°$ and $60°$. Diffraction angle $\theta = 20°$. The *dotted lines* correspond to the $\psi = \chi + \chi_S$ relation. The *vertical line* indicates the limit of the HI-STAR detector range.

Chapter 3

Hydrogenation thermodynamics in metallic hydrides by optics: the PdH$_x$ case

3.1 Introduction

The standard approach for the search of new hydrogen storage materials is to synthesize bulk samples and to use volumetric,[12,52] gravimetric[53] or calorimetric[54] techniques to follow (de)hydrogenation or heat evolution in the sample. The great disadvantage of this approach is that a bulk sample is needed for each investigated chemical composition. Thin films provide an interesting alternative to bulk, as they can be deposited in a combinatorial way to screen potentially interesting materials systems very efficiently. Moreover, surface science combined with optical detection techniques allow for a fast screening of the hydrogen absorbing compositions.[39,55–57]

There are various reasons to start this thesis by the hydrogenography of PdH$_x$ thin films. It is natural to establish the method for a binary hydride first, with well-known hydrogenation thermodynamic properties, both in bulk and thin film. PdH$_x$ is also catalytically active to split the hydrogen molecule and not prone to oxidation at room temperatures. It can therefore be studied as a single layer on a substrate, where most hydride systems need an additional capping layer to be handled in air. Many systems studied optically so-far (YH$_x$, Mg-Transition metal-H) exhibit a metal-to-semiconductor transition during hydrogenation, resulting in a large contrast in optical transmission and reflection. This large optical contrast in the visible range between the metals and the semiconductor hydrides facilitate the optical measurements. However, as some potential hydrogen storage materials may not undergo a metal-to-semiconductor transition, it is important to demonstrate the applicability of hydrogenography to *metallic* hydrides like PdH$_x$.

The palladium-hydrogen system is considered as an archetypal metal hydride system and has been extensively studied in bulk,[58,59] cluster[60,61] or thin film form.[62,63] Pressure-concentration-isotherms (PCI) of PdH$_x$ exhibit wide

plateaus at the equilibrium pressure where a transition from an α phase with a low solubility of hydrogen to a non-stoichiometric β Pd-hydride phase takes place. As hydrogen absorption induces changes in the electronic density of states near the Fermi edge, the $\alpha \rightarrow \beta$ transition can also be detected with visible light.[64] From Lambert-Beer's law, the logarithm of the optical transmission $\ln(T/T_{\mathrm{M}})$ is expected to vary linearly with the hydrogen concentration in a film of initial transmission T_{M}.[56] This is confirmed by joint electrochemical and optical measurements.[65,66] We will show here that this enables us to record pressure–*optical-transmission*–isotherms (PTI) that are equivalent to PCIs obtained with standard volumetric or gravimetric methods,[a] with the advantage that, due to the thin film geometry, the usual heat and diffusional issues encountered during the recording of PCIs are minimized. This allows to record a PTI in a few hours and opens up new possibilities to quickly compare subsequent PTIs taken on the same system under different conditions.

The 3.54% lattice mismatch[67] (11% in volume) between the α and the β phases results in an expansion upon hydrogenation that generates large compressive stresses. Thin films are clamped to the substrate and therefore cannot expand freely in the in-plane direction. Thus hydrogenation of Pd thin films generates large compressive in-plane stresses and strains[68] and microstructural defects.[69]

The measurements of isotherms in thin films and bulk are influenced by the potential presence of these various microstructural defects, like (sub)surface sites, dislocations, grain boundaries or vacancies.[69] However, in thin films with a thickness > 50 nm,[b] microstructural defects generally have a marginal effect on the isotherm shape and hysteresis width, the main contribution coming from stress and strain.[69,71,72] Schematically, stress and strain may affect four features of the isotherms: (i) Hysteresis width: the coherency strain at the interface between the transforming α and β phases is sufficient to open an hysteresis in pressure.[72,73] Coherent strain induced by the elastic boundary condition (i.e. clamping to the substrate) widens the hysteresis further.[74] (ii) Critical temperature T_c: for clamped films, the elastic boundary condition decreases the effective H-H interaction energy and reduces T_c relatively to bulk.[75] (iii) Phase boundaries: comparative studies of films deposited on soft and hard substrates show that the α phase solubility limit $c_{\alpha,\mathrm{max}}$ increases with increasing stress in the film.[76,77] (iv) Slope of the coexistence plateau: inhomogeneously distributed strains in the film result in a distribution of site energies and therefore in a sloping plateau.

For example, Lee et al.[62] report that extensive H-cycling is necessary to obtain non-sloping, reproducible PCIs on thin PdH$_x$ films deposited on sapphire substrate, without however giving details about the film microstructure.

---

[a] Note that $\ln(T/T_0)$ only gives information about hydrogen concentration differences, as the concentration in the metallic state is not *a priori* known.

[b] For even thinner films (thickness $\leq$ 10 nm), finite size effects[70] might become preponderant.

On the contrary, Feenstra et al.[63] attribute the good agreement of their PdH_x isotherms with bulk results to the use of rough (10 μm rms) quartz substrates and pre-annealing.

Ultimately, the repeated stress-strain cycles induced by hydrogen ab- and desorption result in large plastic deformations of the films like buckles.[78] Buckling is an effective mechanism to reduce stress locally, e.g. the elastic energy stored in a clamped film can be reduced by more than 90% in the buckled areas of Nb films of comparable thickness.[79] It is therefore of primary importance to understand the stress relaxation processes active in hydride thin films to compare hydrogenography with bulk results.

This chapter is divided in two parts. In the first part, we present a quasi-equilibrium method to record the hydrogen pressure-transmission-isotherms of thin hydride films. The method is demonstrated with the Pd-H system. The entropy ΔS_0 and enthalpy ΔH of both hydrogen absorption and desorption processes are determined from the temperature dependence of the plateau pressure in the PTIs. The central result of this part is that the ΔS_0 and ΔH values determined optically are in remarkably good agreement with experimental bulk and thin film values. We also show that the non-standard entropy value of PdH_x can be explained if the configurational and vibrational contributions to ΔS_0 are taken into account. Finally, we present an alternative off-equilibrium method to determine the equilibrium plateau pressure and compare its results to the quasi-equilibrium approach.

In the second part, we use hydrogenography to measure the PTIs and kinetics of PdH_x films as a function of hydrogen ab/desorption cycle number. The evolution in PTI shape and hysteresis width is correlated to a) the microstructure and in-plane stress measured by X-ray diffraction (XRD) and b) the surface morphology by Scanning electron microscopy (SEM), atomic force microscopy (AFM) and optical microscopy in reflection and transmission. This allows us to sort out the various stress relaxation contributions to the isotherms and leads to an improved assessment of the comparability between thin film PTIs and conventional bulk PCIs.

3.2   Experimental

3.2.1   Film deposition

Polycrystalline Pd (65 nm) thin films are prepared in a ultra-high-vacuum dc magnetron co-sputtering system (base pressure 10^{-7} Pa, deposition pressure 0.3 Pa) at room temperature on 70 x 5 mm^2 sapphire substrates.

3.2.2   Structural characterization

The structural characterization is performed in a Bruker D8 Discover X-ray diffractometer (XRD) (Cu-Kα, λ=1.5418 Å) equipped with an Euler sample

goniometer, a HI-STAR area detector and the GADDS software. The 2θ and χ axis denote the two directions of the detector. A beryllium hemispherical dome is mounted on the sample for controlling (hydrogen) pressures between 1 and 10^5 Pa. The residual stress in the film is measured by XRD with the $\sin^2\psi$ method.[51] The method consists in measuring a given diffraction peak at $2\theta_{hkl}$ as a function of Euler angle ψ. Here the (111) reflection is used, as it is the only one to yield reasonable intensity for all angles. ψ denotes the angle between the [111] direction and the normal to the substrate, and is calculated from the angle χ of the detector, the angle χ_S of the sample and the diffraction angle θ (see 2.2.4). If the layer is isotropic in-plane, and in the absence of texture, large in-depth stress gradient and shear stress, the plot of $d_{\psi\varphi}$ as a function of $\sin^2\psi$ is linear:[80]

$$d_{\psi\varphi} = d_0 \left(1 - \frac{\nu}{E} 2\sigma_\varphi + \frac{1+\nu}{E} \sigma_\varphi \sin^2\psi \right) \tag{3.1}$$

with σ_φ the biaxial in-plane stress, d_0 the interplanar distance in the absence of stress, the Young modulus $E = 124.8$ GPa and $\nu = 0.385$ the Poisson ratio of Pd.[81] The in-plane biaxial stress is then obtained from the slope m of the linear fit:

$$\sigma_\varphi = \frac{mE}{(1+\nu)d_0} \tag{3.2}$$

The stress measurements are calibrated with isotropically strained bulk Pd powder.

3.2.3   Surface morphology

The thin film morphology is investigated with a JEOL field emission scanning electron microscope (SEM) operated at 4 keV and 15° from normal incidence. A Veeco MultiMode SPM atomic force microscope (AFM) is used to measure the topography of the surface in tapping mode. Optical reflection and transmission images are recorded under white light with an Olympus BX60 optical microscope. A dichroic filter is used to emphasize thickness differences in reflection.

3.2.4   Optical transmission

After deposition, the metallic films are transferred into an optical cell to monitor their optical transmission during hydrogenation.[42] A 150 W diffuse white light source illuminates the sample from the substrate side, and a 3-channel (RGB) SONY XC-003 charged-coupled device (CCD) camera with bandwidth $1.1 < \hbar\omega < 3.3$ eV continuously monitors the transmitted light as a function of hydrogen pressure. The gas pressure is controlled by a MKS 248/250 forward

Proportional-Integral-Differential (PID) system that regulates both inlet and outlet gas flows.

The Lambert-Beer law is used to relate the optical transmission T to the normalized hydrogen concentration ($0 \leq c = x/x_\beta \leq 1$) in the sample. The light intensity going through the sample is:

$$I = I_0 \left\{ \exp\left[-\mu_\alpha t(1-c) - \mu_\beta tc \right] + f \right\} + I_b \tag{3.3}$$

where I_0 is the intensity of the light in the absence of sample, I$_b$ the background intensity of the CCD camera, f the fraction of the film surface occupied by cracks, t the film thickness and μ_α, μ_β the optical absorption coefficients of the as-deposited α-PdH$_x$, respectively fully hydrided β-PdH$_x$ averaged over the measured photon-energy bandwidth.

Defining the optical transmission of the PdH$_x$ film as

$$T(c) = I(c) - I_b - fI_0, \tag{3.4}$$

the logarithm of the optical transmission normalized by the transmission in the metallic state T_M (c $\cong$ 0) becomes then:

$$\ln\left(\frac{T(c)}{T_M} \right) = (\mu_\alpha - \mu_\beta)t \cdot c. \tag{3.5}$$

The logarithm of the intrinsic optical transmission is thus directly proportional to the hydrogen concentration in the sample.

The kinetics of hydrogen ab/desorption as a function of cycle number is recorded as follows: for each cycle, in absorption, the same hydrogen pressure step (10^4 Pa) is applied and maintained 600 s. Desorption is subsequently obtained by evacuating the cell during 900 s. The optical transmission is recorded every 2 s.

PTIs are recorded by continuous pressure sweeps between 10^2 and 10^4 Pa of 7.2×10^4 s duration. To ensure that hydrogen gas is in (quasi)-equilibrium with PdH$_x$, the relaxation of the transmission upon stepwise pressure increases is also checked (see 3.3.1).

3.3 Hydrogenation thermodynamics of relaxed PdH$_x$ thin films

3.3.1 Isotherms, enthalpy and entropy in quasi-equilibrium

Activation

Pd bulk samples usually require an activation process before reproducibly ab/desorbing hydrogen. The standard procedure is to perform several ab- and desorption cycles before actually measuring a PCI. A similar procedure is applied here: for each cycle, the same hydrogen pressure (10^4 Pa) above
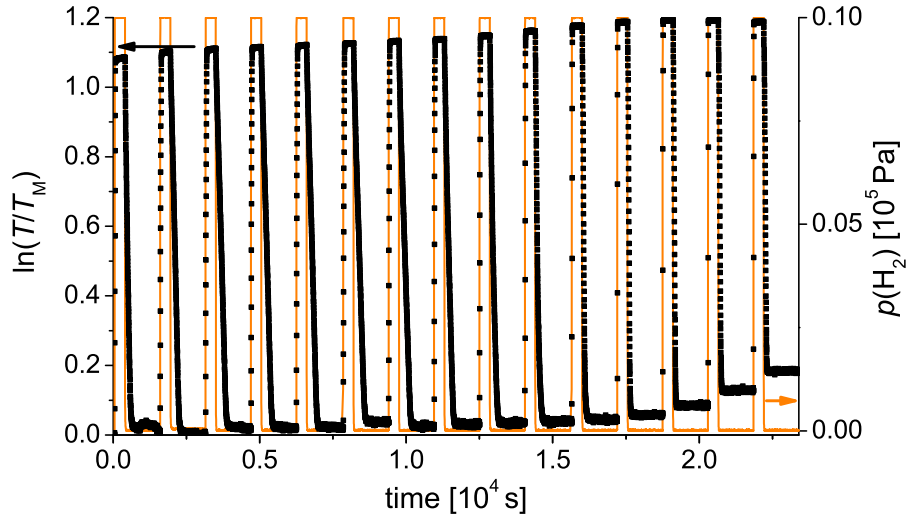
Figure 3.1: *Squares*, Optical transmission of a 65 nm PdH$_x$ thin film over the first 15 hydrogen ab/desorption cycles. The hydrogen pressure (*full gray line*) is varied between 10^4 Pa (hold time: 600 s) and 10 Pa (hold time: 900 s).

the $\alpha \rightarrow \beta$ plateau pressure is applied and maintained until full absorption. Desorption is subsequently obtained by evacuating the cell. The optical transmission is recorded every 2 s to follow the kinetics of the process. Figure 3.1a shows the logarithm of the normalized transmission $\ln(T/T_0)$ during the first 15 cycles at 295 K. The transmission at 10^4 Pa H$_2$ is approximately 3 times higher than in the as-deposited state. This change corresponds to the transition from the α to the β phase of PdH$_x$.

Pressure-optical–transmission-isotherms

After activation, PTI measurements are performed. To ensure (quasi)-equilibrium between the gas phase and H in Pd, the pressure is increased stepwise, letting the transmission relax between each step (Fig. 3.2a). The transmission after each relaxation step is then plotted as a function of pressure to obtain an isotherm (Cycle 18, empty circles in fig. 3.2b). Once the minimum relaxation time is known, subsequent PTI are recorded by continuous pressure sweeps of the same overall duration (Cycle 1 and 19 in fig. 3.2b). The reproducibility of the isotherms of cycles 18 and 19 is good, demonstrating the equivalence of the stepwise and continuous procedures. Plateaus in pressure occur both in ab- and desorption, as a result of the coexistence of the α and β PdH$_x$ phases. The PTI before (cycle 1) and after (cycle 19) activation at 296 K are also compared in fig. 3.2b. The hysteresis between absorption and desorption and the slope of the plateaus is significantly reduced by the activation. Recently, the reproducible hysteresis in metal hydride transformations has been attributed to the coherency strain generated by the transforming phase[72]. In general, the total strain energy depends on the microstructure of the coexisting coherent phases. In particular, in buckled thin films there is much less in-plane additional strain energy involved during hydrogen absorption than in films fully clamped on the substrate[79]. The strain reduction induced by buckling and cracking is most probably responsible for the observed shrinkage of the hysteresis loop between cycles 1 and 18. In fig. 3.2b, the good agreement between desorption PTIs of cycles 18-19 and the bulk desorption PCI[82] indicates that strain due to clamping to the substrate has been considerably reduced by the activation process.
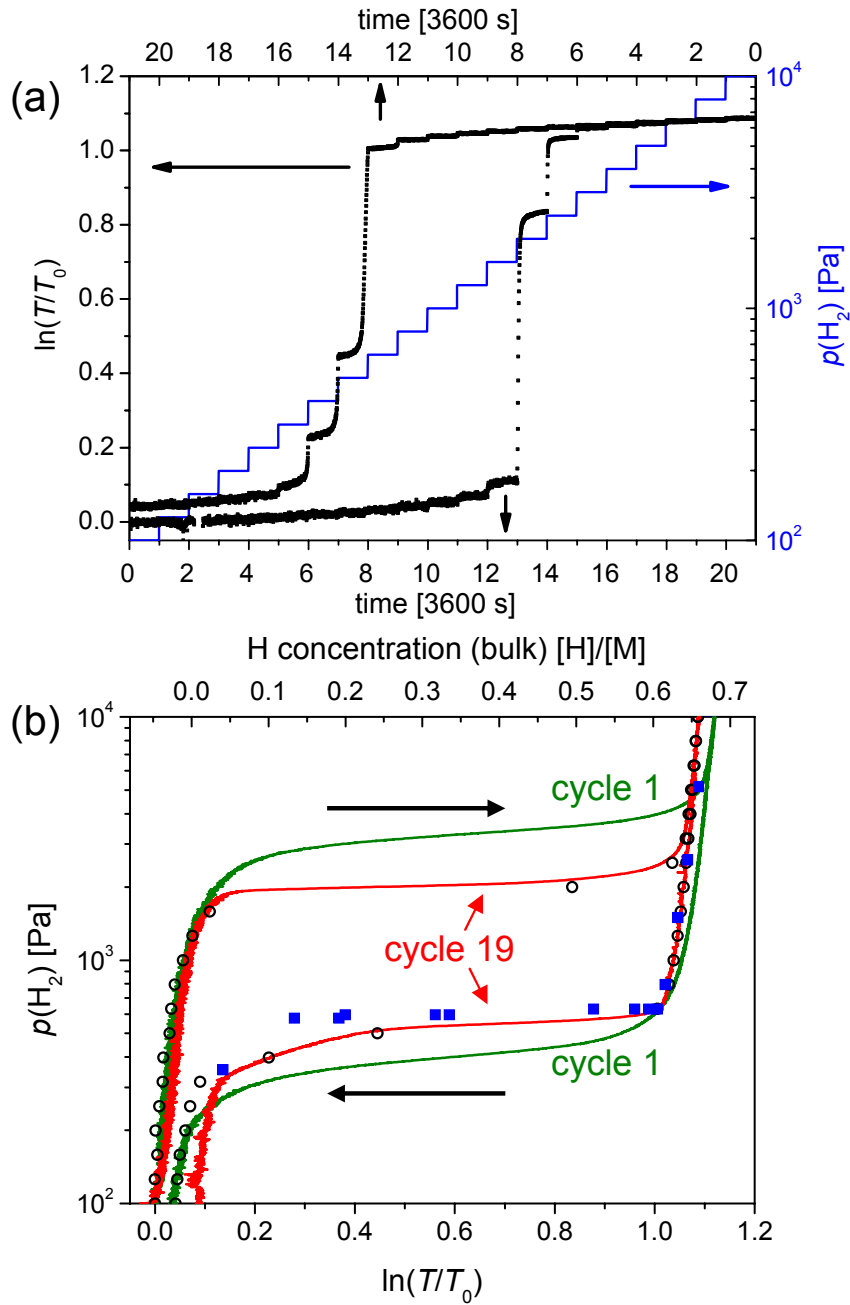
Figure 3.2: **(a)** *Dots*, transmission of a 65 nm PdH_x thin film as a function of hydrogen pressure steps at 294 K (cycle 18). Each pressure step (*full line*) is maintained 3600 s to ensure relaxation of the film with the hydrogen environment. The transmission T is normalized by the transmission in the as-deposited metallic state T_0. **(b)** *Open circles*, equilibrium transmission after each pressure step in **(a)** (cycle 18). *Full lines*, ab- and desorption pressure–optical-transmission–isotherms for cycles 1 and 19 obtained by continuous sweeps of the hydrogen pressure at 294 K. *Filled squares*, pressure-concentration-isotherm of bulk PdH_x at 293 K.[82] The relation $\ln(T/T_0) = 1.47 \times c$ is used.
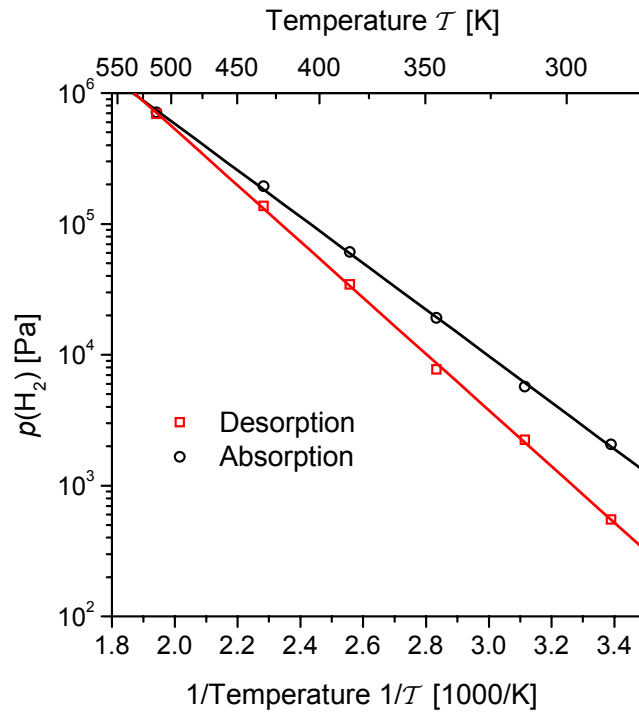
Figure 3.3: *Symbols*, optically determined temperature dependence of the plateau pressure (Van 't Hoff plot) in desorption ($\beta \rightarrow \alpha$) and absorption ($\alpha \rightarrow \beta$) for a 65 nm PdH$_x$ thin film deposited on a sapphire substrate. The *full lines* are the linear fit used to determine the enthalpies and entropies of hydride formation/decomposition.

Table 3.1: Desorption ($\beta \rightarrow \alpha$) and absorption ($\alpha \rightarrow \beta$) transition enthalpies ΔH in [kJ (mol H$_2$)$^{-1}$] and entropies ΔS in J (K mol H$_2$)$^{-1}$] for the Pd-H system.

$\Delta H_{\beta \rightarrow \alpha}$	$\Delta S_{\beta \rightarrow \alpha}$	$\Delta H_{\alpha \rightarrow \beta}$	$\Delta S_{\alpha \rightarrow \beta}$	Technique	Reference
-41.1 $\pm$ 0.4	-96.0 $\pm$ 1.2	-34.0 $\pm$ 0.4	-82.4 $\pm$ 1.0	optical	this work
-41.2 $\pm$ 0.8	-99.4 $\pm$ 1.6	-36.4 $\pm$ 0.8	-90.8 $\pm$ 1.6	gravimetric	thin film[63]
-39.0 $\pm$ 0.5	-92.5 $\pm$ 1.3	-37.4 $\pm$ 0.3	-92.5 $\pm$0.8	volumetric	bulk[58]
-41.0 $\pm$ 0.4	-97.5 $\pm$ 0.8	-	-	volumetric	bulk[59]
-	-94.4	-	-	-	theory[83]

Experimental enthalpy and entropy determination

In the subsequent cycles, PTIs are measured at various temperatures up to 500 K. The Van 't Hoff plots (Fig. 3.3) of the equilibrium plateau pressures are remarkably linear over 3 orders of magnitude in pressure. Enthalpy and entropy are then obtained from a linear fit of $\ln(p_{eq}/p_0)$ vs $1/\mathcal{T}$, according to the Van 't Hoff relation (Eq. 1.2).

The obtained desorption enthalpy and entropy values agree very well with the ones determined on bulk Pd (see Table 3.1). While the absorption enthalpy value is close to experimental data as well, the absorption entropy is 8-10 J(K mol H$_2$)$^{-1}$ less negative than other data reported in the literature. The critical temperature $\mathcal{T}_c = (\Delta H_{\alpha \rightarrow \beta} - \Delta H_{\beta \rightarrow \alpha})/(\Delta S_{\alpha \rightarrow \beta} - \Delta S_{\beta \rightarrow \alpha}) = 528$ K is therefore lower than in bulk samples ($\mathcal{T}_c =$565 K).[82] In thin films,[c] residual clamping to the substrate is known to reduce the attractive long range H-H interaction and $\mathcal{T}_c$.[75] However, the good agreement found between buckled thin film and bulk in desorption shows that thermodynamic quantities determined on thin films are relevant for the search for hydrides if the strain induced by clamping to the substrate is reduced by the proper activation procedure.

---

[c]Feenstra et al.[63] used quartz substrates with a 10 μm finish instead of the flat sapphire substrates used here. This most probably helped to minimize the residual clamping. This is supported by their critical temperature ($\mathcal{T}_c = 542$ K), that lies between the bulk value ($\mathcal{T}_c = 565$ K) and our thin film value ($\mathcal{T}_c = 528$ K).

The entropy of the hydride: Case study of PdH$_x$ an NbH$_x$

The following subsection has been originally published in the Master thesis of
C. P. Broedersz.[83] We include it here to explain why the absolute value of the
entropy change for the PdH$_x$ system departs significantly from the entropy of
hydrogen gas ($\Delta S^0_{H_2}$ = -131 J(K mol H$_2$)$^{-1}$).
The entropy contribution of the atomic hydrogen in the lattice (see eqs. (2.12)
and (3.9)) is commonly neglected with respect to the entropy of the hydrogen
gas. Although this is justified for many systems, it does not apply in general.
This is demonstrated by the the Van't Hoff plots of various systems in fig-
ure 2.1. The intersection with the vertical axis of a Van 't Hoff plot is given by
$-\frac{\Delta S}{R}$. The Van 't Hoff plots in figure 2.1 do not a have a common intersection
with the vertical axis, which implies that ΔS varies between the systems.

In this subsection we discuss the thermodynamic data of two typical metal
hydride systems, Pd-H and Nb-H. These materials demonstrate the importance
of the entropy contribution of the atomic hydrogen in the metal. We describe
quantitatively all contributions to the entropy term ΔS in the Van t' Hoff
equation (see eqs. (2.11) and (2.15)) using the lattice gas model extended
with the Einstein model to incorporate the vibrations of the hydrogen atoms.

Pd has an FCC structure and in principle all octahedral sites (1 site per
Pd) can contain 1 hydrogen atom. Figure 3.4 shows the isotherms and the
phase diagram of the Pd-H system. Surprisingly, the isotherms diverge at a
concentration significantly smaller than c_H=1. This remarkable behavior has
an electronic cause. The Fermi energy of Pd is located in the narrow d-band
with a *high* density of states. As the Pd absorbs roughly 0.6 H/Pd, the Fermi
energy is pushed above the d-band into a broad sp-band with a *low* density
of states. Consequently, the addition of more hydrogen becomes energetically
expensive, which leads to a slowly diverging isotherm. This is known as the
band structure effect.[84]
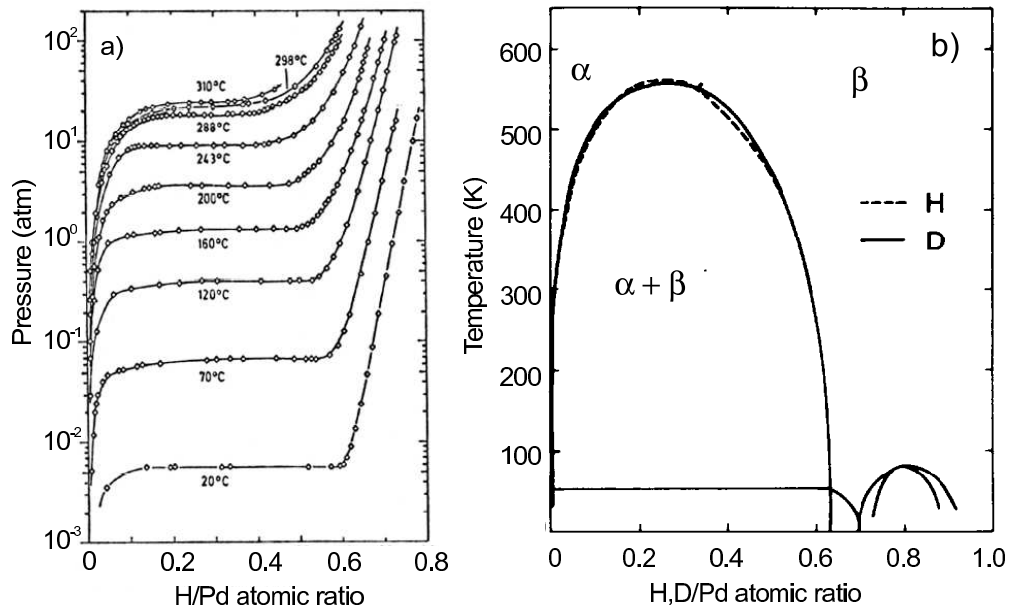
Figure 3.4: a) Pressure-composition isotherms for H in Pd.[82,85] b) The phase diagram of PdH$_x$ and PdD$_x$.[82,86]
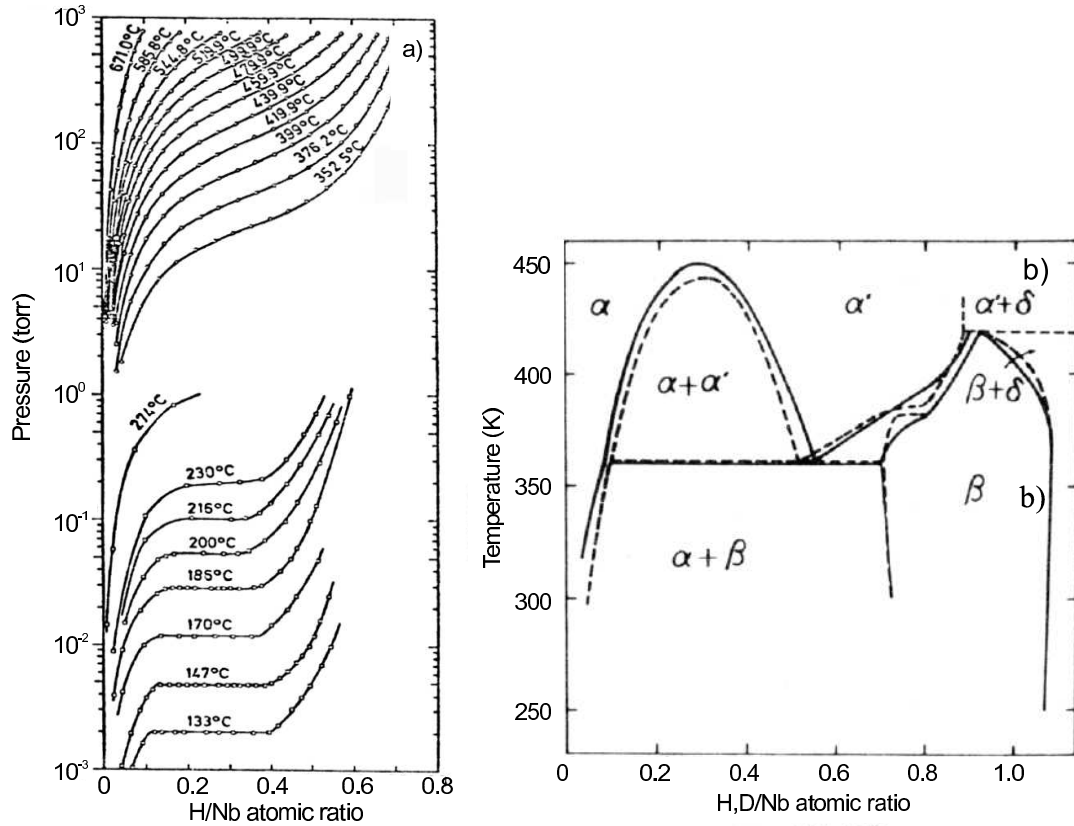
Figure 3.5: Pressure-composition isotherms for H in Nb.[87] b) The phase diagram of NbH$_x$ (solid line) and NbD$_x$ (dotted line).[88,89]

The band structure effect has a dramatic consequence for the coexistence region in the metal hydride phase diagram. Figure 3.4 b) shows that there is a coexistence region between a dilute α- and a dense β-phase extending to a concentration $c_H \approx 0.63$; the critical concentration is c_c=0.26 instead of 0.5. Similar behavior is found in the Nb-H system. Figures 3.4 a) and b) show the isotherms and the phase diagram of the Nb-H system. The phase diagram reveals a coexistence region between an α-phase and an α'-phase with a critical concentration $c_c = 0.25$.

The Van 't Hoff plots determined at the critical concentration for bulk Pd-H and Nb-H give

Pd-H: ΔH=-41.0 kJ (mol H$_2$)$^{-1}$ and ΔS=-97.5 J K^{-1} (mol H$_2$)$^{-1}$

Nb-H: ΔH=-89.0 kJ (mol H$_2$)$^{-1}$ and ΔS=-110.6 J K^{-1} (mol H$_2$)$^{-1}$

In both cases we see a significant deviation from the expected value $\Delta S = -131$ JK^{-1}(mol H$_2$)$^{-1}$. In the following discussion we try to account for this deviation by the configurational entropy.

The general expressions for the hydride contribution to ΔS is derived in subsections 2.1.2 and 2.1.3 (see eqs. (2.12) and (3.9)). This contribution is

summarized as

$$S^\dagger = \begin{cases} 2\bar{S}_H & \text{if } T > T_c \\ 2\frac{S_H(c_\beta) - S_H(c_\alpha)}{c_\beta - c_\alpha} & \text{if } T < T_c \end{cases} \qquad (3.6)$$

Although the lattice gas model presented in section 2.1.4 does not include the band structure effect, the expression for the configurational entropy is still valid for these systems, since the counting of distinguishable configurations of the hydrogen in the metal lattice is not affected by the band structure effect. We can therefore use the expressions for the partial molar entropy $\bar{S}_H$ and the entropy S_H of the lattice gas model

$$\bar{S}_H = -R \ln\left(\frac{c_H}{1 - c_H}\right) \qquad (3.7)$$

and

$$S_H = -R\left(c_H \ln c_H + (1 - c_H)\ln(1 - c_H)\right). \qquad (3.8)$$

Figure 3.6 shows a plot of the partial molar entropy $\bar{S}_H$ and the entropy S_H for the lattice gas model. In the standard situation the coexistence region is symmetric around a critical concentration c_c=0.5. Above the critical temperature $S^\dagger = \bar{S}_H$, which is zero at $c = c_c = 0.5$. For $T < T_c$ the numerator in $S^\dagger$ goes to zero as $(c_\alpha - c_\beta)^2$. Therefore $S^\dagger$ vanishes also below T_c. We conclude that ΔS=-131 J K^{-1} (mol H$_2$)$^{-1}$ when the critical concentration is 0.5.

In the Pd-H and Nb-H systems, however, the critical concentration is not 0.5. This has an interesting consequence for the configurational contribution to ΔS. If we define $c_\beta = c_c + \delta$ and $c_\alpha = c_c - \delta$ and make a series expansion of $S^\dagger$ in δ for $T < T_c$, we find to second order in δ

$$S^\dagger(T < T_c) = S^\dagger(T > T_c) = -2R \ln\left(\frac{c_c}{1 - c_c}\right). \qquad (3.9)$$

Note that this function is anti-symmetric around $c_c \neq 0.5$ and, consequently, may contribute both positively or negatively. Using this expression we can compute the ΔS for Nb-H and Pd-H:

Pd-H: $\Delta S = S_{conf}$-131=17.4-131=-113.6 J K^{-1}(mol H$_2$)$^{-1}$ (exp. -97.5 J K^{-1} (mol H$_2$)$^{-1}$)

Nb-H: $\Delta S = S_{conf}$-131=18.3-131=-112.7 J K^{-1}(mol H$_2$)$^{-1}$ (exp. -110.6 J K^{-1}(mol H$_2$)$^{-1}$)

The agreement with the experimental value is reasonable in the case of Nb-H in contrast to Pd-H.

Next, we include the entropy contribution of the vibrations of the hydrogen atoms in the lattice. We expect this contribution to be larger for the Pd−H system than for the Nb−H system, because the Einstein temperature for Pd−H Θ_E=662 K is significantly smaller than for Nb-H Θ_E=1324 K. The partial molar entropy due to the lattice vibrations is given by[46]

$$\bar{S}_{vib} = -3R \log\left(1 - e^{-\Theta_E/T}\right) + \frac{3R\Theta_E}{T}\frac{1}{e^{\Theta_E/T} - 1} \qquad (3.10)$$
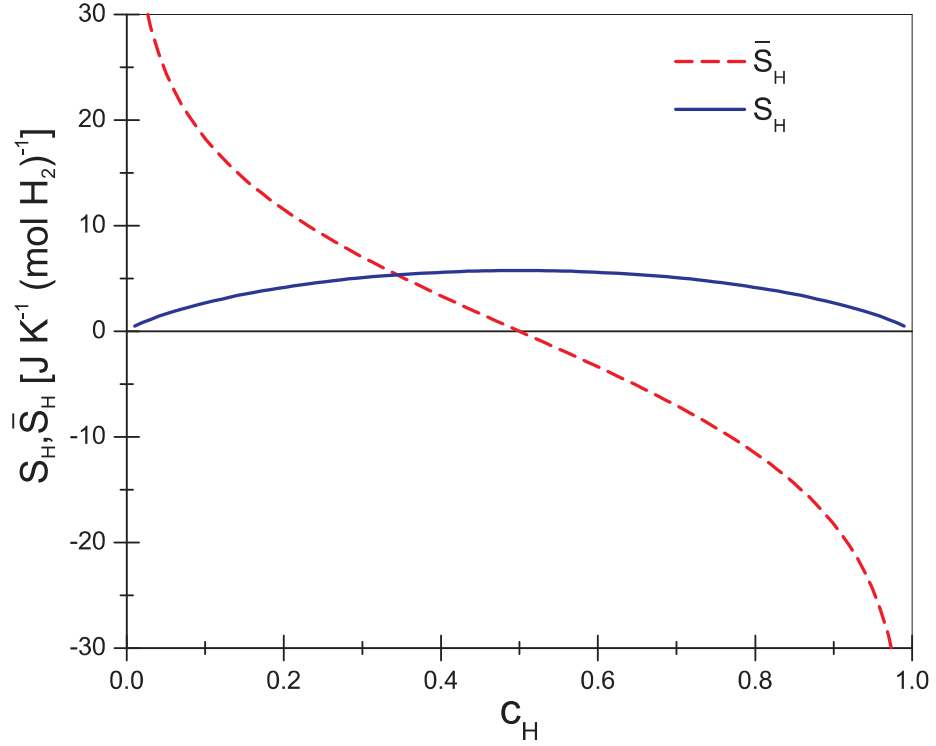
Figure 3.6: Configurational partial molar entropy (red line) and the configurational entropy (blue line).

When we include this contribution we find values for ΔS in good agreement with the experimental results,

Pd: $\Delta S = S_{conf.} + S_{vib.} - 131 = 17.4 + 19.2 - 131 = -94.4$ J K^{-1}(mol H$_2$)$^{-1}$ (exp. -97.5 J K^{-1} (mol H$_2$)$^{-1}$)

Nb: $\Delta S = S_{conf.} + S_{vib.} - 131 = 18.3 + 3.2 - 131 = -109.5$ J K^{-1}(mol H$_2$)$^{-1}$ (exp. -110.6 J K^{-1} (mol H$_2$)$^{-1}$)

In summary, we can model the surprisingly large hydride contribution to ΔS using the lattice gas model (configurational entropy) and the Einstein model (vibrational entropy). The estimated values agree well with the experimental results.

3.3.2   Off-equilibrium method

We present now an alternative to the pressure step or sweep method described in 3.3.1 to determine the equilibrium plateau pressure of thin film hydrides. In certain cases, the time needed to reach quasi-equilibrium between hydrogen gas and the hydrides phases is too long for practical measurements of pressure-transmission-isotherms. This is an especially acute problem for light-weight complex hydrides (e.g. alanates and boranates), where extensive diffusion of metal atoms, in general much slower than H diffusion, is needed. This is probably the reason for the scarcity of reported PCTs in the literature of these systems.

A possibility to circumvent this problem is to measure the rate $R = d\ln(T)/dt$ of the optical change for various hydrogen pressures above/below the equilibrium plateau pressure. The equilibrium pressure is then obtained from an extrapolation to zero rate ($R = 0$ at $p = p_{eq}$). The shape of the $R(p)$ dependence is simple for extreme cases when a single rate-limiting step can be assumed. For example, if hydrogen dissociation at the surface of the film is the rate-limiting step and diffusion processes are neglected,[90,91] $R(p) \propto (p - p_{eq})$. For hydride films, diffusion can be reduced at will by taking thinner film if necessary, and the surface-limited regime can generally be reached.[d]

Figure 3.7 shows five ab/desorption cycles at 297 K after activation (cycles 25-29) under different pressure conditions above the absorption and below the desorption equilibrium pressure. Both ab- and desorption rates depend obviously on the applied pressure. A peculiar feature in desorption is that, after a relatively fast decrease due to hydrogen release, the transmission increases again slowly to stabilize finally at a higher transmission value than in the previous cycle. On the other hand, the transmission in the hydride state does not change significantly with cycling. Observation of desorption under the microscope shows that a network of cracks is present on the film (see Fig. 3.14). These cracks close during absorption and reopen slowly after hydrogen desorption when stress relaxes in the film (See Fig. 3.16), explaining the transmission increase in desorption. The overall increase of the transmission with cycling in the metal state is due to an increase of the number of cracks.

We determine the rate of absorption and desorption from linear fits of the transmission jumps in Fig. 3.7. As expected from the high catalytic activity of the Pd surface and the fast diffusion in a film of this thickness, the pressure dependence of the rate is linear, which is the sign for a surface-limited kinetics. We therefore obtain the equilibrium pressure from a linear extrapolation of $R(p)$ to zero rate. For comparison we show also the equilibrium pressure at the same temperature as determined from the Van 't Hoff plot measured by the quasi-equilibrium method (Fig. 3.3). While the agreement is excellent in absorption, in desorption the extrapolation yields a higher equilibrium pressure

---

[d]A notable exception is MgH$_2$, in which the hydrogen diffusion is practically too slow.[92]
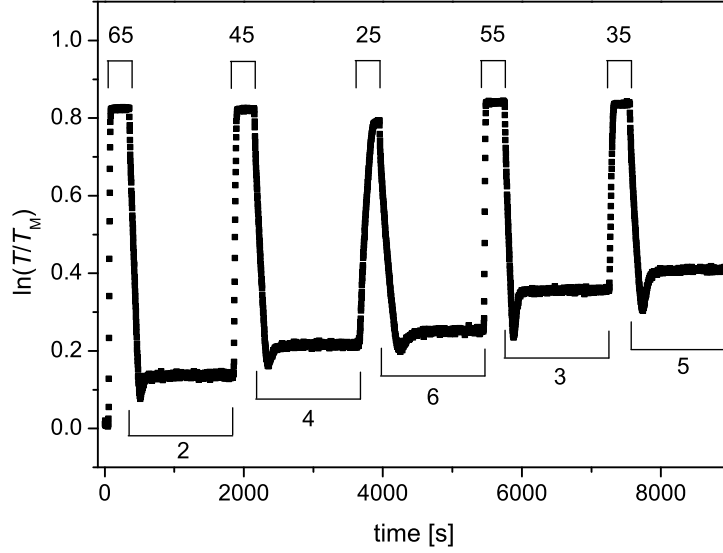
Figure 3.7: Optical transmission during five ab/desorption cycles of a 65 nm PdH$_x$ thin film deposited on sapphire. The different hydrogen pressures (in [mbar]) applied for each ab and desorption are indicated on the plot.

than with the quasi-equilibrium method. This discrepancy might be due to an extra kinetics barrier during desorption.

Using the Van' t Hoff equation 1.2, we evaluate the potential influence of this difference in equilibrium pressure on the desorption enthalpy or entropy:

$$\ln\left(\frac{p_{\text{eq,off-eq}}}{p_{\text{eq,quasi-eq}}}\right) = \frac{\Delta H_{\text{off-eq}} - \Delta H_{\text{quasi-eq}}}{R\mathcal{T}} - \frac{\Delta S_{\text{off-eq}} - \Delta S_{\text{quasi-eq}}}{R} \qquad (3.11)$$

With equilibrium pressures $p_{\text{eq,off-eq}} = 8.8$ mbar and $p_{\text{eq,quasi-eq}} = 6.2$ mbar for the off-equilibrium method and quasi-equilibrium method, respectively, this gives a maximum change of the enthalpy and entropy of:

$$\Delta H_{\text{off-eq}} - \Delta H_{\text{quasi-eq}} = 0.9 \text{ kJ(mol H}_2)^{-1} \quad \text{if } \Delta S_{\text{off-eq}} = \Delta S_{\text{quasi-eq}} \qquad (3.12)$$

and

$$\Delta S_{\text{off-eq}} - \Delta S_{\text{quasi-eq}} = -2.9 \text{ J (Kmol H}_2)^{-1} \quad \text{if } \Delta H_{\text{off-eq}} = \Delta H_{\text{quasi-eq}} \qquad (3.13)$$
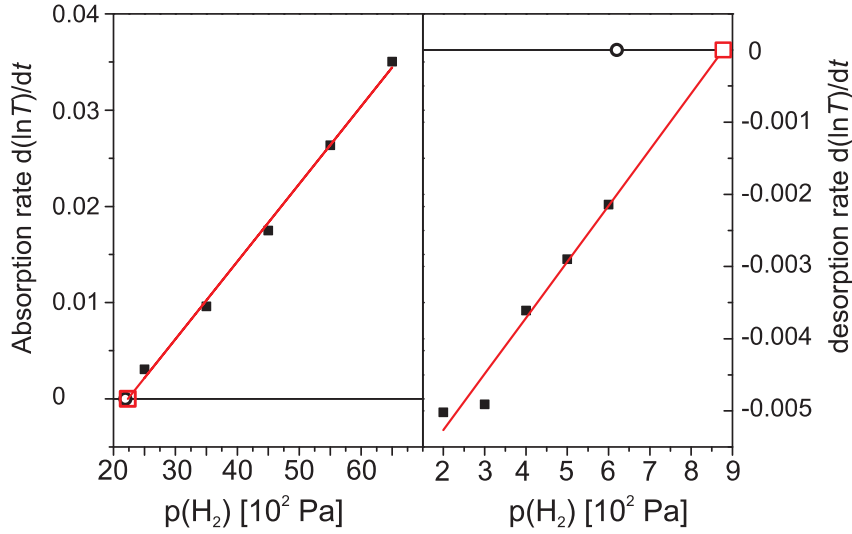
Figure 3.8: *Filled squares*, ab- and desorption rates $R(p)$ at 297 K as a function of hydrogen pressure determined from a linear fit of the transmission jump in Fig. 3.7. The *empty squares* are equilibrium pressures determined from a linear fit of $R(p)$. For comparison, *empty circles* give the equilibrium pressures determined by the Van 't Hoff plot in Fig. 3.3 (quasi-equilibrium method).

In summary, we demonstrated an off-equilibrium method to determine the thermodynamics of (de)hydrogenation for a Pd thin film. For Pd in absorption, both off- and quasi-equilibrium methods give the same result, while in desorption, the indirect off-equilibrium approach seems to reach a pressure value closer to equilibrium. However, the maximum discrepancy between the two methods remains small. We will also show in the following that this method remains valid for a typical bilayer configuration where the optically active metal-hydride layer is covered by a second protective and catalytic layer (see 4). However, because it necessitates many measurements and the use of extrapolation to determine a single equilibrium pressure, the off-equilibrium approach should be reserved to systems with an intrinsic slow, though reproducible, kinetics.

3.4 Influence of stress relaxation processes on thin film PdH$_x$ isotherms

3.4.1 Optical isotherms during relaxation

Figure 3.9 shows pressure–optical-transmission-isotherms for cycles numbers between 1 and 24. The transmission for each cycle is normalized to the transmission at the beginning of the absorption according to equation 3.5.

All ab/desorption isotherms exhibit an $\alpha - \beta$ coexistence region, the slope and shape of which changes with cycle number. The first cycle exhibits a single sloping plateau and the largest hysteresis. From cycle 9 on, the coexistence region splits into two parts, with first a flat plateau at lower pressures in absorption (respectively higher pressures in desorption) and a sloping continuation. The flatter plateau then develops with further cycling, at the expense of the sloping one. Until cycle 16, the maximum $\ln(T/T_{\mathrm{M}})$ attained in the β-PdH$_x$ phase at 10^4 Pa H$_2$ pressure stays constant. In contrast, at cycle 24, only the flat plateau remains, resulting in a considerable reduction of the transmission in the β-PdH$_x$ phase. This evolution in the isotherms causes a notable decrease of the (pressure) hysteresis width.

Another noticeable feature is the optical transmission value and shape of the isotherms at the α-phase solubility limit in absorption, just before entering the coexistence region. While $\ln(T(\alpha_{\mathrm{max}})/T_{\mathrm{M}}) = 0.2$ during the first cycle, it is $\ln(T(\alpha_{\mathrm{max}})/T_{\mathrm{M}}) = 0.14$ at cycle 9 and 0.06 at cycle 24.

While the maximum attainable $\ln(T/T_{\mathrm{M}})$ in the β-phase remains constant up to cycle 16, it is considerably reduced at cycle 24. Furthermore, the transmission after desorption does not recover to the initial T_{M} value, indicating the presence of a large amount of new cracks during this cycle. Observation of the film under the microscope reveal that cracks close during H absorption to reopen during desorption. This causes a decoupling of the optical transmission T from the H concentration c for cycle 24.
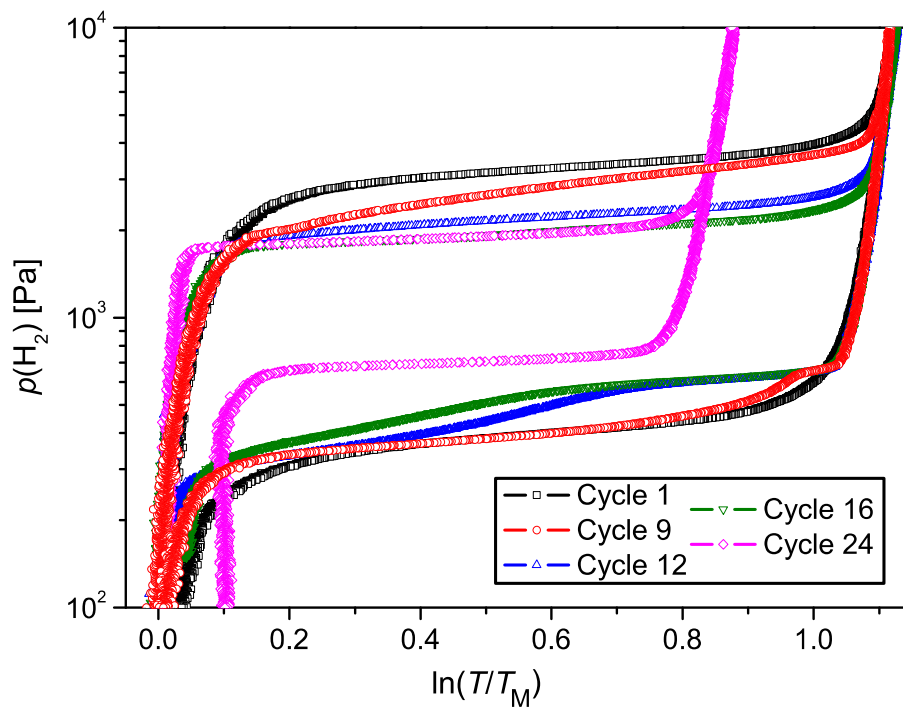
Figure 3.9: Evolution at $\mathcal{T}$ = 297 K of ab/desorption pressure–optical-transmission–isotherms as a function of cycle number for a 65 nm PdH$_x$ thin film on a sapphire substrate.

3.4.2 (Micro)structure

To understand the PTIs evolution with hydrogenation cycle number, the structure and microstructure of the PdH$_x$ is investigated as a function of cycle number, in the α and β hydride phases.

Structural evolution

In the as-deposited state, the 65 nm Pd films are polycrystalline, with the 111 and 200 ring reflections present in the 2D XRD diffraction patterns, as shown in the inset of Fig. 3.10 The film is slightly oriented, with the [111] direction as preferred normal-to-substrate out-of-plane orientation.

XRD patterns of the first hydrogen ab/desorption cycle are shown in Fig. 3.10. Exposure of the film to a hydrogen pressure $p(H_2) = 10^4$ Pa is sufficient to form the β-PdH$_x$ hydride phase. Due to hydrogen-induced expansion both 111 and 200-reflections of the β-phase appear at lower angle in the pattern than those in the α-phase. The process is reversible, but it is interesting to note that after desorption, the α-phase reflections are present at a higher angle than in the as-deposited state (about 0.1° in 2θ) and match the one in bulk metallic Pd. Obviously, the first cycle relaxes the tensile strain in the direction normal to the substrate induced by deposition.

The 2θ 111-PdH$_x$ peak positions during subsequent cycles are displayed in Fig. 3.11a. The intensity is integrated from 80° to 100° in the χ direction (normal to substrate: 90°). While the 2θ position of the β reflection stays approximately constant for cycles 2 and following, we find a slight decrease of the α-peak position. This behavior might be due to some residual stress build-up and/or irreversibly trapped H upon cycling. Hydrogen cycling also increases the out-of-plane intensity and alters the χ distribution of the 111-reflection (see Fig. 3.11b): the repeated stress-strain cycles induced by hydrogen ab/desorption most probably result in a denser, energetically more favorable packing of the Pd atoms and consequently the film reorients itself more in the out-of-plane [111] direction.
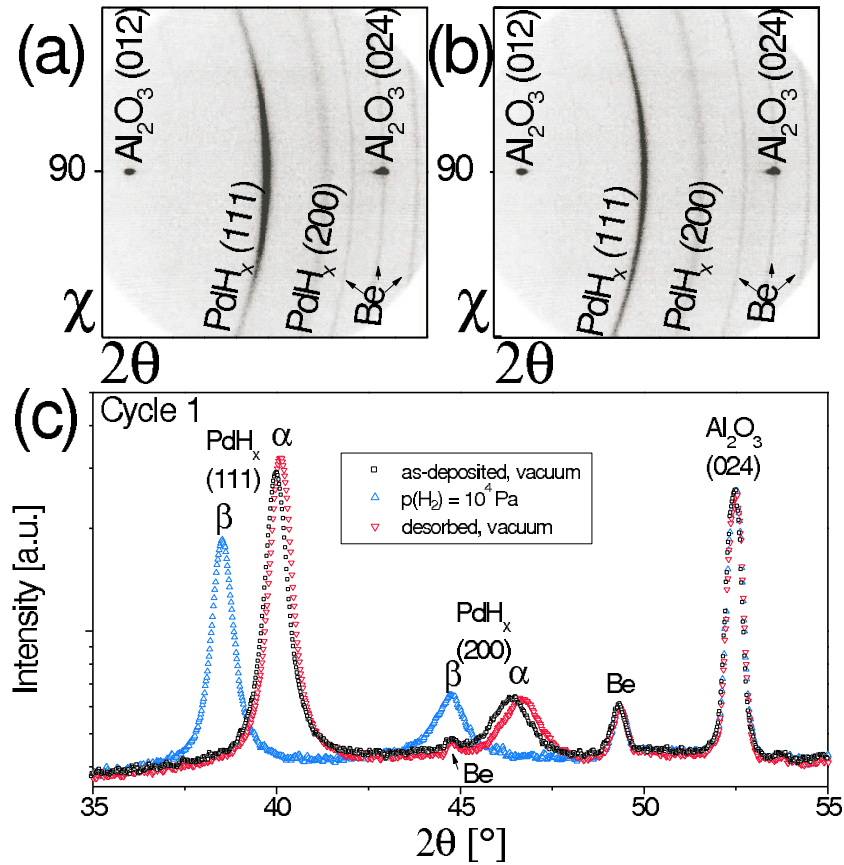
Figure 3.10: X-Ray diffraction patterns for a 65 nm PdH_x thin film on a sapphire substrate (Al_2O_3) during the first hydrogen ab/desorption cycle. Be indicates reflections from the Beryllium dome. 2D diffraction pattern for the (a) as-deposited sample, (b) Sample exposed to a hydrogen pressure $p(H_2) = 10^4$ Pa at $\mathcal{T} = 297$ K. (c) Corresponding 1D diffraction patterns obtained by integration of the 2D pattern along the χ axis ($80° \leq \chi \leq 100°$).

(a)

(b)
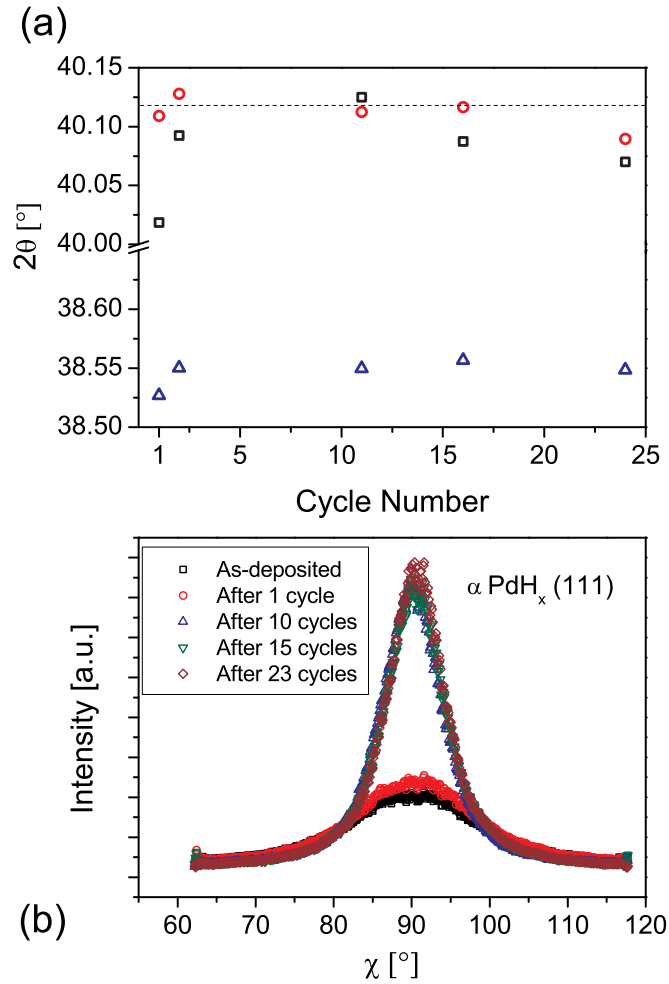
Figure 3.11: (a) Out-of-plane ($80° \leq \chi \leq 100°$) 2θ position of the 111-PdH$_x$ reflection at 297 K in the α-phase in vacuum before absorption (*Black squares*), in the β-phase at $p(H_2) = 10^4$ Pa (*Blue triangles*) and in the α-phase in vacuum after desorption (*Red circles*) as a function of cycling. *Dotted line*, position of the 111-reflection for bulk Pd. (b) χ distribution of the 111-PdH$_x$ reflection as a function of cycle number.

Peak broadening analysis

The broadening of the diffraction peaks originates from the combined effect of the size of the coherently diffracting domains (CDD), the microdistortions (non-uniformly strained grains), and the instrumental contributions (beam divergence, detector resolution). The different contributions are obtained by fitting the peak of interest with a Voigt function, which is the convolution of Gaussian and Lorentzian profiles.[93] It is then appropriate to assume that the Lorentzian and Gaussian components of the structurally broadened profile are due to size and respectively strain broadening.[94] In practice, a reasonable estimate of the crystallite domain size $\langle D \rangle$, is obtained by the Scherrer equation:

$$\langle D \rangle = \frac{\lambda}{\beta_L cos(\theta)} \tag{3.14}$$

where β_L is the Lorentzian integral width and $\lambda = 1.5418$ Å the wavelength of the Cu K$_\alpha$ source. The Lorentzian integral width is related to the full width at half maximum of the Lorentzian component of the fit ω_L (taken on a 2θ scale) by $\beta_L = (\omega_L - \omega_L^i)/0.63662$, where ω_L^i is the instrumental contribution to the Lorentzian width and is obtained from a Voigt fit of the (012) Al$_2$O$_3$ single crystal substrate peak.

Figure 3.12a shows the background subtracted 111-PdH$_x$ peaks for cycles 1, 11 and 24 together with the Voigt fits used to determine the CDD sizes. The obtained Lorentzian widths and CDD sizes as a function of cycle number are reported in Fig. 3.12b. Astonishingly, a notable increase of the CDD size occurs between cycle 1 and 11: hydrogen obviously facilitates the movement of Pd atoms and increases the crystallite perfection, as it improves orientation in the [111] direction. However, no further changes in the CDD size is observed after cycle 11.

The measure of the microdistortions was not possible as the Gaussian component of the broadened profile comes mainly from the 50μm collimator.
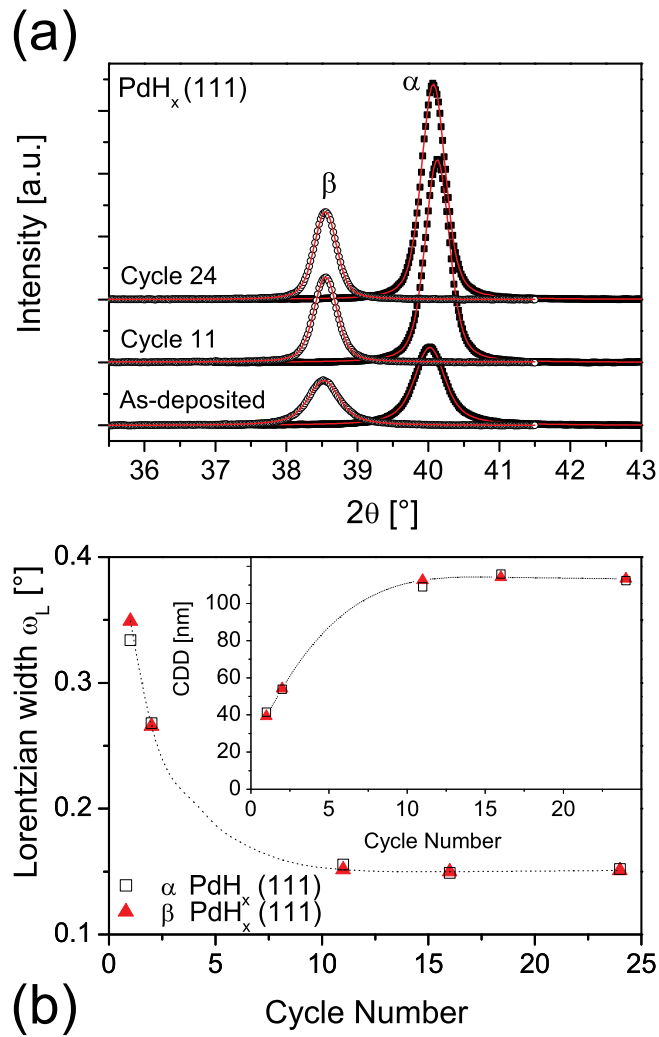
Figure 3.12: (a) Background subtracted PdH$_x$ 111-reflection in the α-PdH$_x$ in vacuum (*Squares*) and β-PdH$_x$ under p(H$_2$) = 10^4 Pa (*Open circles*) phases. *Lines*, corresponding Voigt fits. (b) Lorentzian width in the α-PdH$_x$ (*Squares*) and β-PdH$_x$ (*Triangles*) phases as a function of cycle number. *Inset*, coherent diffraction domain size as a function of cycle number. *Dotted lines* are a guide to the eye.

Surface morphology

The surface morphology is investigated by SEM in the as-deposited state and after ab-desorption cycles. Figure 3.14 shows that while the as-deposited state (a) is completely smooth at the micrometer scale, a single cycle (b) and its associated stress build up is sufficient to produce large ($\sim 10~\mu m$) disconnected buckles. These buckles indicate a reduction of the clamping to the substrate and remain visible after desorption. Furthermore, this irreversible pattern of plastic deformations evolves with cycle number: After cycle 8 (c), the buckles have branched and start to interconnect, while after cycle 15 (d), a complete network has appeared, interconnecting thin (2-3 nm wide) buckles and cracks. This network divides the surface into smaller areas of a few tens of micrometer diameter. Further cycling (e) results in a further reduction of the clamping: buckles and cracks do not overlap on the same network anymore, and some parts of the film are completely delaminated.

The buckles-cracks network observed after cycle 15 is particularly interesting as it subdivides the film surface into smaller areas, in a similar way as in the bulk, where H cycling provokes the decrepitation of the materials into micrometer-size grains. Figure 3.13 shows the AFM surface corrugation image after desorption of a film cycled 15 times. Buckles reach $\sim 0.8~\mu m$ in height for a lateral extension of 4-7 μm. In the area enclosed by the network, the film surface appears flat.

The morphology changes observed by SEM and AFM have an influence on the local optical properties of the Pd layer. However, if cracks extend throughout the layer, or if the thickness distribution is not uniform anymore, morphology changes will also be seen indirectly in the Hydrogenography measurements, for which the optical transmission is averaged over a large area. It is thus also important to study the evolution with cycling of the optical reflection and transmission under the optical microscope. Figure 3.15 shows the Pd film in reflection (R) and transmission (T) after 8 (a), 15 (b), and 23 cycles (c). R and T images are from the same area. After 8 cycles, transmission shows clearly that the irreversible buckle network, appearing darker, has almost completed. This is less clear in reflection, as different parts of the network reach different heights and so do not scatter light evenly. The most interesting features are found after 15 cycles: in transmission, cracks extending throughout the film are seen as bright spots, while the buckle network is delimitated by dark lines. While AFM shows that the buckle-free area of the film is essentially flat on a μm scale, these regions are seen in optical transmission as a dark center surrounded by a more transmissive ring (Fig. 3.15b and inset). The only explanation for this behavior is that the film is thinner at the periphery than in the center of the buckle-free areas. This suggests that thickness differences *within* buckle-free areas have developed and implies that H-cycling at room temperature readily enables large displacements of Pd

atoms.
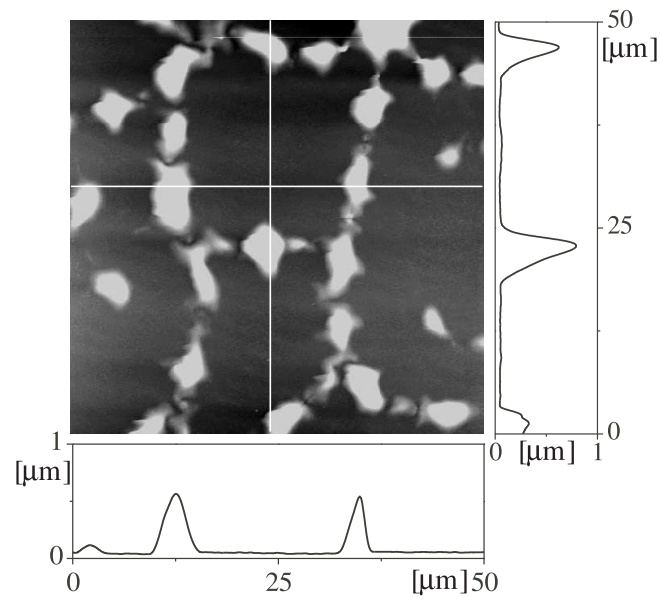
Figure 3.13: AFM image of the surface corrugation for a 65 nm PdH$_x$ film after 15 hydrogen ab/desorption cycles.
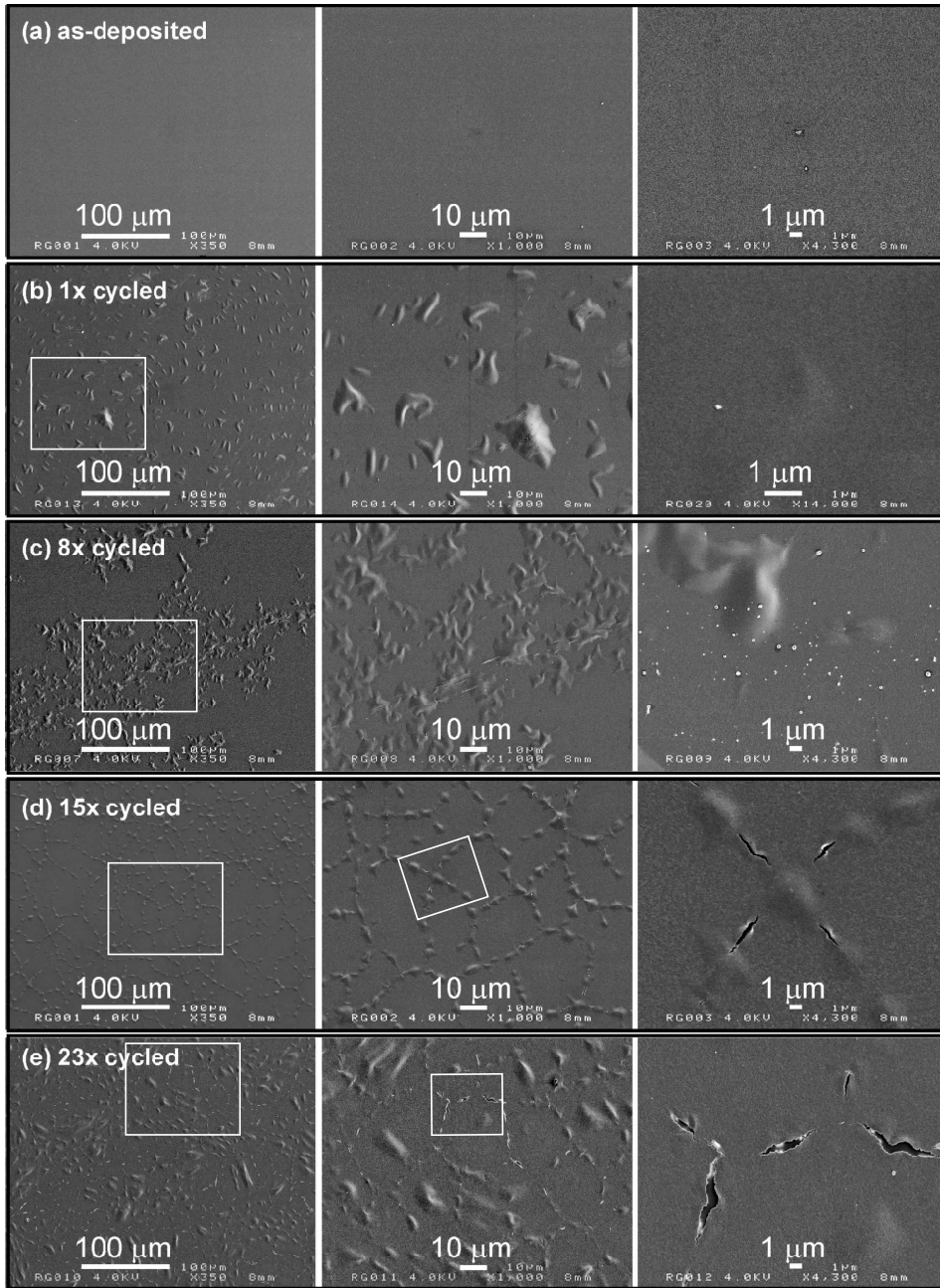
Figure 3.14: From *top* to *bottom*: SEM image of a 65 nm PdH$_x$ film as a function of cycle number, after hydrogen desorption. From *left* to *right*: increasing magnification. *White rectangles* indicate the area of the next magnified image to the right.
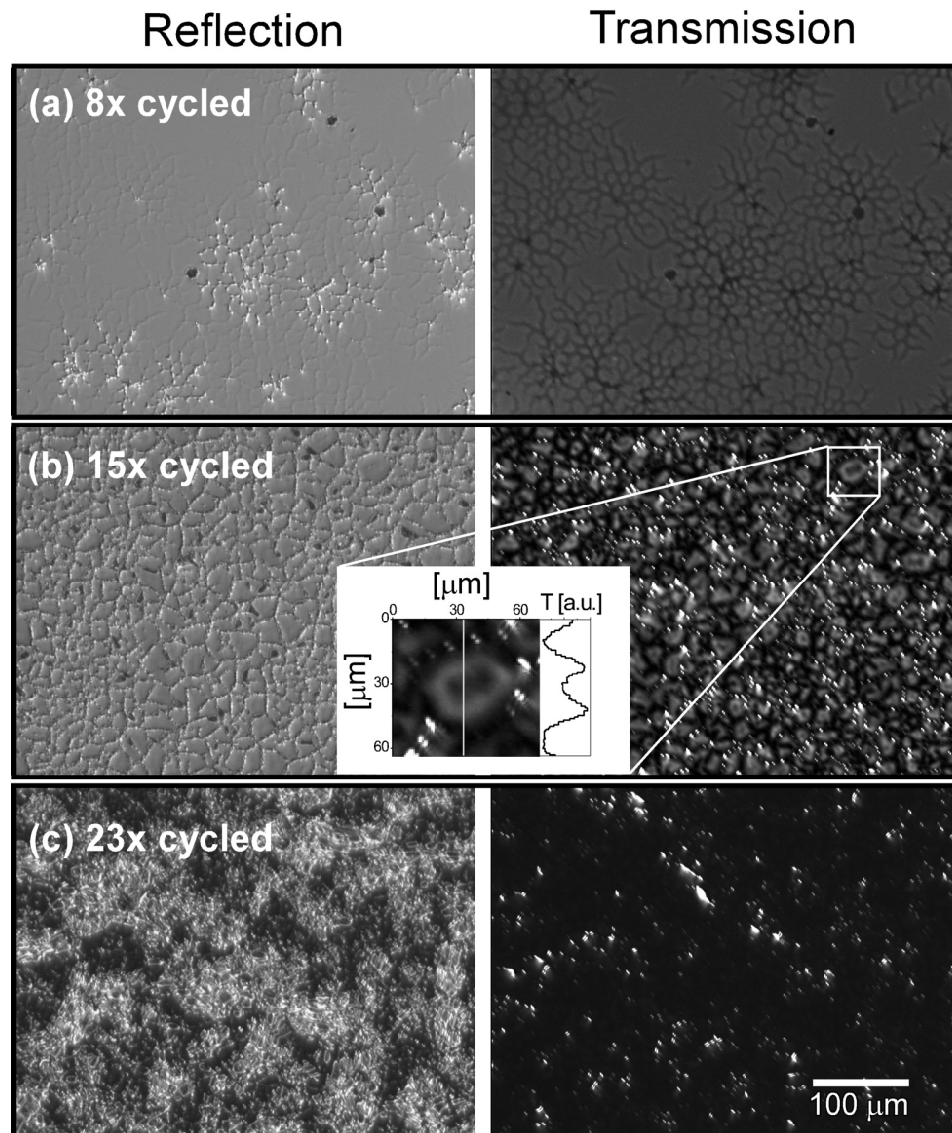
Figure 3.15: Optical microscope images in reflection (*left*) and transmission (*right*) of a 65 nm PdH$_x$ thin film in air after various hydrogen ab/desorption cycles. The buckle network is seen as bright lines in reflection, respectively dark lines in transmission, while cracks are visible as bright spots in transmission. Inset: detail of the film in transmission after 15 cycles showing transmission differences within one of the areas enclosed by the buckle-crack network.
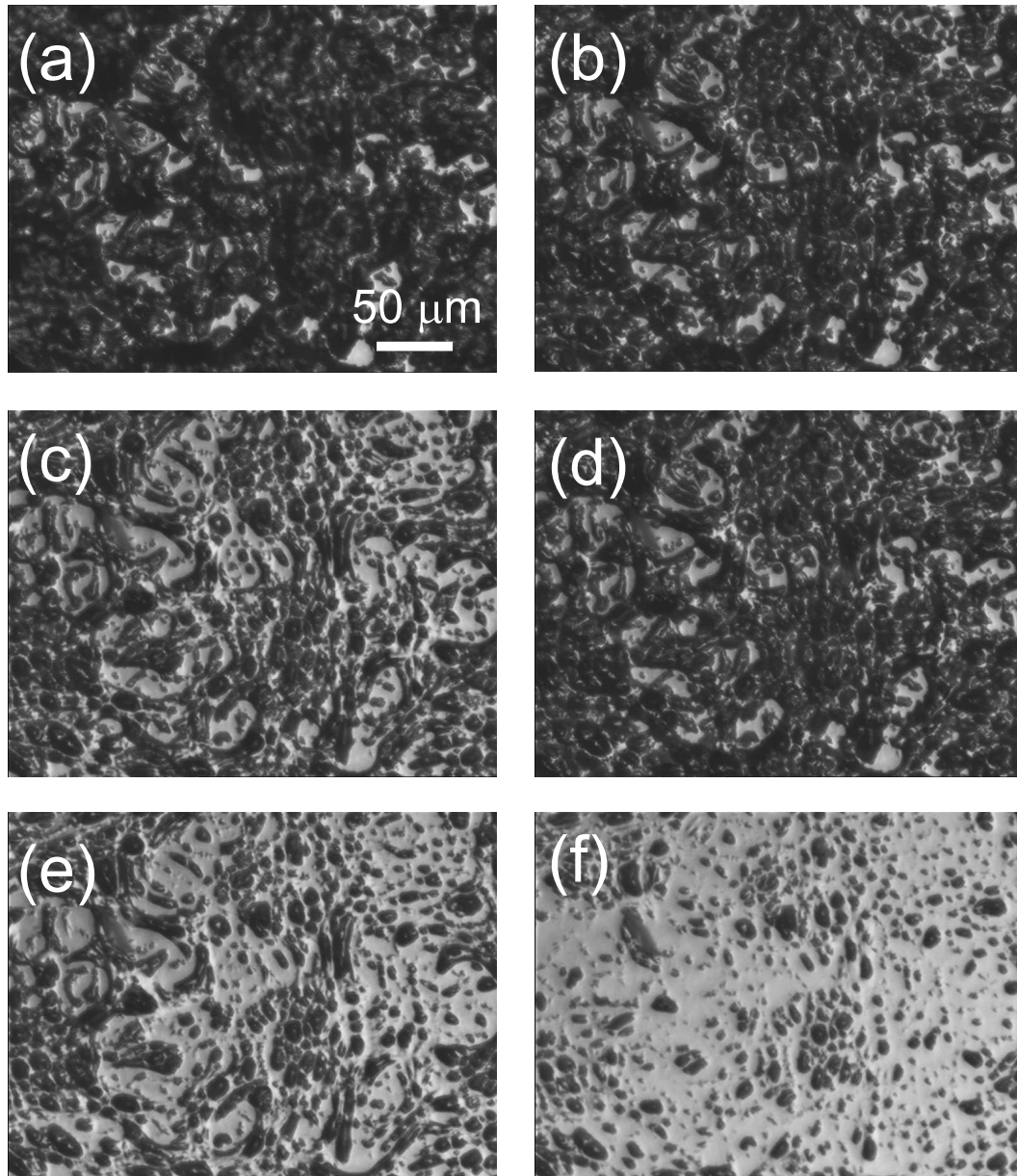
Figure 3.16: From (a) to (f), optical microscope images in reflection (same region) of a 24x cycled 65 nm Pd thin film on sapphire substrate during desorption in air. Time delay of 300 s between each frame. The part of the film in contact with the substrate is seen as light grey while the buckled part is dark. Note that even if after frame (a) most of the hydrogen has already desorbed, much more time is needed for the film to relax onto the substrate again.
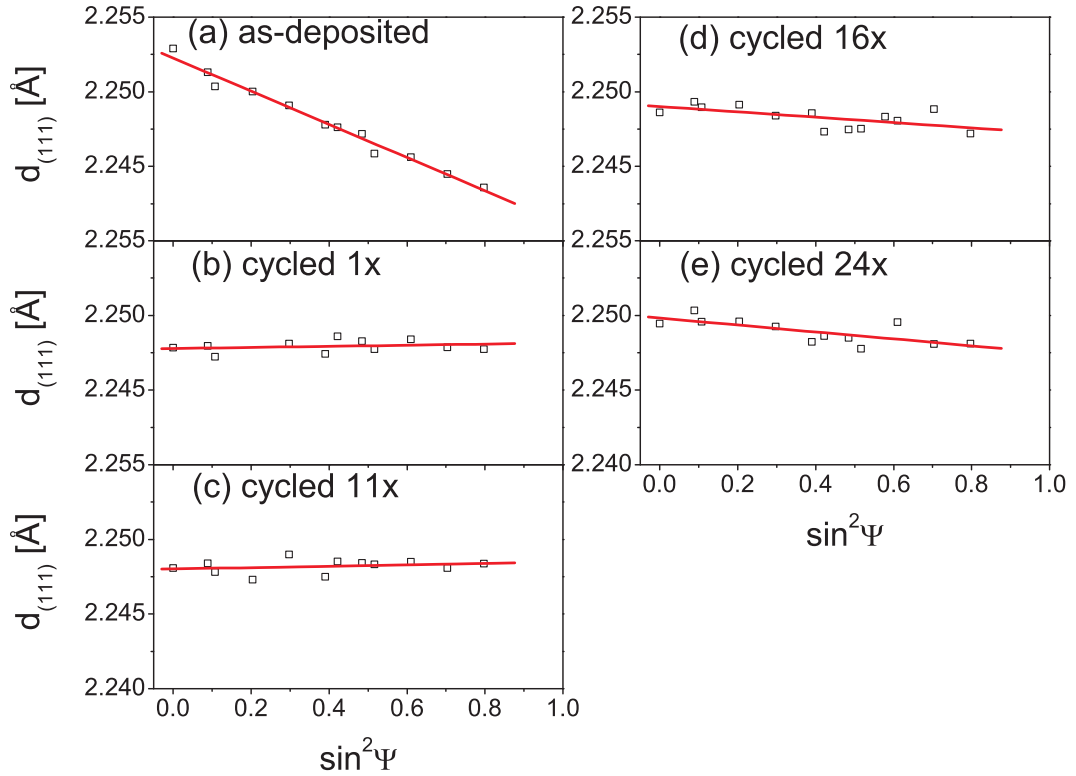
Figure 3.17: 111-distance as a function of $\sin^2(\psi)$ strain plots for different cycle numbers on α-PdH$_x$. *Dashed lines*, linear regression fits used to determine the in-plane residual stress in the layer.

Residual stress measurement: Sin^2 ψ method

Figure 3.17 shows the d$_{111}$ interplanar distance as a function of $\sin^2\psi$ plots in the α-phase before loading, for increasing cycle number. All plots are linear, implying that no significant shear stress or large in-depth stress gradients are present in the film. In the as-deposited state, the slope is negative, indicating a compressive in-plane stress (Fig. 3.18). This is consistent with the out-of-plane d$_{111}$ tensile stress relaxation observed during the first cycle. One hydrogenation cycle is enough to relax the initial stress, and up to cycle 10, the film is under slight in-plane tensile stress. This is probably due to the surface morphology evolution: irreversible buckling leave large in-between areas under tension, resulting in an average positive stress value for the film. After cycle 10, however, the average in-plane stress gets compressive again. Irreversibly absorbed H, but also the subdivision of the film in a network of lots of smaller areas are probably the reason for the film to remain in compression after unloading.
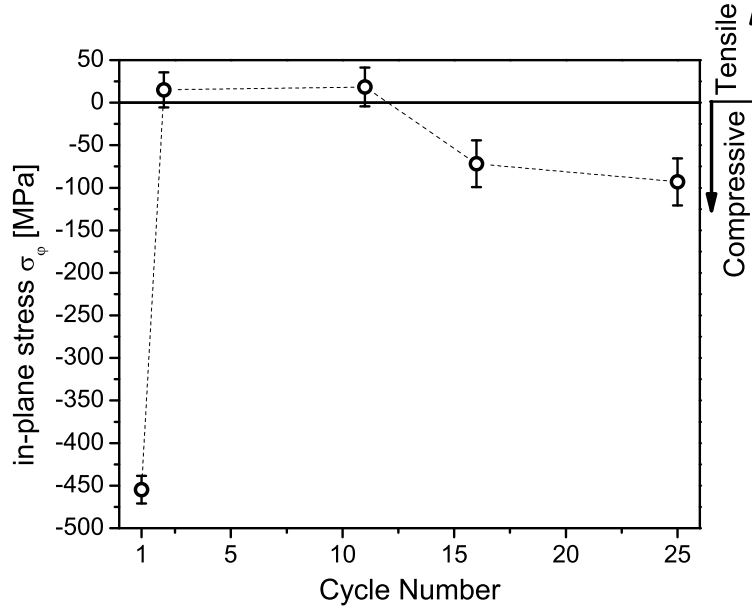
Figure 3.18: Residual in-plane stress before hydrogenation (α-phase) as a function of cycle number.

3.4.3   Discussion

The aim of this discussion is to correlate the observed change in the kinetics (fast cycles) and in the isotherms (cycles in quasi-equilibrium) as a function of cycling with the morphological and microstructural evolution, and eventually to gain insight in the most effective mechanisms to relax stress in the film.

Hydrogenation kinetics

Figure 3.1 shows $\ln(\mathrm{T/T_M})$ during the 15 first cycles at 295 K. The transmission values in the ab- and desorbed state are approximately constant up to cycle 8, after which both values increase with cycle number. The increase of $\ln(\mathrm{T/T_M})$ with cycling is however larger for the metallic state than in the β-phase. To follow the evolution of the kinetics, the rate of ab/desorption $R = d\ln(T)/dt$ is plotted in Fig. 3.19. The rate is approximately 10 times higher for absorption than for desorption. However, both exhibit the same trends: after an initial decrease during the first two cycles, the rate is approximately constant up to cycle 8. It then increases by a factor $\sim$4 at cycle 12 and then starts to decrease again.

By continuously creating fresh clean surface, cracks explain the drastic improvement of kinetics in both ab- and desorption for cycle 9 and following. As

they extend throughout the film, they also contribute in the overall transmission. The larger increase in $\ln(T/T_M)$ in the α- than in the β-phase is caused by partial closing of the cracks under hydrogen exposure.

Pressure-transmission-isotherms

We discuss here further the isotherms as a function of cycle number shown in Fig. 3.9 in light of the information gained about the film microstructure and morphology.

First hydrogenation cycle   The first cycle is characterized by a broad, gradual transition between the α and $\alpha + \beta$ regions and sloping plateaus. The hysteresis, though the largest of all cycles, is only about one order in pressure wide ($p_{abs}/p_{des} = 8.2$). As seen by SEM, buckles already appear during the first cycle. As buckles have a size distribution and do not cover the whole film surface, a wide distribution of strains is present in the the film, resulting in the observed sloping plateau and the gradual transition to the coexistence region. The large $T_{\alpha,max}$ shows that a fraction of the film is still under large stress.

Subsequent cycles   Little change is visible in the isotherms while the buckling pattern branches and starts to network. The α solubility limit decreases
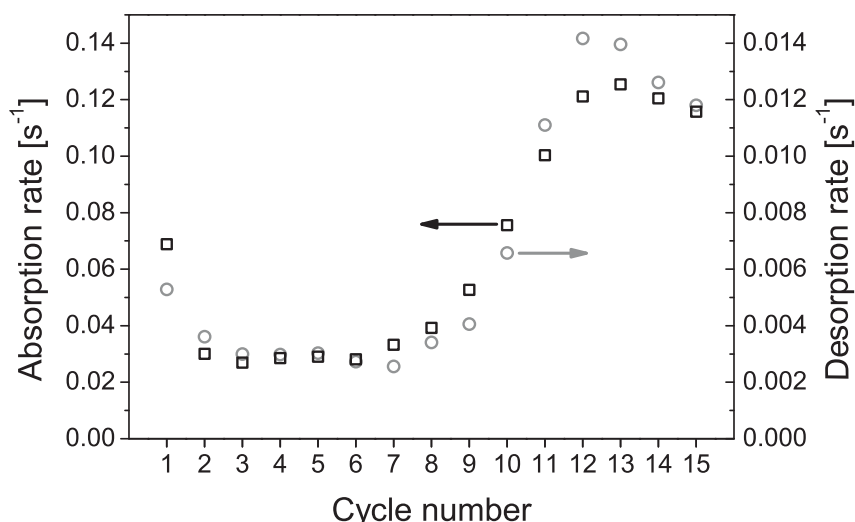
Figure 3.19: Rate of hydrogen ab/desorption $d\ln(T)/dt$ as a function of cycle number at 295 K. Note the factor 10 between absorption and desorption rates.

gradually with cycling. All the increase in CDD size and the enhanced [111] orientation observed by XRD happen before cycle 10. These microstructural changes could reduce the number of grain boundaries and consequently $\ln\left(T(\alpha_{\max})/T_{\mathrm{M}}\right)$. However, the α solubility limit still continuously decreases after cycle 10 (see Figure 3.21a), confirming that microstructural effects alone cannot explain the change of the phase boundaries with cycling.

It is only from cycle 9 on, when the buckle network completes (see Figure 3.15a) that a short flat section in the isotherms appears . The flat part in the isotherms develops, both in ab- and desorption, leading to a further decrease of the hysteresis. The increasing flat part in the isotherms indicates that the biaxial in-plane stress induced by clamping is reduced to the same extent in a large fraction of the film. The relaxation of the isotherms coincides with the appearance of cracks (cycles 9-15), that can be followed both directly by SEM and indirectly by recording the increase in optical transmission with cycling (see Fig. 3.1). After 15 cycles, the film is subdivided in areas of a few tens of μm^2 surrounded by buckles and cracks, in which the in-plane biaxial stress induced by hydrogen absorption is able to relax more homogeneously. With the subdivision in smaller areas, the film looses long-range coherency. This is evident from the residual stress evolution, that changes from tensile at cycle 10 when the film is still fully interconnected, to compressive for disconnected areas at cycle 16. As a result of the coherency strain reduction, after 24 cycles the hysteresis decreases to $p_{ab}/p_{des} = 2.7$, considerably closer to the theoretical hysteresis $p_{ab}/p_{des} = 1.94$ at $\mathcal{T} = 297$ K, treating PdH$_x$ as an open two-phase systems with coherent interfaces.[72,81] To investigate the effect of the buckle-and-crack network on the stress relaxation in the film, PTIs during cycle 18 are compared in Fig. 3.20 for 65 nm Pd films, with and without a 2 nm Ti adhesion layer between Pd and the sapphire substrate. The Ti adhesion layer provides improved sticking to the substrate, and these films are cycled up to 24 times without observing buckle formation.[95] Direct comparison in Fig. 3.20 shows that the relaxation of the stress through buckling reduces the hysteresis from $p_{\mathrm{abs}}/p_{\mathrm{des}} = 18.5$ (well-clamped films, no buckles) to $p_{\mathrm{abs}}/p_{\mathrm{des}} = 3.8$ (buckled PdH$_x$ film, without Ti adhesion layer). Note that we however cannot exclude the existence of yet another relaxation relaxation mechanism in the clamped film.

3.5   Conclusion

In summary, an *optical* method to determine the enthalpy, entropy and hysteresis of hydrogen ab- and desorption of thin metal films has been demonstrated for a *metallic* hydride. Pressure–optical-transmission–isotherms of the Pd-H system have been measured over wide pressure and temperature ranges. The method works for both interstitial hydrides, such as PdH$_x$ that remain metallic upon hydrogenation and hydrides that undergo a metal-insulator transition
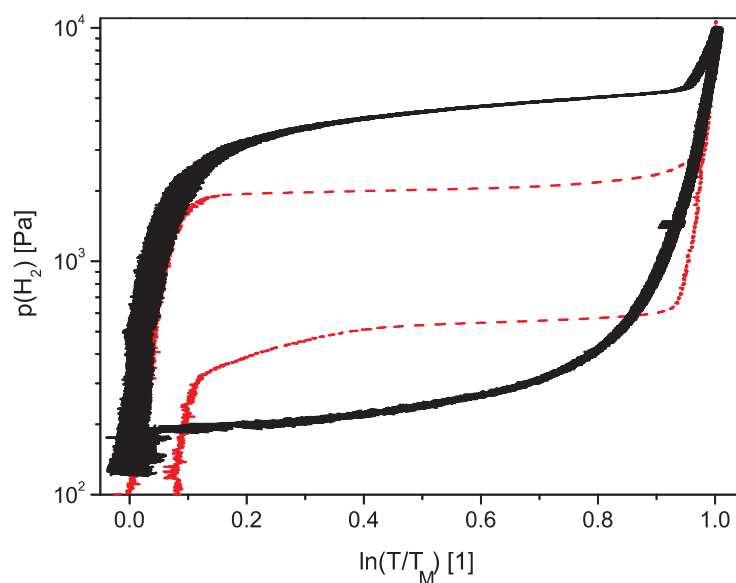
Figure 3.20: Comparison at 297 K of first cycle PTIs of 65 nm Pd thin films with (*Full line*) and without (*Dashed line*) a 2 nm Ti adhesion buffer layer between the Pd layer and the sapphire substrate.

(see next chapter). This shows that optical transmission can be used as a general screening tool for the combinatorial search of hydrogen storage materials.

The evolution with hydrogenation cycle number of ab- and desorption isotherms measured by Hydrogenography correlated with the film morphology and microstructure evolution provides essential information on the stress relaxation processes active in thin hydride films initially clamped to a substrate: The relatively small initial hysteresis compared to fully clamped films shows that buckling relaxes the H-induced stress build up in thin films effectively. However, buckling does not relax stress homogeneously in the film. It is only after the formation of a buckle-and-crack network that the film surface is fractionalized enough to enable a more homogeneous stress relaxation. This is clearly seen upon cycling in the isotherms, as a flat section progressively appears to replace the initially sloping plateaus, and corresponds to the transition from inhomogeneous to homogeneous stress distribution in the film. At the contrary to buckles and cracks, the observed microstructural changes (CDD size and preferred film orientation) do not have a noticeable effect on the hysteresis width and plateau slope, and hence do not contribute significantly to the stress relaxation in this case.

The final film morphology mimics bulk Pd and results in isotherms with flat plateaus and an hysteresis close to the theoretical limit. Therefore, thin film Hydrogenography gives results comparable to bulk if the in-plane stresses
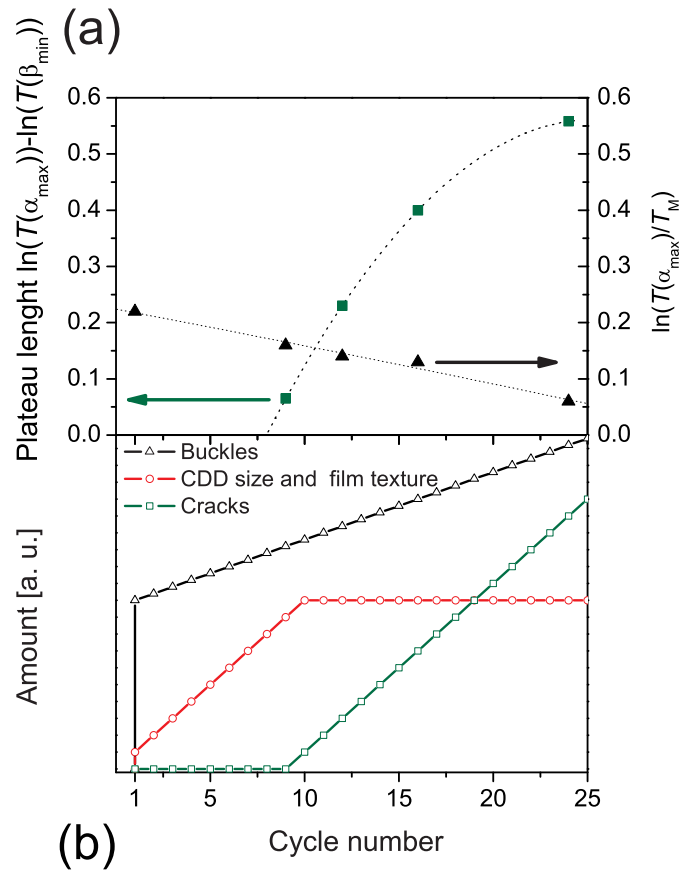
Figure 3.21: (a) *Squares*, PTI length of the flat part of the coexistence plateau in desorption, *triangles*, maximum transmission reached in the α phase $\ln\left(T(\alpha_{\mathrm{max}})/T_{\mathrm{M}}\right)$ in absorption, and (b) scheme of the morphological (buckles, cracks) and microstructural (CDD size, texture) changes observed as a function of cycle number. *Dotted lines* are guides to the eye.

are properly relaxed. This finding has been recently confirmed by pressure-resistivity-isotherms measurements on thin PdyAg$_{1-y}$H$_x$ films.[96]

Furthermore, H-cycling provokes reorganization of atoms on a micrometer scale at room temperature. This is encouraging for the study of complex hydrides in thin film form, where large movement of atoms is needed during cycling.

This study offers new possibilities to compare hydrogenation thermodynamics of thin films and bulk for the search of new light-weight hydrides. If compositional gradients are used, different compositions could be compared with each other even if the film remains clamped to the substrate, as the H-induced stress build-up is expected to be of similar magnitude for all composi-

tions. Applications in H-selective membranes[97], hydrogen sensors,[98], electrode materials for batteries[99] or smart coatings for adaptive solar collectors are also possible.[100]

Chapter 4

The ternary $Mg_yNi_{1-y}H_x$ system

4.1 Introduction

Pure MgH_2 would in principle be an attractive system for hydrogen storage as it contains as much as 7.6 wt% of hydrogen. However, its large negative enthalpy of formation ($\Delta H = -76$ kJ (mol H_2)$^{-1}$)) implies that high temperatures are needed to desorb hydrogen from MgH_2 at ambient pressure. Furthermore, the diffusion of hydrogen in the MgH_2 phase is very slow, and unless high temperatures are used, a blocking layer of the hydride forms that prevents further hydrogenation of Mg.[101] Many attempts have been made to destabilize MgH_2 and improve its kinetics by alloying it with transition metals (TM). The complex hydrides Mg_2NiH_4 is one of the most promising: it has a capacity of 3.6 wt% and a desorption enthalpy $\Delta H = -64$ kJ (mol H_2)$^{-1}$ [102]. Furthermore, the existence of the parent metal alloy, Mg_2Ni, helps it to make the hydrogenation fast and reversible, even at room temperature.[103] The reversible change of MgH_x and Mg_2NiH_x from a metallic to a transparent state upon hydrogen absorption makes them ideally suited for application as switchable mirrors[64,103,104] or hydrogen sensors[98,105,106]. Both hydrides are semiconductors with an optical band-gap of 5.6 eV and 1.68 eV for MgH_2,[64] respectively Mg_2NiH_4.[107] Thanks to this large energy difference in band-gaps, they can be easily discerned when coexisting in the same material.[108]

Bulk alloys with composition between Mg_2Ni and pure Mg (Hereafter referred to as "non-stoichiometric" alloys) decompose in these two phases, and hydride independently.[102,109] For the metallic and hydride phase diagrams, refer to Fig. 4.1 and Zheng et al.[110], respectively. Some early work on non-stoichiometric alloys focussed on the addition of few percent of Ni to improve the intrinsic poor Mg sorption kinetics.[111–114] The best results in term of kinetics are found near the eutectic composition ($y = 0.883$ in Mg_yNi_{1-y}) and were attributed to the intimately mixed morphology of the coexisting Mg and Mg_2Ni phases.[114,115] In general, the possibility to synthesize non-stoichiometric, metastable Mg-Ni alloys opens a lot of possibilities to under-
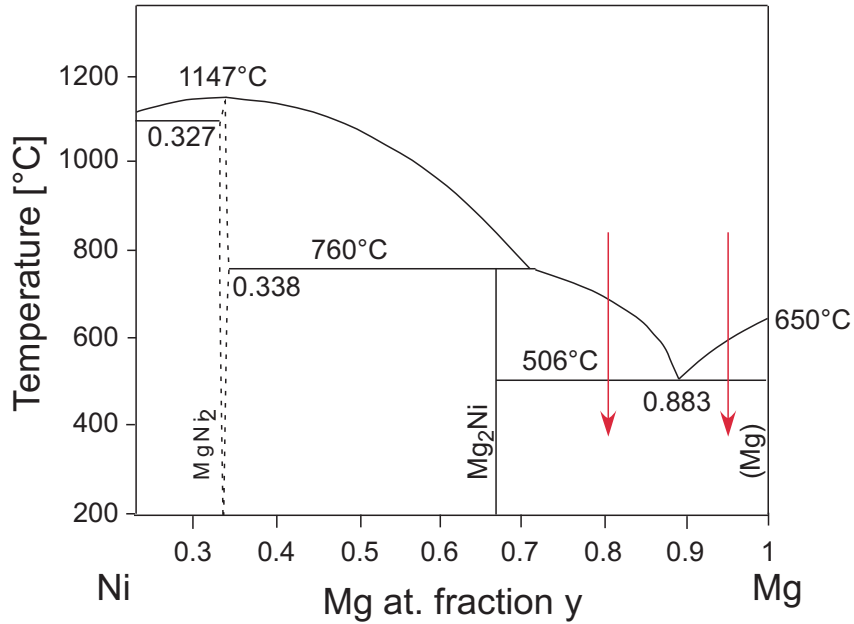
Figure 4.1: Bulk Mg-Ni phase diagram.[116] Arrows show the intrinsic rapid quenching occurring during sputter-deposition.

stand and improve their functional properties as hydrogen storage materials, switchable mirrors or hydrogen sensors. For example, the use of techniques such as ball-milling, sputtering or pulverization made possible to prepare nanocrystalline Mg_2Ni or amorphous MgNi ($y \simeq 0.5$) hydrides.[17,117] A Mg_4Ni alloy ($y = 0.8$) obtained by high-pressure synthesis was also reported. [118] From this rose the question whether metastable non-stoichiometric phases can also be present in sputtered $Mg_yNi_{1-y}H_x$ thin films. Indeed, the highest optical contrast[106,119,120] in these films is found between Mg_4NiH_x and Mg_8NiH_x. However it turned out that the smoothly changing optical properties in this compositional range are due to an increasing doping of Mg_2NiH_4 by Mg.[108]

In this chapter, we present our results on the hydrogenation properties of Pd-capped, co-sputtered Mg_yNi_{1-y} thin films with a gradient in the Mg fraction y. We focus mainly on the $0.5 < y < 0.95$ range that contains the interesting hydride forming compositions. We see that the structural, morphological, optical, kinetic and thermodynamic properties of the films depend strongly on the location in the metallic phase diagram. The chapter is organized in three parts. We present first the methods developed to characterize the various phases in the gradient thin films, both in the as-deposited and hydrided state. We show that optical spectrophotometry is particularly suited to scan quickly all compositions and identify the compositional extension of the hydride phases found. In the second, kinetics part, the rate of hydrogen absorption is determined from the optical transmission of all composition si-

multaneously and then modeled with a two-step approach. Simple expressions are derived for different rate-limiting step conditions and the experimental results on $Mg_yNi_{1-y}H_x$ thin films are then compared with the model. The third part treats the thermodynamics of the same films and presents the compositional dependence of the pressure–optical-transmission–isotherms and Van 't Hoff plots and discusses the derived hydride formation enthalpy values.

4.2 Experimental

Mg_yNi_{1-y} thin films (30-300 nm) are prepared in a 7-gun ultra-high-vacuum dc/rf magnetron co-sputtering system (base pressure 10^{-7} Pa) at room temperature. A 5-20 nm Pd capping layer is added *in situ* for oxidation protection and to promote further hydrogen uptake in the subsequent experiments. For optical measurements and X-ray diffraction, quartz, Si, sapphire or CaF_2 substrates are used whereas for electrolytical loading glass substrates covered with a 180 nm ITO (indium doped tin oxide) layer are used. The conducting (and transparent) ITO layer is necessary to ensure a homogeneous potential and hence a homogeneous H-uptake over the entire surface area during electrochemical loading. For Hydrogenography measurements, Mg_yNi_{1-y} thin films with a compositional and thickness (30-100 nm) gradient are prepared on 70 x 5 mm^2 quartz substrates. Mg and Ni are facing each other in tilted off-axis sputtering guns. By adjusting the power applied to each gun the desired compositional region of the binary phase diagram is obtained. Typical deposition rates are: 0.7-3Å/s for Mg (120 W RF power), 0.5-1.6Å/s for Ni (20 W DC power) and 1.3Å/s for Pd (50 W DC power). The local composition of the gradient films is determined by Rutherford Backscattering Spectrometry on films grown in the same deposition run on amorphous carbon substrates. The structural characterization is performed in a Bruker D8 Discover X-ray diffractometer (Cu-Kα, $\lambda = 1.5418$ Å) mounted in a $\theta - 2\theta$ geometry and equipped with a slit detector. Gradient thin films for dc resistivity measurements consists in 23 electrically isolated 2.5 x 5 mm^2 zones. The electrical resistivity is measured in a home-made apparatus which enables successive resistivity measurement in each zone by the Van der Pauw method.[121] The apparatus has a transparent Perspex arm that can slide perpendicularly to the sample on which four gold, spring damped needles with a tip diameter of 25 μm are mounted in a 2 x 2 mm^2 square. The optical spectra in the visible range are recorded with two dispersive OCEAN OPTICS fiber optics spectrometer with an energy range of 1.1-3.3 eV. Reflection and transmission are measured through a custom-made hydrogenation cell by means of two optical fibers facing each other at normal incidence. The 6 radially distributed cores of a 7-core fiber serve for the illumination from a Tungsten-halogen source, while the remaining central core carries the reflected light to the first spectrometer through a light splitter. The light transmitted through the sample is collected by a second, single-core

fiber facing the illumination fiber connected to the second spectrometer. Both fibers are connected to an automatized moving stage to spatially scan in the x- and y directions samples up to 76 mm in diameter. The light spot size is ≈ 1 mm^2 and the stage positioning better than 0.1 mm. Optical reflection and transmission spectra in the infrared are with a Bruker IFS66 Fourier transform spectrometer with an energy range of 0.120.6 eV ($1/\lambda = 9674839$ cm^{-1}). The IR-spectrometer is equipped with a reflection and transmission unit with near normal incidence of the incoming beam and a hydrogen loading cell to follow the optical properties during hydrogen uptake. Hydrogen pressures up to 10^5 Pa H$_2$ can be applied in both optical systems. For electrolytical loading a standard three electrode setup is used with a HgO/Hg reference electrode and a Pt counter electrode in 1 M KOH electrolyte. During the loading, transmission and reflection are measured simultaneously at a fixed wavelength λ=635 nm (1.95 eV). Hydrogenography kinetics and thermodynamics measurements are performed with the Hydrogenography setup (see Sec. 2.2.2).

4.3   Phase identification

4.3.1   Metallic state

X-ray diffraction

X-ray diffraction measurements on as-deposited Mg_yNi_{1-y} ($0.55 < y < 0.89$) thin films with a compositional gradient indicate the presence of crystalline Mg$_2$Ni through its 003 and 006-reflections (see Fig. 4.2). The fact that these are the only observed reflections in this range points to an oriented growth of the hexagonal lattice with the c-axis out of plane. The c-axis parameter slightly increases from 13.23 Å for $y = 0.6$ to 13.30 Å for $y = 0.80$. The c-axis parameter values are in all cases close to the bulk value (13.20 Å).[66] To get information about the amount and compositional extension of the crystalline Mg$_2$Ni, the integrated 006 peak intensity is plotted in Fig. 4.3. The intensity has been corrected for film thickness differences. Due to the sputtering target geometry, the c-axis preferential orientation varies between $-5 \leftrightarrow +10°$ relatively to the substrate normal.[122] This effect is taken into account during acquisition of the 006-reflection by always choosing the optimum sample θ angle. Crystalline Mg$_2$Ni is only observed between $0.58 < y < 0.81$. Interestingly, the crystallinity is not only high around a Mg$_2$Ni composition ($y = 0.67$), but stays also high up to $y \simeq 0.75$. Apart from Mg$_2$Ni, no other phases could be detected in the $0.41 < y < 0.89$ range. The rutile Mg 002-reflection is only observed for compositions $y > 0.89$, i.e. above the Mg-Mg$_2$Ni eutectic composition (See Fig. 4.1).

X-ray diffraction establish the presence of Mg$_2$Ni in Mg_yNi_{1-y} films that are sputter-deposited at room temperature. To satisfy the overall stoichiometry, crystalline Mg$_2$Ni should coexist with an amorphous metallic matrix consisting
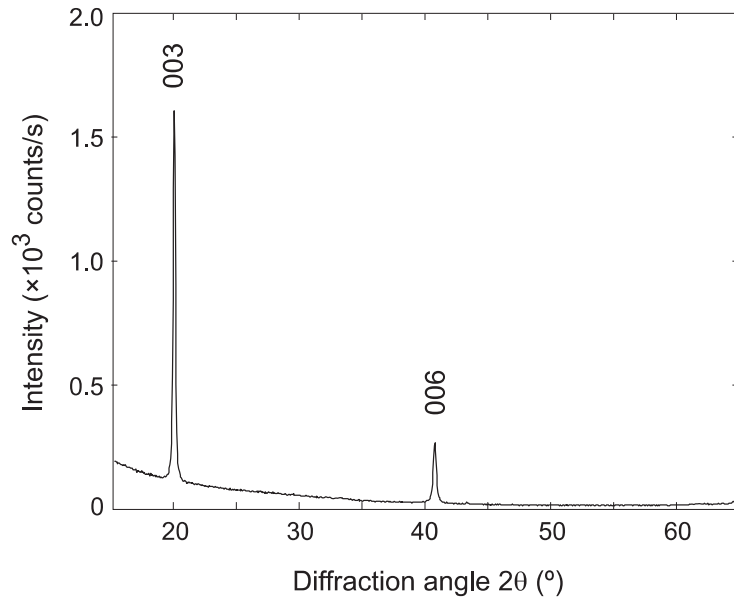
Figure 4.2: X-ray diffraction pattern of as-deposited sputtered Mg_yNi_{1-y} on a Si substrate for $y = 0.68$. The Mg_2Ni 003 and 006-reflections indicate that the c-axis of the hexagonal lattice is out-of-plane.
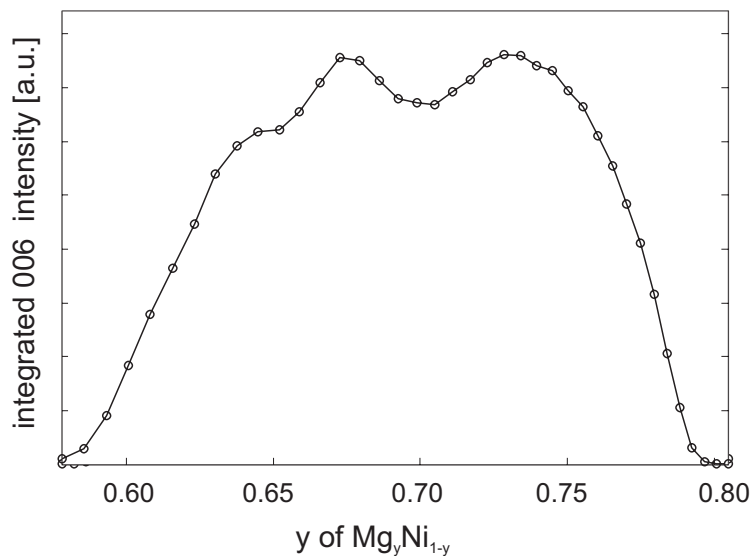
Figure 4.3: The Mg_2Ni integrated 006-reflection intensity as a function of Mg fraction y in a Mg_yTi_{1-y} compositional gradient thin film. For each composition, the sample angle θ is adjusted for the maximum intensity of the rocking curve. [122]

of Mg_2Ni, $MgNi_2$, Mg and Ni, depending on the composition y.[123]

Electrical dc resistivity

Resistivity measurements are carried out for Mg_yNi_{1-y} compositions between $0 < y < 1$ on glass substrates. The experimental electrical resistivity of pure Mg ($y = 1$) and pure Ni ($y = 0$) thin films are $\rho_{Mg} = 5.69 \pm 0.06$ and $\rho_{Ni} = 10.59 \pm 0.09\mu\Omega$cm, respectively, which is slightly higher than literature values. This is probably due to a thin oxide layer on top of the film, to impurities in the film and/or to structural imperfections due to the deposition technique. Theoretically, the room temperature electrical resistivity of a concentrated binary metallic alloy system can be described by Nordheim's rule.[124] This predicts the resistivity to be parabola-shaped with a maximum around the equiatomic composition (See e.g. Mg-Al, Fig. 7.3). This maximum resistivity indicates a disordered arrangement due to a random mixture of the component atoms.
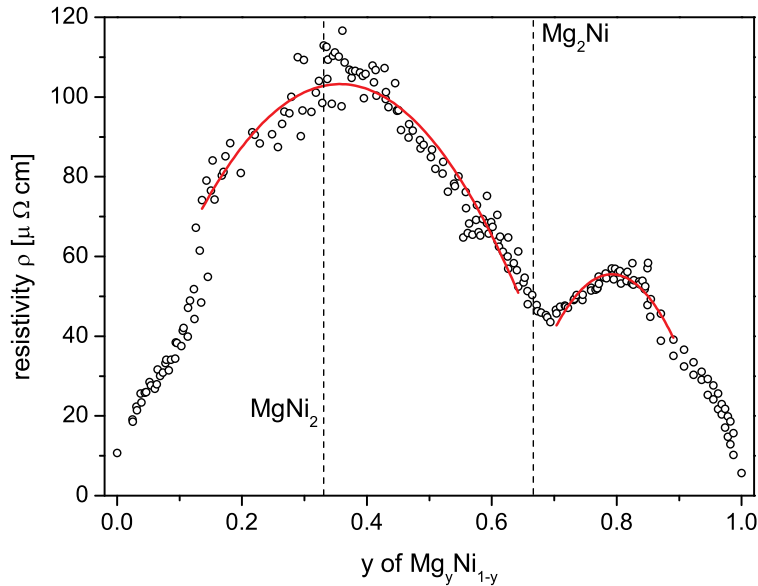
Figure 4.4: Compositional dependence of the measured room temperature dc resistivity ρ of $Mg_yNi_1 - y$. The fitted parabolas reflect the effect of disorder scattering.

Fig. 4.4 shows the experimental room temperature dc resistivity of Mg_yNi1_{1-y}. As the composition of the $MgNi_2$ phase is exactly centered around this maximum it indicates this phase to be structurally disordered. Note further the low resistivity around $y = 0.67$. In several alloys of specific stoichiometric compositions, the unlike atoms can preferentially populate distinct lattice sites creating

an ordered arrangement of the atoms on the crystal lattice sites.[125] The ordering processes result in a reduction of the residual resistivity of the alloy. The resistivity dip is centered around the composition of the Mg_2Ni phase, which means that contrary to $MgNi_2$, the Mg_2Ni phase has a well-ordered structure.

4.3.2 Hydride state

Contrary to the metal state case, during hydrogenation only the $Mg_2NiH_{0.3}$ hydride solid solution phase can be observed with XRD.[66] In the fully hydrogenated state, the crystallinity of the expected stoichiometric hydrides (Mg_2NiH_4, MgH_2) is too poor for theses to be resolved by XRD. We show in the following that optical techniques, which do not require long-range order of the atoms and allow for a parallel measurement of all compositions, are ideally suited to characterize thin hydride films with a gradient in composition.

Infrared Spectrophotometry

Fig. 4.6 shows R and T of a $Mg_{0.62}Ni_{0.38}H_x$ sample in the midinfrared ($\hbar\omega$ = 0.13 to 0.5 eV) exposed to 1 bar H_2 pressure. A broad absorption peak centered around $E_{ph} = hc/\lambda = 0.197$ eV (corresponding to 1585 cm^{-1}) due to a NiH stretch vibration[126] of the $[NiH_4]^{4-}$ unit is observed. For bulk Mg_2NiH_4, the infrared absorption has been reported to be at 1638 cm^{-1}.[126] The presence of the NiH vibration which is strongest for $0.6 < y < 0.8$ demonstrates the formation of the ternary hydride although the shift to lower energies indicates a disturbance of the Ni-H bond. For $y > 0.80$ the absorption line can still be observed however the signal strength gets weaker.[122] The characteristic vibrations of MgH_2 (around 1000 cm^{-1}) could not be accessed in the current setup.

Spectrophotometry in the visible

The optical appearance of the hydrided $Mg_yNi_{1-y}H_x$ gradient can be schematically divided in 3 parts: (i) for compositions $y < 0.67$, the film has a brownish appearance in transmission and has a relatively high reflection. (ii) for $0.67 \leq y < 0.89$, it gradually changes from red to yellow in transmission. Reflection in this range shows an interference-induced rainbow pattern due to the changing film thickness. (iii) Both reflection and transmission drops suddenly for $y > 0.89$ and the film appears black under these illumination conditions. In the following, we will discuss the origin of these color changes.

The optical reflectance R and transmittance T spectra in the visible light range as a function of composition y on the $Mg_yNi_{1-y}H_x$ gradient sample are recorded by means of a fiber optics spectrometer. As the light spot size (1 mm^2) is small relatively to the sample size (70 x 5 mm^2), abrupt changes of the optical properties with composition y are resolved. Figure 4.7 shows R and
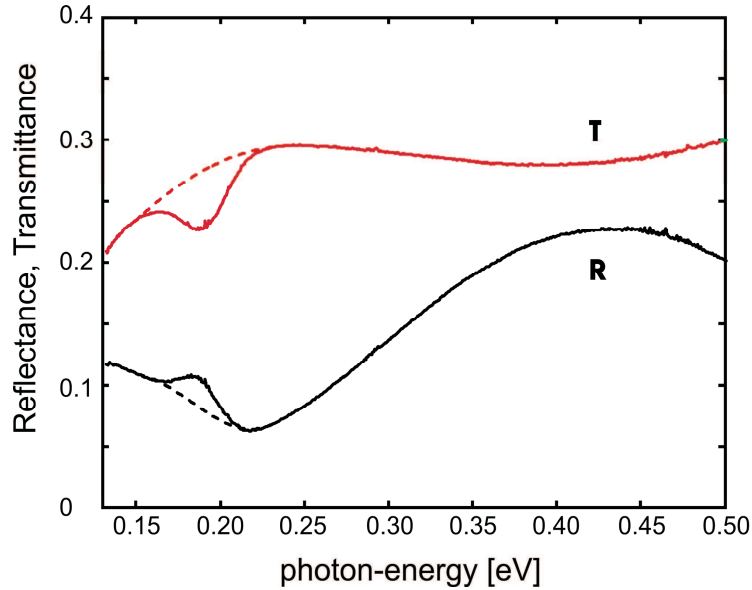
Figure 4.5: The infrared optical transmittance (T) and reflectance (R) at $y = 0.62$ in the hydrogenated state (solid lines). The $[NiH4]^{4-}$ phonon absorption is centered around $\hbar\omega = 0.197$ eV. The *dotted line* is a guide to eye for the absorption-free signal.
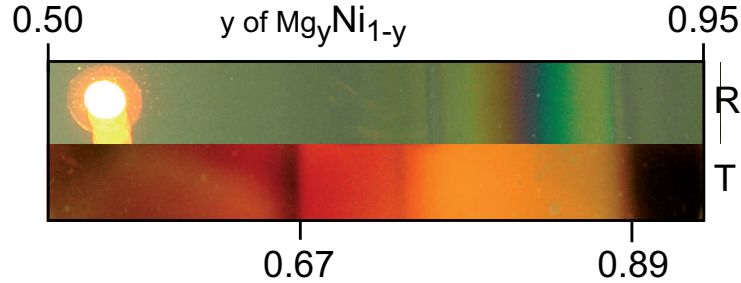
Figure 4.6: Visual appearance of the $Mg_yNi_{1-y}H_x$ in the hydrogenated state after 120 h at $2\cdot 10^5$ Pa H_2 and room temperature. The bright spot on the left comes from a light source below the sample.

T for a spot corresponding to a nominal Mg_2NiH_x composition ($y = 0.67$) on a gradient sample exposed to a $2\cdot10^5$ Pa H_2 pressure at room temperature for 120 h. The wide minimum in reflectance around 1.7 eV is due to a destructive interference between light reflected at the film surface and at the interface with the substrate. Similarly, the high-frequency oscillation at low energy is caused by interference between the hydrogenation cell window and the substrate. The transmittance shows an absorption edge, starting from about 1.8 eV, which we attribute to the presence of the semiconducting hydride Mg_2NiH_4. From conductivity measurements,[107] the energy gap of bulk Mg_2NiH_4 is 1.68 eV,

while thin film literature measurements at the stoichiometry ($y = 0.67$) report
values between 1.6 and 1.9 eV.[66,104,108]
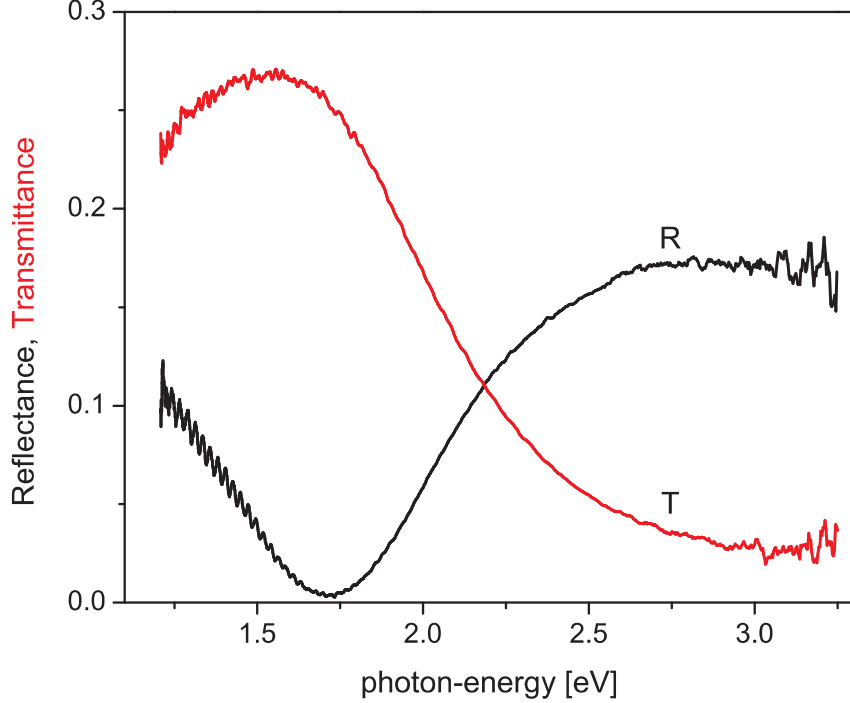
Figure 4.7: The visible optical transmittance (T) and reflectance (R) at $y = 0.67$ (Mg_2NiH_x) in the hydrogenated state.

A detailed analysis of the reflectance and transmittance spectra for discrete
$Mg_yNi_{1-y}H_x$ composition has already been described elsewhere[108] and will not
be repeated here. To learn more on the compositional extension and phase
boundaries of the hydride phases, we will focus instead on the compositional
dependence of R, T and the absorption coefficient α:

$$\alpha = -\frac{1}{t}\left[\ln\left(\frac{T}{1-R}\right) + \alpha_{Pd}t_{Pd}\right], \tag{4.1}$$

where t is the thickness of the $Mg_yNi_{1-y}H_x$ film and R and T are the
reflectance and transmittance at each energy. t_{Pd} and α_{Pd} denote the thickness
of the Pd capping layer and its absorption coefficient which was obtained from
the known extinction coefficient k of Pd[49] and

$$\alpha = \frac{2k\omega}{c}, \tag{4.2}$$

ω is the angular frequency and c the speed of light.

Figure 4.8 displays R, T and α as a function of atomic Mg fraction y for
two photon-energies: $\hbar\omega = 1.6$ eV and 3.0 eV. A remarkable feature at both

energies is the abrupt ($\Delta y \approx 0.01$) drop of both R and T around the $y = 0.886$ composition. This composition corresponds, within the measurement error, to the Mg_2Ni-Mg eutetctic ($y = 0.883$).[127] According to the phase diagram (see Fig. 4.1), the metallic Mg_yNi_{1-y} layer consists in a mixture of Mg and Mg_2Ni for composition both directly above *and* below the eutectic composition. Yet the films are deposited using sputtering, which is a non-equilibrium technique: atoms coming from the elemental targets have a relatively high kinetic energy (1-15 eV)[48], energy which is dissipated quickly as the atoms encounter the substrate. This process is analogue to a rapid temperature quenching in the phase diagram (see the *red arrows* in Fig. 4.1), followed by relaxation in the equilibrium phases (Mg_2Ni and Mg). The microstructure of the Mg_yNi_{1-y} layer, therefore, is quite different depending on the location respectively to the eutectic composition: below the eutectic, Mg_2Ni crystallizes at higher temperature than Mg. This higher respective mobility of atoms yields large enough Mg_2Ni grains to be detected by XRD, with a coherence length ~ 20 nm.[66,122] At the contrary, Mg is nanocrystalline or amorphous and cannot be detected by XRD in this range. Above the eutectic, the situation is reversed, and nanocrystalline Mg_2Ni grains are dispersed in the Mg matrix. This change in microstructure of the staring metal alloy is responsible for the jump in optical properties of the hydride: Below the eutectic point, Mg-doped Mg_2NiH_4 is present for all compositions,[108] which gives a high transmittance and low reflectance for energies below the band gap (Fig. 4.8(a)) of Mg_2NiH_4 and a low transmission and high reflection above the band gap (Fig. 4.8(b)). Above the eutectic point, if all of the Mg present in the layer would hydride, transmission should be high and reflection low for both photon-energies considered, as MgH_2 is a wide band-gap semiconductor ($E_g = 5.6$ eV). However, at room temperature, full hydrogenation of Mg is hampered by the slow diffusion of H in the MgH_2 phase,[101] and a large amount of metallic Mg remains in the layer. The incomplete hydrogenation results, like in the case of pure Mg,[128] in a "black" state (low transmission and reflection) due to the coexistence of metallic Mg and semiconducting MgH_2 nanograins. Note that the R and T spectra in Fig. 4.8(a) and (b) depend on the thickness of the Mg_yNi_{1-y} layer and of the Pd caplayer. The absorption coefficient α takes these effect into account and makes it possible a fair comparison between different compositions. The compositional dependence of α for a photon-energy $\hbar\omega = 1.6$ eV in Fig. 4.8(c) shows that between the stoichiometric Mg_2Ni and the Mg_2Ni-Mg eutectic compositions ($0.67 < y < 0.886$), the absorption coefficient is approximately constant. For Ni-richer compositions, it gradually increases, most probably due to non-reacting nanocrystalline/amorphous components such as $MgNi_2$ or Ni. Above the eutectic composition, α is also constant, but at a higher value than in the Mg-doped region, due to the unreacted Mg. At $\hbar\omega = 3.0$ eV, α shows a similar behavior, although shifting to higher values due to the extra absorption above/in the Mg_2NiH_4 band gap. In summary,

composition-dependent spectroscopy immediately give information on the hydride phases formed in the $Mg_yNi_{1-y}H_x$, their boundaries (eutectic) and on the relative metallic amount left in the layer. An overview is obtained in Fig. 4.9, where the variation of the absorption coefficient with composition y and photon-energy is plotted as a color map (a) and for selected compositions below (b) and above (c) the eutetic point. In (a) and (b), it is obvious that the absorption edge energy continuously shifts upwards with increasing Mg fraction y. This has been already reported for samples of homogenous compositions above the [Mg]:[Ni] = 2 stoichiometry ($y = 0.67$),[108] and has been attributed to an increase of the free carrier density due to doping by Mg of the Mg_2NiH_4, which makes the lowest states in the conduction band inaccessible (Burstein-Moss shift[129–131]). What is new in our measurement of the $Mg_yNi_{1-y}H_x$ gradient is that *sub-stoichiometric* compositions present a band-gap which is *narrower* than the intrinsic Mg_2NiH_4 energy gap of 1.68 eV[107] (Fig. 4.10). Such a band-gap narrowing is probably due by the Ni-excess for $y < 0.67$, adding donor levels into the energy gap and resulting in an effective smaller band-gap. Another possibility is that, due to the Ni-doping, many body effects could shift valence and conduction band toward each other, with a narrower energy gap as net effect.[132] In total, the energy gap can be varied by 0.5 eV, from 1.5 to 2 eV, by changing the Mg fraction from $y = 0.53$ to 0.77, after which it saturates.
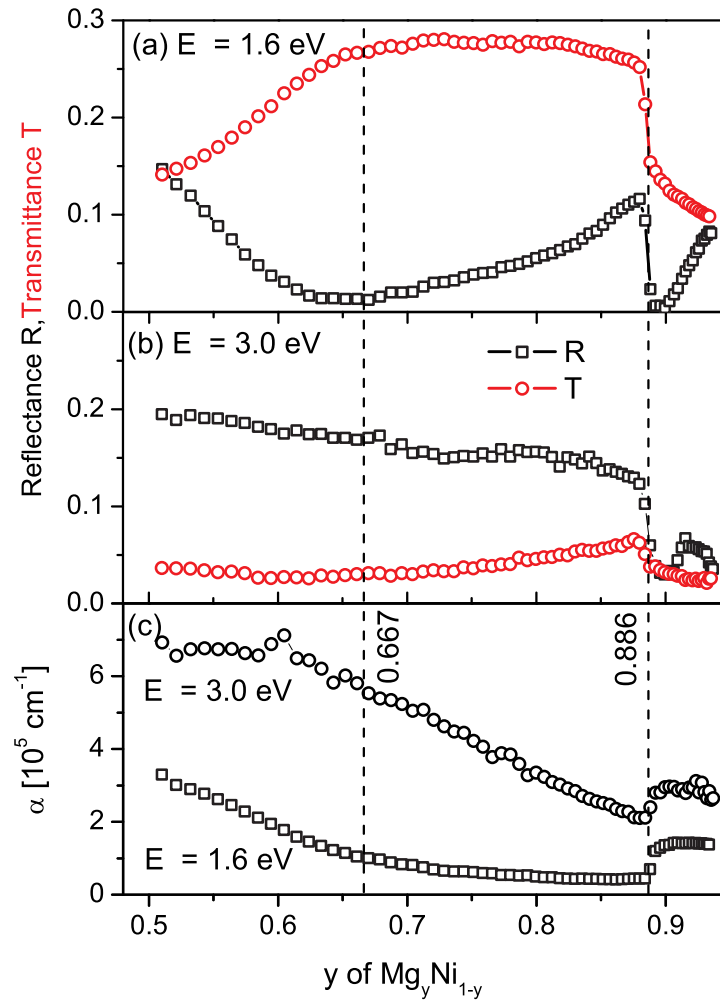
Figure 4.8: $Mg_yNi_{1-y}H_x$ compositional dependence of optical reflectance and transmittance at (a) $\hbar\omega = 1.6$ eV (775 nm wavelength) and (b) $\hbar\omega = 3.0$ eV (4.13 nm wavelength)photon-energy. (c) Corresponding absorption coefficient α for these 2 photon-energies.
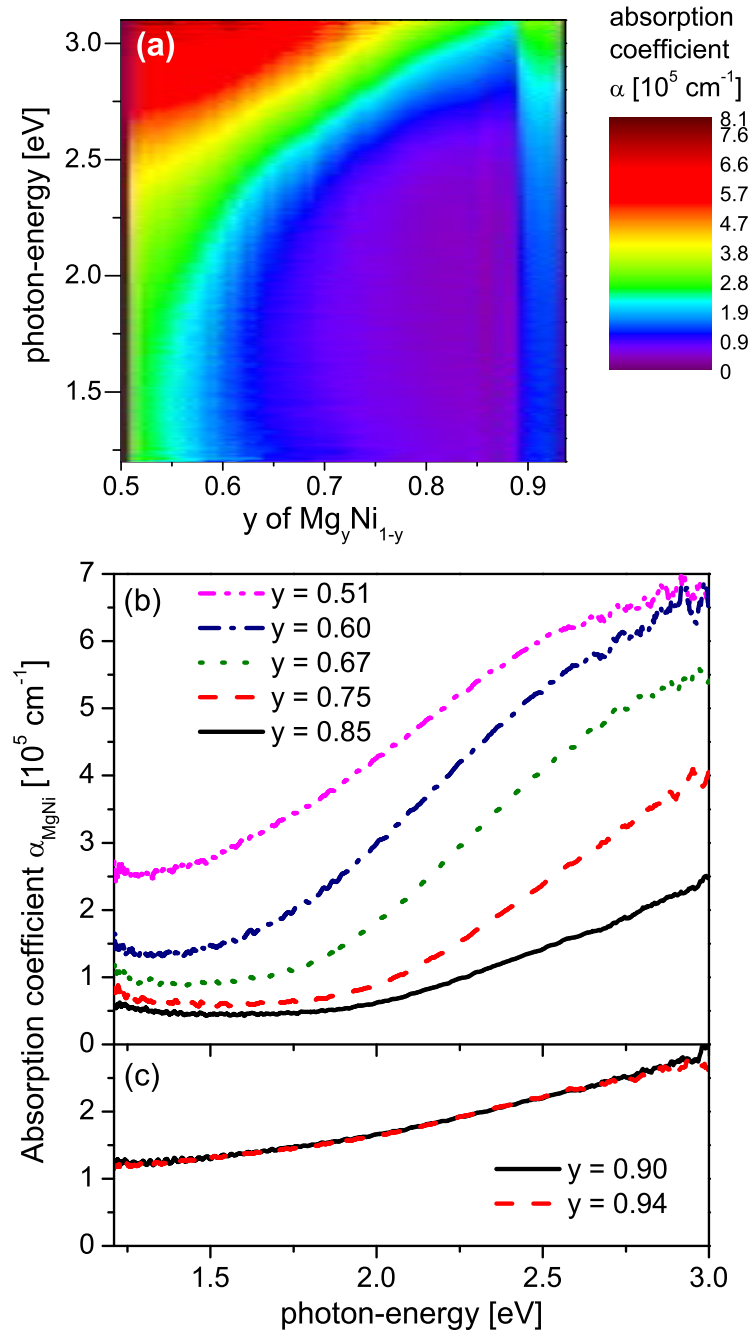
Figure 4.9: Energy dependence of the optical absorption coefficient α for a $Mg_yNi_{1-y}H_x$ gradient thin film: (a) Compositional dependence map, (b) and (c) α for various compositions y.
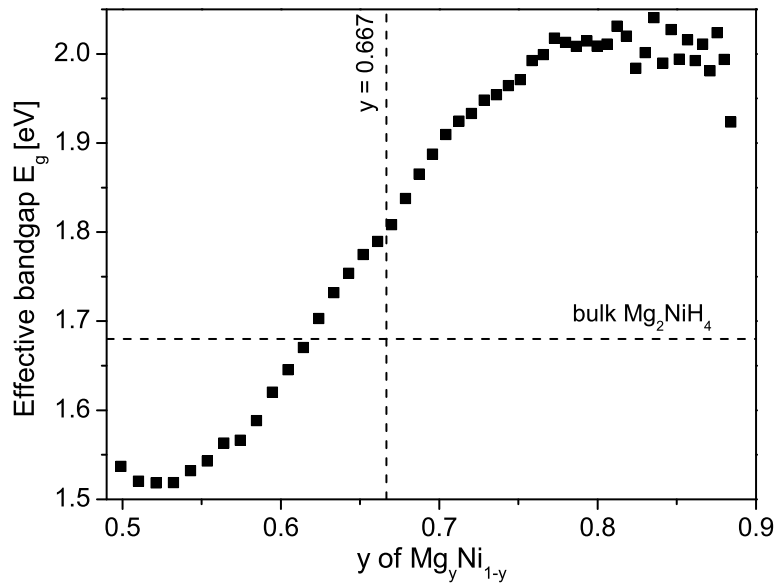
Figure 4.10: $Mg_yNi_{1-y}H_x$ compositional dependence of the effective optical bandgap energy E_g. The vertical line indicates the [Mg]:[Ni] = 2 stoichiometric composition and the horizontal line the band-gap of bulk Mg_2NiH_4.[107]

4.4 Kinetics: the rate of H absorption

This section is divided in two parts. In the experimental part, the optical measurement and analysis method to determine the rate of H absorption in thin $Mg_yNi_{1-y}H_x$ films is presented. Issues and results on the reproducibility of the absorption rate with cycle number and the pressure dependence of the rate are addressed here. In the second part, we develop a simple two-step model for hydrogen sorption incorporating i) hydrogen dissociation at the surface (here Pd) followed by ii) migration into a diffusion layer (in this case the $Mg_yNi_{1-y}H_x$ layer). The output of the model is an expression for the temperature and hydrogen pressure dependence of the H absorption rate. The model predictions are tested on the experimental hydrogen absorption rates in $Mg_yNi_{1-y}H_x$ gradient thin films.

4.4.1 Experimental rate

Optical rate determination

Thanks to the large optical contrast between the metallic and fully hydrogenated $Mg_yNi_{1-y}H_x$ at all Mg fractions y, the kinetics of H absorption can be monitored by recording the change in optical transmission after application of a sudden change in the applied hydrogen pressure, from below to above the equilibrium plateau pressures of the hydrides. Here the transmission is preferred to the reflection: during loading, the growing hydride layer creates an additional interface between metal and hydride and the reflection shows an oscillating behavior due to the interference between the light reflected on this moving interface and the interface with the substrate as seen in Fig. 4.25(a). In contrast, the transmission increases smoothly, as shown in Fig. 4.11. To further decrease the influence of interferences, the light intensity is averaged over a wide photon-energy band (1.1-3.3 eV). The top panel represents a false color map of the logarithm of the optical transmission T (where blue stands for low an red for high transmission) as a function of composition y and time after a sudden change of the hydrogen pressure from vacuum ($p < 10$ Pa) to $p(H_2)$=2020 Pa. In the bottom panel, we show $\ln(T)$ (Symbols) as a function of time for various compositions between $0.77 < y < 0.93$. A clear change of kinetics occurs around the eutectic composition: while for compositions $y < 0.88$ the entire optical change occurs within 100 s, for Mg-richer compositions hydrogenation takes approximately 10x more time. To extract the hydrogenation rate, we fit the change of transmission with time with a Boltzmann function:

$$\ln \frac{T}{T_M} = \left[1 - \frac{1}{1 + \exp\left(\frac{t - t_{1/2}}{\Delta t}\right)} \right] \ln\left(\frac{T_{MH}}{T_M}\right) \tag{4.3}$$

with the start, respectively final transmission T_M and T_{MH}, the half-time $t_{1/2}$

and the width Δt as fit parameters. The hydrogenation rate R is taken as:

$$R = \max\left(\frac{d\ln(T)}{dt}\right) = \ln\frac{T_{\mathrm{MH}}}{T_{\mathrm{M}}} \cdot \frac{1}{4\Delta t} \tag{4.4}$$

The lines in the bottom panel of Fig. 4.11 show the Boltzmann fits for the compositions $0.77 < y < 0.93$. For compositions well below ($y < 0.86$) and above ($y > 0.90$) the eutectic, the fits satisfactorily follow the change in optical transmission. In contrast, around $y = 0.88$, the fit departs significantly from the data. As the Boltzmann function is a simple model to represent saturating, *single* processes, the non-applicability of this fitting procedure indicates that probably two types of kinetic regimes are coexisting around the eutectic composition.
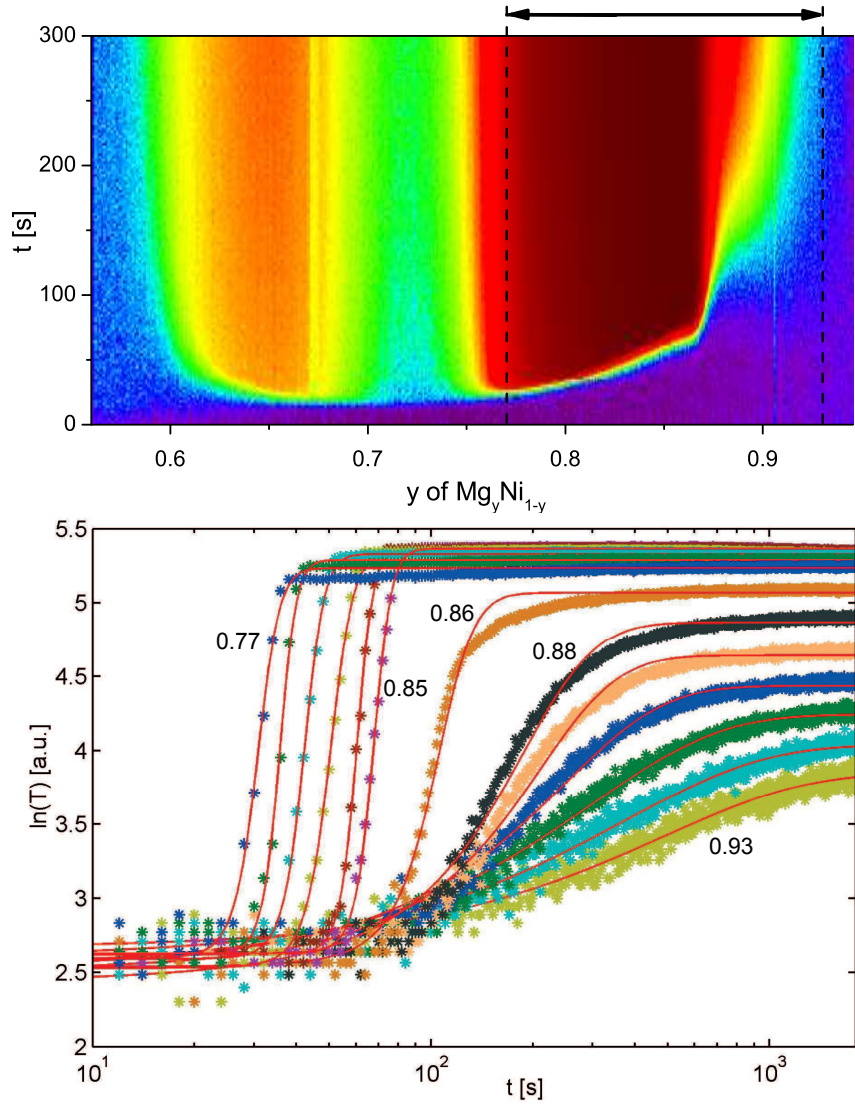
Figure 4.11: *Top*: False color map of $\ln(T)$, the logarithm of the transmission, as a function of time and composition y of Mg_yNi_{1-y} after the application of a $p(H_2) = 2020$ Pa pressure step at temperature $\mathcal{T} = 333$ K (first loading). *Blue* stands for low and *red* for high transmission. *Bottom*, *Symbols*, $\ln(T)$ as a function of time for various composition between $0.77 < y < 0.93$. The lines are Boltzmann fit used to determine the hydrogen absorption rate.

Reproducibility

To reliably compare the sorption kinetics as a function of hydrogen pressure, temperature and Mg fraction in the film, an important issue is to achieve a reproducible rate for each ab/desorption cycle. The Pd caplayer protects the film against oxidation and catalyzes hydrogen dissociation. However, this layer degrades upon cycling and its catalytic activity varies depending on the gases (type and coverage) it might be exposed to. Below a minimum thickness, the caplayer is not completely closed and the underlying oxidized metal encapsulates the Pd clusters. This effect, known as strong metal-support interaction (SMSI), deactivates the Pd clusters in less than 10 cycles.[133] A minimum thickness of 15 nm is therefore needed to ensure a closed Pd film and extend the H cyclability (i.e. conserved optical contrast upon cycling) of the underlying film up to approximately 200 cycles.[134]

Figure 4.12(a) shows the H absorption rate R as a function of cycle number for a constant pressure step on a $Mg_yNi_{1-y}H_x$ gradient thin film of 30-100 nm thickness capped by a 20 nm Pd caplayer. It is noteworthy that R actually *increases* with the number of cycles. To understand whether this behavior is intrinsic to the $Mg_yNi_{1-y}H_x$ layer or induced by an increase of the catalytic activity of the Pd layer, we capped *in situ* a second batch of samples with a 50 nm sputtered polytetrafluoroethylene (PTFE) overlayer. Capping the film with PTFE avoids polluting the Pd surface during transport in air, as the permeability coefficient through PTFE is about 6 times higher for hydrogen than for oxygen.[135] The rates as a function of cycle number of the PTFE capped sample, obtained simultaneously and under the same conditions as the uncapped one, are shown in Fig. 4.12(b). After activation during the first cycle, all subsequent cycles yield an amazingly similar rate for all Mg fractions. This proves that the improvement in rate observed for the PTFE uncapped sample is indeed due to a self-cleaning process on the surface of the Pd layer. It is known that adsorbed oxygen on the Pd surface inhibits hydrogen permeation by water formation.[136] As our samples are transported in air after deposition, a certain amount of oxygen/water is certainly present on the Pd surface. Repeated cycling with hydrogen in a closed cell makes water desorb again,[137] cleaning the surface and gradually improving the H absorption rate again by freeing sites for hydrogen.

In summary, this particular stack of layer (PTFE/Pd/Mg_yNi_{1-y}) makes it possible, by providing a reproducible rate from cycle 2 on[a], to suty in detail the influence of pressure, temperature and Mg fraction y on the H absorption rate using the same sample.

---

[a] i.e. without extensive cycling, like for pure Pd thin films studied in Chap. 3.
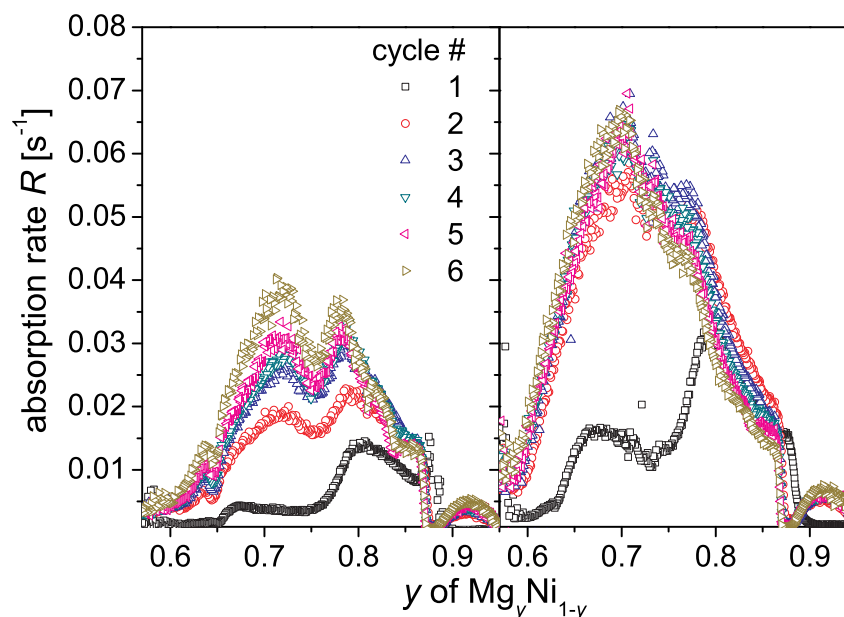
Figure 4.12: Comparison of the hydrogen absorption rate at p(H_2) = 200 Pa and $\mathcal{T}$ = 305 K for Pd-capped $Mg_yNi_{1-y}H_x$ (20/30-100 nm) thin films as a function of hydrogenation cycle number (a) without (b) and with a 50 nm PTFE in situ sputtered top layer.

Pressure dependence of the rate and equilibrium plateau pressure

Figure 4.13 displays optical transmission maps at 305 K as a function of time and Mg atomic fraction y for a 50/20/30-100 nm PTFE/Pd/Mg_yNi_{1-y} gradient film on a glass substrate after pressure steps applied at $t = 50$ s. Remarkably, the compositional range Δy of compositions that reacts can be tuned by changing the applied pressure: While only a very narrow range of Mg-doped Mg_2NiH_4 forms around $y = 0.72$ for $p(H_2)$= 80 Pa, this range extends in both directions with increasing applied pressure until all compositions below the eutectic are hydrogenated at $p(H_2)$= 420 Pa. Besides Mg_2NiH_4, free Mg transforms into MgH_2 for all pressures shown here, as the plateau pressure of this hydride is lower than < 10 Pa at this temperature. We attribute the shallow transmission band observed for $y > 0.9$ to MgH_2, as it is present at all applied pressures and metallic Mg is detected by XRD in this composition range. Additionally, there is most probably segregated MgH_x in the alloy for all compositions $y < 0.75$, as a distinguishable transmission step occurs when the pressure step is applied ($t = 50$ s) in all maps.

The rates of H absorption R are extracted from each map using the fitting procedure explained in Sec. 4.4.1, and summarized in Fig. 4.14. In hatched areas, absorption curves are not properly fitted and the data are not used
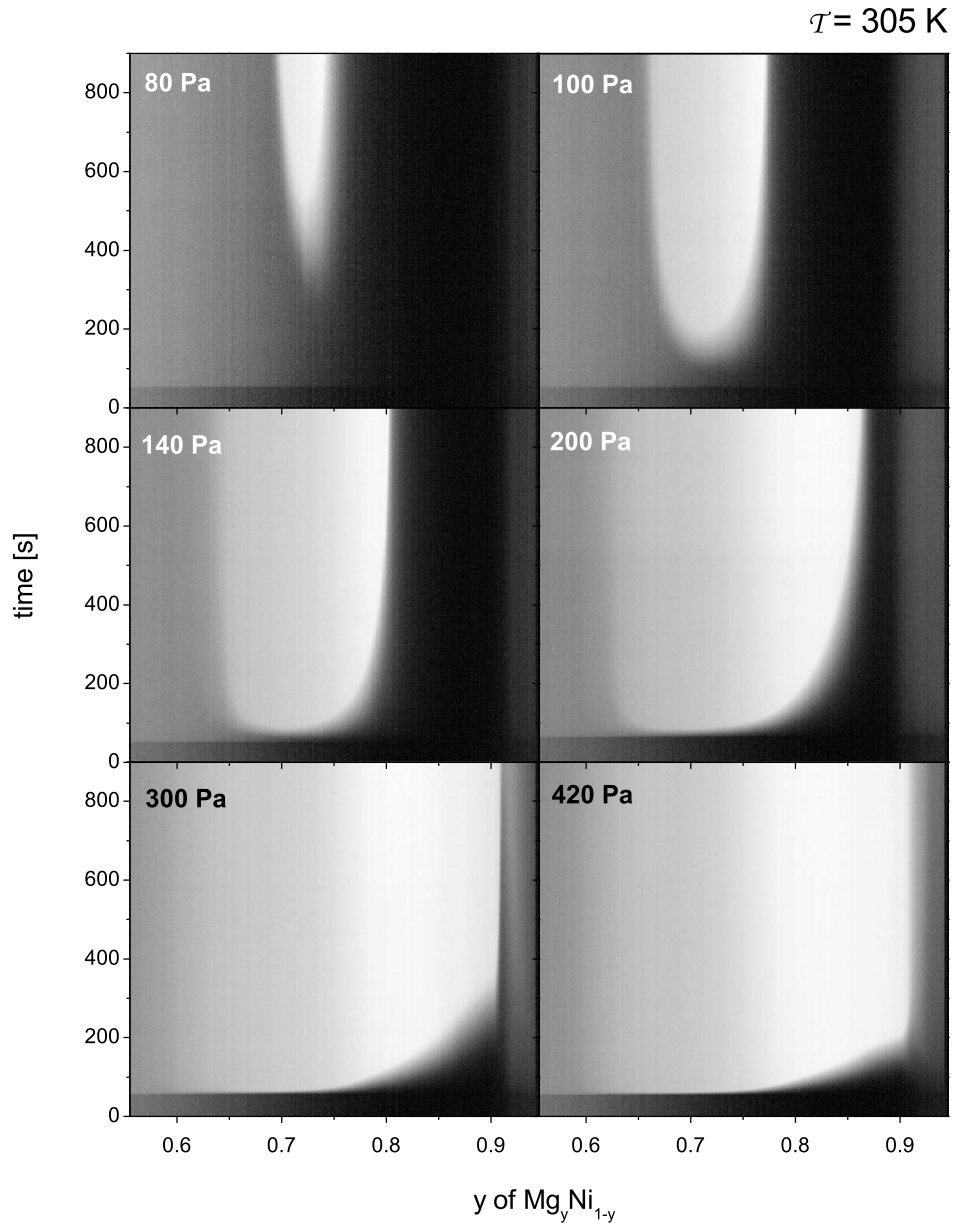
Figure 4.13: Maps at $\mathcal{T} = 305$ K of the logarithm of the optical transmission T as a function of time and Mg atomic fraction y for a 50/20/30-100 nm PTFE/Pd/Mg$_y$Ni$_{1-y}$ gradient film on a glass substrate after a pressure step applied at $t = 50$ s. The various applied pressures are written on the figure. *Black* means low, *white* high transmission.
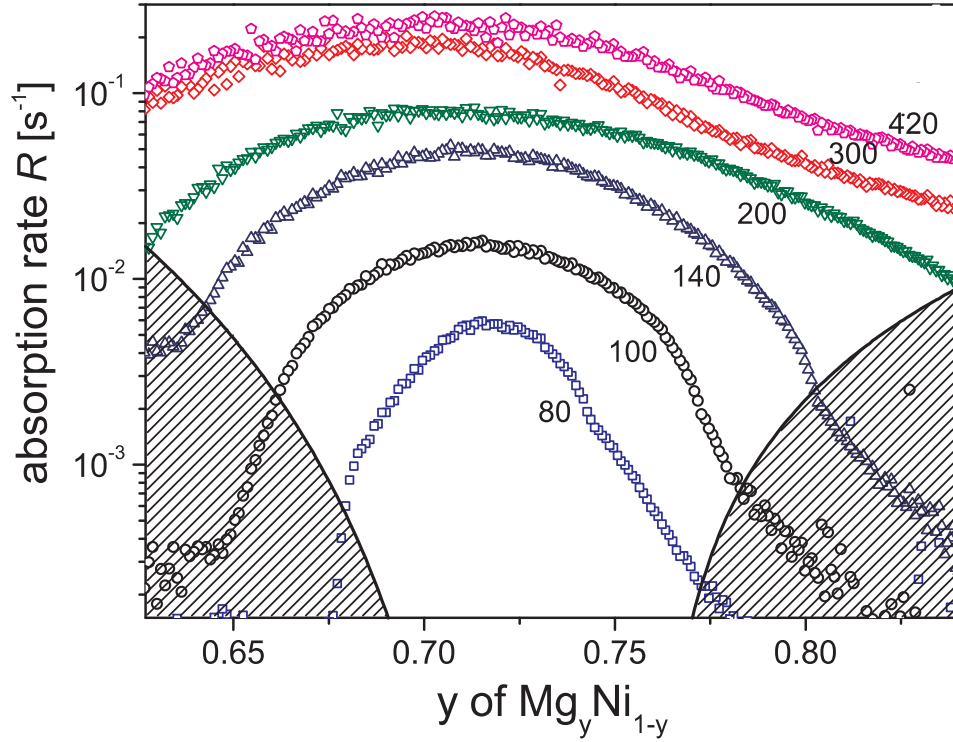
Figure 4.14: Compositional dependence of the hydrogen absorption rate for various applied hydrogen pressure steps $p(H_2)$ in Pa, obtained from a Boltzmann fit of the data showed in Fig. 4.13. Rates values in hatched areas are not considered in the further analysis.

in the further analysis. For the lowest pressures considered, the rate goes to zero for Mg- or Ni-rich compositions, meaning that a pressure of 80 Pa at a temperature of 305 K is in fact *below or equal* to the equilibrium plateau pressure for some compositional ranges in $Mg_yNi_{1-y}H_x$. Indeed, exactly at the plateau pressure, there is no driving force for hydrogenation. This means that, per definition:

$$R(p_{eq}) = 0. \tag{4.5}$$

Equilibrium pressure: off-equilibrium method   We use the condition in Eq. 4.6 to extrapolate the equilibrium pressure p_{eq} for each composition y from the recorded rate as a function of pressure. We show an example for such an extrapolation in Fig. 4.15(a) for the stoichimetric composition Mg_2NiH_x ($y = 0.67$). The rate as a function of pressure is approximated well by a linear expression:

$$R(p) = A(p - p_{eq}). \tag{4.6}$$

This indicates that kinetics is dominated by dissociation of hydrogen at the Pd surface (see Table 4.2). As we will show in the comparison with the model developed in the next section, this is the case for all compositions below the eutectic point at $y = 0.88$. The obtained equilibrium pressures are displayed in Fig. 4.15(b). The minimum p_{eq} is found at $y = 0.70$, near the $[Mg]:[Ni] = 2$ stoichiometric composition. For other compositions, p_{eq} steadily increases to reach values about 2.5 times higher than the minimum value around $y = 0.85$. See Sec. 4.5 for a further discussion over this observed destabilization with increasing Mg content.
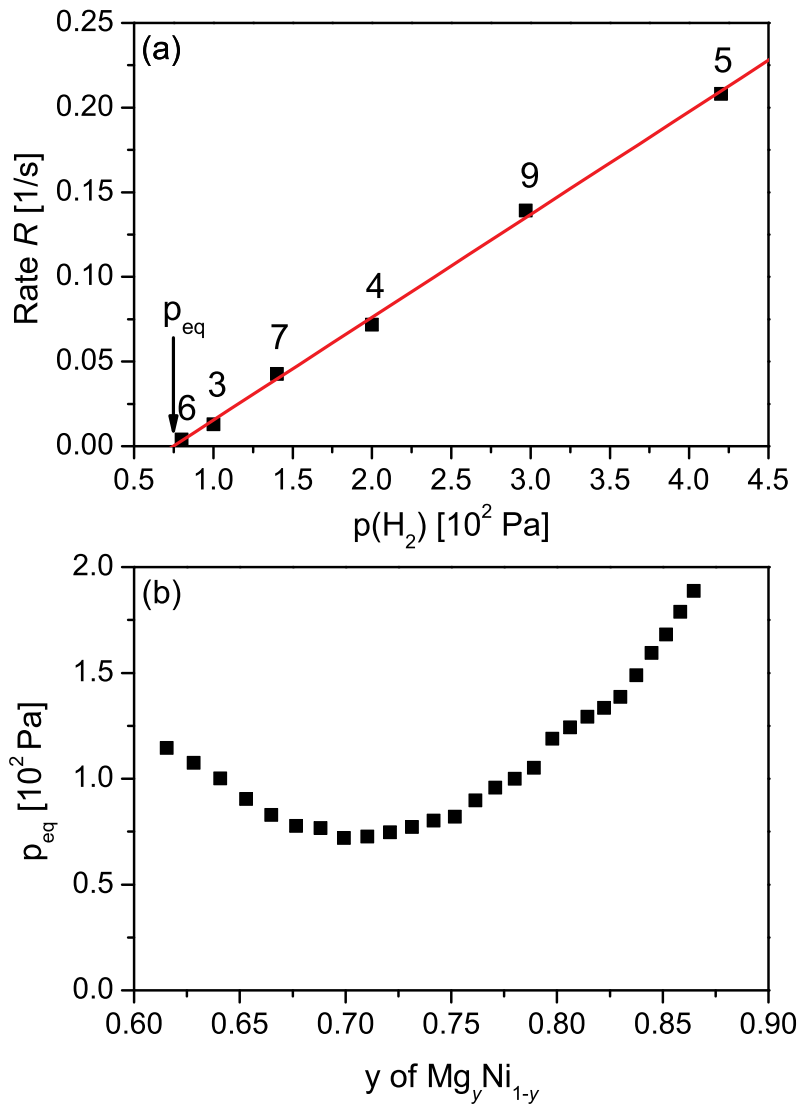
Figure 4.15: (a) *Squares*, absorption rate at $\mathcal{T} = 305$ K as a function of applied pressure above the equilibrium plateau pressure p_{eq} for the stoichiometric Mg_2NiH_x ($y = 0.67$) composition. The cycle number for each point is mentioned in the plot. The pressure dependence of the rate is linear (see Sec. 4.4.2) and can be used to determine p_{eq} as extrapolation to $R = 0$. (b) Compositional dependence of the extrapolated equilibrium plateau pressure for $Mg_yNi_{1-y}H_x$ at $\mathcal{T} = 305$ K.

4.4.2 Rate modeling: interplay between diffusion and dissociation mechanisms

The search for novel hydrogen storage materials has triggered the investigation of the interaction of hydrogen with hundreds of materials.[5,138] As the main interest often lies in the technical applicability of specific materials for hydrogen storage, the emphasis is usually not put on well-defined determination of fundamental physical parameters. This complicates the comparison of published experimental results, since the data depend often on specific details of the followed experimental procedures. A typical example of such a situation is found for $LaNi_5H_6$, a hydrogen storage materials with appropriate thermodynamics and sufficiently fast kinetics. The physical origin of its activation process has intensively been investigated, in particular the influence of the preparation method on the H-sorption kinetics.[139–144] On the fundamental side, kinetic barriers such as dissociation and diffusion barriers were calculated by ab-initio models.[145–148] Due to uncertainties in model and experimental parameters, only the calculated activation energies of such barriers are compared to experimentally derived values. And even this with relatively small success. An enlightening analysis of this problem is the publication of Andreasen et al. [149] Assuming an Arrhenius behavior of the rate R

$$R = R_0 e^{-\frac{E_{AA}}{kT}}, \tag{4.7}$$

they compared the activation energies derived from published experimental results on the kinetics of $LaNi_5H_6$. These energies, which we are calling from now on 'apparent activation energies' E_{AA}, range from less than 0.2 eV to more than 0.5 eV. Simultaneously, the logarithm of the prefactor $\ln R_0$ scales linearly with E_{AA}, so as to compensate the influence of the activation energy. This leads to the so-called Constable-Cremer relation[150] or compensation effect[151] as coined by catalysis research.[152] The underlying problem originates from the fact that Eq. 4.7 neglects any changes of the initial and final states, which are separated by an energy barrier. This, on the other hand, is the principle basis of hydrogen storage in metal hydrides, where the rate (i.e. uptake or release of hydrogen) is determined by the unbalance between the chemical potential of hydrogen in the gas phase and in the metal hydride. The *thermodynamic* driving force results from the gradient of the chemical potential $\frac{\partial \mu}{\partial x}$, and the rate is given by:

$$R = -\pounds \frac{\partial \mu}{\partial x} \tag{4.8}$$

as demanded by Onsager's kinetic theory.[153] $\pounds$ is a phenomenological coefficient, which depends on temperature and H concentration. The activation energy of the process is included in $\pounds$. μ is temperature dependent, and thus an Arrhenius analysis is difficult. Equation 4.8 can be solved for simple cases, e.g. binary diffusion, giving Fick's law. In complex systems, due to the multiplicity of processes (surface, subsurface, intermediate layers etc.),[154] neither an

analytical solution of eq. 4.8 is possible, nor are all mandatory fundamental parameters known (e.g. coverage, energy barriers, thermodynamic parameters), which would allow for a numerical solution.

In this section we develop a simplified two-step model of the hydrogen sorption kinetics in metal hydrides considering dissociation and diffusion. Basis of the calculation is relation 4.8, which is specified to fit the processes. The obtained differential equations are approximated to allow for an *analytical* solution, from which the time-, temperature- and pressure dependence of ab- and desorption kinetics and the influence of several materials parameters involved in the process are derived. The central result of this section is that kinetics can hardly be described by a single rate-limiting step. Kinetics is in most cases the result of an interplay of dissociation and diffusion. Very similar to heterogenous catalysis, the observed compensation effect can be explained by the interplay of these two processes. The model is successfully tested on $Mg_yNi_{1-y}H_x$ thin films. Particular emphasize is laid on the calculation of the apparent activation energy, which depends now on temperature and pressure. These dependencies complicate the correct interpretation of measured activation energies.

Model

Basic assumptions   We consider a system consisting of a hydrogen absorbing metal covered by a surface layer as sketched in Fig. 4.16. Hydrogen enters the metal through the top layer and forms the metal hydride via several intermediate steps, which have characteristic energy parameters (See Table).

It is not practical to consider all the steps involved in hydrogen sorption. We can however already gain valuable insight from a simple model involving one surface barrier, one diffusion barrier and one constant hydrogen reservoir. In the following we give some arguments to underline the validity of this simplification for many relevant hydride systems.

Since physisorption of gas molecules on surfaces requires almost no activation energy and the impingement rate of H_2, the gas phase can be assumed to be in equilibrium with the physisorbed state. Furthermore, the heat of formation ΔH_{phys} is very small and the molecule is not dissociated. This step is thus neglected in our model. For chemisorption, the hydrogen molecule has to split, and for that it has to overcome an in most cases high dissociation barrier of $0 \leq \Delta E_{diss} < 2$ eV. Hydrogen is relatively strongly bound to metal surfaces ($\Delta H_{chem} \simeq -1$ eV/H). Thus, the coverage θ is high under technical conditions (at hydrogen pressures of 1-100 bars and 300-500 K it varies between 0.8 and 0.9 for transition metals.[161]) The next step is the hopping of H from a surface site to a subsurface site. The corresponding energy barrier is $\Delta E_{sub} - \Delta H_{chem}$ for absorption in a subsurface site. The moving species is atomic hydrogen and thus this step can be considered as a diffusion process between two phases
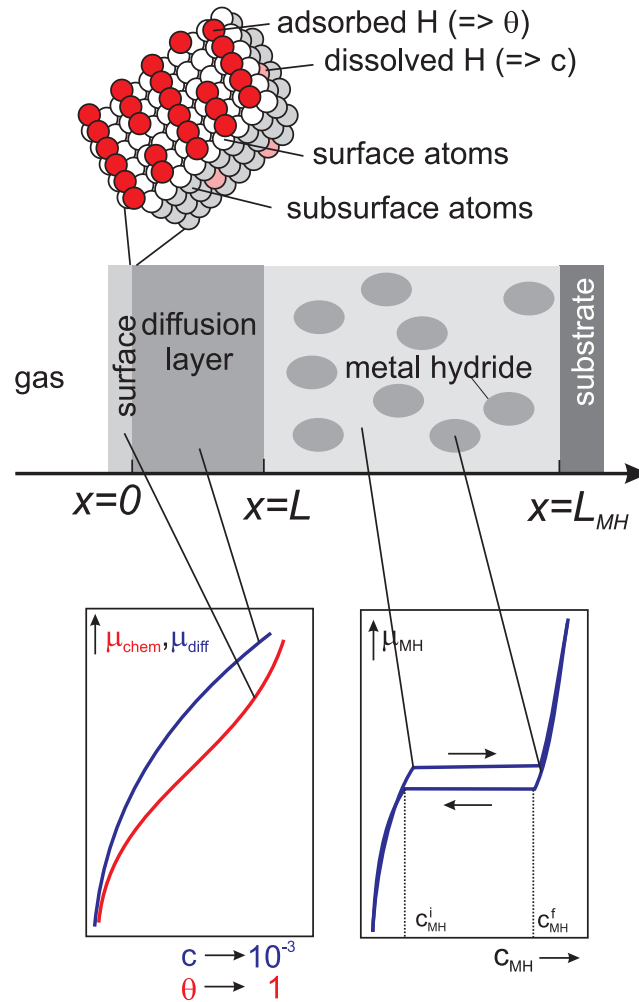
Figure 4.16: *Top panel*, the various layers considered in the model. The surface layer consists of hydrogen adsorbed on surface atoms (amount of H is described by θ) attached to subsurface atoms, which belong to the diffusion layer. Diffusion inside the metal/metal hydride layer is fast, and the metal hydride nucleates homogeneously. Main diffusion barrier is the surface. *Bottom panels*, schematic representation of the concentration dependence of the hydrogen chemical potential in (*left*) the diffusion layer and (*right*) in the metal hydride for a given temperature. The hydrogen concentration in the diffusion layer is labeled c, the concentration in the metal hydride c_{MH}.

Table 4.1: Main processes involved in hydrogen sorption. Activation energies ΔE_i are defined as the difference in initial and final states, enthalpies ΔH_i are relative to the gas phase at normal conditions.

Physical mechanism	Reaction	Relevant energy	Typical value
1. Physisorption	$H_2^{gas} \rightleftharpoons H_2^{phys}$	ΔH_{phys}	≤ -0.05 eV/H_2 [155]
2. Dissociation and chemisorption	$H_2^{phys} \rightleftharpoons 2H^{chem}$	ΔE_{diss} ΔH_{chem}	0... 2 eV [156] $+0.1...$ -1 eV/H [157]
3. Surface penetration	$H^{chem} \rightleftharpoons H^{sub}$	ΔE_{sub} ΔH_{sub}	0.5...1 eV [158] $-0.25... +1.2$ eV/H [157]
4. Diffusion through surface layer		ΔE_{diff} ΔH_{sol}	$\simeq 0.5$ eV [159] $-0.2... +0.2$ eV/H [67]
5. Diffusion in metal and H solubility		ΔE_{diff} ΔH_{sol}	≤ 0.2 eV [160] $-0.2... +0.2$ eV/H [67]
6. Hydride formation	$H^{sol} \rightleftharpoons H^{MH}$	ΔH_{MH}	$\simeq -0.5$ eV/H [67]

(surface and subsurface). Furthermore, as the heat of hydrogen solution in the subsurface layer is similar to that in the following layers, i.e. $\Delta H_{sub} \simeq \Delta H_{sol}$, and $\Delta E_{sub} \simeq \Delta E_{diff}$, we equate the subsurface hydrogen with 'regularly' dissolved atomic hydrogen in the surface layer, i.e. step 3 and 4 are modeled by *one* diffusion process between the surface and bulk hydrogen. This diffusion barrier can be an oxide skin and/or diffusion in the metal, in which the metal hydride nucleates and grows. In most metals, hydrogen diffusion is fast, and thus our model calculations considers only one (averaged) diffusion barrier. A prerequisite of our model is that the diffusion parameters (e.g. diffusion layer thickness) are constant or their change is slow compared to the other processes (quasiequilibrium). The metal and randomly distributed metal-hydride nuclei are assumed to be in thermodynamic equilibrium ('hydride plateau'), which is mainly determined by the heat of hydride formation ΔH_{MH}. Furthermore, supersaturation is assumed to be small (corresponds to a small hysteresis, see later).

Summarizing, the two step model includes a surface layer with a dissociation barrier (E_1, corresponds to ΔE_{diss}), and a diffusion layer with a diffusion barrier E_{diff}. After dissociation at the surface (near $x = 0$), hydrogen passes
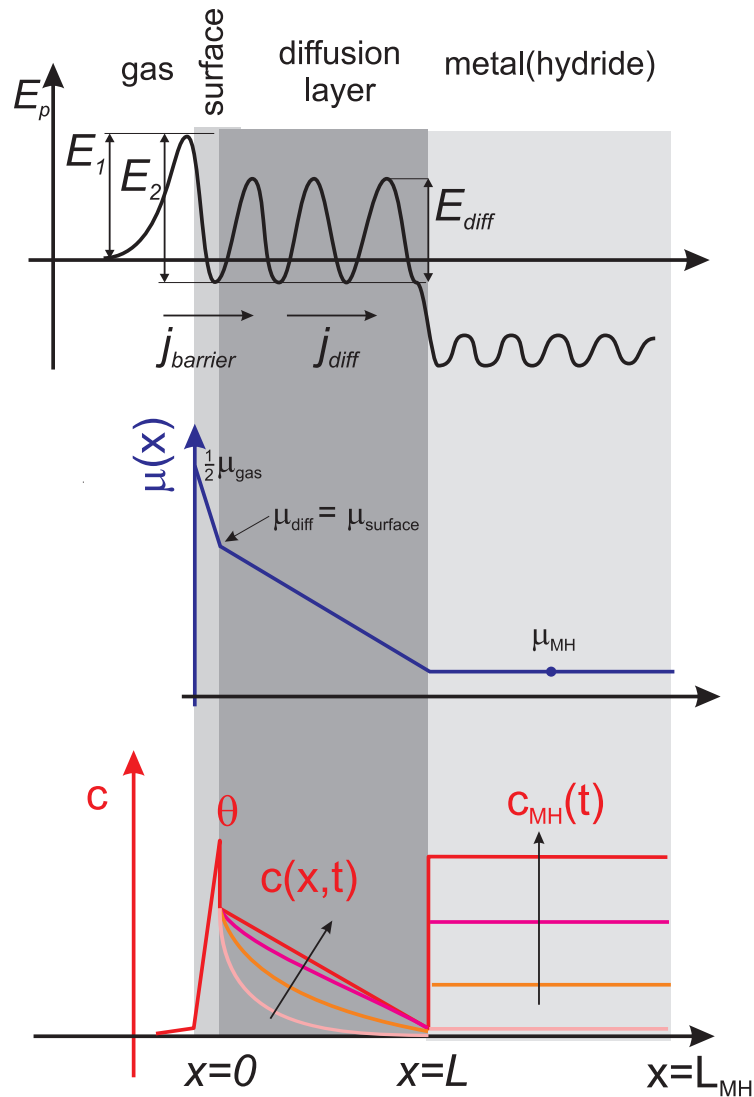
Figure 4.17: Scheme of the two-step model to define the variables used in this work. Potential energy, chemical potential and concentration of hydrogen as a function of the location. In the metal-(hydride) the diffusion is assumed to be infinite, there is therefore no concentration gradient for $x \geq L$. Therefore, the concentration of hydrogen is determined by the current $j_{diff}(x = L, t)$. The diffusion current $j_{diff}(x = 0, t)$ is equal to the current $j_{barrier}$ through the surface barrier with height E_1. For simplicity, the subsurface site energy is not included in the present scheme.

through a subsurface site and diffuses through the diffusion layer (binding energy $(E_1 - E_2$, corresponds to $\Delta E_{diss} - \Delta H_{chem})$ to enter the hydride at $x = L$. The corresponding energy potential is drawn in the top panel of Fig. 4.17. Energy minima represent stable states of hydrogen in matter, i.e. chemisorbed hydrogen, hydrogen dissolved in the catalyst (diffusion layer) and hydrogen in the hydride. The hydrogen concentration profiles at various times during hydrogen loading are schematically indicated in the lower panel of Fig. 4.17. The chemical potential is continuous (see middle panel) even at $x = 0$, where it changes over a very short distance due to the dissociation barrier. The hydrogen concentration dependence of the chemical potential is sketched for the diffusion layer $(0 < x < L)$ and the metal hydride in the two panels at the bottom of Fig. 4.16. The metal-hydride is assumed to have a flat plateau at pressure p_{pl} for concentrations between $0 \simeq c_{MH}^i < c_{MH} < c_{MH}^f \simeq 1$. An additional difficulty, which is first neglected during derivation of the model, is the difference of the absorption plateau pressure and desorption plateau pressure (hysteresis). We describe now the mathematics and simplifications of the two step model:

1. Particle current at the surface: The net particle current $j_{barrier}$ consists of an inward current over the barrier E_1 and an outward current over the barrier E_2. The inward current is proportional to the density of H_2 molecules at the surface and the fraction of unoccupied surface sites $(1 - \theta)^2$ (at least two vacancies are needed),[162] where θ is the fraction of surface sites occupied by atomic hydrogen. The outward current is proportional to θ^2 since two hydrogen atoms have to recombine to form an H_2 molecule. The prefactors a and b are constants, which will be defined later.

$$j_{barrier} = ap(1 - \theta)^2 e^{-E_1/kT} - b\theta^2 e^{-E_2/kT} \tag{4.9}$$

This surface barrier leads to a step in the chemical potential from hydrogen as a gas to hydrogen chemisorbed at the surface. Further, the chemical potential is assumed to be continuous. For simplification the concentration $c(x = 0)$ in the diffusion layer is assumed to be in equilibrium with θ. The equality of the chemical potentials leads to the following relation between θ and c:[163,164]

$$\frac{\theta}{1 - \theta} e^{-\mu_{surface}/kT} = \frac{c}{1 - c} e^{-\mu_{MH}/kT} \tag{4.10}$$

$\mu_{surface}$ and μ_{MH} are the chemical potentials, which are mainly determined by the binding energy of hydrogen on the surface ΔH_{chem} and in the bulk ΔH_{sol}, respectively.

In most cases, the binding energy of hydrogen is larger at the surface than in the bulk,[165] and thus the surface concentration is larger, too (see bottom panel of Fig. 4.17). As we are only interested in situations where the concentration c is much smaller than 1 we take

$$\frac{\theta}{1 - \theta} = g \cdot c \tag{4.11}$$

with g a surface enrichment factor, and write Eq. 4.9 as

$$j_{barrier} = (1 - \theta)^2 \left(ape^{-E_1/kT} - bg^2c^2e^{-E_2/kT}\right). \tag{4.12}$$

The 'self-blocking factor' $s^2 = (1 - \theta)^2$ is:

$$s^2 = \left(1 - \frac{gc}{1 + gc}\right)^2. \tag{4.13}$$

In many cases, s^2 can be assumed to be constant, which is equivalent to the effect that hydrogen is 'trapped' on a surface due to the high negative heat of chemisorption (large g) and thus the coverage is high (typical 3d-metals $\theta \geq 0.7$ at high pressures[161], see Fig. 4.18). The deviation from the equilibrium value of the self-blocking factor induced by a change of the bulk hydrogen concentration c is therefore low.

The latter assumptions are critical, as they are indispensable for an analytical model on hand, but may oversimplify nature on the other hand. To underline the validity of the assumptions, we show the dependence of coverage and dissolved hydrogen in Ni on the applied pressure (Fig. 4.18). The coverage does not change much within the typical pressure range of 0.1 to 100 bars, while the amount of dissolved hydrogen changes drastically (Sievert's regime). The relation between coverage and hydrogen concentration is shown to be well approximated by equation 4.11.

2. Diffusion current at $x = 0$: In dynamic equilibrium, the overbarrier current $j_{barrier}$ must be equal to the diffusion current j_{diff} at the beginning of the diffusion layer. Thus,

$$j_{barrier} = j_{diff}(x = 0, t) = -\pounds \frac{\partial \mu}{\partial x}|_{x=0}, \tag{4.14}$$

where μ is the chemical potential of hydrogen in the diffusion layer. The coefficient $\pounds$ depends on the hydrogen concentration since in the limit of low concentrations the diffusion current is given by Fick's law:

$$j_{diff} = -D\rho \frac{dc}{dx}, \tag{4.15}$$

with a constant diffusion coefficient D and ρ the density of available hydrogen sites per m^3. In addition, $\pounds = \pounds_0(1 - c)$, since hydrogen can only jump to an unoccupied interstitial site. Assuming an ideal solution model with

$$\mu = kT \ln\left(\frac{c}{(1 - c)}\right) + \Delta H_{sol}. \tag{4.16}$$

we obtain

$$\frac{d\mu}{dc} = \frac{kT}{c(1 - c)} \tag{4.17}$$
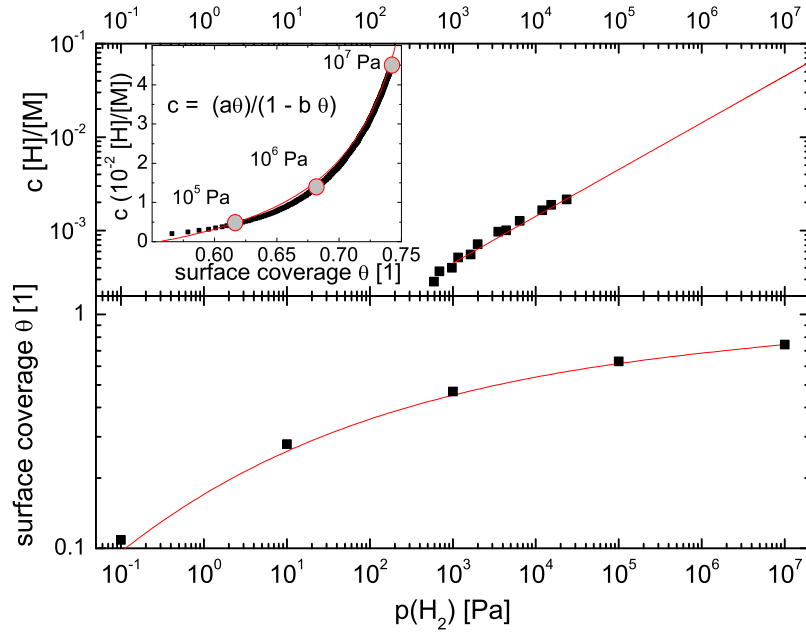
Figure 4.18: Pressure dependence at 600 K of the surface coverage[161] and hydrogen bulk concentration[166] of Ni. Red lines are extrapolations to plot the bulk concentration as a function of the surface coverage (inset). A good fit (red line) to these values is $c(\theta) \propto \theta/(1 + a\theta)$ with $a \simeq -1.25$, in agreement with the used approximation (eq. 4.11).

and

$$j_{diff} = -\pounds \frac{d\mu}{dx} = -\pounds_0 (1 - c) \frac{d\mu}{dc} \frac{dc}{dx} \quad (4.18)$$

$$= -\pounds_0 \frac{kT}{c} \frac{dc}{dx},$$

and consequently, after comparison with Fick's 1st law $j = -D\rho \frac{dc}{dx}$ we obtain

$$\pounds_0 = \frac{cD\rho}{kT}, \text{ and } \pounds = D\rho \frac{c(1 - c)}{kT} \quad (4.19)$$

and can rewrite eq. 4.15 as

$$j_{barrier} = j_{diff}(x = 0, t) = -D\rho \frac{\partial c}{\partial x}|_{x=0}. \quad (4.20)$$

This is the standard diffusion equation. Note, however, that the chemical potential of hydrogen is continuous throughout the sample while the concentration can have discontinuities, e.g. at $x = L$.

3. Diffusion current in the diffusion layer. Fick's 2nd law determines the diffusion in the diffusion layer $(0 < x < L)$:

$$\frac{\partial c}{\partial t} = D\frac{\partial^2 c}{\partial^2 x} \tag{4.21}$$

In the diffusion layer, hydrogen is bound with $E_1 - E_2 \equiv 2\Delta H_{sol}$ where ΔH_{sol} is the heat of hydrogen solution in the diffusion layer.[b]

4. Concentration inside the metal hydride. The number of hydrogen per s and per m^2 entering/leaving the metalhydride MH is

$$j_{diff}(x = L, t) = (L_{MH} - L)\rho\frac{dc_{MH}}{dt}, \tag{4.22}$$

where $(L_{MH} - L)$ is the thickness of the metal hydride layer. Since the metal hydride plateau is assumed to be flat from c_{MHi} to c_{MHf} (see sketched $\mu(c_{MH})$-curves in Fig. 4.16)and the diffusion very rapid (i.e. $D_{MH} \to \infty$), c_{MH} does not depend on x and the chemical potential μ_{MH} is taken to be equal to a constant μ_{pl}. The continuity of the chemical potential at the interface between the diffusion layer and the metal hydride implies

$$\mu(x = L, t) = \mu_{pl}. \tag{4.23}$$

With this the concentration $c(x = L, t) \simeq c_{pl}$ in the diffusion layer at $x = L$ is related to the plateau pressure p_{pl} in metal hydride through

$$kT\ln\left(\frac{c_{pl}}{1 - c_{pl}}\right) + \Delta H_{sol} - \frac{\Delta S_0}{k} = \frac{1}{2}kT\ln\left(\frac{p_{pl}}{p_0}\right), \tag{4.24}$$

where p_0 is the standard pressure and ΔS_0 the entropy change at standard conditions. As we assume that the metal hydride has relatively low pressure plateaus, we are in the low concentration limit in the diffusion layer and Sievert's law is valid (see sketched $\mu(c_H)$-curves in Fig. 4.16):

$$c(x = L, t) = c_{pl} = \alpha\sqrt{p_{pl}}, \tag{4.25}$$

where α is Sievert's constant. The temperature dependence of α is $\alpha \propto \exp(-\Delta H_{sol}/kT)$. In equilibrium, i.e. $j_{barrier} = 0$, the concentration is the same everywhere in the whole diffusion layer and in particular $c(x = 0) = c_{pl}$. With this we can correlate the bulk constant with the surface parameters via eq. 4.12:

$$\alpha = \sqrt{\frac{a}{bg^2}}\exp\left(\frac{E_2 - E_1}{2kT}\right). \tag{4.26}$$

5. Summary. Taking all the points mentioned above into consideration we obtain for the

---

[b] The factor 2 results from different units: $[E_i] = \text{eV/H}_2$, $[\Delta H_{sol}] = \text{eV/H}$

Surface at $x = 0$:

$$\left(1 - \frac{gc}{1+gc}\right)^2 \left(ae^{-E_1/kT}p - bg^2e^{-E_2/kT}c^2\right) = -D_0 e^{-E_{diff}/kT}\rho\frac{\partial c}{\partial x}|_{x=0}$$
(4.27)

D_0 is the prefactor of diffusion, E_{diff} the diffusion barrier height (see Fig. 4.17).

Diffusion layer at $0 < x < L$:

$$\frac{\partial c}{\partial t} = D\frac{\partial^2 c}{\partial x^2} \quad c(x, t=0) = 0, \quad c(L, t) = c_{pl}.$$
(4.28)

Metal hydride at $x \geq L$:

Here, $\frac{\partial c_{MH}}{\partial x} = 0$ and thus

the sorption rate is $R = (L_{MH} - L)\rho\dfrac{dc_{MH}}{dt}, \quad R = -D\dfrac{\partial c}{\partial x}|_{x=L}$ (4.29)

The aim of the next sections is to solve eq. 4.28 and from that to calculate R in eq. 4.29. A general analytical time-dependent solution is not known. Valuable insight can, however, be gained from the analysis of representative special cases.

Special cases: Time dependent cases In Fig. 4.17 we have sketched the intermediate states before reaching a steady-state in the diffusion layer. We show here that the time necessary to reach steady state inside the diffusion layer is significantly shorter than that of the overall process. For this it is sufficient to consider the situation, where $p_{pl} = 0$, which corresponds to $p >> p_{pl}$.

The rate of H absorption is time dependant, as the surface is connected to the underlying metal hydride via the time-dependent diffusion equation (4.28). In the following, we will give the time dependence of it for extreme cases, all with the assumption that the plateau pressure in the metal hydride is zero. This assumption is made to simplify the calculations.

Three cases are discussed:

(A) dissociation limited uptake: The dissociation barrier E_1 is large and thus $\theta \simeq 0 \Rightarrow c(x = 0) \simeq 0$, $s^2 \simeq 1$; the re-desorbed hydrogen $bc^2\exp(-E_2/kT)$ is assumed to be negligible, the plateau pressure is low, and therefore the rate of dissociation determines the uptake rate: $\frac{\partial c}{\partial x} = ae^{-E_1/kT}p$ at $x = 0$, and $c(x = L, t) = c_{pl} \simeq 0$.

One obtains [167,168]

$$R \propto 2Ap[\text{erfc } \xi - \text{ erfc } 3\xi + \text{ erfc } 5\xi - ...]$$
(4.30)

For simplicity, we wrote $\xi = L/2\sqrt{Dt}$.

(B) Equilibrium of the surface with gas phase. Here, the concentration of the outmost layers determines the rate:

$c(x = 0, t) = c_s \Rightarrow s^2 = const.$ and $c(x = L, t) = c_{pl} \simeq 0.$

In this case, the rate is modeled by[167]

$$R \propto \frac{2c_s\sqrt{D}}{\sqrt{\pi t}} \left[e^{-\frac{L^2}{4Dt}} + e^{-\frac{3^2 L^2}{4Dt}} + e^{-\frac{5^2 L^2}{4Dt}} + ... \right] \qquad (4.31)$$

The rate equations for (A) and (B) are numerically solved and the rate is shown in Fig. 4.19. For short times and small diffusion lengths the rate is indeed time dependent for **both** cases. However, the rate saturates quickly. To discuss the relevance of the time dependence, we calculate the time, after which more than 90% of the rate is reached:

$$\frac{R(t)}{R_{max}} > 0.9 \text{ for } t > \frac{L^2}{D} \qquad (4.32)$$

Typical diffusion parameters are between 10^{-10} m^2/s (Pd at 300 K) and D = $4.0 \cdot 10^{-13}$ m^2/s (Mg at 300 K).[169] With typical diffusion lengths of around 10 nm = 10^{-8} m one obtains diffusion times in the order of milliseconds. The time dependence is therefore negligible, as typical sorption cycles take several minutes. Therefore, the rate through a thin diffusion layer is in all cases time-independent. In other words: it is impossible to distinguish between dissociation- or diffusion processes on/in a thin cover layer via the time dependence of the total kinetics.

To include all possibilities, we have to solve

(C) Chemisorption limited uptake: The chemisorption enthalpy is large (i.e. $E_2 >> 0$) and with it $\theta \simeq 1$. Thus gc is large: $\left(1 - \frac{gc}{1+gc}\right)^2 \simeq 0$, but not constant.

As considered in case (A) and (B), reaching steady-state in the diffusion layer is fast compared to the overall process. We neglect this time-dependence and thus

$$R \propto \left(1 - \frac{gc}{1 + gc}\right)^2 ae^{-E_1/kT}p \propto p, \qquad (4.33)$$

as $c \propto c_{pl} = const.$ in steady-state. The constant concentration results from the assumed constant chemical potential of the metal hydride at the plateau. *Before* reaching steady-state, i.e. in the α-phase of hydrogen in the metal hydride layer, a time-dependence is expected, i.e. $c = c(t)$. This was experimentally observed in the H-uptake in Mg-films.[170] The authors report from decreasing hydrogen uptake in the α-phase, where
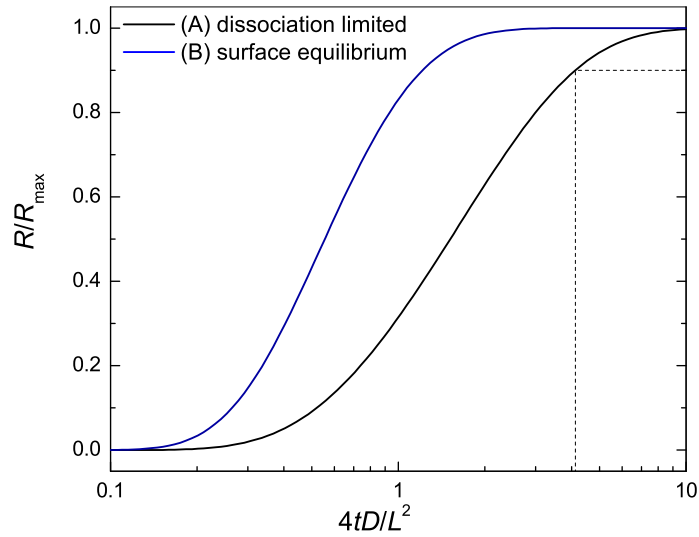
Figure 4.19: Time dependence of the hydrogen uptake, limited by dissociation (case (A)) and limited by the solubility of the surface layers (case (B)). The *dashed line* refers to the condition expressed in Eq. 4.32.
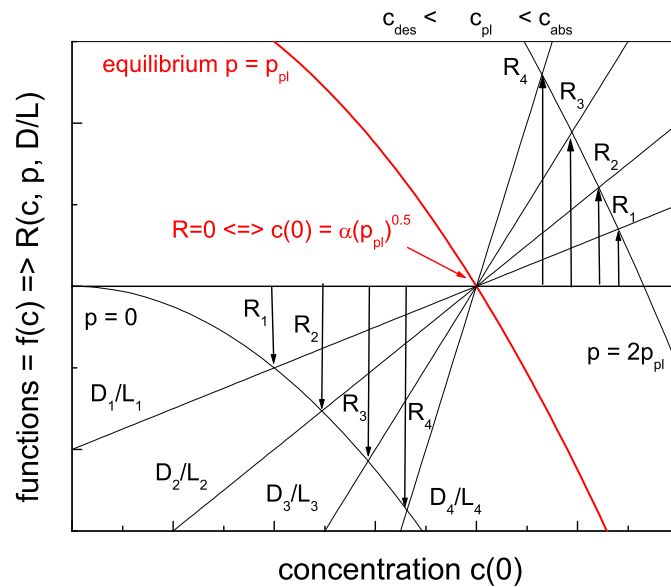
Figure 4.20: Graphical Solution of equation (4.34) for various pressures and diffusion parameters $D_4/L_4 > D_3/L_3 > D_2/L_2 > D_1/L_1$ to highlight the interdependence of the uptake rate on the concentration at the surface.

the chemical potential increases until the plateau has been reached. Unfortunately, the corresponding equations cannot be solved analytically anymore ($c(t) \propto \int R(t)dt$). If a time-dependence is observed, we can conclude that the external parameters, e.g. p_{pl} change during the process. In this publication, we focus on the sorption kinetics in the plateau region, where p_{pl} and thus s^2 are time-independent.

Stationary case As estimated in the previous section, 'steady-state' is reached within short times compared to the time scale of a typical sorption process. The diffusion process can then be well described by a linear concentration gradient in the diffusion layer without time-dependence, and thus

$$Ap - Bc^2(0) = D\frac{c(0) - \alpha\sqrt{p_{pl}}}{L} \equiv R \tag{4.34}$$

$$Bc^2(0) + \frac{D}{L}c(0) - \frac{\alpha D}{L}\sqrt{p_{pl}} - Ap = 0 \tag{4.35}$$

For simplification, we assume the self-blocking factor s^2 to be constant and include it in the parameters a, b. The concentration under the surface $c(0)$ is

$$c(0) = \frac{-\frac{D}{L} + \sqrt{\left(\frac{D}{L}\right)^2 + 4B\left(\frac{D}{L}\sqrt{\frac{A}{B}p_{pl}} + Ap\right)}}{2B}. \tag{4.36}$$

Where we replaced $\alpha^2 by A/B$. Finally, we obtain a rate

$$R \equiv \frac{D}{L}\left[\frac{-\frac{D}{L} + \sqrt{\left(\frac{D}{L}\right)^2 + 4B\left(\frac{D}{L}\sqrt{\frac{A}{B}p_{pl}} + Ap\right)}}{2B} - \sqrt{\frac{A}{B}p_{pl}}\right] \tag{4.37}$$

For simplification, we assume the coverage to be constant and to be included in the parameters a and b. The role of the various parameters entering eq. 4.37 is best discussed by means of its graphical representation given in Fig. 4.20. The left hand side of eq.(4.34) is an inverted parabola with a maximum at p, the right hand side a straight line with slope D/L. At equilibrium (i.e. $R = 0$, $p = p_{pl}$), the two curves intersect the abscise at $c_{pl} = \alpha\sqrt{p_{pl}}$. The concentration and rate R are also determined by the intersection of the two functions in non-equilibrium, i.e. when $p \neq p_{pl}$. For applied pressures below the equilibrium pressure p_{pl}, the rates become negative (i.e. desorption occurs), and vice versa. However, the results are not point-mirrored (Fig. 4.20). For a given value of $\frac{D_1}{L_1}$ the desorption rate R_1 (down pointing arrow) corresponds to the lowest applicable pressure (i.e. perfect vacuum) with $p = 0$. For comparison the curve for an applied pressure of $p = 2p_{pl}$ is also drawn

(i.e. $\Delta p = p_{pl}$ in both cases). The absorption rate R_1 (down pointing arrow) is under no circumstances equal to that of desorption. Another source of asymmetry between hydrogen absorption and desorption is also due to the inherent hysteresis of the p-c-isotherms of any metal-hydride (see Fig. 4.16). For the situation considered in the present article this means that p_{pl} during absorption is necessarily higher than p_{pl} during desorption and, consequently, that the desorption rate can be significantly lower than the absorption rate driven by the same pressure difference $|p - p_{pl}|$. A third important point is that the surface concentration during absorption is inherently larger than that for desorption. This implies that a catalyst that affects the surface coverage will affect the sorption rate asymmetrically. If it is beneficial for absorption it will negatively influence desorption and vice versa. Furthermore the absorption kinetics might be completely different form the desorption kinetics. This is well illustrated by the numerical and experimental results of Pasturel et al.,[171] who found that a diffusion layer with a high solubility (i.e. large α) on top of a metal hydride supports desorption, but hinders absorption. This result is in perfect agreement with eq. 4.37, as the term $\alpha\sqrt{p_{pl}}$ has to be as large as possible for desorption, but as small as possible for absorption. It is noted, however, that the solubility leads to this result, if the applied hydrogen pressure is $p \leq p_{pl}$ or $p \simeq p_{pl}$. For $p >> p_{pl} \simeq 0$, the behavior is reversed. Here, a high solubility accelerates the absorption kinetics.[159] Hence, the effect of a specific parameter on the kinetics is relative. Therefore, we estimate Eq. 4.37 for various pressure regimes and relevances of parameters.

We start with a Taylor series approximation of eq. 4.37:

$$R(p)|_{p \simeq p_{pl}} = A\beta^{-\frac{1}{2}}(p - p_{pl}) - A^2 B^2 \frac{L^2}{D^2}\beta^{-\frac{3}{2}}(p - p_{pl})^2 + ... \qquad (4.38)$$

with

$$\beta = 1 + 4\frac{L}{D}\sqrt{ABp_{pl}} + 4AB\frac{L^2}{D^2}p_{pl} \qquad (4.39)$$

For $ABp_{pl} << D^2/L^2$, the kinetics is 'dissociation limited', and the prefactor of the quadratic term is much smaller than that of the linear term. The kinetics can then be well described by

$$R(p) = A'(p - p_{pl}) \qquad (4.40)$$

as frequently given in literature.[172,173] The prefactor $A' \simeq A$ involves an activation energy E_1. With a heat of hydride formation ΔH_{MH} the plateau pressure is $p_{pl} \propto e^{2\Delta H_{MH}/kT}$, and the apparent activation energy of the rate becomes

$$E_{AA} = E_1 + \frac{p_{pl}}{p - p_{pl}}2\Delta H_{MH} \simeq E_1 \text{ for } p > p_{pl}. \qquad (4.41)$$

The non-linearity increases with larger pressures and/or decreasing diffusivity, i.e. $Ap >> D/L$. Eventually, this ends up in a square-root function:

$$R(p)|_{Ap>>D/L} \simeq \frac{D}{L}\sqrt{\frac{A}{B}}\left[\sqrt{p} - \sqrt{p_{pl}}\right], \tag{4.42}$$

in good agreement with numerical results from Martin et al.[172] and Bloch.[173] Equation 4.42 might be simplified by

$$R(p)|_{Ap>>D/L} \propto \left(k'\frac{\sqrt{p}}{\sqrt{p_{pl}}} - 1\right). \tag{4.43}$$

Frequently, desorption is measured in or near vacuum conditions. In the very limit, equation 4.42 becomes

$$R(p = 0) \simeq -\frac{D}{L}\alpha\sqrt{p_{pl}} \quad \text{for } B >> \frac{D}{L}$$

For the surface limited kinetics, eq. 4.37 is estimated by a Taylor series of the square root around $Ap \simeq 0$:

$$R(p \simeq 0) = \frac{D^2}{2BL^2}\left(-1 + 1 + 2\gamma - 2\gamma^2 - \frac{2L}{D}\sqrt{ABp_{pl}}\right). \tag{4.44}$$

with

$$\gamma^2 = \left(\frac{L}{D}\sqrt{ABp_{pl}} + ABp\right)^2$$

$$\simeq A^2B\frac{L^2}{D^2}p_{pl} + 2\frac{L}{D}p\sqrt{A^3B^3p_{pl}}.$$

This can be estimated for $B << \frac{D}{L}$ by

$$R(p)|_{p\simeq 0} = -A\left[p_{pl} - p\right], \tag{4.45}$$

and thus

$$R(p = 0) \simeq -Ap_{pl} \quad \text{for } B << \frac{D}{L} \tag{4.46}$$

It is convenient to use the reduced rate

$$R(p)|_{p\simeq 0} \propto \left(k''\frac{p}{p_{pl}} - 1\right), \quad p < p_{pl}. \tag{4.47}$$

It is worth to mention that the parameters k', k'' in equations 4.47, 4.42 can be taken as a measure for the quality of the fit of the kinetics. Per definition, $R(p = p_{pl}) \equiv 0$, and therefore $k' \simeq 1 \simeq k''$. In this case, the parameters A, B, α are interrelated: $\alpha = \sqrt{A/B}$. Deviations of k', k'' from one means that even if

the fit was well adapted on a local scale, an extrapolation of the results would be problematic.

The activation energy is again a complicated function of pressures and temperature. Three extreme cases can be distinguished: (i) and (ii) plateau pressure $p_{pl} << p$, which corresponds to absorption at very high pressures, and (iii) $p_{pl} > 0$, corresponding to desorption at low pressures ($p \simeq 0$) and high temperatures ($p_{pl} >> 0$). For cases (i) (high dissociation barrier) and (ii) (small diffusion) one obtains

$$(i) \quad E_{AA} = E_1 \text{ for } p >> p_{pl} \tag{4.48}$$

$$(ii) \quad E_{AA} = \frac{1}{2}(E_1 - E_2) + E_{diff} \text{ for } p >> p_{pl}, \tag{4.49}$$

in good agreement with the previous paper of Borgschulte et al.[159] Case (iii) is derived via a Taylor approximation (eq. 4.44). The apparent activation energy becomes

$$(iii)a \quad E_{AA} = E_1 - 2\Delta H_{MH} \text{ for } \frac{D}{L} >> B, \tag{4.50}$$

and

$$(iii)b \quad E_{AA} = E_{diff} - \Delta H_{MH} \text{ for } \frac{D}{L} << B. \tag{4.51}$$

The intermediate solution diverges similar to eq. 4.41.

The equations resemble the Temkin equation,[174–176] if a reaction A $\rightarrow$ B with one single activation barrier E_{AB} is coupled to an equilibrium state C with stability ΔH_C:

$$A \leftarrow mB \rightleftharpoons mC \quad E_{AA} = E_{AB} - m \cdot \Delta H_C$$

For the diffusion limited case, atomic hydrogen (H) diffuses inside the metal hydride MH_x, i.e. $m = 1$:

$$\left(\frac{1}{2}H_2 \leftarrow\right) H_{chem} \leftarrow H_{diff} \rightleftharpoons MH_x.$$
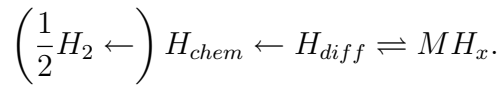
For the surface limited case, two atomic hydrogen recombine at the surface to H_2, i.e. $m = 2$:

$$H_2 \leftarrow 2H_{chem}(\leftarrow 2H_{diff}) \rightleftharpoons 2MH_x.$$
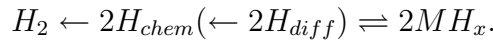
The change of the parameter m corresponds to a transition from a diffusion to a surface limited sorption. Thus, $r = m/2$ is also called *reaction order*.[176] This is in special cases reflected by the pressure dependence of the rates. A linear pressure dependence corresponds to a surface limited kinetics, a square-root dependence corresponds to a diffusion limited kinetics, respectively.

To highlight the various cases and to simplify discussion, Table 4.2 gives an overview.

Table 4.2: Overview of the various estimates of the pressure dependence of equation 4.37 and the corresponding apparent activation energies.

rate-limiting step conditions	simplified kinetics	activation energy
dissociation $p >> p_{pl}$	$R = Ap$	E_1
dissociation $p \simeq p_{pl}$	$R = A(p - p_{pl})$	$E_1 + \frac{p_{pl}}{p - p_{pl}} 2\Delta H_{MH}$
diffusion $p >> p_{pl}$,	$R = \frac{D}{L}\sqrt{\frac{A}{B} \cdot p}$ $= \frac{D}{L}\alpha \cdot \sqrt{p}$	$\Delta H_{sol} + E_{diff}$
diffusion $p \simeq p_{pl}$	$R = \frac{D}{L} \cdot$ $\alpha\left[\sqrt{p} - \sqrt{p_{pl}}\right]$	$\Delta H_{sol} + E_{diff} + \frac{\sqrt{p_{pl}}}{\sqrt{p} - \sqrt{p_{pl}}}\Delta H_{MH}$
diffusion $p_{pl} >> p \simeq 0$,	$R = -\frac{D}{L}\sqrt{\frac{A}{B}}\sqrt{p_{pl}}$ $= \frac{D}{L}\alpha \cdot \sqrt{p_{pl}}$	$\Delta H_{sol} + E_{diff} - \Delta H_{MH}$
recombination $p_{pl} >> p \simeq 0$	$R = -Ap_{pl}$	$E_1 - 2\Delta H_{MH}$
best-fit kinetics		
dissociation	$R \propto \left(k'' \frac{p}{p_{pl}} - 1\right)$	-
diffusion	$R \propto \left(k' \frac{\sqrt{p}}{\sqrt{p_{pl}}} - 1\right)$	-

Comparison with $Mg_yNi_{1-y}H_x$ thin films

Hydrogen uptake kinetics have been measured for a huge number of hydride systems. We restrict ourselves here to the representative example of the H-uptake in $Mg_yNi_{1-y}H_x$ thin films. Thin films resembles the geometry of the theoretical model, and are thus ideal to test the model. The comparison of the sorption kinetics of bulk $LaNi_5H_6$ and Mg-MgH_2 with our model is presented elsewhere.[177]

Figure 4.21 shows the pressure dependence of H-absorption in $Mg_y Ni_{1-y}$ thin films for various compositions y measured at room temperature. The gradient film is completely covered with a uniform layer of Pd, making it likely that we are dealing with the same surface properties. An increased amount of Mg leads in first order to a decrease in diffusivity of H in $Mg_y Ni_{1-y}$. Furthermore, the formed phases change from a Mg-doped $Mg_2 NiH_4$ to a Ni-doped MgH_2. This has consequences for the thermodynamical properties, in particular for the equilibrium pressures. The plateau pressures are obtained as extrapolation to zero rate using expression 4.40 based on the model derived above (see Fig. 4.21). The heat of formation is obtained by repeating the measurements at various temperatures. (see Sec. 4.5) The method holds also for non-linear kinetics (Mg-rich samples, see inset of Fig. 4.21), although the extrapolation to zero-rate becomes more difficult.

Here, we emphasize that measuring a linear pressure dependence does not mean that the uptake rate is determined by surface properties only since they are equal for all compositions on a given gradient sample: The sample is covered with the Pd of the same thickness and all compositions are probed simultaneously under the same conditions - still large difference in uptake kinetics is measured. This can be easily understood as the linear relation (eq. 4.40) is a first order approach. Evidently, the rates are determined by one rate-limiting step only in extreme cases. Most of the rates can be fitted by a linear relation, though the linearity of the data points decreases (decreasing of the correlation coefficient, see Fig. 4.21), which is an indication of the increasing influence of the bulk. A purely diffusion limited case is not found either. To underline the statement, we plot the rates as a function of $(p/p_{pl} - 1)$ (eq. 4.47). Linear fits to the experimental data reveal the same slope for all curves. Evidently, the uptake rate can be well described by eq. 4.47 with the same proportionality parameter, i.e. with the same properties of the surface layer (Pd). It is noted that the deviation from 0 for p/p_{pl} of the Mg-richest sample is the smallest of all samples (see inset in Fig. 4.21). Thus, the linear approximation is still very well suited, even if a different behavior is to be expected at higher supersaturation.

The interdependence of elementary steps solves a controversial debate: how can the change of bulk properties (e.g. diffusion) influence an uptake rate, which was considered to be "surface rate-limited" on the basis of a traditional single-step by an evaluation of the time dependence[178] or pressure dependence[179] of the desorption of MgH_2? In our model, this controversy does not arise. The coverage at the surface θ is directly connected to the bulk concentration $c(x = 0)$ at the surface, which depends on the diffusion gradient in the volume, which further depends on the plateau pressure of the absorbing material. The surface coverage, however, determines the hydrogen dissociation (parameters A, B), and thus a bulk process influences a surface process.

We can also discuss the validity of the simplifications of the two-step model
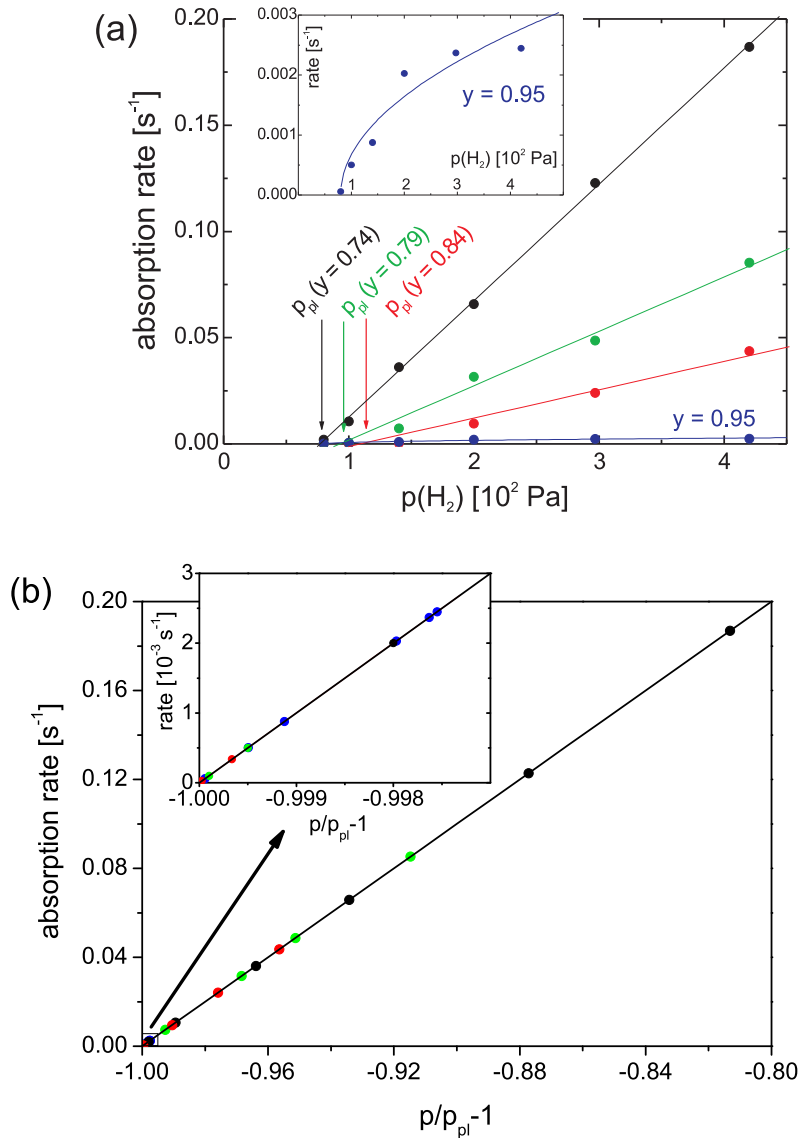
Figure 4.21: (a) Pressure dependence of H-absorption rate of Mg_yNi_{1-y} thin films for various compositions y measured at room temperature ($y = 0.78$ black dots, 0.73 green dots, 0.71 red dots, 0.87 blue dots). The solid lines are linear fits, from which the plateau pressures are derived. The regression coefficient decreases from nearly one (0.9997, black dots) to 0.9011 (blue dots). *Inset*, enlargement of the Mg-rich sample ($y = 0.95$), which clearly shows the non-linear pressure dependence. The extrapolation to zero-rate defines the equilibrium pressure p_{pl}. (b) The plateau pressures from Fig. 4.21 are used to plot the rate as a function of p/p_{pl}. Solid curves are linear fits to the experimental data revealing the same slope for all curves. *Inset*, enlargement in the low-rate region

along this experimental example. It is not expected that the absolute value of θ changes significantly in the used pressure range (between 100- and 400 Pa), and thus the simplification in equation 4.34 is plausible. Furthermore, the results are in good agreement with literature data. Hydrogen uptake of Mg-thin films in the α-regime shows a time dependent behavior, while absorption in the plateau regime is time-constant.[170]

An important outcome of the two-step model is that the apparent activation energy depends on the exact thermodynamic regime, in which this property is measured. To validate this experimentally, we measured optically the hydrogen uptake rate of a Pd-capped Mg_2Ni film at various temperatures and pressures. The uptake-rate is plotted as a function of the applied pressure in Fig. 4.22. The linear behavior as already discussed above is hint for a dissociation limited rate. The extrapolated onset pressures represent the equilibrium pressures. From the temperature dependence, a heat of hydride formation of -44 kJ/mol H_2 is obtained as shown by the corresponding Van 't Hoff plot in Fig. 4.23. The linear extrapolation to higher temperatures of the thin film values matches exactly the equilibrium pressures obtained from bulk p-c isotherms.[66,102] This underlines the applicability of the method. Without considering any models, the apparent activation energy is calculated according to equation 4.7 from the change of the rate at two different temperatures:

$$E_{AA} = k \frac{1}{4} \left(T_1 + T_2 \right)^2 \frac{\ln R_2 - \ln R_1}{T_2 - T_1} \qquad (4.52)$$

At a given pressure, e.g. 4000 Pa (marked with (1) in Fig. 4.22), the rate *decreases* with increasing temperature. The corresponding apparent activation energy is thus *negative*. At higher pressures, though, the activation energy is positive (point (2)). The reason for this is obvious due to the different thermodynamic driving forces $(p - p_{eq})$. Assuming dissociation limiting kinetics, the apparent activation energy is zero at

$$\frac{-E_1}{2\Delta H_{MH}} = \frac{p_{eq}}{p - p_{eq}} \qquad (4.53)$$

The intercepts of the curves in Fig. 4.22 correspond to zero apparent activation energy and are found around $p/p_{eq} = 4$. The surface barrier height $E_1 = 0.13$ eV is obtained from an Arrhenius plot of the parameter A' (from eq. 4.40), shown in Fig. 4.24. Using this value, a zero apparent activation energy is expected at $p/p_{eq} = 4$ and indeed found.

The experimental surface barrier height of 0.13 eV is in good agreement with the value for hydrogen dissociation on Pd as derived from surface science results. Hydrogen dissociation on Pd surfaces is non-activated, i.e. $E_{diss} \leq 0$. However, at higher coverage, the chemisorbed hydrogen changes the electronic structure (poisoning),[180] which shifts the energy potential by around 0.2 eV. The experimental activation energy of hydrogen absorption in pure Pd was
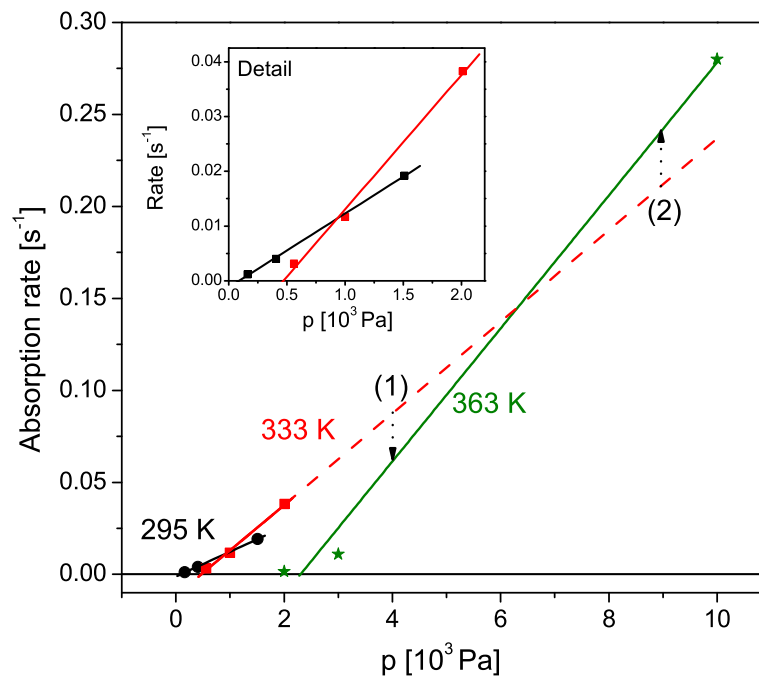
Figure 4.22: H-uptake rate of Mg_2Ni at various pressures and temperatures measured optically. Points marked with *(1)* and *(2)* indicate *negative* and respectively *positive* apparent activation energy (see text).
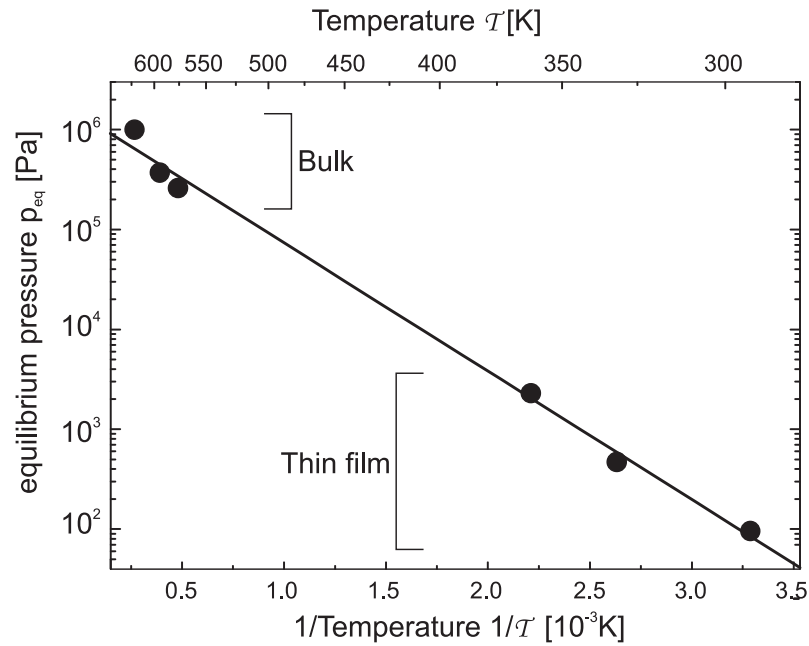
Figure 4.23: Van 't Hoff plots of Mg_2Ni. Equilibrium pressures from Fig. 4.22 (thin films) and Ref.[102] (bulk), respectively.
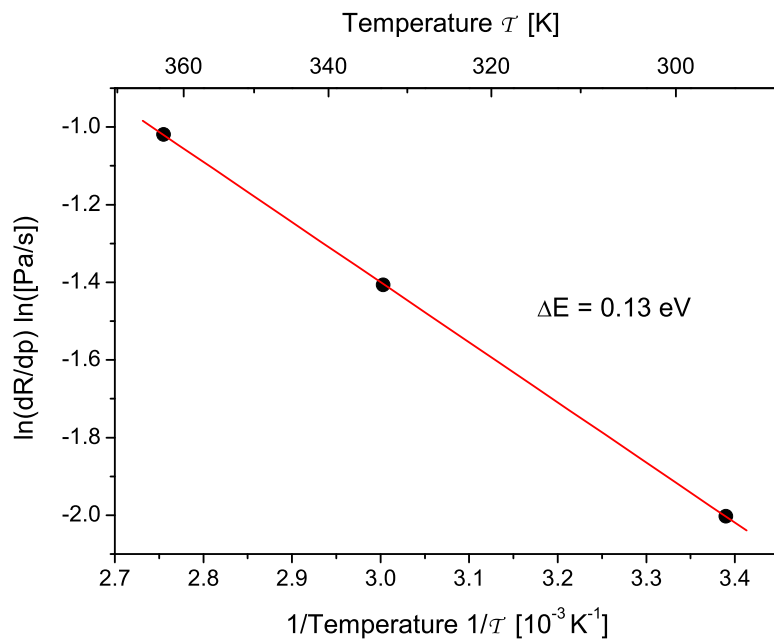
Figure 4.24: Surface activation energy E_1 of Pd-capped Mg_2Ni thin films as obtained from an Arrhenius plot of the parameter $A' = R/(p - p_{pl})$ (eq. 4.40).

found to be 0.2 eV, but the authors did not distinguish between surface- and diffusion activation energy.[59]

4.5   Thermodynamics

Dependence of the optical properties on the H concentration

The hydrogen concentration dependence of optical properties can be obtained from measurements in an optical-electrochemical cell. In this case, optical reflection and transmission at 1.95 eV are measured simultaneously with the hydrogen content. Equilibrium potentials U_{eq} during hydrogenation are obtained using the galvanostatic intermittent titration technique (GITT).[66] The pressure-concentration-isotherm (PCI) can be derived from U_{eq} by means of the Nernst equation:

$$\ln(\frac{p}{p_0}) = -\frac{2F}{R\mathcal{T}}(U_{eq} + 0.926) \qquad (4.54)$$

with p the H_2 pressure in Pa, $\mathcal{T}$ the temperature, $p_0 = 1.013 \cdot 10^5$ Pa the standard pressure, $F = 96485.3$ C/mol and $R = 8.3144$ J/mol K the Faraday and gas constant, respectively.

Fig. 4.25 shows (a) the optical reflection and transmission at a photon-energy $\hbar\omega = 1.95$ eV (635 nm wavelength) together with (b) the corresponding (2nd) absorption electrochemical GITT pressure-composition-isotherm for a $Mg_{0.64}Ni_{0.34}$ composition. The oscillating behavior of the reflection comes from the self-organized two-layer ($Mg_2NiH_4/Mg_2NiH_{0.3}$) (phase) nucleation and growth process (see Sec. 4.4.1).[181] The transmission T is plotted on a logarithmic scale to emphasize that despite interferences, $\ln(T)$ increases quasi-linearly with the hydrogen concentration c as soon as the Mg_2NiH_4 phase starts to nucleate (Coexistence plateau for $c \geq 0.2$). The fact that $\ln(T) \propto c$, i.e. that Lambert-Beer's law applies, makes it possible to record pressure–*optical transmission*–isotherms (PTI) that are analogous to pressure-concentration-isotherms (PCI) obtained with standard volumetric or gravimetric methods [182]. In PTIs, $\ln(T/T_M)$, the logarithm of the optical transmission T in a film of initial transmission T_M is plotted as a function of the hydrogen pressure. Similarly to a PCI, a PTI contains a plateau when the metal and hydride phase coexist.

Figure 4.26 displays the PTI constructed from the optical and electrochemical data shown in Fig. 4.25. The main differences with the PCI is that the solid solution $Mg_2NiH_{0.3}$ is not visible in the PTI and that $\ln(T/T_M)$ first decreases due to the interference-induced dip in the transmission at low concentration.
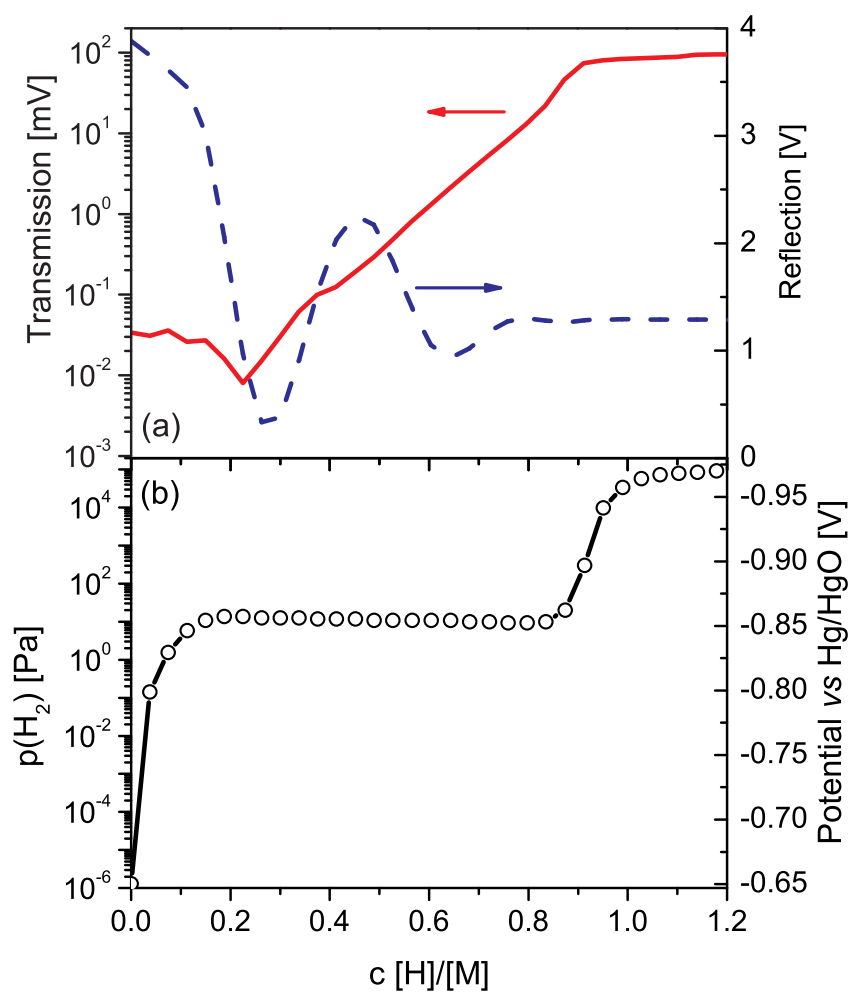
Figure 4.25: (a) Optical reflection and transmission at a photon-energy $\hbar\omega = 1.95$ eV (635 nm wavelength) and (b) corresponding absorption electrochemical GITT pressure-composition-isotherm at 293 K for $Mg_{0.64}Ni_{0.34}$. Reflection is measured from the substrate side. The plateau at high hydrogen concentration is due to H_2 gas evolution on the sample.
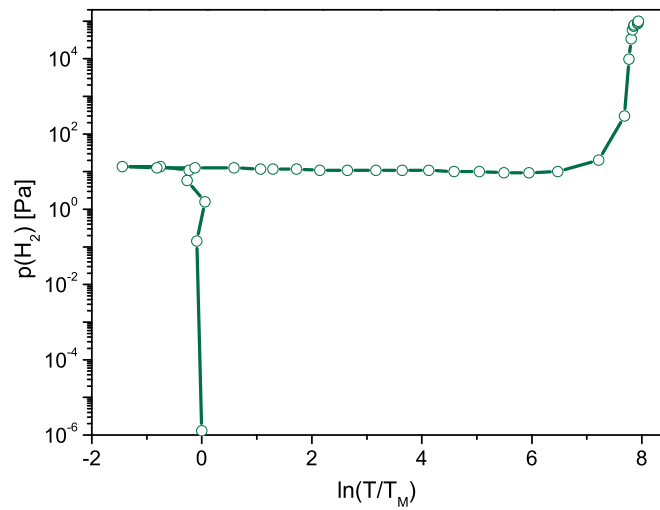
Figure 4.26: Pressure–optical-transmission–isotherm (PTI) for a $Mg_{0.64}Ni_{0.34}$ composition at a photon-energy $\hbar\omega = 1.95$ eV (635 nm wavelength). The negative values of $\ln(T/T_M)$) are due to interference effects caused by the use of a monochromatic light source.

4.5.1 Pressure–optical-transmission–isotherms

We make use of the continuous change of optical transmission with hydrogen concentration to record simultaneously PTIs with the Hydrogenography setup for all compositions of the Mg_yNi_{1-y} gradient thin film. To record isotherms, the hydrogen pressure around the Mg_yNi_{1-y} gradient is slowly increased while the transmitted light intensity is monitored continuously. This results in an isotherms "map" containing $\ln(T)$ as a function of alloy composition y and H_2 pressure (Fig. 4.27(a)). The PTIs for a selection of compositions y are plotted in (b). Here, the optical transmission T is normalized by the transmission in the metallic state T_M. For all compositions, the optical transmission increases with increasing pressure. No interference-induced effects in the transmission are observed, in contrast to the electrochemical isotherm in Fig. 4.26. This is probably due to the optical setup: While the transmission in the electrochemical is recorded by means of a red laser (narrow photon-energy band around 1.95 eV), the Hydrogenography setup is illuminated by white light and the transmission recorded with a CCD (1.1-3.3 eV energy-bandwidth). The energy-dependent interferences are therefore averaged and vanish from the PTIs.

The isotherms width and shape vary however significantly with the Mg fraction y. The isotherm width increases with the Mg fraction. This is partly due to the increase in thickness with y of the Mg_yNi_{1-y} layer, from 30 to 100 nm. This effect is even reinforced by the increasing transparency (at constant thickness) of the hydride with increasing Mg content up to the eutectic composition (see Fig. 4.9). Following the isotherms from start to end pressure, we notice that first an initial step in the transmission occurs, at the lowest pressure applied to the sample. We attribute this step, which is more marked for $y = 0.6$ and 0.7, to the hydrogenation of free Mg. More interesting a feature is the variation in isotherm shape that occurs at higher pressures: For $y = 0.6$ and 0.7, the isotherm contains only a single plateau, which we attribute to the Mg_2NiH_4 formation. In contrast, for Mg-richer compositions ($y = 0.8$ and 0.9), the transmission first increases gradually, and then the Mg_2NiH_4 plateau develops at higher pressure. We know from spectrophotometric results that excess Mg for compositions above the stoichiometry ($0.67 < y < 0.88$) is incorporated as a dopant in the Mg_2NiH_4 structure, and not phase segregated. [108] The small initial step in the transmission for Mg-rich compositions indeed indicates that only a minute amount of Mg is free and confirms the Mg-dopant scenario. Furthermore, the gradual increase of transmission with pressure for $0.7 < y < 0.9$ before the plateau is probably due to hydrogenation of Mg-rich sites.

The "V" shape in the map of Fig. 4.27(a) is created by the strong contrast between low and high transmission (i.e the plateau in the isotherms), and indicates directly the equilibrium plateau pressure. By applying a fitting
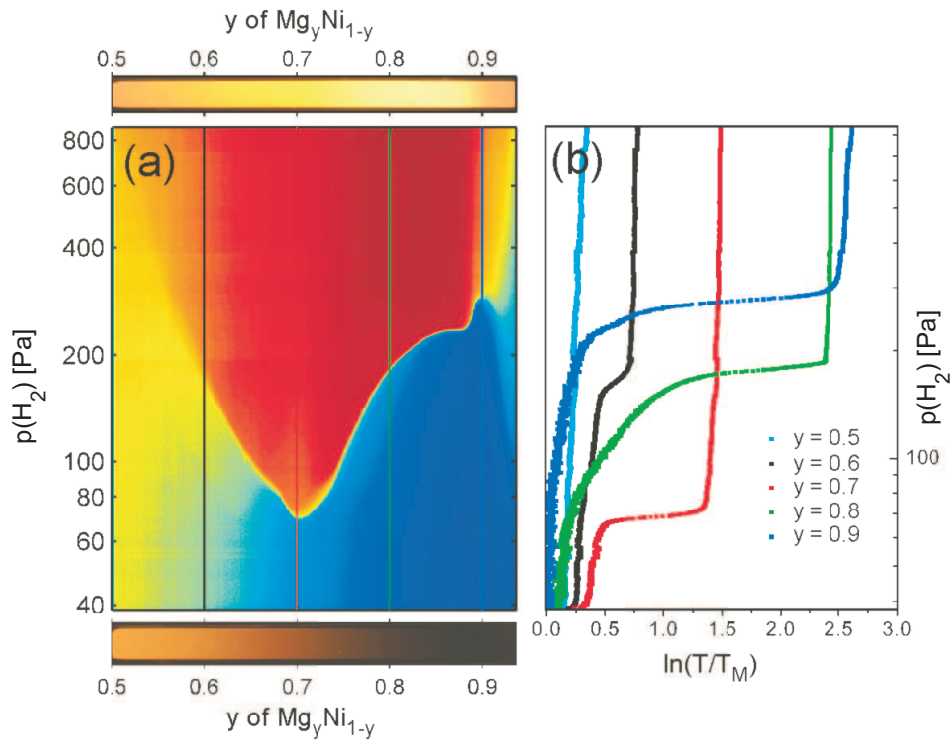
Figure 4.27: PTIs of $Mg_yNi_{1-y}H_x$ at $\mathcal{T} = 305$ K. (a) Optical transmission map (blue: low transmission, red: high transmission) as a function of Mg fraction y and hydrogen pressure p. *Top* and *bottom*, images in transmission of the gradient film in the as-deposited and hydrided state, respectively. (b) PTIs (p vs $\ln(T/T_M)$) for various compositions y. The pressure is increased logarithmically during 24 h.

procedure to the isotherms (see Sec. 5.7.1 for details), we directly extract the equilibrium pressure at the beginning of the plateau. We call this method of obtaining p_{eq} "quasi-equilibrium", in contrast to the "off-equilibrium" method used in the kinetics section of this chapter. The compositional dependence of p_{eq} from both methods is compared in Fig. 4.28. In the Ni-rich part, values from both methods agree well with each other, while in the Mg-rich part, the quasi-equilibrium gives p_{eq} slightly higher than the off-equilibrium method. A discrepancy between the two approaches is expected, as in the off-equilibrium determination, we extrapolate p_{eq} down to zero rate, while in a pressure sweep, a slight overpressure is needed for the absorption reaction to happen. The difference between both results increases with Mg-fraction in accordance with kinetics results: as can be seen from the slopes of the pressure dependence in Fig. 4.21(a), the prefactor A in Eq. 4.6 decreases with increasing Mg content. Therefore, the more Mg in the layer, the higher the overpressure needed to trigger the reaction and achieve the same rate.

The equilibrium pressure from quasi-equilibrium reaches a maximum approximately at the eutectic composition and then decreases steadily. As the isotherms show very sloping isotherms for $y > 0.90$, this behavior is probably the result of mixed phases and intrinsic slow kinetics. We will therefore not consider compositions above the eutectic in the coming analysis.
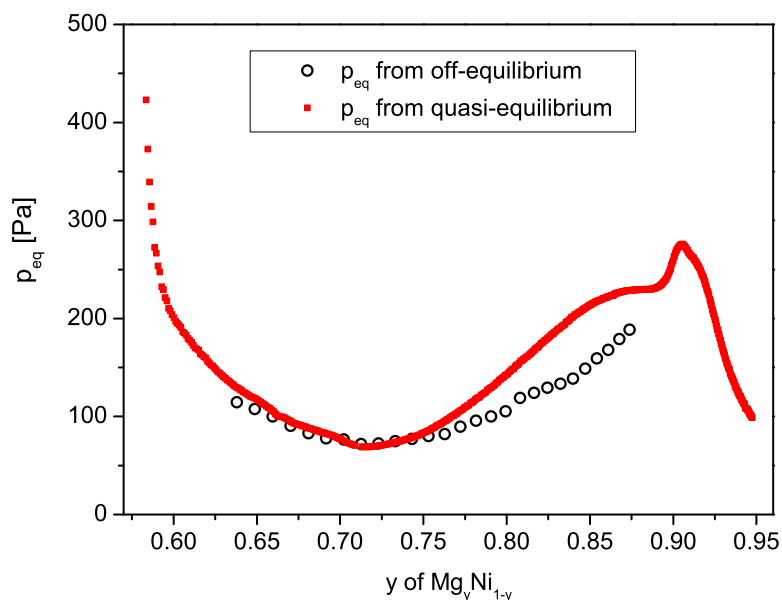
Figure 4.28: Comparison of the equilibrium plateau pressures of $Mg_yNi_{1-y}H_x$ determined by means of the off-equilibrium and quasi-equilibrium methods at $T = 305$ K.

4.5.2 Hydride formation enthalpy

Quasi-equilibrium measurements can easily be extended to other temperatures. This is exemplified in Fig. 4.29, where the compositional dependance of p_{eq} is plotted for 6 temperature between 295 and 363 K. It is remarkable that for all temperatures, p_{eq} exhibits the same characteristic "V" shape. For higher temperatures, the sample did not react, probably due to phase segregation and/or intermixing of the Pd caplayer with the Mg-Ni layer.
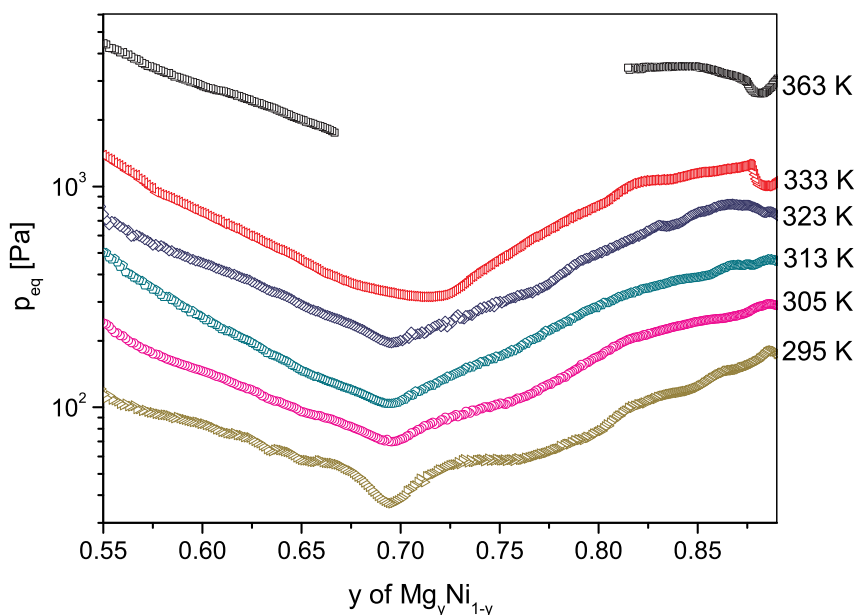
Figure 4.29: Equilibrium plateau pressure of $Mg_yNi_{1-y}H_x$ compositional gradient thin film for 6 temperatures. At 363 K, part of the gradient did not react, explaining the broken curve.

For each composition y, the equilibrium pressures as a function of temperature are reported in a Van 't Hoff (VTH) plot and, as for pure Pd, the enthalpy of hydride formation is obtained from its slope using the VTH relation (Eq. 1.2). Figure 4.31 displays a few $Mg_yNi_{1-y}H_x$ VTH plots for compositions y across the whole gradient. For $0.56 \leq y \leq 0.80$, the VTH plots are remarkably parallel, indicating that the slope (i.e. enthalpy) is not varying much in this range. The variation in equilibrium pressure comes thus mainly from the change in intercept with the y-axis (i.e. entropy). It is only for compositions $y > 0.8$ that the slope of the VTH plots decreases significantly. The enthalpy values obtained from a linear regression of the VTH plots are shown in Fig. 4.31. For $0.56 \leq y \leq 0.80$, the enthalpy amounts ΔH = -46 to -50 kJ(mol H_2)$^{-1}$. This is about 12-16 kJ(mol H_2)$^{-1}$ less negative than bulk

Mg_2NiH_4 measured in absorption (ΔH =-62 kJ(mol H_2)$^{-1}$)[109,110,183,184]. This difference, also observed for $Mg_yTi_{1-y}H_x$ films, most probably comes from the clamping to the substrate. Indeed, unlike Pd, Mg and Ni stick very well to the substrate and no buckles or cracks were observed even after several hydrogenation cycles. As a clamped thin film can only expand in one direction, the repeated H-induced expansion/contraction during cycling produces large microstructural changes.[69] This materials reorganization costs a considerable amount of energy and makes the enthalpy measured on thin films less negative.[35–37]
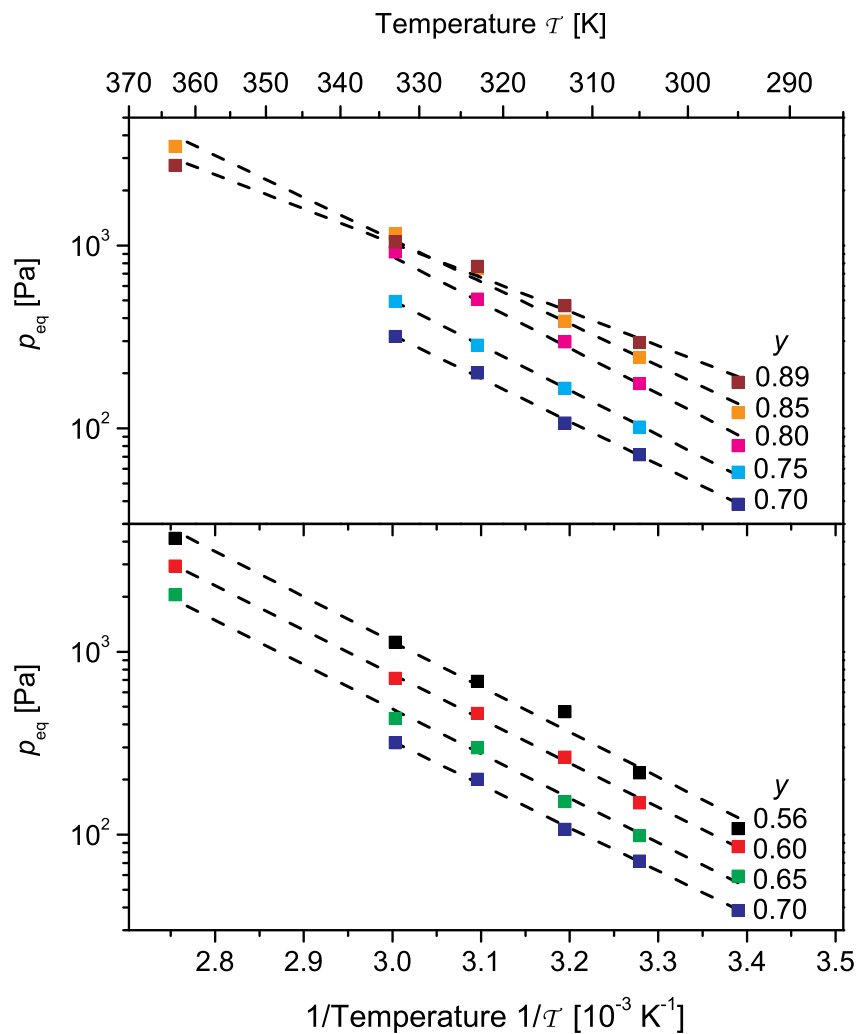
Figure 4.30: *Symbols*, equilibrium pressure data obtained from the automatic PTI fitting procedure, and *lines*, corresponding Van 't Hoff plots (linear regression) for 9 representative alloy compositions y in Mg_yNi_{1-y}.

The interesting part in the compositional dependence of the enthalpy comes between $0.8 < y < 0.88$, where ΔH steadily increases from -50 to -36 kJ$(mol\,H_2)^{-1}$ while going towards the Mg_2Ni-Mg eutectic composition. [c] Such a reduction of the stability has been predicted by Van Setten et al. for substitution of Ni by other transition metals,[185] but the case of non-stoichiometric Mg-rich Mg_2NiH_4 had not been addressed. They recently performed density functional theory (DFT) calculations on this system to compare with the enthalpy we obtain with Hydrogenography.[186] Starting from the experimental positions and lattice parameters,[187] they relaxed the crystal structure of Mg_2NiH_4. All lattice parameters and atomic positions are relaxed, minimizing the total energy of the electron ion system. From the relaxed structure with minimum total energy, they then construct the non stoichiometric models. They start with a conventional unit cell and remove nickel atoms. Subsequently they relax the atomic positions and lattice parameters. The magnesium atoms are then expected to donate two electrons to either, single hydrogen atoms, which then form a two electron 1s closed shell (as in MgH_2) or a NiH_4 complex, which then forms an eighteen electron closed shell configuration (as in Mg_2NiH_4). An inspection of the densities of states of the non stoichiometric models confirms this picture. Because in this way all electrons are in closed shell configurations all models become semiconductors. Using the total energies of the non stoichiometric model systems and the values for the total energies of bulk magnesium, magnesium hydride, Mg_2Ni, and H_2 reported earlier,[185] the hydrogenation enthalpy with respect to Mg_2Ni and bulk magnesium is then calculated. From Figure 4.32 it is clear that all models for the Mg-rich non stoichiometric systems are metastable with respect to decomposition into MgH_2 and Mg_2NiH_4 and that the hydrogenation enthalpy is less negative than that of Mg_2NiH_4.

An essential ingredient however cannot be taken into account by DFT: the presence of the Mg_2Ni-Mg eutectic at $y = 0.883$ and the two different microstructures that have to coexist at this composition (See "Spectrometry in the visible" in Sec. 4.3.2). Around a eutectic, the overall microstructure consists usually in very well mixed phases, with lamellae[114] or nanocrystalline morphology[115]. In our case, just below the eutectic, the $Mg_yNi_{1-y}H_x$ layer is most likely nanocrystalline or amorphous as no XRD peak is detected there, and Mg_2Ni and Mg are intimately mixed in the as-deposited state. Ouyang et al.[115] recently calculated that, if Mg and Mg_2Ni grains are assumed to be spheres with an average diameters of 40 and 20 nm, the enthalpy of the eutectic metallic alloy, and hence the hydrogenation reaction, will be destabilized by 5 kJ$(mol\,H_2)^{-1}$ by the extra interfacial energy. This mixing effect probably explains part of the enthalpy increase measured towards the eutectic composition.

---

[d]Note that the increase in ΔH is partly compensated by the increase in ΔS, resulting in a not too dramatic increase in plateau pressure.
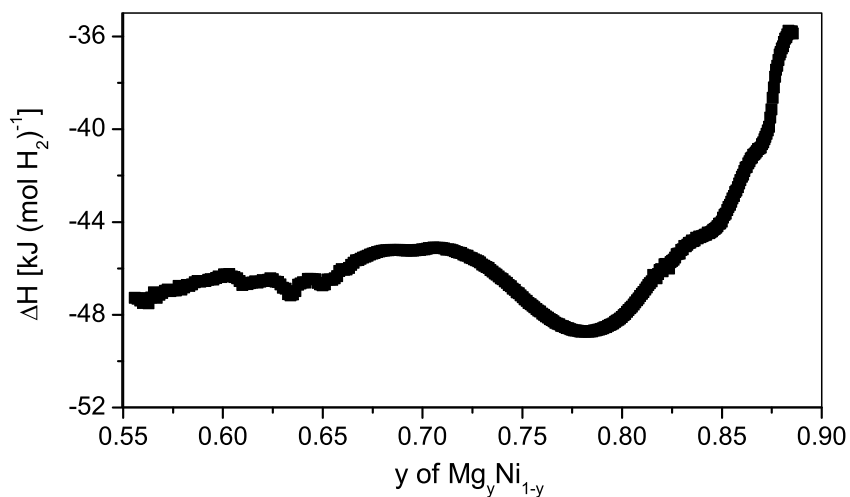
Figure 4.31: Compositional dependence of the enthalpy of hydride formation for $Mg_yNi_{1-y}H_x$ measured optically by Hydrogenography. The ΔH values are determined from 500 plots similar to those in Fig. 4.30. The error is $\pm 1 - 2$ kJ$(mol\ H_2)^{-1}$.
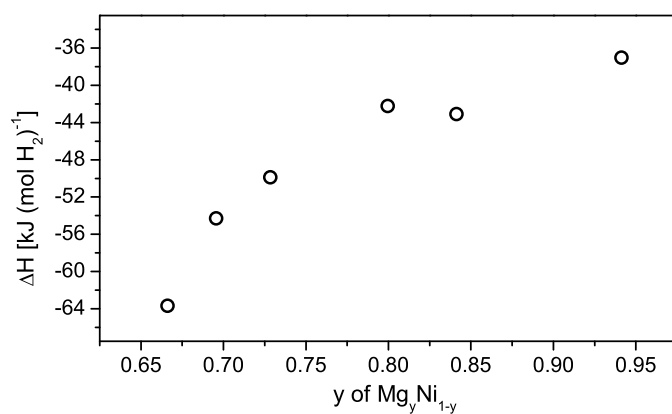
Figure 4.32: Enthalpy of hydride formation for $Mg_yNi_{1-y}H_{2y}$ calculated by DFT by M. van Setten.[186]

4.5.3 Selective hydrogenation: kinetics/thermodynamics interplay

Combining what we know from the kinetics and thermodynamics of hydrogenation of $Mg_yNi_{1-y}H_x$ thin films allows us to run an interesting confirmation experiment. Schematically, two hydride phases can be formed in the sample: Mg- (or Ni-)doped Mg_2NiH_4 or Ni-doped MgH_2. We show here that, as their thermodynamic and kinetics properties differ markedly, it is possible to *selectively* hydride one or the other phase at will. As seen in Fig. 4.33, the pressure-temperature space occupied by the VTH plots of both phases is well-separated. This implies that if we choose the $(p,\mathcal{T})$ settings corresponding to the *left dot* between the two VTH regions in Fig. 4.33, only MgH_2 will be formed. If on the contrary a pressure above both VTH at room temperature (*right dot*) is applied, the slow kinetics of MgH_2 compared to Mg_2NiH_4 makes sure that first only Mg- (or Ni-)doped Mg_2NiH_4 will form.

Figure 4.34 shows the transmission maps for both experiments. In the upper part, at room temperature, the H_2 pressure is increased from vacuum to $p(H_2)$=1500 Pa at time $t = 0$ s. We follow then the transmission change as a function of time. The line graphs on top of the transmission map corresponds to $\ln(T)$ after 400 s and shows the extension of doped Mg_2NiH_4 in the compositional gradient. As expected, all compositions below the Mg_2Ni-Mg eutectic point do hydride; there is however a non-negligible amount of Mg_2NiH_4 formed also *above* the eutectic.

In the lower part of Fig. 4.34, the temperature is $\mathcal{T} = 403$ K and the applied pressure $p(H_2)$=4000 Pa. Thermodynamically, only MgH_2 can form, and the high temperature provides a high enough hydrogenation speed. The transmission reveals the usual MgH_2 compositional region above the Mg_2Ni-Mg eutectic. Unexpectedly, MgH_2 also forms in the Ni-rich region, just below the Mg_2Ni stoichiometric composition ($0.6 < y < 0.67$). The presence of MgH_2 there might be due to Mg phase segregation induced by annealing at 403 K.

This example shows that Hydrogenography can be used as a detection method to locate precisely known hydrides in thin film compositional gradients.
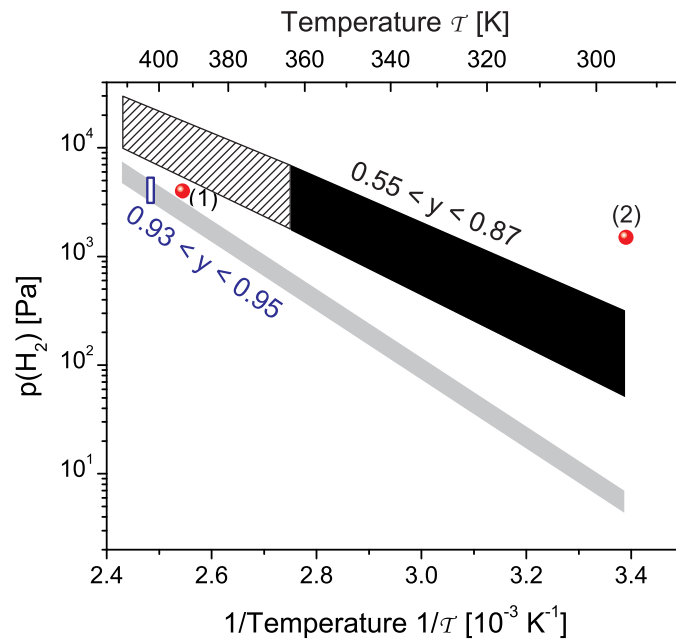
Figure 4.33: *Red balls*, measurement settings ((1) $p = 4000$ Pa, $\mathcal{T} = 393K$ and (2) $p = 1500$ Pa, $\mathcal{T} = 295K$) for the phase-selective hydrogenation of $Mg_yNi_{1-y}H_x$ thin films. The *black area* is the pressure-temperature space occupied by Van 't Hoff plots for compositions between $0.55 < y < 0.87$ (first loading, off-equilibrium method), and the dashed region its extrapolation to higher temperature. The *empty rectangle* is the equilibrium pressure range for Mg-rich compositions ($0.93 < y < 0.95$), and the *grey area* the Van 't Hoff plot region for these compositions assuming an enthalpy of hydride formation of a pure Mg thin film ($\Delta H = -60.7$ kJ (mol H_2).[101]
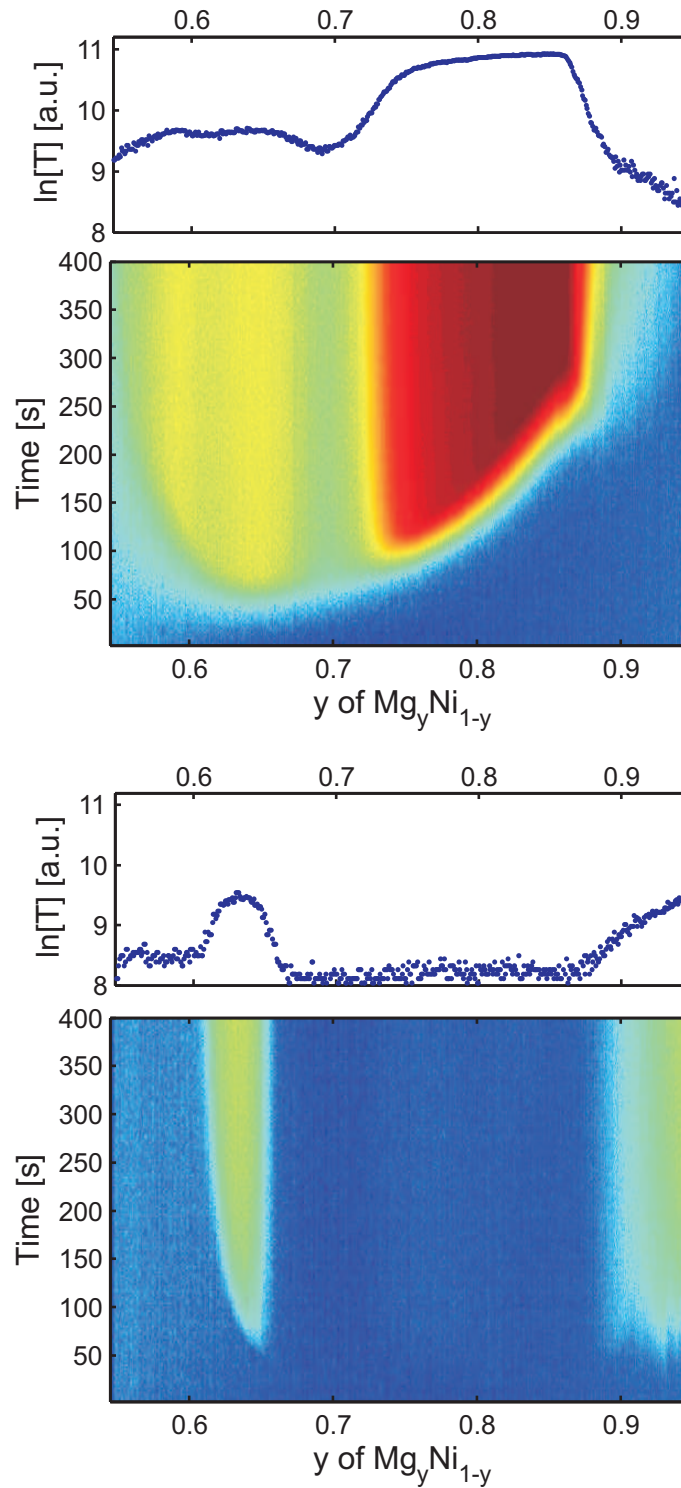
Figure 4.34: Selective MgH$_2$ and Mg$_2$NiH$_4$ formation (first hydrogenation). *Top color map*: ln(T) as a function of time and composition y at room temperature after the application of a hydrogen pressure step of p(H$_2$)=1500 Pa at time $t = 0$ s. *Bottom color map*: same, for a p(H$_2$)=4000 Pa step at 403 K. *Blue* and *red* colors mean low, respectively high transmission. *Line graphs*: ln(T) at $t = 400$ s.

4.6 Summary and conclusion

4.6.1 Phase identification

With the all-optical hydrogenography approach, we are able to address the essential questions when it comes to characterize thin metal films deposited in a combinatorial way. The nature and compositional extension of the hydride phases is quickly determined by screening the gradient thin film with infrared and visible spectrophotometry. The change in optical absorption reveals abrupt microstructural changes at the Mg_2Ni-Mg eutectics but also smoothly changing optical properties due to increasing Mg or Ni doping of Mg_2NiH_4. In the metallic state, crystalline Mg_2Ni is only observed between $0.58 < y < 0.81$. Apart from Mg_2Ni, no other phases could be detected in the $0.41 < y < 0.89$ range. The rutile Mg 002-reflection is only observed for compositions $y > 0.89$, i.e. above the Mg-Mg_2Ni eutectic composition. In the hydrided state, the hydride consists in Ni-doped Mg_2NiH_4 below the $[Mg]:[Ni] = 2$ ($y < 0.67$) stoichiometric composition, and Mg-doped Mg_2NiH_4 between the stoichiometric and eutectic compositions ($0.67 < y < 0.89$). For $y > 0.89$, MgH_2 is the main phase formed, although small amounts of Mg_2NiH_4 are also detected close to the eutectics. Full hydrogenation of Mg is hampered by the slow diffusion of H in the MgH_2 phase, and a large amount of metallic Mg remains in the layer.

4.6.2 Kinetics

Measurements

The optical measurements of the H sorption rate as a function of composition, pressure and temperature serve to test the two-step modeling of the kinetics. Thanks to the *in situ* deposition of a 50 nm PTFE overlayer that greatly reduces oxygen permeability and therefore the adsorption of water on the Pd surface, it is possible to record reproducible rates during different hydrogenation cycles, on the same sample, under exactly the same conditions and for all compositions. From the temperature dependence of the rate, we obtain the surface activation energy of the Pd-capped $Mg_yNi_{1-y}H_x$ films. The H_2 pressure dependence of the rate makes it possible to extrapolate the *true equilibrium* coexistence plateau pressure p_{eq} as a function of composition y. This result is used in a later stage to compare and validate p_{eq} results obtained from PTIs recorded under quasi-equilibrium conditions.

Modeling

Recent measurements of activation energies of various hydrogen storage materials posed intriguing questions about their physical meaning. In order to rationalize the experimental results, a one-dimensional model is set up to es-

timate the time-, temperature- and pressure dependence of sorption kinetics and the relevance of several materials parameters involved in the process. The model, which incorporates explicitly surface *and* diffusion processes, results in three main conclusions:

1. It is impossible to distinguish between dissociation- or diffusion processes on/in a thin cover layer via the time dependence of the total kinetics.

2. In most cases, a *single rate limiting step* does not exist.

3. The apparent activation energy E_{AA} and the pressure dependence of the sorption rate are functions of the relative importance of the elementary processes involved in H-sorption. E_{AA} is thus not an intrinsic materials property.

These conclusions are in good agreement with published experimental results. For example, the time dependence of diffusion as investigated by Crank[167] agrees well with our results as do the pressure relations of the rates. The pressure dependence of the activation energy was also reported in Refs.[188] and [189], which is a hint that the apparent activation energy is in general not a material property. Our model considers the interdependence of surface and diffusion processes and can thereby calculate the apparent activation energy from intrinsic materials properties. However, the estimates of the pressure and temperature dependencies for extreme cases are the same as those as obtained by assuming single rate-limiting steps.[172,173]

The model is successfully tested on $Pd/Mg_yNi_{1-y}H_x$ thin films. Thin films have the advantage to have the same geometry as our one-dimensional model, and have well-defined surface properties. With thin films it is possible to demonstrate experimentally the interdependence of surface and bulk processes. The mathematical description of practical hydrogen storage materials is complicated by their 3d-morphology. Nevertheless, the main results from the present one-dimensional model remain valid, as for example demonstrated by the good description of the pressure dependence of the H-absorption kinetics in $LaNi_5$ bulk.[177] The model is also applicable to the sorption kinetics of Mg-MgH_2.[190] Here, the geometry is a function of time changed. Yet, the principles of the model can be transferred, e.g. pressure dependence. The model sheds also light on the functioning of additives in MgH_2, which are found to enhance the surface properties also for a 'diffusion-limited' kinetics.[177]

Can we make use of these findings, to e.g. optimize hydrogen storage materials? One interesting fact is that a change of many parameters (except E_1 and D) improving ab- or desorption can worsen the reversed reaction. One example described by Pasturel et al.[171] is the increase of the solubility of the diffusion layer, which improves desorption, but drastically worsens absorption. The same holds for the surface coverage, in the presented model described by the parameters a and b.

The present model is applicable to the sorption kinetics of 'classical' metal hydrides, which is mainly determined by dissociation and diffusion of hydrogen. In complex hydrides, additional elementary steps have to be included. Still, there is experimental evidence that also their thermodynamics and kinetics are strongly interdependent.[191,192] We are planning to extend our model to include these cases.

4.6.3 Thermodynamics

Pressure–optical-transmission–isotherms are recorded for all compositions *simultaneously*. We are thus able to compare the relative stability of the different hydrides forming in the $Mg_yNi_{1-y}H_x$ layer at different composition. While MgH_2 forms first, at higher pressures the plateau corresponding to the Mg_2NiH_4 complex hydride formation is visible. Ni- and Mg-doping slightly increases the equilibrium pressure of Mg_2NiH_4, the lowest p_{eq} being found close to the stoichiometry ($y \simeq 0.7$). The compositional dependence of the enthalpy is derived from Van 't Hoff plots measured between 295 and 363 K. The enthalpy values, though approximately constant within most of the measured compositional range, diverge strongly for compositions close to the eutectic ($0.8 < y < 0.88$). Although a destabilization with increasing Mg content is predicted by density functional calculations, the sharp divergence close to a major microstructural change at the eutectic indicates that the interfacial energy stored in the Mg_2Ni and Mg phases boundaries might contribute to the total hydrogenation enthalpy.

This joint kinetics and thermodynamics study draws a comprehensive picture of the hydrogenation of $Mg_yNi_{1-y}H_x$ gradient thin films. This study shows that multi-phase hydride systems containing complex hydrides with low or no crystallinity can by effectively addressed, and their kinetics and thermodynamcis measured using the all-optical Hydrogenography approach. This should be especially useful in the future characterization of light-weight alanates and boranates thin films.

Chapter 5

The ternary $Mg_yTi_{1-y}H_x$ system

5.1 Introduction

Recently, Notten and coworkers[99,193] reported on the excellent hydrogen storage capacity of Mg-Ti-H thin films which is approximately 5 times larger than that of conventional metal hydride electrodes in NiMH-batteries. Rather surprisingly, the same material has also remarkable optical properties.[100] While metallic in the as-deposited state (high optical reflectance and very low optical transmittance), the films become highly absorbing (low reflectance and transmittance) upon hydrogen uptake. The high degree of mixing between Mg and Ti in sputtered films is directly responsible, via a lowering of the plasma frequency,[194] for this unusual "black" optical state. For example, fully hydrogenated $Mg_{0.80}Ti_{0.20}H_{\sim1.7}$ (5.5 wt.% H) thin films combine a high absorption (87% of the solar spectrum) with a low thermal emissivity (only 10%), while after removal of hydrogen $Mg_{0.80}Ti_{0.20}$ absorbs no more than 1/3 of the solar spectrum. The energy conversion performance of fully hydrogenated $Mg_{0.80}Ti_{0.20}H_{\sim1.7}$ is comparable to those of advanced solar coatings such as ceramic-metal composite materials.[195] Mg-Ti-H however has the great advantage of being switchable. The switching between the two optical states is fast, robust and reversible. The combination of these properties highlights the applicability of Mg-Ti-H thin films as switchable smart coatings for solar collector applications.[100,196] Moreover, the fast switching together with the high optical contrast between the reflective and absorbing states makes Mg-Ti-H films also interesting for hydrogen sensor applications.[196,197]

One of the most surprising properties of Mg-Ti-H films is their structural stability. Mg and Ti are considered as immiscible, as their enthalpy of mixing is positive ($\Delta H_{mix} > 30$ kJ/g atom)[198] and the binary phase diagram of Mg with Ti indicates that no stable bulk compounds are formed (see Fig. 5.1). However, alloying of Mg and Ti does take place in mechanically alloyed bulk samples,[199,200] in physical vapor deposition,[201] e-beam deposition,[99,193] and sputtering of thin films.[65,100,202] On the other hand, the only Mg-Ti-H phase identified so far is Mg_7TiH_x, obtained in bulk alloys by Kyoi et al.[203] This

phase was synthesized in a high-pressure anvil cell by compressing a mixture of MgH_2 and $TiH_{1.9}$ at 8 GPa and 873 K. However, no Mg_7Ti phase was left after high temperature dehydrogenation.
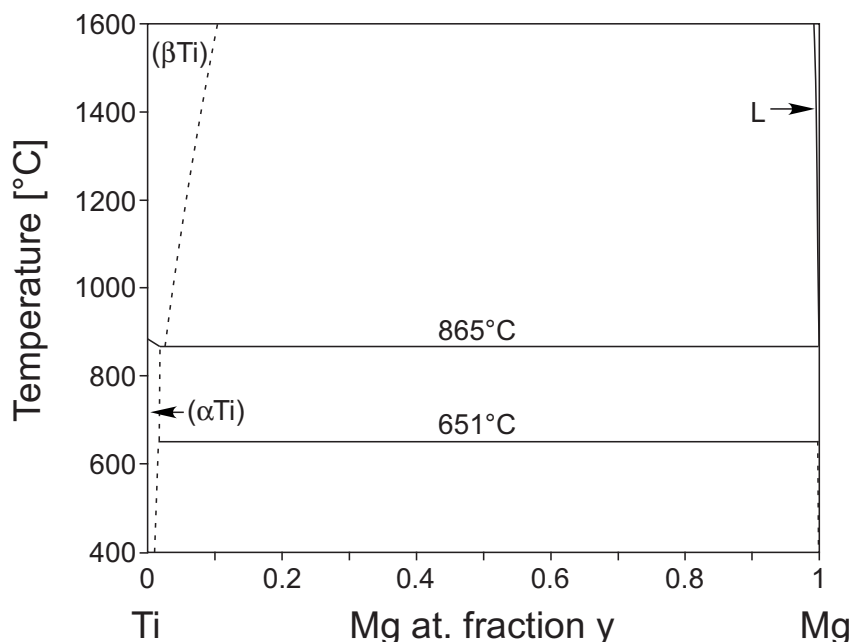
Figure 5.1: Bulk Mg-Ti phase diagram.[127]

In Sec. 5.3 we investigate the structural properties of $Mg_yTi_{1-y}H_x$ thin films obtained by co-sputtering of Mg and Ti at room temperature. Quite remarkably, the crystallinity and coherence of the films is preserved during hydrogenation at all intermediate steps. While the optical properties vary continuously with metal composition,[65] the structure is rutile MgH_2 for high Mg content compositions (y>0.87) and fluorite otherwise. Combining conventional X-ray diffraction with the local probe Extended X-Ray Absorption Fine Structure (EXAFS) technique[44] we find that $Mg_yTi_{1-y}H_x$ is a system made of coherently coupled MgH_x/TiH_x grains.

The optical change in optical transmission upon hydrogen absorption makes $Mg_yTi_{1-y}H_x$ thin films also ideally suited for hydrogenography. The pressure–*optical-transmission*–isotherms (PTI), enthalpy, and entropy for hydrogen absorption are presented in Sec. 5.4. Furthermore, the simultaneous measurement of more than 500 compositions under the same conditions over a wide range of temperatures yields data of unprecedented quality to study correlations between enthalpy and entropy.

In general, understanding the degree of mixing achievable in immiscible systems is of considerable scientific and technological interest.[204–207] In particular, the fact that reproducible and reversible switching from metal to hydride

without noticeable segregation of the metal constituents occurs in $Mg_yTi_{1-y}H_x$ thin films makes it an even more fascinating model system to study. As already pointed out, $Mg_yTi_{1-y}H_x$ films are structurally coherent at the XRD scale but locally partially chemically segregated. It is thus of interest to probe how much and on what spatial scale decomposition has occurred. To characterize their overall degree of chemical segregation as a function of composition y we use the chemical short-range order (CSRO) parameter defined as:[208]

$$s = 1 - \frac{N_{BA}}{Ny} \tag{5.1}$$

for a A_yB_{1-y} system where N_{BA} is the nearest neighbor coordination number of A atoms around a B atom (here A=Mg, B=Ti), N is the total coordination number in the nearest neighbor shell, and y is the atomic fraction of A. Positive, zero, and negative CSRO parameters indicate clustered, random, and ordered spatial distributions of atoms, respectively. In Sec. 5.5, we show that, through the modeling of hydrogenography PTIs, hydrogen can be used as a probe to track the degree of chemical segregation in an immiscible system. The formation enthalpy of bulk TiH_2 (ΔH = -130 kJ (mol H_2)$^{-1}$) is almost twice as negative as the one of bulk MgH_2 (ΔH = -76 kJ (mol H_2)$^{-1}$).[67] In a fully segregated sample, one would therefore expect Ti to form a hydride at lower pressures than Mg in the film, resulting in two well-defined plateaus in the PTIs. However, both PTIs[209] and electrochemical isotherms[193] of $Mg_yTi_{1-y}H_x$ thin films present an unusual shape that is not compatible with a sequential formation of TiH_2 and MgH_2.

To understand this unusual hydrogenation, we develop a multi-site lattice gas model for optical isotherms and apply it on PTIs measured by hydrogenography on $Mg_yTi_{1-y}H_x$ sputtered thin films. The model reproduces the measured PTIs well and allows to derive experimental values of the chemical short-range order parameter (CSRO) s which are in good agreement with the local surrounding of Ti and s values determined by EXAFS.[44] Furthermore, the model gives information on the local lattice's departures from the average lattice given by Vegard's law.

5.2 Experimental

5.2.1 Sample preparation

Mg_yTi_{1-y} thin films are prepared in a 7-gun ultra-high-vacuum dc/rf magnetron co-sputtering system (base pressure 10^{-7} Pa) at room temperature on quartz substrates. Various compositions in the 0.55<y<0.95 range are studied. Typical deposition rates are: 2Å/s for Mg (150 W RF power), 0.1-1Å/s for Ti (25-160 W DC power) and 1.3Å/s for Pd (50 W DC power). For single composition samples, a homogenous composition and thickness over the en-

tire substrate area is ensured by continuously rotating the substrates during sputtering. Mg_yTi_{1-y} thin films with a compositional gradient are prepared on 70 x 5 mm^2 quartz substrates. Mg and Ti are facing each other in tilted off-axis sputtering guns. By adjusting the power applied to each gun the desired compositional region of the binary phase diagram is obtained. The local composition of the gradient films is determined by Rutherford Backscattering Spectrometry on films grown in the same deposition run on amorphous carbon substrates. The Mg atomic fraction y along the length of the sample varies between 0.6 and 0.89. All the films are covered in situ with a Pd layer (5-20 nm) to prevent oxidation of the Mg-Ti film and to promote dissociation of H_2. [1,159]

5.2.2   Data collection

The structural properties of the films are investigated by means of X-ray diffraction (XRD) in a Bruker D8 Discover X-ray diffractometer equipped with a two-dimensional (2D) detector which can perform real-time diffraction data collection over a large area with high speed, high sensitivity and low background. A Be dome allows for *in situ* X-ray measurements upon hydrogenation. XRD patterns are also measured during dehydrogenation (in air, at room temperature). The dehydrogenation time (few minutes for a 50 nm $Mg_{0.70}Ti_{0.30}$/30 nm Pd film) depends on the thickness of the film and can be improved by decreasing the thickness and/or increasing the temperature[98,100]. All the measurements are done using the Cu-Kα radiation (λ=1.5418Å). Additionally, TEM plan-view and cross-sectional images were recorded using a JEOL 2010F electronic microscope working at 200 kV (point resolution 0.23 nm and information limit 0.11 nm). This TEM is also equipped with an Energy Dispersive X-Ray Spectrometer and a Gatan Imaging Filter (GIF 2000). The plan-view samples were obtained by directly depositing the films on silicon nitride membranes (30 nm thick). Hydrogenated samples were prepared using a 1 nm Pd cap layer. Cross-section samples were made by cutting, polishing and ion milling with 4 kV Ar-ions with an Gatan PIPS. To measure the hydrogen content, electrochemical measurements (loading/unloading) are done in a standard three electrode setup containing a Hg/HgO reference electrode and a Pt counter electrode in a 1 M KOH electrolyte. The reflection and the transmission at λ=635 nm (1.95 eV) can be measured simultaneously in the electrochemical setup. [210,211]

For hydrogenography measurements, the as-deposited, metallic films are transferred into an optical cell to monitor their optical transmission during hydrogenation. [144] The whole cell is placed in an oven to control temperature up to 300 °C. A 150 W diffuse white light source illuminates the sample from the substrate side, and a 3-channel (RGB) SONY XC-003 charged-coupled device (CCD) camera continuously monitors the transmitted light as a function of

hydrogen pressure. The 3-channel transmission intensities are added, resulting in a 1.1 to 3.3 eV photon energy bandwidth.

For the determination of optical absorption coefficients, spectrophotometric reflection and transmission measurements of Mg and Ti in the metallic and hydrogenated states are performed in a Perkin Elmer Lambda 900 diffraction grating spectrometer with an energy range from 0.495 to 6.19 eV (wavelength $\lambda = 2500$ - 200 nm).

5.3 Structural properties

Structural data obtained from X-ray diffraction measurements are summarized in Figs. 5.2 to 5.4. X-ray $\theta - 2\theta$ scans measured on $y=0.70$ and $y=0.90$ samples are shown in Fig. 5.2. Here we compare spectra corresponding to the as-prepared (initial), fully hydrogenated (at room temperature in 1 bar H_2) and dehydrogenated (after exposure to air) state.

In the XRD spectra there are reflections from the Mg-Ti layer and the Pd cap layer. The peak at $\sim 40.1°$ corresponds to the (111) reflection of Pd. Upon hydrogenation, the peak shifts to lower scattering angles, indicating thus the formation of PdH_x. The reflection of Pd is absent for samples with a composition $y = 0.90$, even though the presence of Pd was confirmed by RBS. A similar result was obtained for e-beam deposited Mg-Ti films[99] or pure Mg films.[128] Therefore, on Mg rich surfaces, the Pd appears not to have a preferential orientation, which is necessary for these thin films to produce an XRD reflection. Very likely, this is related to the morphology of the Mg-Ti and Mg layers.

For as-prepared $y=0.70$ and $y=0.90$ samples, (Fig.5.2) there is only one reflection peak that is assigned to the Mg-Ti layer. The 2θ position of this peak depends on the Mg/Ti ratio and is between the (002) reflection of Mg ($2\theta = 34.4°$; hexagonal structure) and the (002) reflection of Ti ($2\theta = 38.52°$; hexagonal structure). This suggests the formation of a Mg-Ti random alloy on deposition with the same hexagonal symmetry as the metal constituents. The formation of a random alloy is however, highly unlikely given the large positive enthalpy of mixing calculated for such an alloy (> 20 kJ/mol[198]). Instead we argue that in fact a coherently coupled mixture of Mg and Ti is formed. The hexagonal symmetry is confirmed by additional TEM plan-view measurements. A typical result measured on a 50 nm $Mg_{0.70}Ti_{0.30}$/5 nm Pd film is shown in Fig.5.5(a). The reflections from the Pd cap layer (diffuse rings due to very small crystallites in the order of 5 nm) can easily be distinguished from those of the Mg_yTi_{1-y} film (well defined rings with individual spots due to crystallites in the order of 50 nm). The reflections from the film are consistent with a $P6_3/mmc$ structure (the same as for Mg and Ti) with lattice spacings ($a = 3.11$ Å, $c = 4.98$ Å) in close agreement with the XRD results.

After hydrogenation, we find a reflection at $2\theta=28.1°$ for the $y = 0.90$
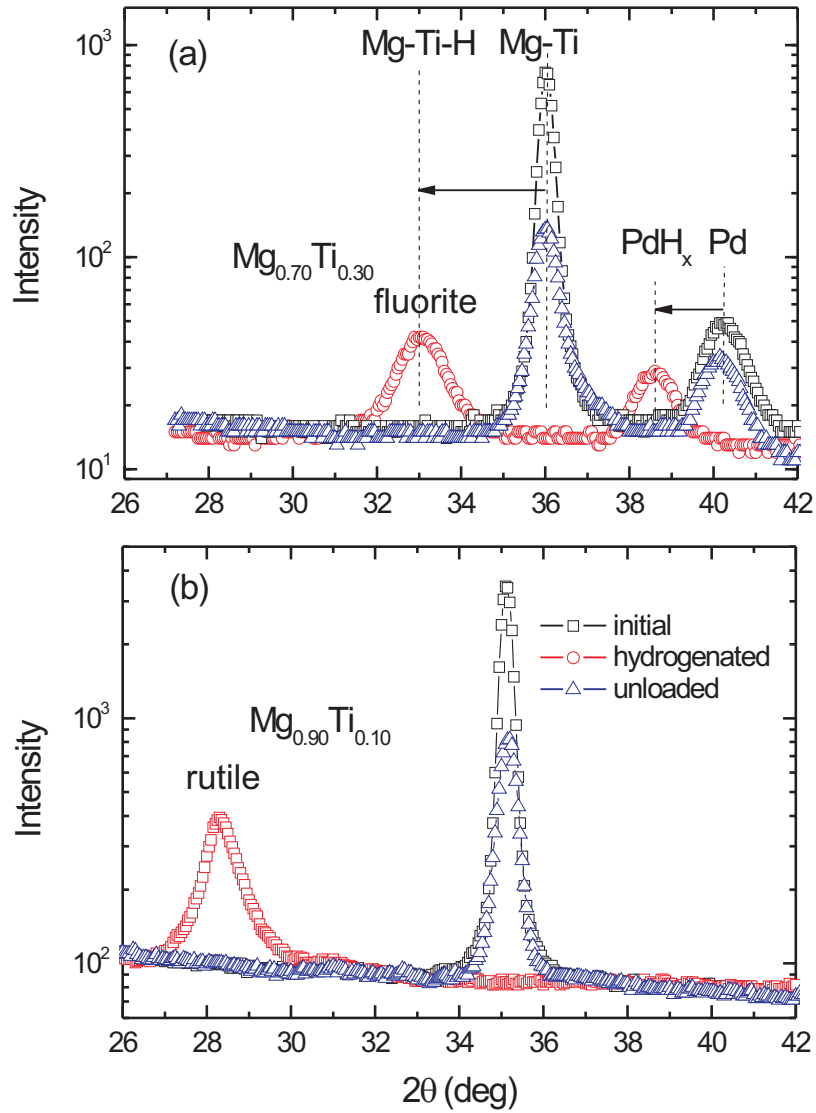
Figure 5.2: $\theta-2\theta$ X-ray diffraction spectra measured on 200 nm $Mg_yTi_{1-y}/10$ nm Pd films ((a) y=0.70, and (b) y=0.90) in the as-prepared (initial), fully hydrogenated (at room temperature in 1 bar H_2) and fully dehydrogenated states.
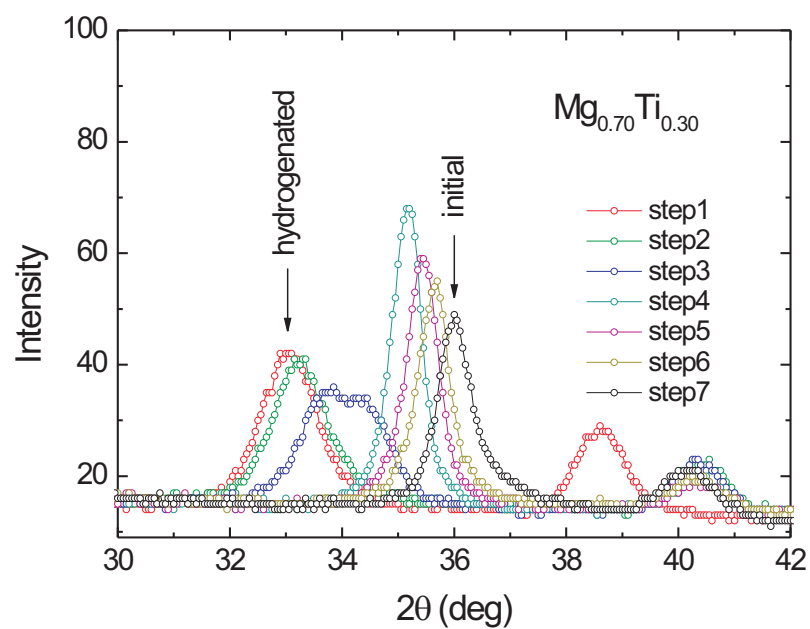
Figure 5.3: Intermediate $\theta - 2\theta$ X-ray patterns during dehydrogenation measured on a $y = 0.70$ sample.
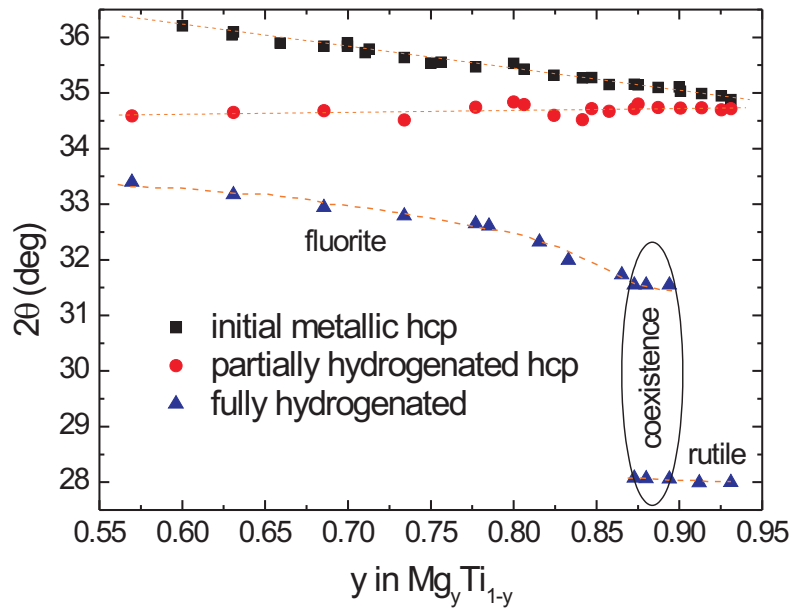
Figure 5.4:   Compositional dependence of 2θ measured with XRD on a Mg_yTi_{1-y} gradient thin films with $0.55<y<0.95$. Peak positions corresponding to as-prepared (initial hcp), intermediate partially hydrogenated hcp and final hydrogenated states (fcc or rutile) are shown.
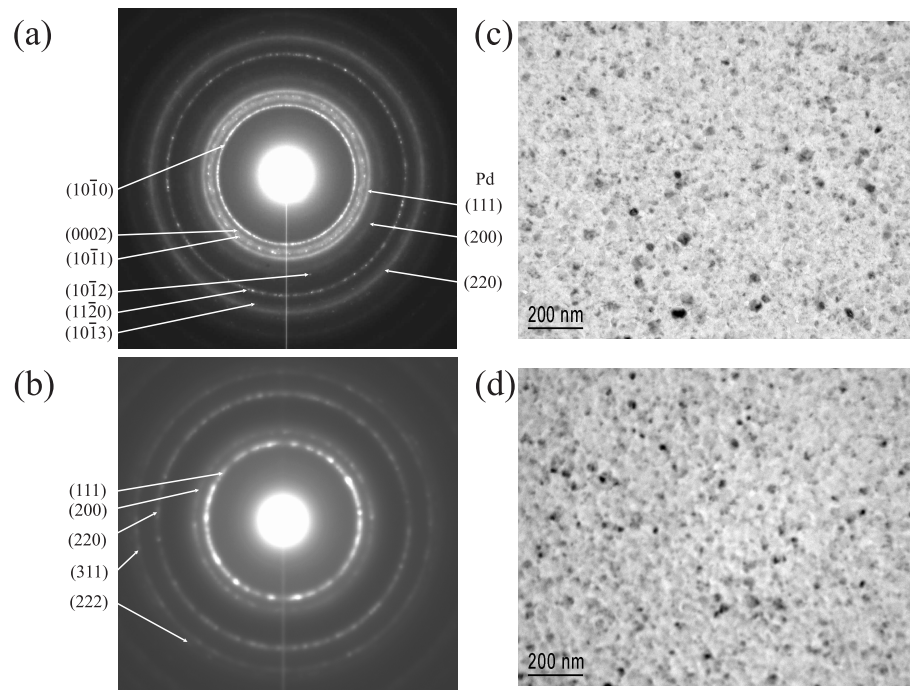
Figure 5.5: Selected area electron diffraction patterns: (a) of a $Mg_{0.70}Ti_{0.30}/$ 5 nm Pd thin film and (b) of a $Mg_{0.70}Ti_{0.30}H_x/$ 1 nm Pd thin film. Arrows identify reflections from the film (Mg-Ti or Mg-Ti-H) and the Pd cap layer (only visible in (a); in (b) the layer is too thin). The corresponding TEM plan-view images of the film surface are shown in (c) and (d).

sample whereas for the $y = 0.70$ sample the hydride peak appears at $2\theta=32.8°$. The difference in peak position suggests a difference in structure of the hydride phase. The peak at $2\theta=28.1°$ we can clearly identify as the (110) reflection of a rutile MgH_2 phase ($2\theta=27.91°$ for pure MgH_2). The small shift can be due either to small Ti doping in MgH_2 or strain in the thin film. On the other hand, the peak at $2\theta \approx 32.8°$ is more difficult to identify. We assume this hydride to have fcc symmetry ("fluorite" phase) as its peak position is close to the (111) reflection of fcc TiH_2 and almost coincides with high-pressure fcc MgH_2.[212] Assuming a fluorite phase, the corresponding lattice spacing is $a = 4.729$ Å. TEM plan-view measurements on hydrogenated $Mg_{0.70}Ti_{0.30}$ films confirm the fcc symmetry (where the (111), (200), (220), (311) and (222) reflections can be identified) and indicate a structural homogeneity at least on a scale above 20 nm (Fig.5.5(b)). The lattice spacing obtained from these measurements is $a = 4.55$ Å. This value is slightly lower than the data obtained from XRD on similar compositions, indicating a partial dehydrogenation due to electron beam bombardment during the TEM measurements.

The reflection at $2\theta \approx 32.8°$ is also close to the 222 reflection reported for the Mg_7TiH_x phase[203] (Ca_7Ge type structure; $a = 9.532$ Å) synthesized in a high-pressure anvil cell by mixing MgH_2 and $TiH_{1.9}$ at 8GPa and 873 K. The structure of this phase was argued to be similar with that of $TiH_{1.9}$ (fcc) but with most of the Ti atoms substituted by Mg in an ordered way, resulting in a superstructure with a doubled unit cell.

As shown in Fig. 5.2 (a) and (b), after full dehydrogenation, the peak shifts back to its initial position which is evidence for the structural reversibility of the system and the absence of phase segregation. This is a surprising result since hydrogen cycling in other Mg-based systems is in general accompanied by a large scale phase segregation.[128,213,214] Also remarkable is the fact that the films remain crystalline during hydrogenation and subsequent dehydrogenation. However, the crystallinity of the films decreases upon hydrogen cycling. This has however little effect on the switching time and the optical response[98,100] and therefore we conclude no major structural changes to take place apart from a reduction in grain size.

To understand the structural transformations and their composition dependence we performed XRD measurements at intermediate stages during hydrogenation (dehydrogenation) on homogeneous samples and also on a Mg_yTi_{1-y} gradient sample with $0.55 < y < 0.95$. In Fig.5.4 we have summarized results as measured on the gradient sample. We find that the position of the Mg-Ti peak varies linearly with Mg/Ti ratio (Fig.5.4) for the entire composition range. This is in accordance with Vegard's law.[215] A small reflection from Ti is only found for $y < 0.65$ compositions but no signs of crystalline Mg is present for all $0.55 < y < 0.95$ compositions. The XRD data suggest that the alloy retains the hexagonal symmetry which was confirmed by TEM plan-view measurements on one composition. The results in Fig. 5.4 suggest three distinct
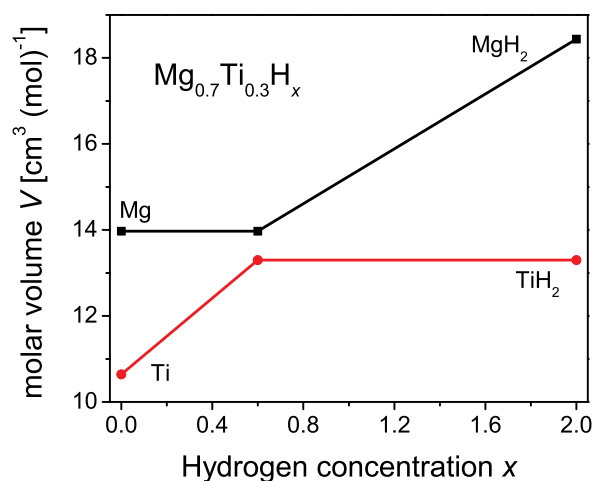
Figure 5.6: Schematic representation of the partial molar volume change of the Mg and Ti fractions of a $Mg_{0.7}Ti_{0.3}$ alloy during hydrogenation. The similarity of the Mg and TiH_2 molar volumes increases the coherency of the alloy at intermediate stages and most probably helps to prevent segregation. Note that this representation is oversimplified as it does not take into account the elastic coupling between MgH_x and TiH_x grains (See Sec.).

structural regimes for the hydrogenated state as a function of composition: (I) single phase fluorite for $y < 0.87$, (II) single phase rutile for $y > 0.90$ and (III) two phase coexistence for $0.87 < y < 0.90$. Within the fluorite regime, the structure varies continuously with composition. At intermediate compositions, coexistence of both phases is found. For all compositions, the FWHM indicates very small crystallites in the order of 10-20 nm. As shown in Fig. 5.3, for a $y = 0.70$ sample, the transformation between the initial and the hydrogenated state is almost continuous and fully reversible. The intermediate steps shown here are measured during H-desorption. Assuming an hcp structure in the as-prepared state and fcc structure in the final state, the intermediate steps should reveal an hcp-fcc phase transformation. Upon H uptake, first the lattice expands continuously (step 4-7). We define as the solid solution state, the whole range of 2θ values which are attained continuously starting from the metallic state. At intermediate hydrogen concentrations (step 3), the double-peak structure of the XRD spectrum points to coexistence of two phases: an fcc phase and an hcp phase. Subsequent H-uptake leads to a further expansion of the fcc phase.

Similar intermediate steps can be defined for all compositions in the $0.55 < y < 0.95$ range. Interestingly, the minimum 2θ angle in the metal solid solution phase is the same for all compositions and corresponds to the scattering angle

of both TiH_2 (111 reflection) and Mg (002 reflection). This results suggests strongly a hydrogenation sequence where hydrogen occupies first Ti-related sites in the Mg-Ti lattice. An indication in favor of this scenario is also the increase in peak intensity in the beginning of the hydrogenation process. The lattice expands and becomes more ordered since the molar volume of TiH_2 (13.3 cm^3) is similar to that of pure Mg (13.97 cm^3, see Fig. 5.6).

5.3.1 Discussion

As suggested in the previous section, the formation of a fully random Mg-Ti alloy on deposition is very unlikely given the large positive enthalpy of mixing. Upon hydrogenation, clear structural indications of a rutile MgH_2 phase are found only for Mg-rich compositions ($y > 0.87$). For $y < 0.87$ compositions, in the hydride state, the XRD data point to a structure with cubic symmetry and a lattice parameter that varies continuously with metal composition in the parent alloy. The occurrence of a single Bragg reflection, both in the metallic and hydride states, is not sufficient to prove the alloy formation on an atomic scale[216,217] but it reflects the coherency of the lattice. The reversibility of the hydrogenation process suggests that this coherency remains intact on cycling. The optical and electrical data on fully hydrogenated films suggest the presence of an insulating MgH_2-like phase for all metal alloy compositions. [65] Besides the insulating component, a second phase with a metallic character should be present to account for the highly absorbing state. For example, for a $y = 0.70$ sample, the volume fraction of the insulating component derived from a Bruggemann approximation is $\sim 75\%$,[65] corresponding thus to hydrogenation of the entire Mg fraction in the metal alloy. In a Mg_yTi_{1-y} homogeneous random alloy, the fraction of Mg_4 clusters (equal to y^4 assuming a binomial distribution) is only $\sim 24\%$, much lower than what is needed to explain the optical and electrical properties.[65] This suggests the presence of a certain degree of chemical segregation in the system. However, on the basis of XRD data, large scale segregation is excluded. The hydride would then consist of partially segregated MgH_x and TiH_x nanosized domains within large structurally coherent grains.

In order to probe local chemical segregation, standard X-Ray diffraction techniques are not sufficient: nanometer scale deviations from a random solid solution would also produce a Vegard's law dependence, provided that the coherency is maintained.[204] Such deviations can arise because of incipient phase separation during the synthesis of the alloy. Local probe techniques such as EXAFS are thus needed to characterize precisely the local atomic ordering. Figure 5.7 shows the EXAFS Fourier transformed signal for 3 Mg_yTi_{1-y} compositions, in the as-deposited and dehydrogenated states, together with the fitted s values.[44] EXAFS data show that Mg_yTi_{1-y} thin films do not form random solid solutions and that a certain degree of atoms rearrangement is
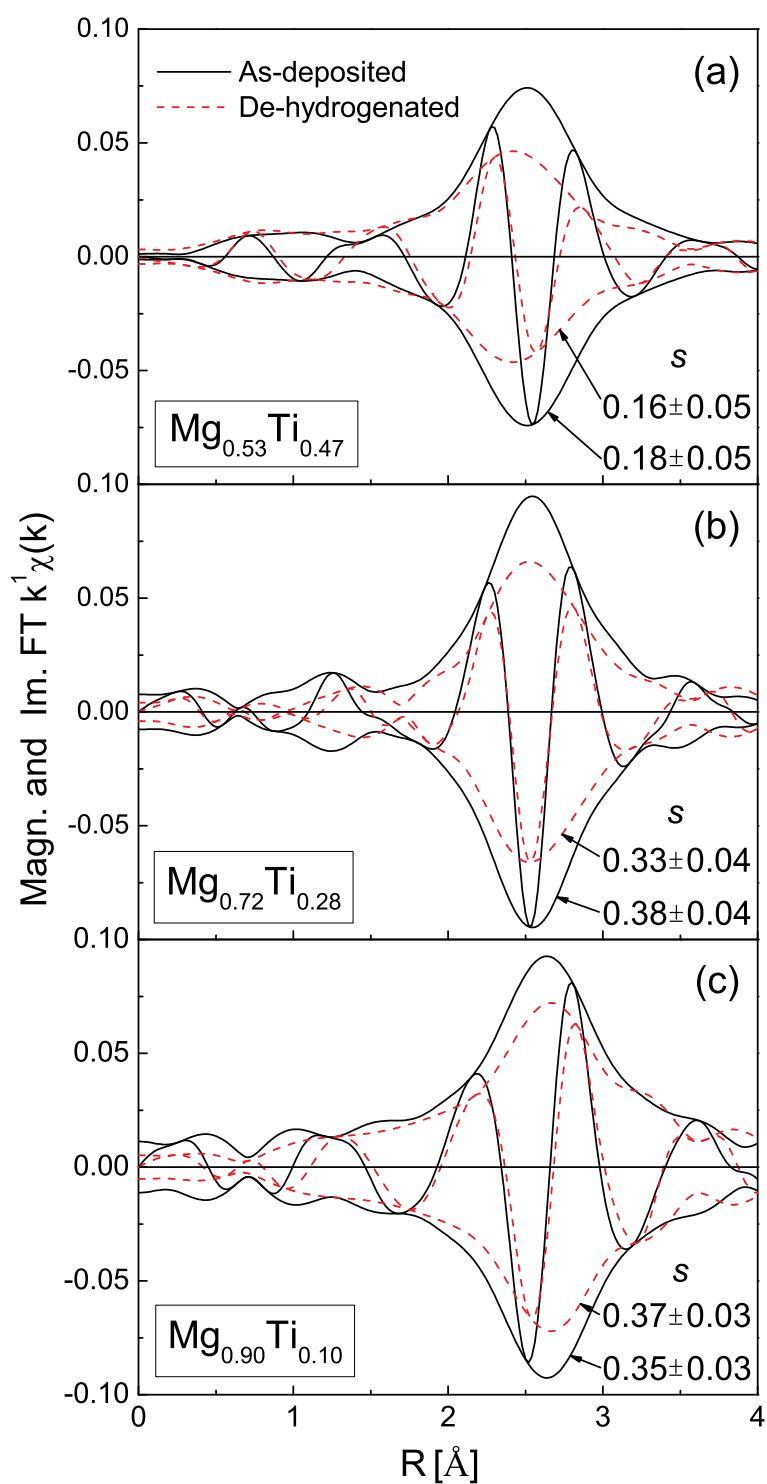
Figure 5.7: EXAFS measurements: magnitude and imaginary part of the phase-uncorrected Fourier transformed $\chi(k)$ for $Mg_{0.53}Ti_{0.47}$, $Mg_{0.72}Ti_{0.28}$ and $Mg_{0.90}Ti_{0.10}$ both in the as-deposited (solid line) and de-hydrogenated (dashed line) states. The numerical values indicate the fitted chemical short-range order parameters s.

already present in the as-deposited films. The slight differences between the
two metallic states (before and after hydrogenation) are mainly due to small
changes in the coordination numbers and to an increase upon cycling of the
Debye-Waller factors for the Ti-Ti shells. As already observed by XRD, hy-
drogen cycling gradually reduces the crystallinity of the samples. This reduces
the magnitude of the EXAFS signal for the dehydrogenated samples.

From XRD and EXAFS we conclude that the $Mg_yTi_{1-y}H_x$ films with
$y < 0.87$ are neither single phase nor completely phase separated. Instead,
the material is a composite of Mg and Ti (in the metallic state) and insulat-
ing MgH_2 and metallic TiH_2 (in the hydrogenated state) regions that form
a coherent crystalline structure. This conclusion is consistent with a hydro-
genation sequence where hydrogen occupies first Ti-related sites. A schematic
representation of a coherent crystalline grain consisting of a Mg and Ti region
is shown in Fig.5.8(a). The local deformation is only schematic and might
deviate from reality. The same crystalline grain after hydrogen uptake in the
Ti-related sites and in the fully hydrogenation state is shown in Fig.5.8(b) and
Fig.5.8(c), respectively. This peculiar hydrogenation sequence is related to the
more negative enthalpy of formation of TiH_2 (-130 kJ$(molH^2)^{-1}$) as compared
to MgH_2 (-76 kJ$(molH^2)^{-1}$).[67] Very likely, hydrogenation of Ti-related sites
in the beginning of the hydrogenation process reduces the mobility of atoms
during further hydrogen uptake and thus prevents the large scale segregation,
observed in many other Mg-based systems. Finally, it is quite remarkable that
in $Mg_yTi_{1-y}H_x$, the coherent structure is preserved at all intermediate states
during hydrogenation. This is likely to be related to the similarities in molar
volume between Mg and TiH_2 (see Fig. 5.6).

With a coherent mixture of the MgH_2 and TiH_2 hydrides, the structural
data for $y < 0.87$ compositions can be understood by assuming that both com-
ponents have a cubic structure. This is expected for TiH_2. On the other hand,
at normal pressured and temperatures, MgH_2 crystallizes in a rutile structure.
A cubic MgH_2 phase was reported to be formed only at high pressures (4GPa).
[212] The theoretical calculations of Vajeeston[218] confirm a similar cubic phase as
being the most stable structure if the unit-cell volume is reduced to 27.5 Å/f.u
(equivalent to a=4.79 Å). The formation of a cubic MgH_2 phase in our thin
films, at normal pressures and temperatures is not entirely clear. Very likely,
it is related to the coherent coupling to Ti/TiH_2 and the local stress induced.
Using the pressure vs volume dependence calculated by Vajeeston,[218] the lat-
tice constant of cubic MgH_2 at normal pressures should be $a(MgH_2)$=4.839 Å.
With this value, the average lattice spacing of fully hydrogenated Mg_yTi_{1-y}
films with $y < 0.80$ is well reproduced by the weighted average of the two
components, as follows:

$$a_{Mg_yTi_{1-y}H_x} = ya_{MgH_2} + (1-y)a_{TiH_2} \qquad (5.2)$$

Then, on average, the hydrogen-to-metal ratio of the crystalline coherent struc-
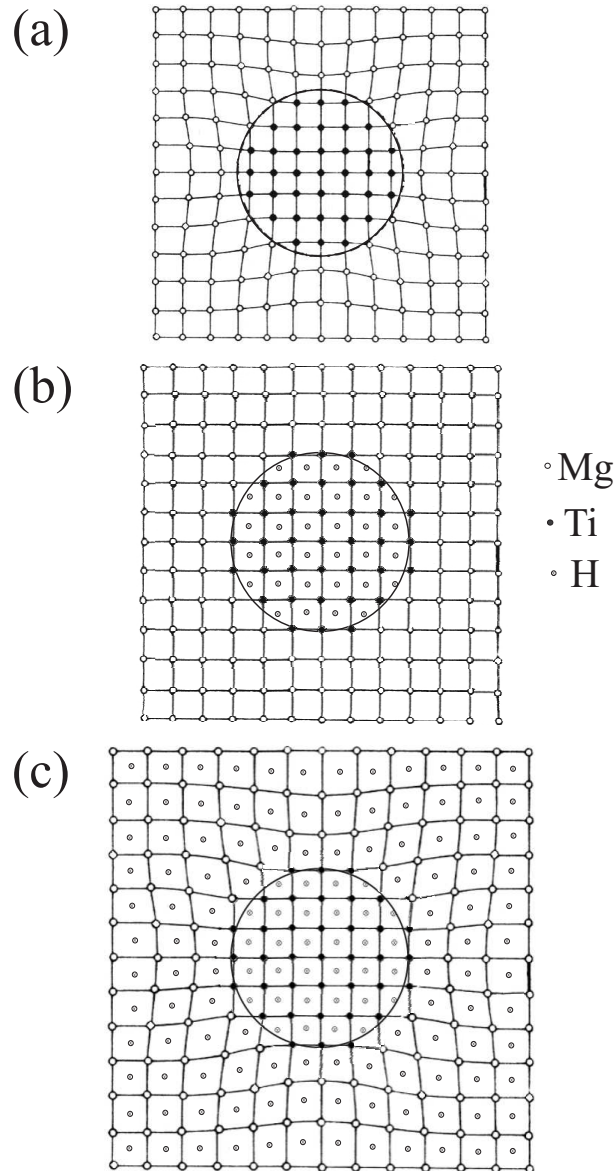
Figure 5.8: (a) Schematic representation of a coherent crystalline grain consisting of a Mg and Ti region; (b) the same crystalline grain after hydrogen uptake in the Ti-related sites; (c) full hydrogenation state. The accidental equality of the molar volumes of TiH_2 and Mg leads to an almost perfect crystal in situation (b). Note that this is an extreme case chosen to illustrate the idea of an elastically coherent lattice with chemical segregation. As developed in Sec. 5.5, in real Mg_yTi_{1-y} films the situation is clearly more complicated.

ture is 2. This value corresponds to a higher hydrogen content than what we measured electrochemically ([H]/[M]=1.55, see Sec. 5.4), and therefore supports the conclusion that an X-ray amorphous component is present which reacts only partly with hydrogen. Since the optical data suggest a high fraction of insulating material, part of this amorphous component must be insulating with properties similar to that of MgH_2. The rest is likely to remain metallic as unreacted or partially oxidized Mg and Ti. Very likely, this amorphous component does not play an active role in maintaining the coherency of the system.

5.4 Hydrogenography

5.4.1 Dependence of the optical properties on the H concentration

The hydrogen concentration dependence of the optical properties can be obtained from measurements in an optical-electrochemical cell. In this case, reflection and transmission at 1.95 eV are measured simultaneously with the hydrogen content. The results obtained for a 100 nm $Mg_{0.70}Ti_{0.30}$/10 nm Pd film in a constant current mode ($I=-133.3$ μA/cm^2) are shown in Fig. 5.9. The total amount of hydrogen that can be incorporated is [H]/[M]$\sim$1.55. This value is below the theoretical limit of [H]/[M]=2 expected for an alloy of two metals forming the dihydrides TiH_2 and MgH_2. Our results are in agreement with the results of Vermeulen et al.[202] measured on e-beam deposited thin films. They moreover showed that the H-content in the fully hydrogenated state decreases with increasing the amount of Ti for all alloy compositions measured. With increasing amount of hydrogen in the sample, the reflection decreases while the transmission increases gradually. Such a behavior is typical for a homogeneous nucleation and growth of a hydride phase within the whole volume of the sample as was observed in Mg-MgH$_2$ thin films[128]. For [H]/[M]<0.5 (dashed line in Fig.5.9), the measured transmission falls below the detection limit of the instrument. Above [H]/[M]>0.5, the logarithm of the transmission increases linearly as expected from Lambert-Beer's law. The fact that Lambert-Beer's law applies has a capital implication for Hydrogenography: It makes possible the recording of pressure–*optical transmission*–isotherms (PTI) that are therefore fully analogous to pressure-concentration-isotherms (PCI) obtained with standard volumetric or gravimetric methods.[182] In PTIs, $\ln(T/T_M)$, the logarithm of the optical transmission T in a film of initial transmission T_M is plotted as a function of the hydrogen pressure.
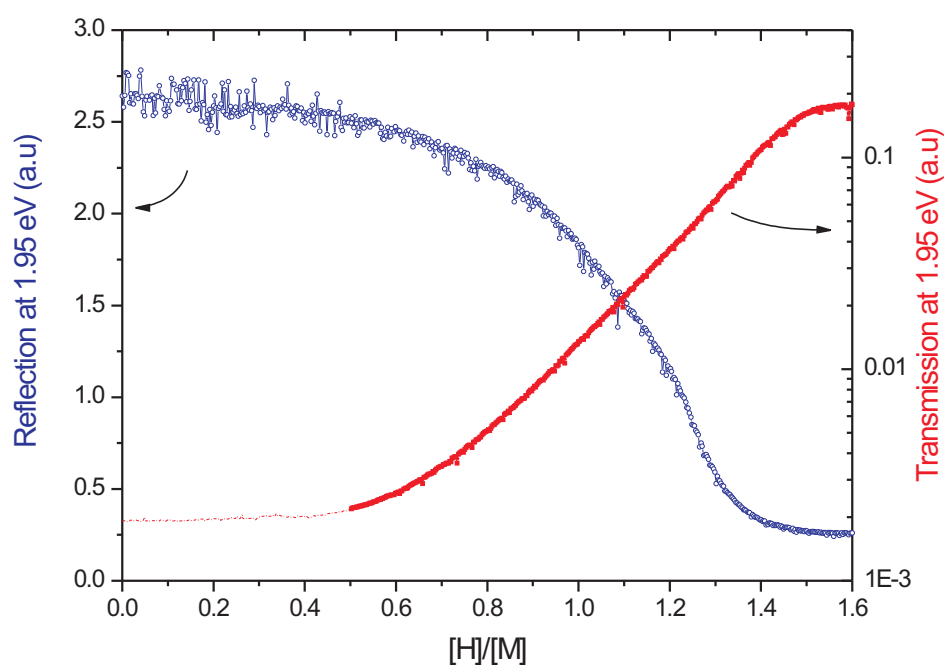
Figure 5.9: Optical reflection and transmission of a 100 nm $Mg_{0.70}Ti_{0.30}$ film capped with 10 nm Pd measured in-situ during galvanostatic loading (current $I=-133.3$ $\mu A/cm^2$). [H]/[M] corresponds to the number of hydrogen atoms per metal atom. In the region indicated by the dashed line, the measured transmission falls below the sensitivity limit of the instrument.

5.4.2   Pressure–optical-transmission–isotherms

We make use of the continuous change of optical transmission with hydrogen concentration to record PTIs for all compositions of the Mg_yTi_{1-y} gradient thin film simultaneously. Figures 5.10 to 5.15 display the isotherms, each figure corresponding to a temperature between 297 K and 433 K. To record isotherms, the hydrogen pressure around the Mg_yTi_{1-y} gradient is slowly increased while the light intensity I going through the sample is monitored continuously. This results in isotherm "maps" of the transmitted light intensity as a function of alloy composition y and H_2 pressure (Figs. 5.10a to 5.15a). The optical transmission $T = I - I_b$ (Eq. 3.4 with $f = 0$) is plotted in (b) for a selection of compositions y. Dashed lines indicate the transmission in the metallic state T_M for each composition. Finally, the PTIs are displayed in (c). For $y > 0.80$, the transmission in the metallic state cannot be distinguished from the thermal background noise of the CCD camera ($I_M \leq I_b$) and therefore the isotherm is not defined in the low transmission range. This explains the truncated isotherms for $y = 0.85$ and 0.89 and the higher noise at $y = 0.80$. Occasional glitches (such as e.g. at $p = 50$ Pa and 297 K) are due to vibrations in the experimental setup. They can, however, be easily isolated as they appear at the same pressure for all compositions y. For all compositions, the optical transmission increases with increasing pressure. Two different regimes can be distinguished:

1. From $y = 0.60$ to $y \simeq 0.85$, starting from low pressures, the transmission first increases gradually, and then a sloping plateau develops at higher pressure. The plateau shifts towards higher pressures and widens with increasing Mg atomic fraction y. Conversely, the gradual transmission increase with pressure is the dominant feature in the isotherms for the Ti-richest compositions ($0.61 \leq y < 0.7$). As checked with pressure-dependent XRD, the gradual increase of transmission with pressure corresponds to the -shifting with pressure- hcp reflection (see Fig. 5.3) while the plateau coincides with hcp $\rightarrow$ fcc transition.

2. From $y \simeq 0.85$ to $y = 0.89$, two plateaus are present in the isotherms. The first plateau, at low pressure, is attributed to the formation of rutile MgH_2, while the upper plateau originates from hydrogenation of the fcc Mg/Ti coherent alloy. The compositional extension in y of the rutile-fcc MgH_2 coexistence region depends on the time spent at high temperature under hydrogen pressure. For example, while no rutile MgH_2 is present for $y = 0.85$ at 363 K (5th hydrogenation cycle, Fig. 5.13), a clear double plateau is visible at the same composition during the 6th hydrogenation cycle at 333 K (Fig. 5.12). This shows that, for high Mg fraction $y \geq 0.85$, the metastable Mg/Ti composite tends to segregate into the more stable rutile MgH_2 and fcc TiH_2 under prolonged annealing

under H_2. This is even clearer at 393 K, where most of the Mg transform into rutile MgH_2 for $y = 0.85$. Compositions $y < 0.85$ are much less prone to segregation, and temperatures as high as 650 K are needed to fully segregate the Mg/Ti composite. Conversely, an effective solution to counteract segregation of rutile MgH_2 is to ramp the pressure faster: H is then absorbed by the Mg/Ti composite before Mg and Ti have time to segregate on a large scale. This is illustrated by the absorption at 433 K (Fig. 5.15). The pressure sweep at this temperature lasts 7200 s, and no evidence for segregation is found (single plateau for all composition), in contrast to the absorption at 393 K that has duration of 65000 s.
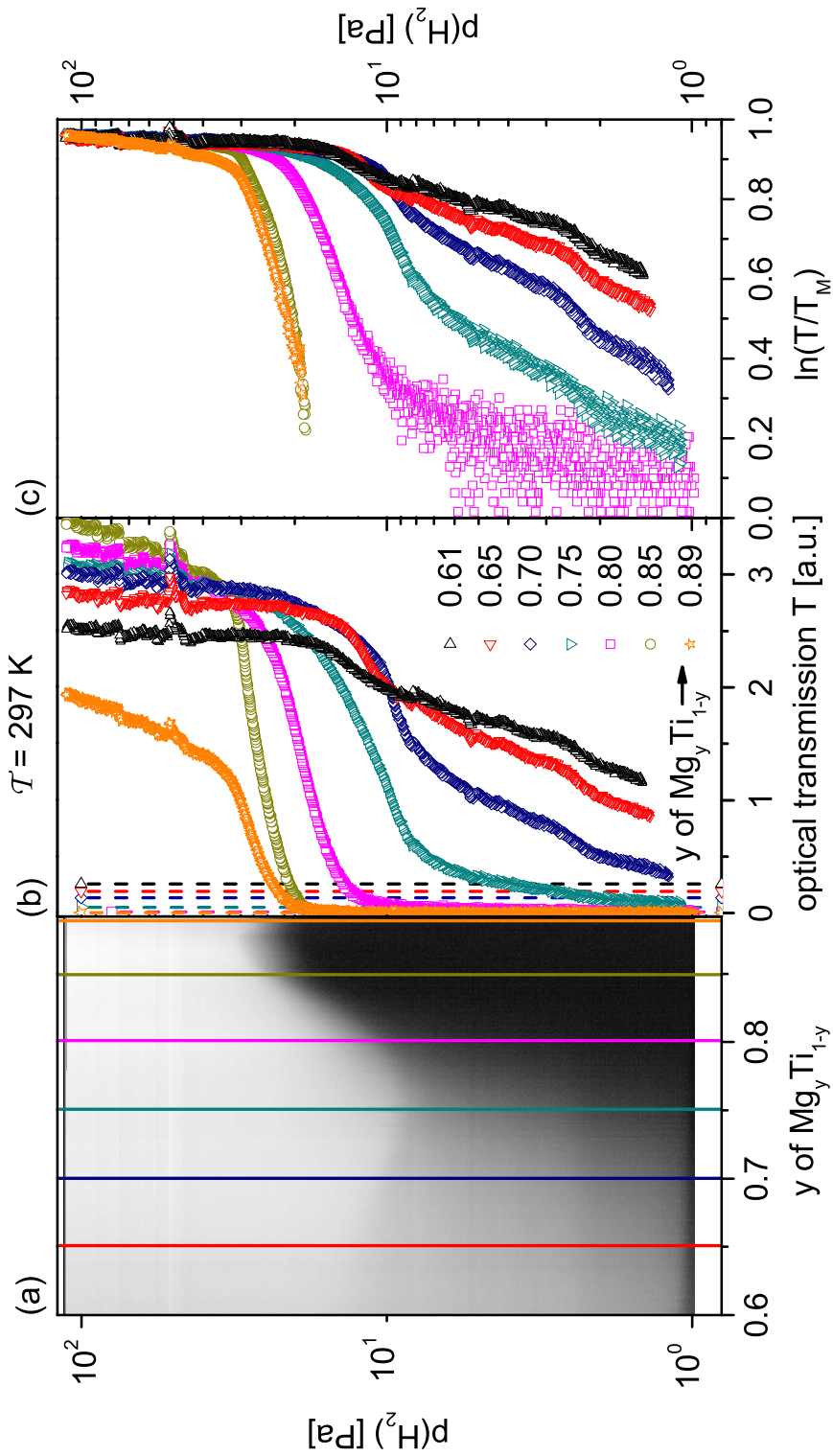
Figure 5.10: PTIs of Mg$_y$Ti$_{1-y}$H$_x$ at $\mathcal{T} = 297$ K. (a) Optical transmission map (black: low transmission, white: high transmission) as a function of Mg fraction y and hydrogen pressure p. (b) Optical transmission T for a selection of compositions y (*vertical lines* in (a)). (c) PTIs (p vs $\ln(T/T_\mathrm{M})$) for the same compositions.
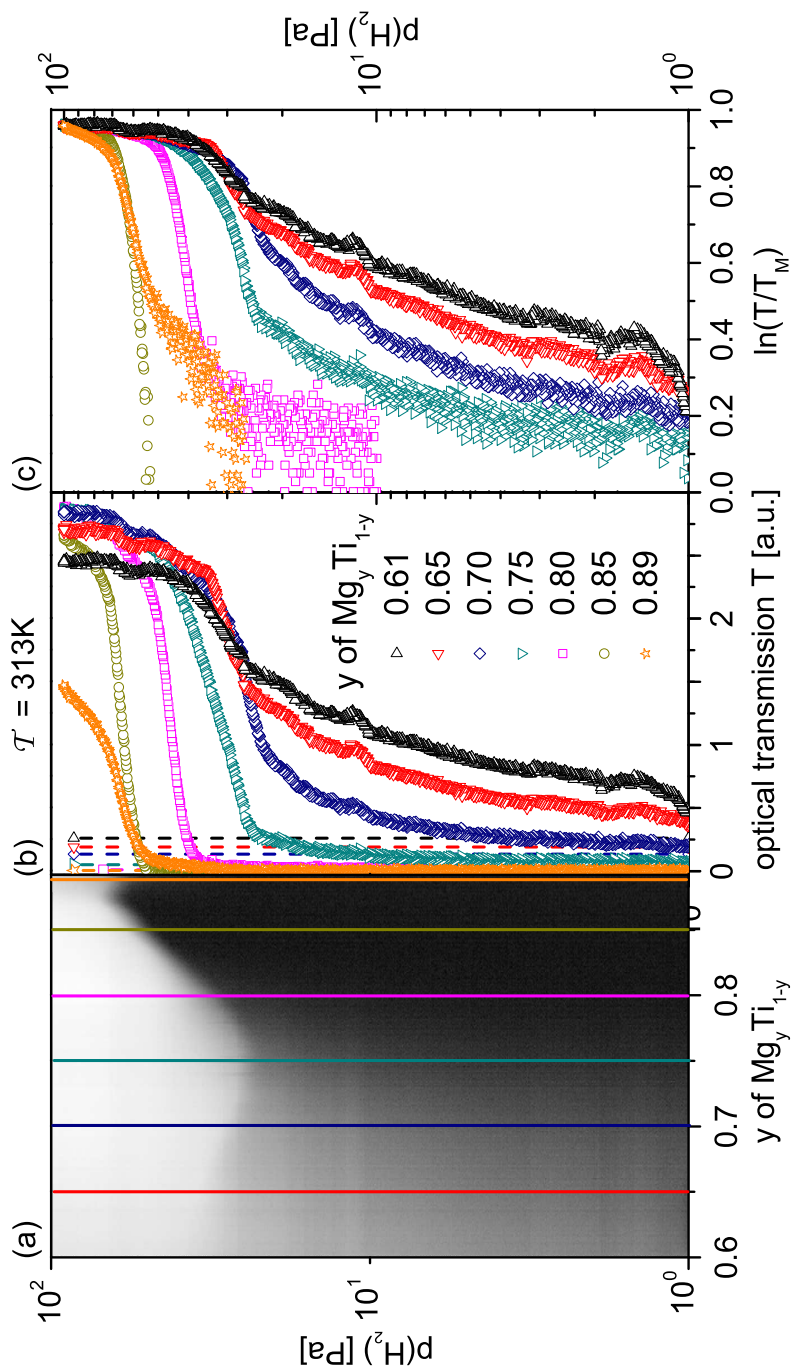
Figure 5.11: PTIs of $Mg_yTi_{1-y}H_x$ at $\mathcal{T} = 313$ K. (a) Optical transmission map (black: low transmission, white: high transmission) as a function of Mg fraction y and hydrogen pressure p. (b) Optical transmission T for a selection of compositions y (vertical lines in (a)). Dashed lines indicate the transmission in the metallic state T_M. (c) PTIs (p vs $\ln(T/T_M)$) for the same compositions.
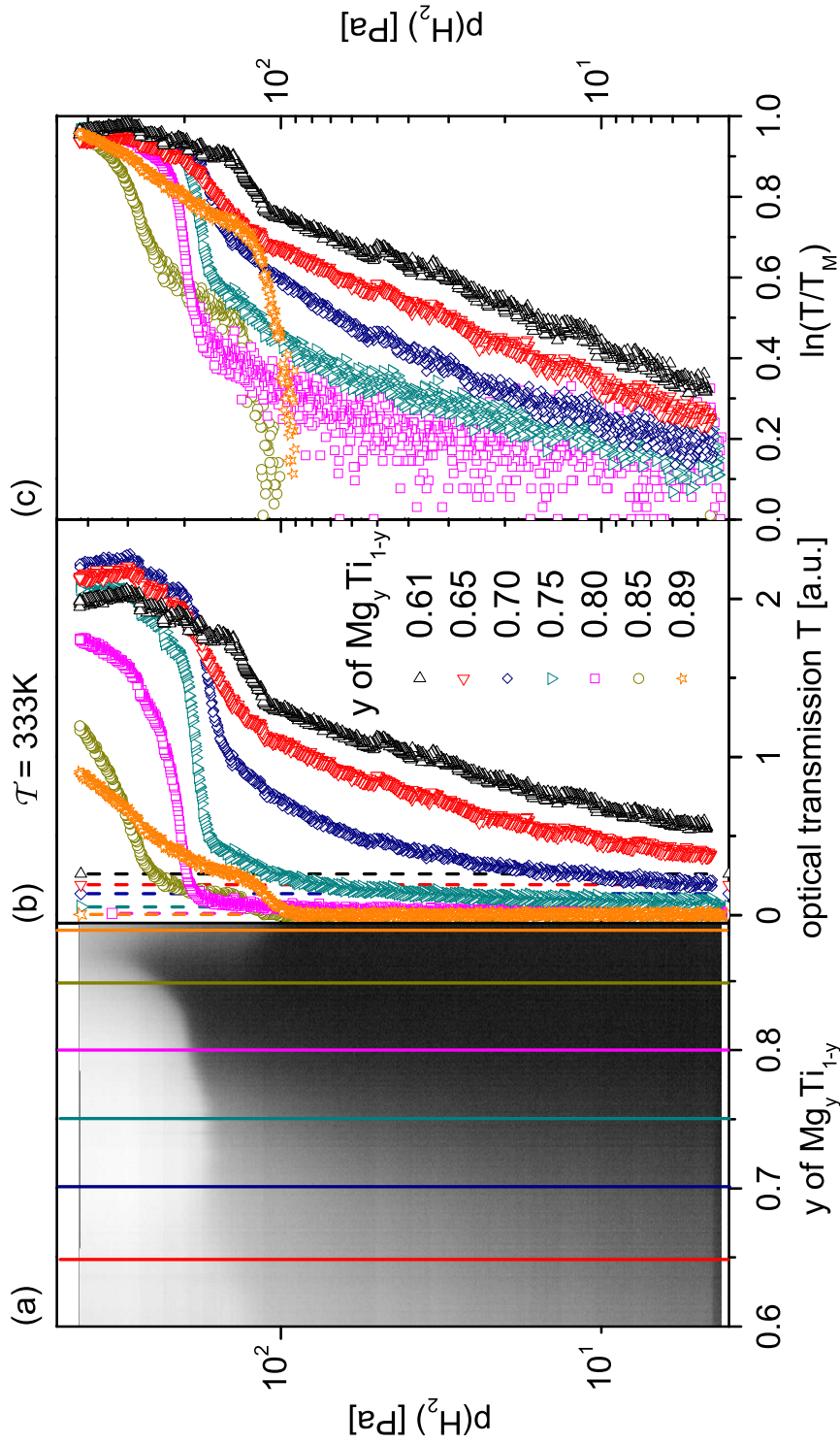
Figure 5.12: PTIs of Mg$_y$Ti$_{1-y}$H$_x$ at $\mathcal{T} = 333$ K. (a) Optical transmission map (black: low transmission, white: high transmission) as a function of Mg fraction y and hydrogen pressure p. (b) Optical transmission T for a selection of compositions y (*vertical lines* in (a)). Dashed lines indicate the transmission in the metallic state T_M. (c) PTIs (p vs ln(T/T_M)) for the same compositions.
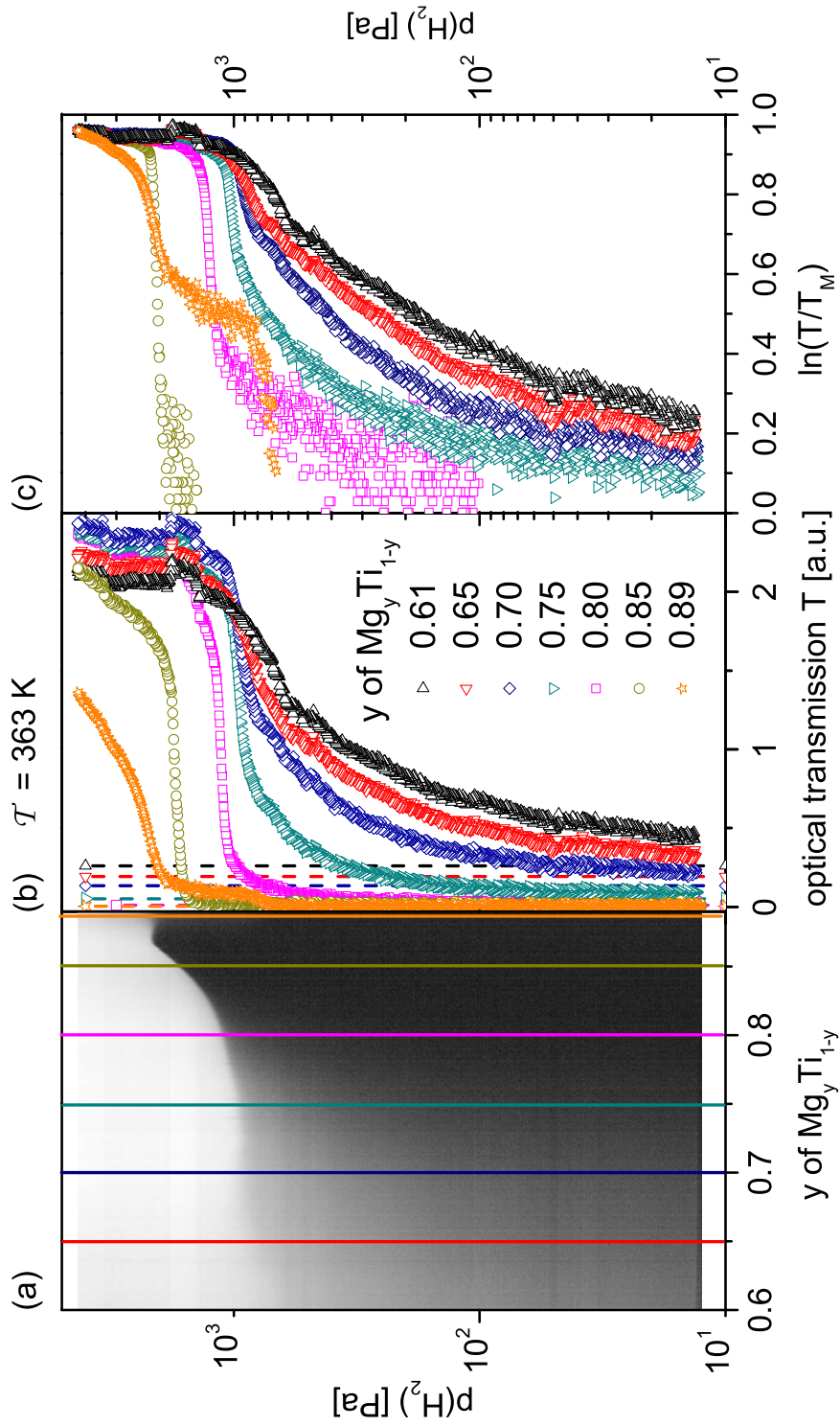
Figure 5.13: PTIs of $Mg_yTi_{1-y}H_x$ at $\mathcal{T} = 363$ K. (a) Optical transmission map (black: low transmission, white: high transmission) as a function of Mg fraction y and hydrogen pressure p. (b) Optical transmission T for a selection of compositions y (vertical lines in (a)). Dashed lines indicate the transmission in the metallic state T_M. (c) PTIs (p vs $\ln(T/T_M)$) for the same compositions.
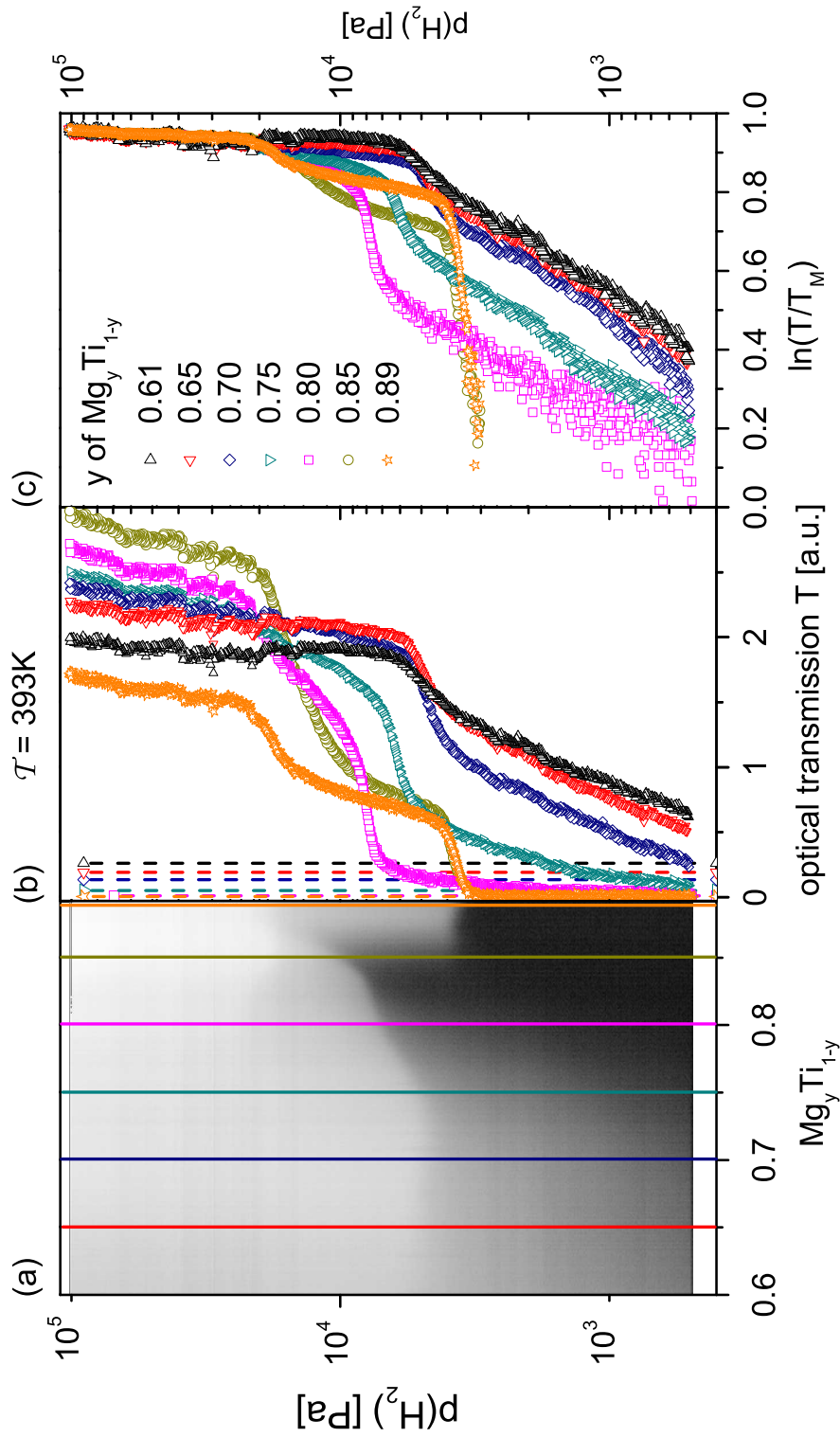
Figure 5.14: PTIs of $Mg_yTi_{1-y}H_x$ at $T = 393$ K. (a) Optical transmission map (black: low transmission, white: high transmission) as a function of Mg fraction y and hydrogen pressure p. (b) Optical transmission T for a selection of compositions y (*vertical lines* in (a)). Dashed lines indicate the transmission in the metallic state T_M. (c) PTIs (p vs $\ln(T/T_M)$) for the same compositions.
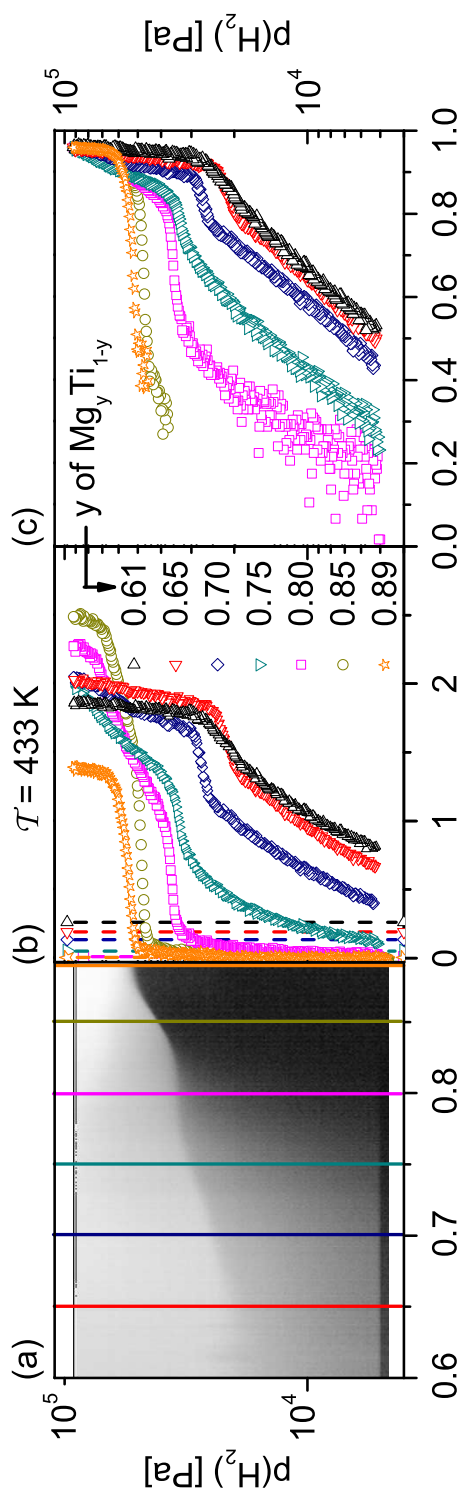
Figure 5.15: PTIs of $Mg_yTi_{1-y}H_x$ at $\mathcal{T} = 433$ K. (a) Optical transmission map (black: low transmission, white: high transmission) as a function of Mg fraction y and hydrogen pressure p. (b) Optical transmission T for a selection of compositions y (vertical lines in (a)). Dashed lines indicate the transmission in the metallic state T_M. (c) PTIs (p vs $\ln(T/T_M)$) for the same compositions.

5.4.3   Enthalpy and entropy

A summary of the PTI maps taken at six temperatures is shown in Fig. 5.16. The y-axis is the pressure on a logarithmic scale. It is remarkable that, despite some differences on the Mg-rich side due to the different stages of segregation, all PTI maps display the same overall feature over 5 orders of magnitude in pressure. On the bottom x-axis are the compositions y of the $\mathrm{Mg}_y\mathrm{Ti}_{1-y}$ compositional gradient and on the top x-axis, the isothermal maps are placed according to their inverse temperature $1/\mathcal{T}$. This synthetic way of plotting exemplifies that, for each and every composition, the plateau pressure at which the main optical change occurs follows Van 't Hoff relation (Eq. 1.2). The enthalpy and entropy of the hydride formation are then extracted from a linear fit of the logarithm of the equilibrium pressures as a function of the inverse temperature. As an illustration the Van 't Hoff plot for $y = 0.80$ is drawn on the figure.

The method for the Van 't Hoff plot construction is explained in Fig. 5.17. In (a), the PTIs for $\mathrm{Mg}_{0.80}\mathrm{Ti}_{0.20}\mathrm{H}_x$ are reported. As $\ln(T/T_\mathrm{M})$ is proportional to the hydrogen concentration c, a natural way to determine the equilibrium pressure would be to take the pressure in the middle of the plateau, so approximately at $\ln(T/T_\mathrm{M}) = 0.7$ (*vertical dashed line* in (a)). The Van 't Hoff plot determined by this method as well as the derived enthalpy and entropy are plotted in (b). The linear fit is good, although some departure from the fit is observed a the lowest temperature (297 K). The slope of the plateau at this temperature is higher due to slower kinetics. Another issue with taking the equilibrium pressure at fixed $\ln(T/T_\mathrm{M})$ is the reproducibility of the optical change, and consequently of the plateau length, for different hydrogenation cycles and temperatures. To solve this issue and minimize kinetics biases, we opt for taking the equilibrium pressure at the onset of the plateau (Fig. 5.17c). This method results in better distributed fit residuals and slightly more negative enthalpy and entropy values.

The same comparison of PTIs at different temperatures is made for the other compositions in Figs. 5.18 and 5.19. For $y = 0.61$, the absence of a clear plateau in the isotherms prevents the determination of the equilibrium pressure. However, for $0.65 \leq y \leq 0.89$, it is possible to find the plateau onset for all isotherms. For $0.85 \leq y \leq 0.89$, when two plateaus are present, the first plateau due to the formation of rutile MgH_2 is not considered and the onset of the second plateau is used to determine the equilibrium pressure.

As they are ~ 500 isotherms for every temperature, we developed an automatic procedure to determine the pressure at the onset of plateaus (See Appendix). Six out of 500 Van 't Hoff plots obtained from the automatic procedure are shown in Fig. 5.20. The linearity of these plots demonstrates the quantitative power of the optical method used in this work. The compositional dependence of the enthalpy for $\mathrm{Mg}_y\mathrm{Ti}_{1-y}\mathrm{H}_x$ is compared with the
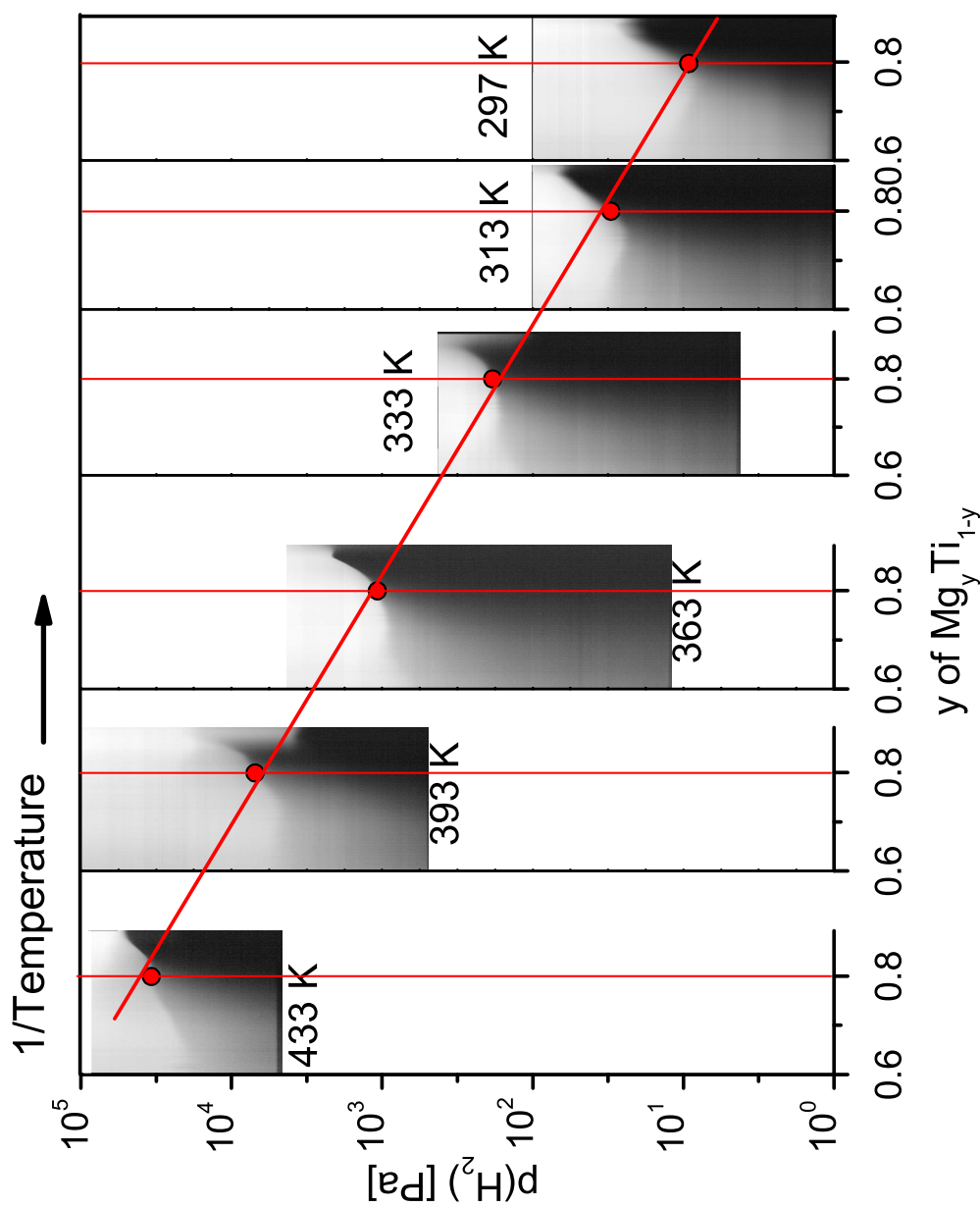
Figure 5.16: Summary of the $Mg_yTi_{1-y}H_x$ Hydrogenography experiments, for all temperatures. The PTIs map are displayed in a "Van 't Hoff plot" way, i.e. separated in the x-direction according to their inverse temperature. The *red dots* show the equilibrium pressure, and the *line* the Van 't Hoff construction for the $Mg_{0.80}Ti_{0.20}H_x$ composition.
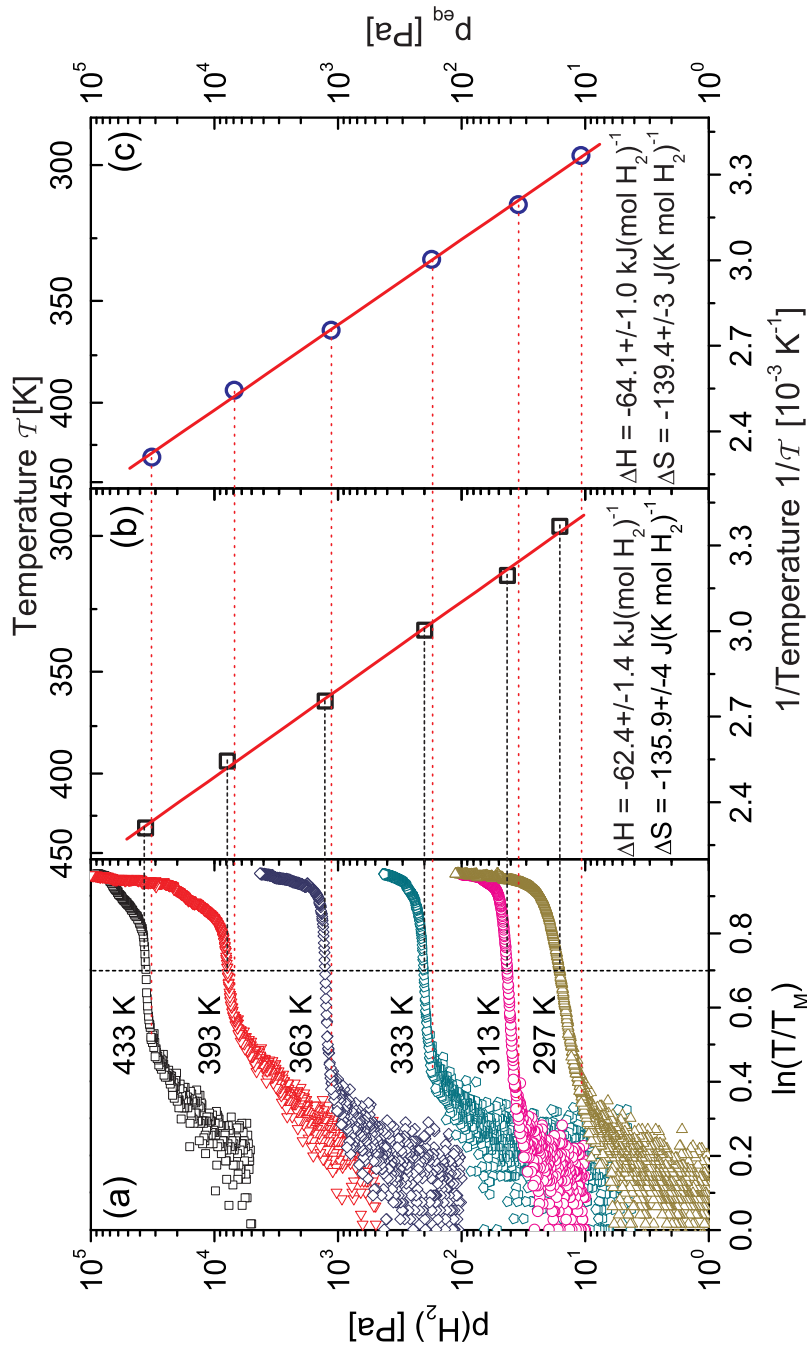
Figure 5.17: Van 't Hoff plot construction. (a) $Mg_{0.80}Ti_{0.20}H_x$ PTIs for temperatures between 297 K and 433 K. (b) *Squares*, equilibrium plateau pressures taken at $\ln(T/T_M) = 0.7$ and *line*, corresponding Van 't Hoff plot (linear regression). (c) *Circles*, equilibrium plateau pressures taken at the plateau onset and *line*, corresponding Van 't Hoff plot (linear regression). The obtained enthalpies ΔH and entropies ΔS values are indicated on the figure.
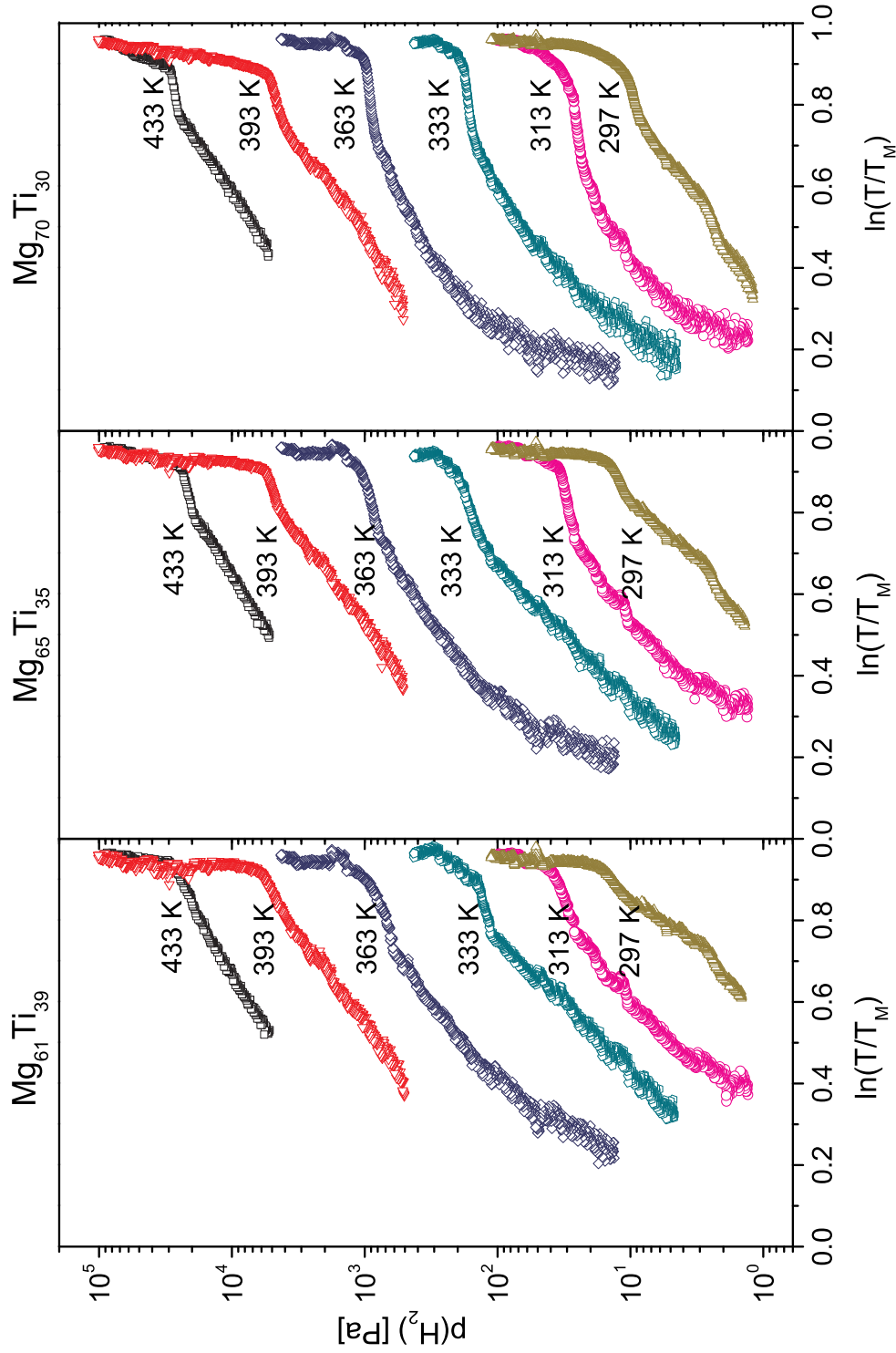
Figure 5.18: Summary of $Mg_yTi_{1-y}H_x$ PTIs for temperatures between 297 K and 433 K and Mg fraction $y = 0.61, 0.65$ and 0.70.
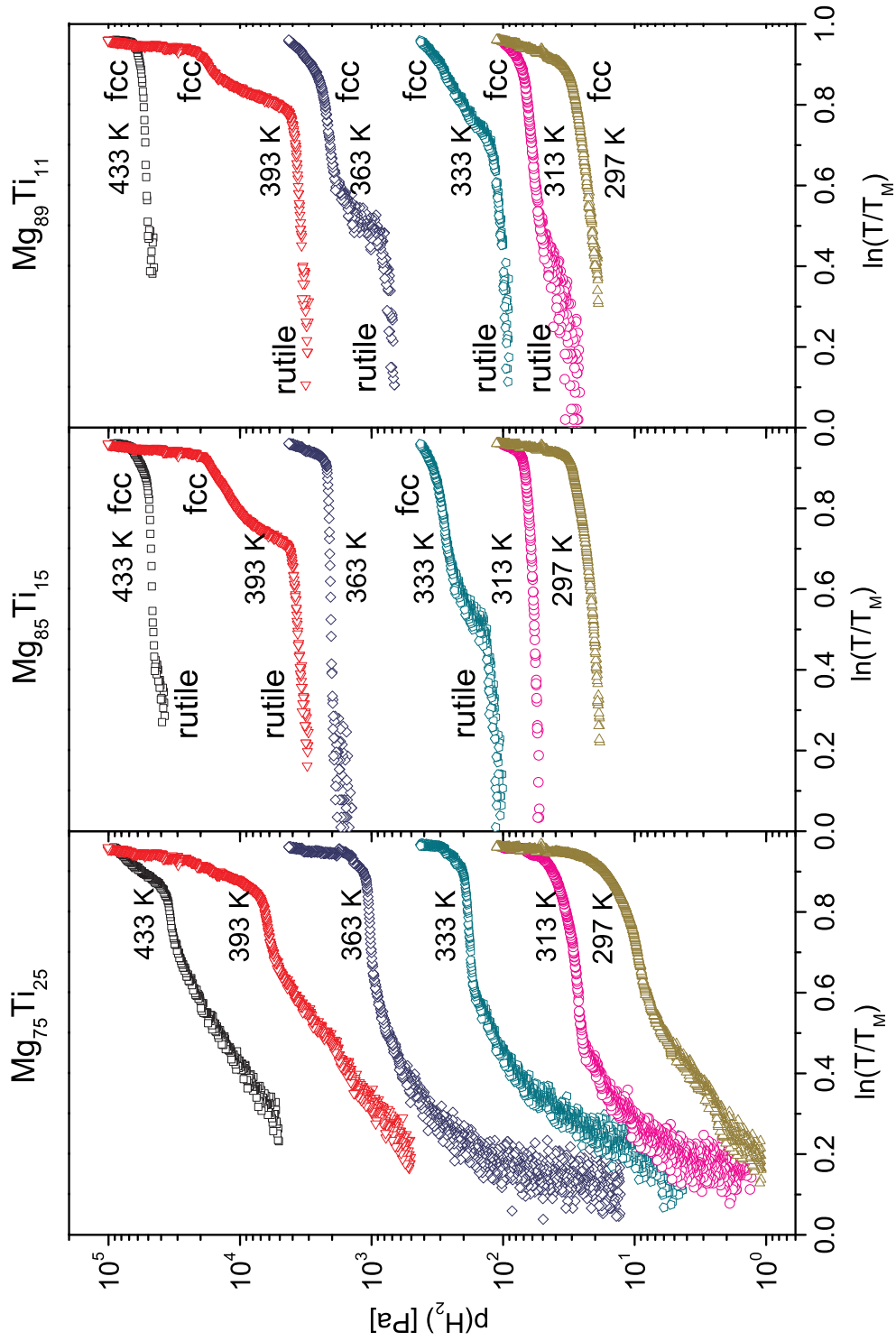
Figure 5.19: Summary of $Mg_yTi_{1-y}H_x$ PTIs for temperatures between 297 K and 433 K and Mg fraction $y = 0.75, 0.85$ and 0.89.

one obtained for $Mg_yNi_{1-y}H_x$ (Chapter 4) in Fig. 5.21. For $Mg_yTi_{1-y}H_x$, the formation enthalpy for Mg fractions $y > 0.86$ is approximately constant at ΔH = -61 kJ $(mol\ H_2)^{-1}$ and is in good agreement with the value reported for MgH_2 in thin films,[101] indicating that Ti doping up to 14 at% has little effect on the stability of Mg-Ti-H. This enthalpy value is approximately 15 kJ $(mol\ H_2)^{-1}$ less negative than ΔH for bulk MgH_2. For $0.65 < y < 0.86$, the Mg-Ti hydrides are cubic and the enthalpy exhibits a minimum at ΔH = -65 kJ $(mol\ H_2)^{-1}$. However, the enthalpy does not differ much from rutile MgH_2 thin films. This is consistent with recent calculations that indicate that the formation energy of MgH_2 does not depend strongly on the lattice symmetry[219]. For $y < 0.85$, the enthalpy measured in $Mg_yNi_{1-y}H_x$ is attributed to the $Mg_2Ni \rightarrow Mg_2NiH_4$ reaction that occurs throughout this y range. Similarly to the MgH_x hydrogenation in Mg-Ti, the thin film is destabilized by 13 kJ$(mol\ H_2)^{-1}$ as compared to bulk Mg_2NiH_4 measured during absorption. [109,110,183,184] This means that even if the absolute value of the enthalpy is somewhat overestimated due to thin films effects (see next Sec. 5.4.3), the relative difference of stability between these two Mg-based systems is still the same as in bulk hydrides.
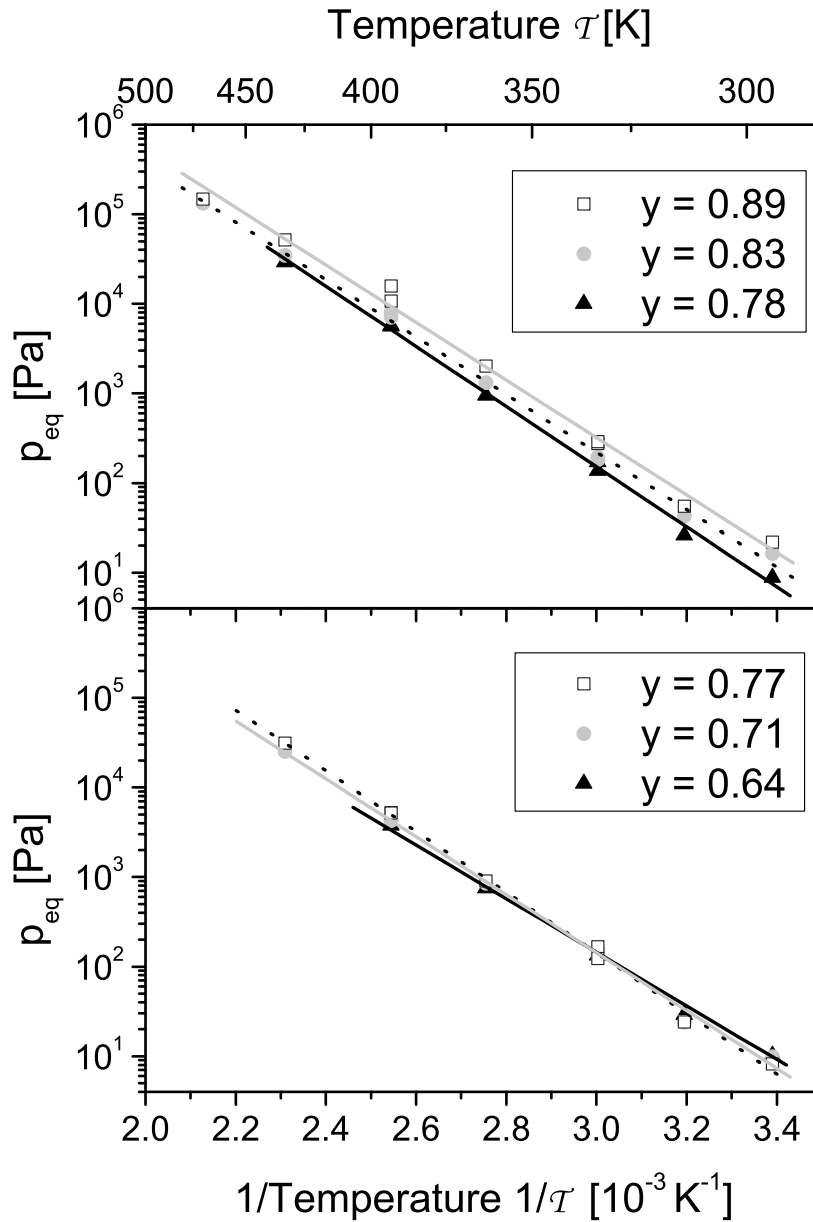
Figure 5.20: *Symbols*, equilibrium pressure data obtained from the automatic PTI fitting procedure, and *lines*, corresponding Van 't Hoff plots (linear regression) for 6 representative alloy compositions y.
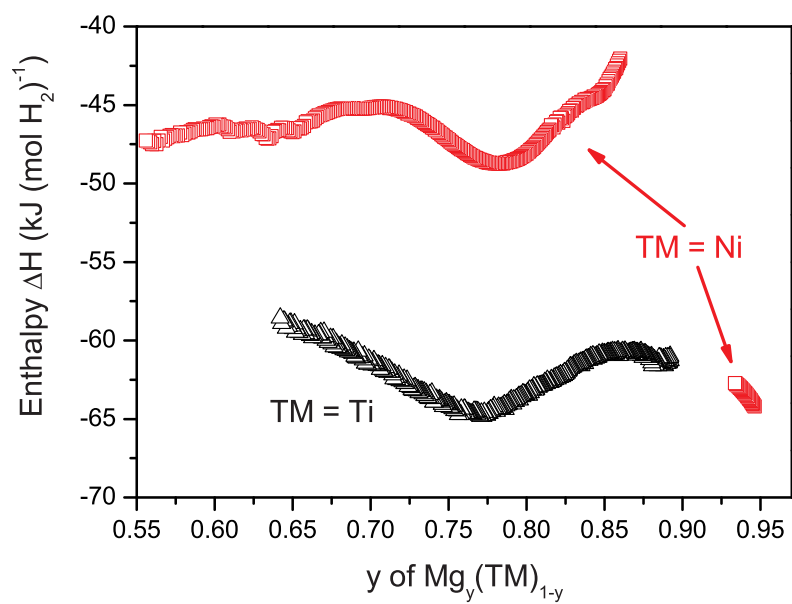
Figure 5.21: Compositional dependence of the hydride enthalpy of formation for $Mg_yNi_{1-y}H_x$ and $Mg_yTi_{1-y}H_x$.

Hysteresis

Recently, Pivak et al. measured $Mg_{0.80}Ti_{0.20}H_x$ PTIs in absorption as well as in desorption.[220] The hysteresis he found for temperatures between 333 K and 423 K spans over more than 2 orders of magnitude in pressure (See Fig. 5.22). This hysteresis, with a ratio of ab/desorption pressures $p_{ab}/p_{de} > 100$, is much larger than what we observed for PdH_x thin films, where $p_{ab}/p_{de} = 2.7$ after full relaxation of the film. The enthalpy value for desorption is $\Delta H_{de} = $ -88 $kJ(mol\ H_2)^{-1}$, about 12 $kJ(mol\ H_2)^{-1}$ less negative than bulk MgH_2.[67] Interestingly, the average enthalpy $(\Delta H_{ab} + \Delta H_{de})/2 = -76\ kJ(mol\ H_2)^{-1}$ is exactly the enthalpy of bulk MgH_2. We conclude that the hysteresis in our thin films is symmetric around the bulk hysteresis.
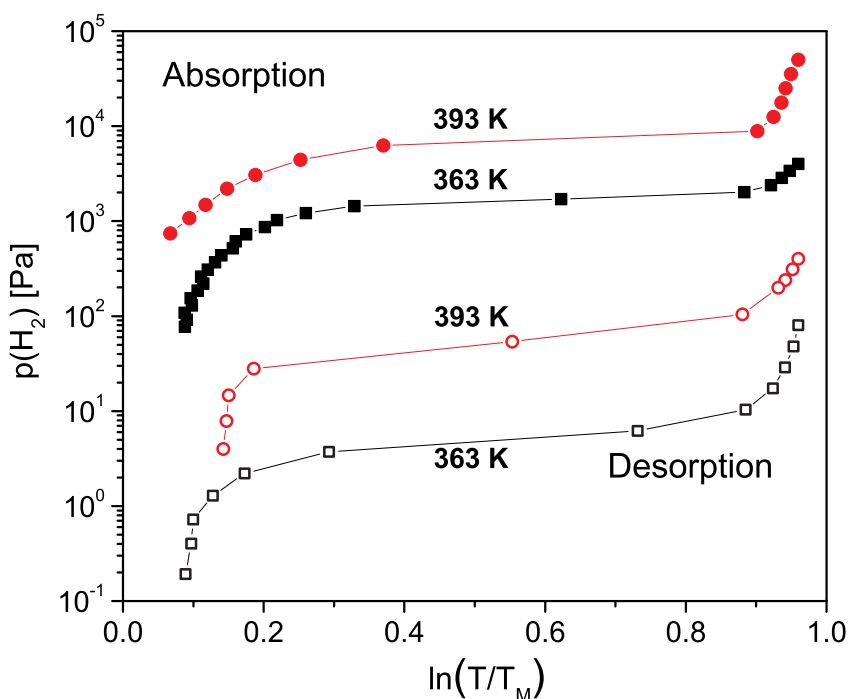
Figure 5.22: Ab- and desorption PTIs for $Mg_{0.80}Ti_{0.20}H_x$ at 363 and 393 K. *Full symbols*, absorption, *empty symbols*, desorption. *Lines* are guides to the eyes.

The origin of this large hysteresis is probably related to the clamping of the film to the substrate. We indeed did not observe any macroscopic relaxation phenomena like buckles and cracks in the Mg_yTi_{1-y} films, probably due to the much better sticking to the substrate of Ti and Mg compared to Pd. As a clamped film can only expand in one direction, the H-induced ex-
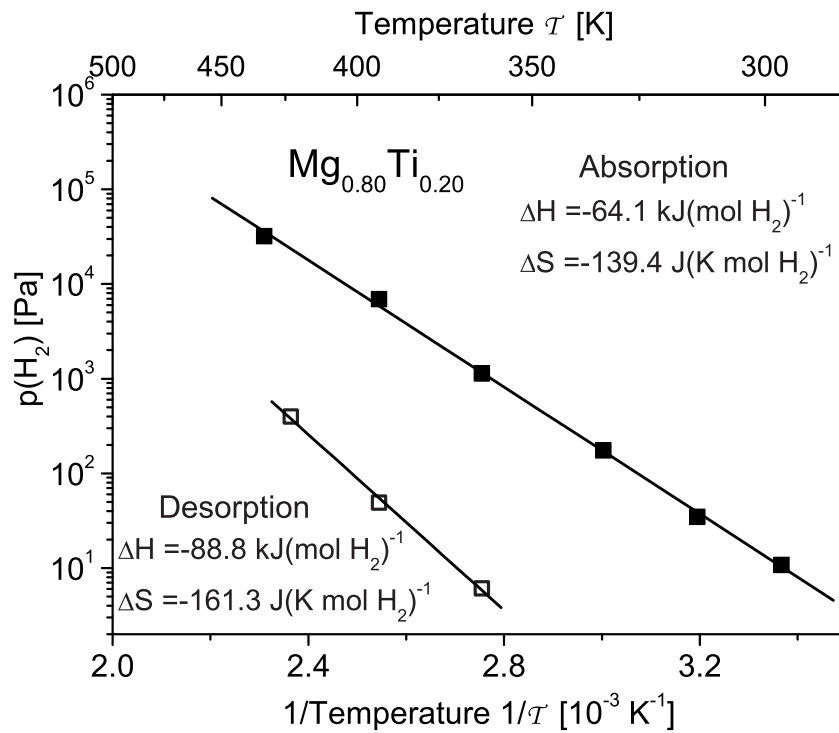
Figure 5.23: Absorption (*filed squares*) and desorption (*empty squares*) Van 't Hoff plots for $Mg_{0.80}Ti_{0.20}H_x$. Desorption data from Y. Pivak.[220] Absorption and desorption enthalpies and entropies obtained from the linear fits (*full lines*) are indicated in the figure.

pansion/contraction will produce large microstructural changes,[69] both during absorption and desorption. Therefore, the unavoidable change of microstructure during each ab/desorption costs a considerable amount of energy and enlarges the hysteresis.[a] The hysteresis might be also accentuated by the larger expansion induced by hydrogenation in Mg (32%) and Ti (25%) than in Pd (11%).[67] Another reason for the large hysteresis in $Mg_yTi_{1-y}H_x$ thin film could be the different phase transformations involved in the two systems: while PdH_x remains cubic during the whole H sorption process, $Mg_yTi_{1-y}H_x$ encounters a hcp to fcc transformation. This is similar to the cubic to hcp phase transformation observed in YH_2-YH_3, were a giant hysteresis, of similar magnitude than in $Mg_{0.80}Ti_{0.20}H_x$, has also been observed.[221]

---

[a] Schwarz and Khachaturyan even state that "the microstructure becomes a self-adjusting internal thermodynamic parameter".[72]

Enthalpy-entropy compensation effects

The compositional dependence of the enthalpy ΔH and entropy ΔS found for the hydrogenation of $Mg_yTi_{1-y}H_x$ thin gradient films is shown in Fig. 5.24a. There is an evident similarity between the two quantities. We show the plot of ΔH as a function of ΔS in Fig. 5.24b. The plot has a "$\sqrt{}$" shape, with three distinguishable compositional regions. Each of them shows a linear correlation between ΔH and ΔS. We indicate the slope, fitted with a linear regression on every portion of the curve. The slope, expressed in Kelvin, is called the compensation temperature $\mathcal{T}_{comp}$.

The strong correlation between ΔH and ΔS is known in the literature as enthalpy-entropy compensation.[222,223] It is defined as a linear relationship between ΔH and ΔS for some series of perturbations or changes in experimental variable other than temperature. In our case the changing experimental variable is the composition of the starting alloy. The linear correlation between ΔH and ΔS is called "compensation" because at temperatures near $\mathcal{T}_{comp}$ the variation in ΔH is *compensated* by the variation in ΔS, which leads to a constant equilibrium pressure. Therefore, this phenomenon is also often referred to as the isoequilibrium effect.

Compensation effects are ubiquitous in biochemistry[224] and in catalysis [149,225], where a correlation appears between the apparent activation energy and the prefactor in the Arrhenius law. Many theories are presented in the literature[222,223,226] for enthalpy-entropy compensation. There is, however, not one commonly accepted theory for this intriguing effect.

Moreover, there is another fact that adds to the controversy around enthalpy-entropy compensation. A compensation effect may be an artifact caused be the determination of ΔH and ΔS from a Van 't Hoff plot.[227,228] The error ϵ in the determined value for ΔH propagates into an error $\epsilon/\mathcal{T}_H$ in ΔS. $\mathcal{T}_H$ is the inverse of the average inverse temperature of the Van 't Hoff plot,

$$\mathcal{T}_H = 1/\left\langle \frac{1}{\mathcal{T}} \right\rangle. \qquad (5.3)$$

$\mathcal{T}_H$ is referred to as the harmonic mean temperature. An interesting example is showed by Cornish[227] who calculated the compensation temperature from an *uniformly and randomly* distributed set of data, and nevertheless found a perfectly linear Arrhenius relation with a compensation temperature within the "measurement" temperature range.

The harmonic mean temperature of the $Mg_yTi_{1-y}H_x$ Hydrogenography experiment is 349 K. Interestingly, this is exactly the value we find for the compensation temperature in the $0.65 < y < 0.77$ range. Because of the relatively large compositional range considered, this compensation temperature is the most precisely determined. It is however most probably an artefact originating from the inherent statistical error, or from a systematic error in the
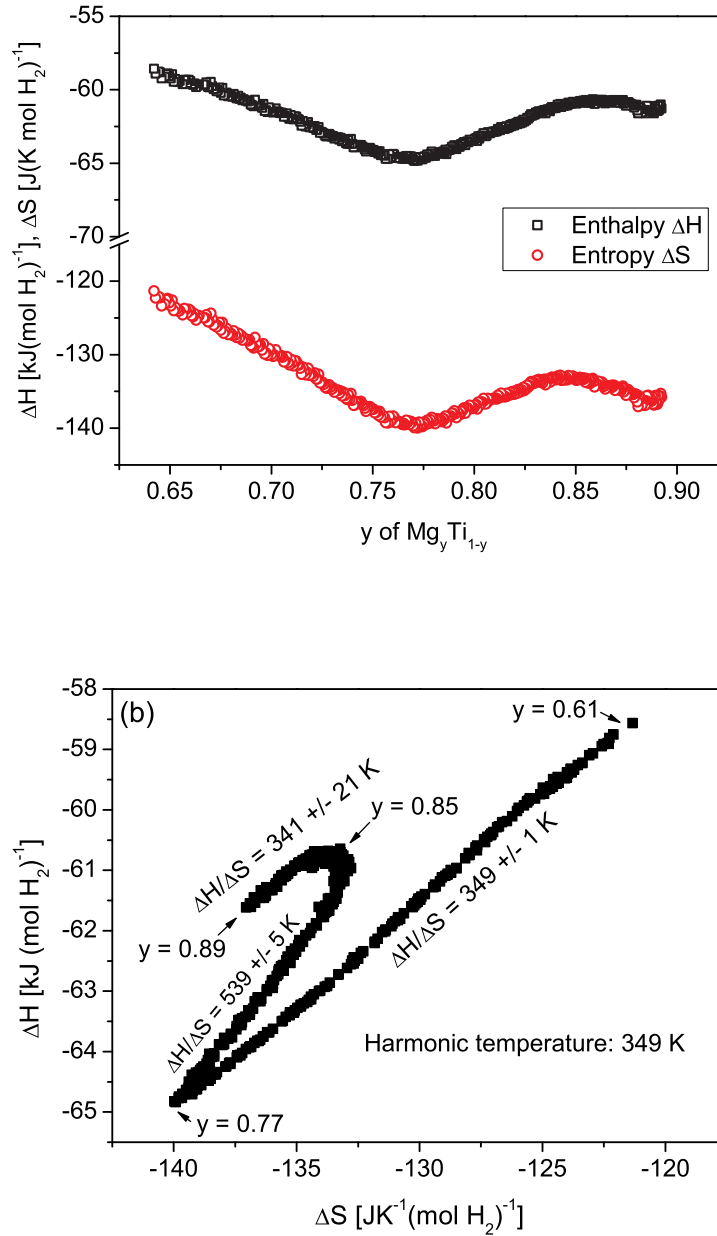
Figure 5.24: (a), Compositional dependence of the $Mg_yTi_{1-y}H_x$ hydride enthalpy and entropy of formation. (b) Correlation between enthalpy and entropy in $Mg_yTi_{1-y}H_x$: the compensation temperature $\mathcal{T}_{comp} = \Delta H/\Delta S$ and its standard deviation for the different compositional regimes are indicated in the figure.

determination of the equilibrium pressure. It is indeed important to remind that the isotherms in this range mainly consist in a gradual increase in transmission with pressure, followed by a short, sloping plateau (see e.g. Fig. 5.13). The determination of the equilibrium pressure is therefore more difficult than in the $0.77 < y < 0.85$ range, where the plateau is the dominant feature in the isotherms. In this range, the compensation $\mathcal{T}_{\text{comp}} = 539$ K is significantly higher than the harmonic temperature $\mathcal{T}_H = 349$ K, and not even within the range of measured temperatures, which points in the direction of a genuine compensation effect. The last linear portion of the $\Delta H - \Delta S$ correlation is in the $0.85 < y < 0.89$ range. The compensation temperature has a large standard deviation and is again very close to the harmonic temperature. This points to an artefact, as in the $0.65 < y < 0.77$ case.

In metal hydrogen systems, compensation effects have been noted in the past by Picraux and Vook.[229] They, however, do not provide a possible explanation for their observations. Recently, G. Thomas[230] also obtained a linear correlation between ΔH and ΔS by compiling the Sandia hydride database.[231]

As far as our literature survey extends, our Hydrogenography method has resulted in the first experiment revealing a potentially genuine compensation effect, where all samples are measured under *exactly* the same conditions. The range of inverse temperatures measured ($1/433$ K^{-1}- $1/297$ K^{-1}) is quite large for a metal-hydride study, and especially large for a study over compensation effects, where a large body of articles pertains to biological systems and is therefore limited to near-room temperatures. This compensation is potentially genuine, i.e. not caused by statistical and/or systematic errors, in the compositional range $0.77 < y < 0.85$ for $\text{Mg}_y\text{Ti}_{1-y}\text{H}_x$ thin hydride films. More analysis is currently under way to assess the validity of this compensation effect. Repeating this type of combinatorial experiments on more simple systems such as compositional gradients of binary alloys that form interstitial hydrides may shed new light on compensation effects. These experiments should be performed over an even larger range of temperatures to confirm that it is a real compensation effect. A dramatic demonstration of the compensation effect would be to perform a pressure sweep experiment at the compensation temperature. At this temperature all compositions would show the hydrogen induced metal-insulator transition at the same pressure.

5.5 Chemical short-range order and lattice deformations

5.5.1 PTI modeling: Lattice gas model for H in a multi-site solid with long-range H-H interaction

In this section, we show that a multi-site lattice gas model[232–234] with tetrahedral interstitial sites Mg_jTi_{4-j} ($0 \leq j \leq 4$) including chemical short-range order[235,236] is suitable to model the PTIs. The six essential ingredients of the multi-site lattice gas model are the:

1. types and fractions of the various interstitial sites,

2. local lattice deformation of the host lattice due to alloying of Mg and Ti,

3. enthalpy of hydrogen solution for each site type,

4. degree of occupation of interstitial sites at thermodynamic equilibrium with the surrounding H_2 gas,

5. long-range H-H interaction in the lattice gas and the

6. relation between the total hydrogen concentration and the optical transmission.

Mg-Ti interstitial sites: types and fractions

The as-deposited Mg_yTi_{1-y} films are neither perfectly random nor fully segregated.[44]

We assume that H in a Mg_yTi_{1-y} alloy can occupy tetrahedral interstitial sites Mg_jTi_{4-j} with $0 \leq j \leq 4$. There are N_j sites of type j and the total number of sites is $N = \sum_j N_j$. Using a cluster model[235] to calculate the fraction $g_j = N_j/N$ of each hydrogen site type, we obtain the following relations:

$$g_0 = (1-y)(1-y+ys)^3 \tag{5.4}$$

$$g_1 = 2(1-y)(1-y+ys)^2 y(1-s) + 2(1-y)^2(1-y+ys)y(1-s)^2 \tag{5.5}$$

$$g_2 = 2(1-y)(1-y+ys)y(1-s)(y+(1-y)s) + 2(1-y)^2 y^2(1-s)^3 \\ +(1-y)^2 y(1-s)^2(y+(1-y)s) + y^2(1-y+ys)(1-s)^2(1-y) \tag{5.6}$$

$$g_3 = 2(1-y)y(1-s)(y+(1-y)s)^2 + 2y^2(1-s)^2(1-y)(y+(1-y)s) \tag{5.7}$$

$$g_4 = y(y + (1 - y)s)^3 \tag{5.8}$$

for Ti_4, $MgTi_3$, Mg_2Ti_2, Mg_3Ti, and Mg_4 sites respectively, with of course $\sum_j g_j = 1$.

Local lattice deformations due to alloying

Magnesium has a larger molar volume than Ti ($V_{Mg} = 13.97$ cm^3/mol, $V_{Ti} = 10.64$ cm^3/mol). This implies that a titanium inclusion in a Mg matrix is somewhat expanded while the Mg matrix is compressed compared to their pure metals volumes.[237] The same applies to clusters of type j. The volume V_j^e of a cluster *embedded* in the alloy matrix is related to the volume V_j^f of a *free* cluster as:[235]

$$V_j^e(y) = (1 - L)V_{metal}(y) + LV_j^f \tag{5.9}$$

where

$$V_j^f = \frac{jV_{Mg} + (4 - j)V_{Ti}}{4}, \tag{5.10}$$

$$V_{metal}(y) = yV_{Mg} + (1 - y)V_{Ti} \tag{5.11}$$

and $V_{Mg, Ti}$ are the molar volumes of the elements. The parameter L accounts for the degree of local deformation of a cluster embedded in an alloy. The meaning of the parameter L is best explained by taking the perfect average crystal with a molar volume $V_{metal}(y)$ given by Vegard's law (see Eq. 5.11). In this hypothetical perfect lattice all cluster have the same volume. This corresponds to $L = 0$. A positive value for L implies that a Mg-rich cluster is slightly compressed while a Ti-rich cluster is slightly expanded with respect to the $L = 0$ case in an alloy with a coherent lattice but locally modulated lattice spacings. To illustrate the effect of extreme L values, we consider the case of a Mg_4 cluster: In the rigid limit, $L = 1$, a Mg_4 cluster keeps the same volume as in pure Mg, while for $L = 0$, it is compressed according to the overall composition of the Mg_yTi_{1-y} metal alloy. Note that Vegard's law still applies to the long-range average lattice for all L values.

Site dependent enthalpies of hydrogen solution

In the simplest approximation, the enthalpies of hydrogen solution (i.e. for hydrogen concentrations $c \to 0$) $\Delta H_j^{0,f}$ for isolated *free* Mg_jTi_{4-j} clusters are taken as the weighted averages of the hydrogen solution enthalpies[b] ΔH_{Mg}^0 and ΔH_{Ti}^0 in pure Mg and Ti:[233]

---

[b] If available, theoretical values obtained for example by means of density functional theory can be used instead of those given by Eq. 5.12.

$$\Delta H_j^{0,\mathrm{f}} = \frac{j\Delta H_{\mathrm{Mg}}^0 + (4-j)\Delta H_{\mathrm{Ti}}^0}{4} \tag{5.12}$$

For a Mg_jTi_{4-j} cluster embedded in a Mg_yTi_{1-y} matrix, $\Delta H_j^{0,\mathrm{f}}$ needs to be corrected for local deformations due to alloying.

Thermodynamically the volume dependence of the enthalpy of hydride formation is given by:[238]

$$\frac{d\Delta H}{d\ln V} = -B(y)V_{\mathrm{H}}(y) \tag{5.13}$$

where $B(y)$ is the bulk modulus of the alloy,

$$V_{\mathrm{H}}(y) = \frac{V_{\mathrm{dihydride}}(y) - V_{\mathrm{metal}}(y)}{2} \tag{5.14}$$

the partial molar volume of H in the alloy,

$$V_{\mathrm{dihydride}}(y) = yV_{\mathrm{MgH_2}} + (1-y)V_{\mathrm{TiH_2}}, \tag{5.15}$$

and $V_{\mathrm{MgH_2}}$ and $V_{\mathrm{TiH_2}}$ the molar volumes of the dihydrides.

Using eq. 5.13, the enthalpy of hydrogen solution for *embedded* clusters becomes:

$$\Delta H_j^{0,\mathrm{e}} \simeq \Delta H_j^{0,\mathrm{f}} + \frac{d\Delta H^0}{d\ln V}\frac{(V_j^{\mathrm{e}} - V_j^{\mathrm{f}})}{V_j^{\mathrm{f}}} = \Delta H_j^{0,\mathrm{f}} - B(y)V_{\mathrm{H}}(y)\frac{V_j^{\mathrm{e}}(y) - V_j^{\mathrm{f}}}{V_j^{\mathrm{f}}} \tag{5.16}$$

The bulk modulus $B(y)$ is taken as the weighted average of the bulk moduli of the metal constituents:

$$B(y) = yB_{\mathrm{Mg}} + (1-y)B_{\mathrm{Ti}}. \tag{5.17}$$

Occupation of the interstitial sites

With increasing hydrogen pressure, hydrogen fills gradually interstitial sites in the Mg_yTi_{1-y} alloy, starting with sites with the lowest enthalpy, in our case Ti_4 sites. The total number of hydrogen atoms absorbed at a certain hydrogen gas pressure p and temperature $\mathcal{T}$ is denoted by N^{H}, and the number of hydrogen atoms occupying a given site type by N_j^{H}. Consequently the fraction x_j of interstitial site j occupied by hydrogen atoms is

$$x_j = \frac{N_j^{\mathrm{H}}}{N_j} \tag{5.18}$$

and the normalized total hydrogen concentration c ($0 \leq c \leq 1$) is

$$c = \frac{N^H}{N} = \sum_{j=0}^{4} \frac{N_j}{N} \frac{N_j^H}{N_j} = \sum_{j=0}^{4} g_j x_j \tag{5.19}$$

Thermodynamic equilibrium between hydrogen gas and hydrogen at each interstitial site requires that

$$\frac{1}{2}\mu_{H_2}(p, T) = \mu_H^j(p, T, x_j, c) \qquad j = 0, ..., 4 \tag{5.20}$$

where the chemical potential of H_2 gas is[239]

$$\mu_{H_2} = RT \left[\ln\left(\frac{p}{p_0}\right) - \frac{S_{H_2}^0}{R} \right] + E_{H_2} \tag{5.21}$$

with $S_0 = 130.68$ JK^{-1}(mol H$_2$)$^{-1}$ the entropy of H_2 gas at standard pressure $p_0 = 1.013 \times 10^5$ Pa, E_{H_2} the binding energy of the H_2 molecule and R the gas constant.

The chemical potential of H at each interstitial site type can be written as

$$\mu_H^j = RT \ln\left(\frac{x_j}{1 - x_j}\right) + E_j(c) \qquad j = 0, ..., 4 \tag{5.22}$$

where the energy $E_j(c)$ of H at the interstitial site Mg$_j$Ti$_{4-j}$ depends in general on the *total* hydrogen concentration c. This is a direct consequence of the infinite range of the elastic H-H interaction in metal-hydrides.[240]

Solving eq. (5.20) for x_j, one obtains. together with eq. (5.19)

$$c = \frac{N^H}{N} = \sum_{j=0}^{4} g_j x_j = \sum_{j=0}^{4} \frac{g_j}{\exp\left\{ \frac{\Delta H_j(c)}{RT} - \frac{1}{2}\left[\ln(\frac{p}{p_0}) - \frac{S_{H_2}^0}{R} \right] \right\} + 1} \tag{5.23}$$

with

$$\Delta H_j(c) = E_j(c) - \frac{1}{2}E_{H_2} \tag{5.24}$$

the concentration dependent enthalpy for H absorption in a site j. Equation (5.23) is a self-consistent equation for $p = p(c)$ that is solved numerically to determine the PCI at temperature T.

H-H interaction

In order to calculate $\Delta H_j(c)$, the H-induced lattice expansion has to be taken into account. Increasing the H concentration makes all interstitial sites more favorable for hydrogen,[241] and results in an infinite range attractive H-H interaction.[242,243] The contribution of this H-H interaction to the enthalpy of formation is to lowest order given by (see Eq. (5.13)):[236]

$$\Delta H_j(c) \simeq \Delta H_j^{0,\mathrm{e}} + \frac{d\Delta H}{d\ln V}\frac{d\ln V}{dc}c = \Delta H_j^{0,\mathrm{e}} - B(y,c)V_\mathrm{H}(y)\frac{V_\mathrm{dihydride} - V_\mathrm{metal}}{2V_\mathrm{metal}}c$$

$$(5.25)$$

with

$$B(y,c) = y\left[cB_{\mathrm{MgH}_2} + (1-c)B_\mathrm{Mg}\right] + (1-y)\left[cB_{\mathrm{TiH}_2} + (1-c)B_\mathrm{Ti}\right]. \quad (5.26)$$

Together with eq. (5.16), the enthalpy of hydride formation at a site j becomes:

$$\Delta H_j(c) \simeq \Delta H_j^{0,\mathrm{f}} - B(y,0)V_\mathrm{H}(y)\frac{V_j^\mathrm{e}(y) - V_j^\mathrm{f}}{V_j^\mathrm{f}} - B(y,c)\frac{V_\mathrm{H}(y)^2}{V_\mathrm{metal}}c \qquad (5.27)$$

The second and third terms in Eq. 5.27 describe the influence on the enthalpy of formation of local lattice deformations at zero hydrogen concentration and of the filling of sites with hydrogen, respectively.

Optical transmission

Lambert-Beer's law is used to calculate the optical transmission T:

$$T = T_0 \prod_{j=0}^{4} \exp\left\{[-\alpha_j^\mathrm{M}(1 - x_j) - \alpha_j^\mathrm{MH}x_j]g_j\right\} \qquad (5.28)$$

where T_0 is the light intensity in the absence of the sample and $\alpha_j^\mathrm{M(H)}$ are the optical absorption coefficients of the metallic and hydrided $\mathrm{Mg}_j\mathrm{Ti}_{1-j}$ clusters averaged over the measured photon-energy $\hbar\omega$ bandwidth, respectively. According to Eq. 5.28, the transmission in the metallic state T_M is:

$$T_\mathrm{M} = T_0 \prod_{j=0}^{4} \exp(-\alpha_j^\mathrm{M}g_j) \qquad (5.29)$$

Combining Eqs. (5.28) and (5.29), the logarithm of the optical transmission normalized by the transmission in the metallic state is

$$\ln\left(\frac{T}{T_\mathrm{M}}\right) = -\sum_{j=0}^{4}(\alpha_j^\mathrm{MH} - \alpha_j^\mathrm{M})x_jg_j \qquad (5.30)$$

If the optical change $\alpha_j^\mathrm{MH} - \alpha_j^\mathrm{M}$ was independent of j, i.e. of the cluster composition, then

$$\ln\left(\frac{T}{T_\mathrm{M}}\right) \propto c \qquad (5.31)$$

This is however certainly not the case, as MgH_2 is a transparent insulator and TiH_2 a metal. The simplest approximation would be to neglect the optical change of the metal and take

$$\alpha_j^{MH} - \alpha_j^{M} \cong j \cdot (\alpha_{MgH_2} - \alpha_{Mg}), \tag{5.32}$$

then

$$\ln\left(\frac{T}{T_M}\right) \cong -(\alpha_{MgH_2} - \alpha_{Mg})\sum_{j=0}^{4} j x_j g_j. \tag{5.33}$$

This shows that Mg-rich clusters have a predominant contribution to the optical transmission.

The last step is to combine Eqs. (5.23) and (5.30) to obtain

$$\ln\left(\frac{T}{T_M}\right) = \sum_{j=0}^{4} \frac{(\alpha_j^{M} - \alpha_j^{MH})g_j}{\exp\left\{\frac{\Delta H_j(c)}{R\mathcal{T}} - \frac{1}{2}\left[\ln(\frac{p}{p_0}) - \frac{S_{H_2}^0}{R}\right]\right\} + 1} \tag{5.34}$$

This is the central result of our model, used to calculate the PTIs.

5.5.2 Comparison with experimental pressure–optical-transmission-isotherms

The present model is applied to pressure–optical-transmission–isotherms measured on $Mg_y Ti_{1-y} H_x$ gradient thin films. This ensures a reliable comparison of the isotherms, as all compositions y are measured simultaneously under exactly the same pressure and temperature conditions.

The determination of the optical absorption coefficients of the pure Mg and Ti metals is done on separately deposited Pd capped Mg and Ti thin films.[66] The consistency of the results is checked with data from Palik.[49] The absorption coefficient of the hydrides MgH_2 and TiH_2 are then determined on the same films exposed to 10^5 Pa H_2 pressure. The absorption coefficients of the intermediate $Mg_j Ti_{4-j}$ clusters ($j = 1, 2, 3$) are to first order the weighted average of values for pure metals, respectively hydrides.[c] We make use of *ab initio* calculations of the optical properties of Mg-Ti supercells[194] to interpolate more precisely the absorption coefficients (see Fig. 5.25).

We use the standard molar volumes $V_{Mg} = 13.97$ cm^3 (mol)$^{-1}$ and $V_{Ti} = 10.64$ cm^3 (mol)$^{-1}$ for the metals. For the hydrides, 32% and 25% volume expansion is assumed for MgH_2 and TiH_2, respectively.[67] Bulk moduli values for the metals are taken as $B_{Mg} = 35.4$ GPa, $B_{Ti} = 105.1$ GPa,[244] and $B_{MgH_2} = 50$ GPa,[245] $B_{TiH_2} = 161$ GPa for the hydrides.[246]

---

[c] The weak curvature of the absorption coefficients difference in Fig. 5.25 shows that if first principle calculation had not been available, a simple linear interpolation would have induced only minor errors. This observation is important for the applicability of our model to alloy system for which experimental (or theoretical) values are not available.

Figure 5.26a displays a calculated PCI and its corresponding PTI obtained
with the multi-site lattice gas model with a realistic set of parameters for a
wide range of pressure. In the PCI, the wide distribution of sites energies
and site fractions results in a gradual increase of the hydrogen concentration
with pressure. In comparison, most of the optical transmission change occurs
in a narrower pressure range in the PTI than in the PCI . The high optical
absorption coefficient difference of Mg-rich clusters is responsible for this be-
havior, giving extra weight in transmission to the filling of Mg_4 and Mg_3Ti
sites. Similarly, the filling of Ti_4 sites results in an initial decrease of the
optical transmission as a consequence of the negative absorption coefficient
difference for these sites (See Fig. 5.25). To put in evidence the contribution
of the different sites to the isotherms, the derivative of the concentration and
of the optical transmission with respect to the logarithm of the pressure are
calculated and plotted in Fig. 5.26b). Five peaks corresponding to the five
interstitial sites are clearly seen in the derivatives. Due to the predominant
Mg fraction ($y = 0.61$) and the positive CSRO parameter ($s = 0.4$) chosen
for this example, Mg-rich sites are contributing most. This effect is even more
pronounced in the $\ln(T)$ derivative because of the high transparency of MgH_2
(See Sec. 5.5.1)
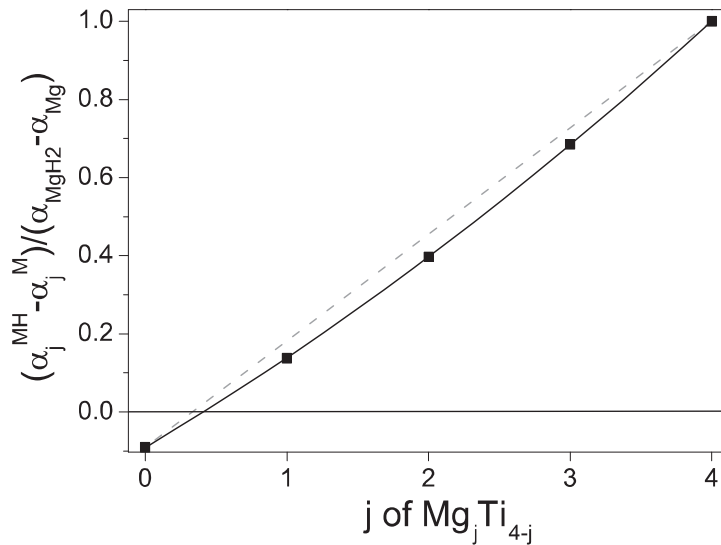
Figure 5.25: *Squares*, normalized absorptions coefficient differences of the
Mg_jTi_{4-j} clusters obtained by density functional theory[194] used in the PTI
simulations. *Dashed line*, linear interpolation between the Mg and Ti values.
The *black line* is a guide to the eye.

The comparison between modeled and experimental PTIs for 5 different
compositions and 3 different temperatures is shown in Fig. 5.27. The so-
lution enthalpies for free Mg_4, respectively Ti_4 clusters are kept constant
for all compositions and temperatures at $\Delta H^0_{Mg} = -36.6$kJ$(molH_2)^{-1}$ and
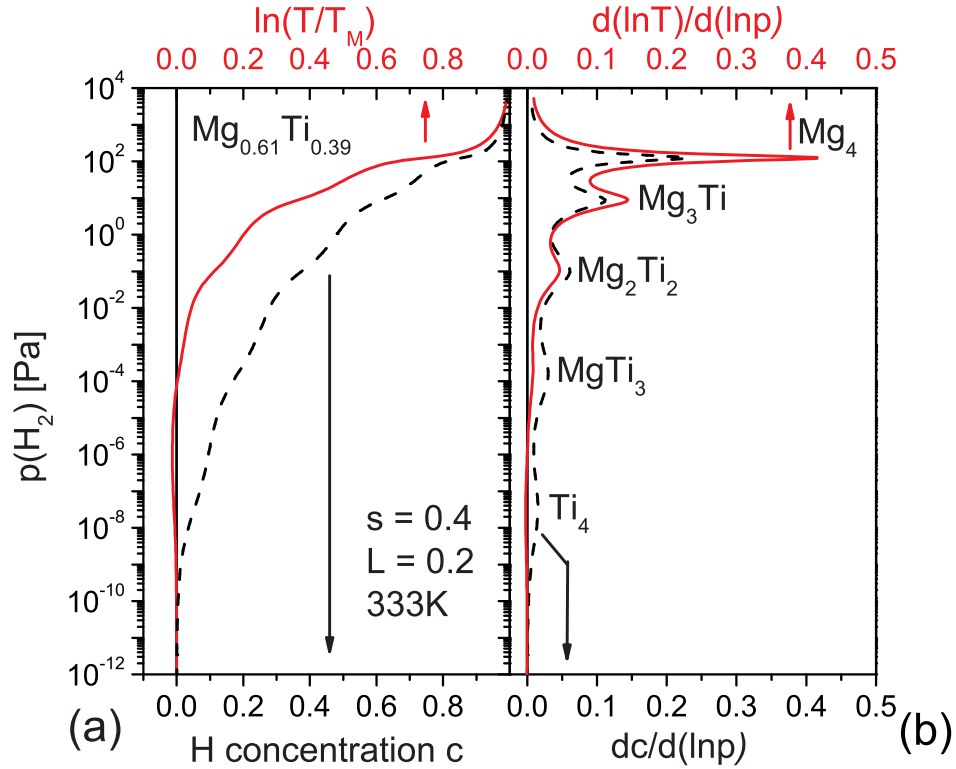
Figure 5.26: (a) Comparison between PCI (*dashed line*) and PTI (*full line*) of $Mg_{0.61}Ti_{0.39}H_x$ at $\mathcal{T} = 333$ K as calculated with the multi-site lattice gas model with $s = 0.4$ and $L = 0.2$ (Model described in Sec. 5.5.1). (b) Derivatives of the H concentration c (*dashed line*) and of $\ln(T)$ (*full line*) with respect to $\ln(p)$.

Table 5.1: Input parameters of the multi-site model, valid for all compositions y of Mg_yTi_{1-y} and temperatures.

V_{Mg}	V_{Ti}	V_{MgH_2}	V_{TiH_2}	B_{Mg}	B_{Ti}	B_{MgH_2}	B_{TiH_2}	ΔH^0_{Mg}	ΔH^0_{Ti}	L
[cm³(mol)⁻¹]				[GPa]				[kJ(molH₂)⁻¹]		
13.97	10.64	18.44[a]	13.30[a]	35.4[b]	105.1[b]	50[c]	162.0[d]	-36.6	-86.6	0.2

[a] F. Manchester[67]
[b] K. A. Gschneider[244]
[c] R. Yu and P. K. Lam[245]
[d] W. Wolf and P. Herzig[246]
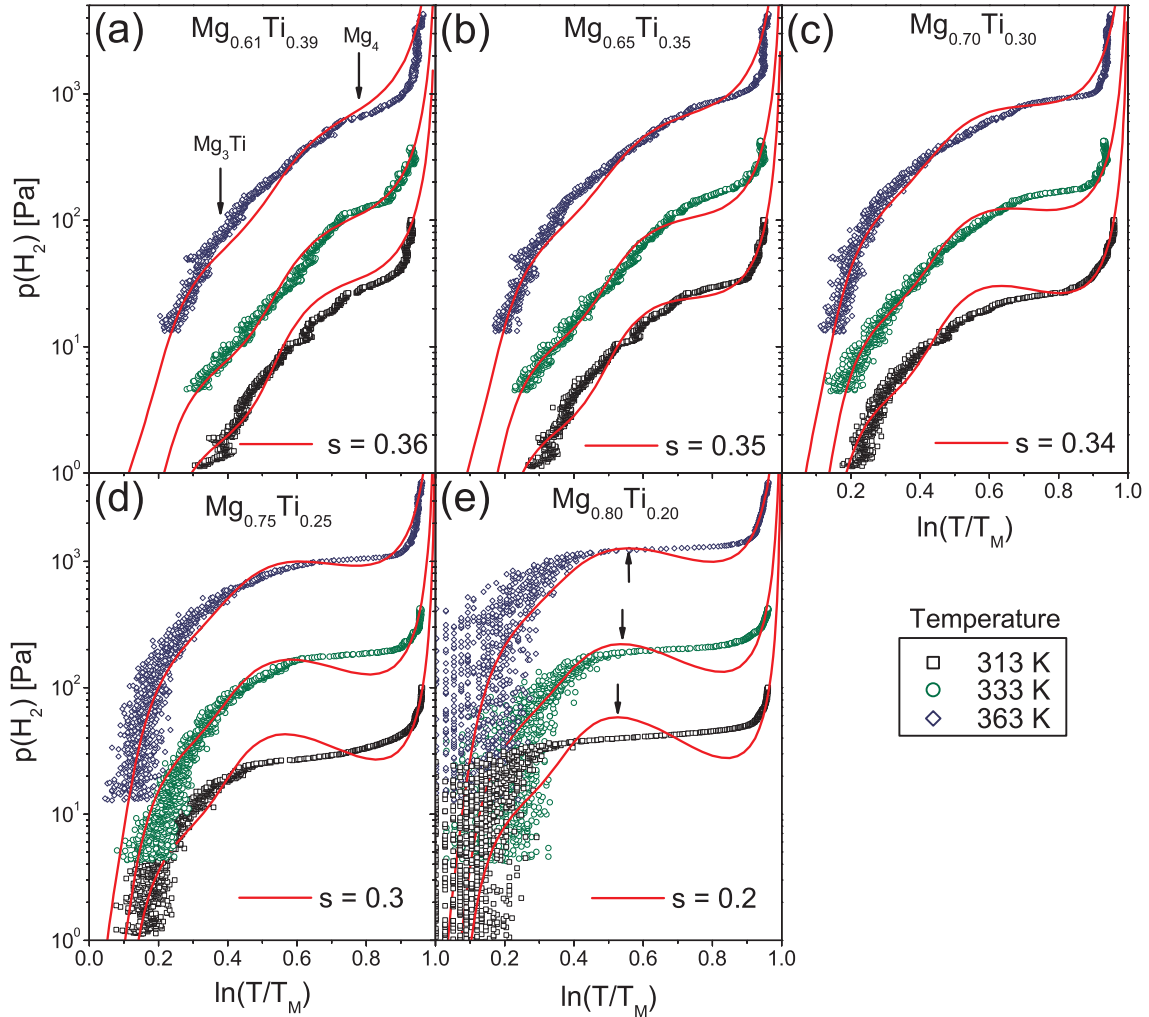
Figure 5.27: *Symbols*, (a)-(e) experimental pressure–optical-transmission-isotherms of $Mg_yTi_{1-y}H_x$ at temperatures $\mathcal{T} = 313$, 333 and 363 K and various Mg fraction y. *Lines*, Multi-site lattice gas PTI simulations for fixed $L = 0.2$. The chemical short-range order parameter s used for each alloy composition is indicated in the figure. Note that s is independent of temperature. The *arrows* indicate: in (a), the transmission at which half of the Mg_3Ti and Mg_4 sites are filled, and in (e) the transmission at the first spinodal concentration (See text).

$\Delta H_{\mathrm{Ti}}^0 = -85.6\mathrm{kJ(molH_2)}^{-1}$ (See Table 5.1). From XRD measurements, the average $\mathrm{Mg}_y\mathrm{Ti}_{1-y}\mathrm{H}_x$ lattice is coherent, with no evidence for large-scale phase segregation.[65] Furthermore, since the molar volumes of Mg and $\mathrm{TiH_2}$ are similar, the hydrogenation of Ti-rich sites reduces the differences in volume between clusters and even increases the structural coherence at intermediate hydrogenation stages. The L parameter, that characterizes the local rigidity of embedded clusters with respect to the average lattice, is therefore expected to take a small value: a constant value of $L = 0.2$ gives satisfactory results for all isotherms. The only free parameter for each composition is then the CSRO parameter s.

For every composition $y < 0.85$, there is a well-defined positive short-range order parameter value that reproduces the experimental data well for the 3 temperatures considered. The observed plateau corresponds to the hydrogenation of $\mathrm{Mg_4}$ sites, while the gradual increase of transmission at lower pressure is due to the gradual filling of Ti-containing sites. For high Mg fractions ($y \geq 0.75$), the PTIs are reproduced best if assuming a plateau starting near the spinodal concentration, i.e. near the local maximum in the simulated isotherm (See the *arrows* in Fig. 5.27e). A plateau pressure higher than the one derived using the Maxwell construction is expected in solid-gas systems where the metal-to-hydride transformation generates coherency strain and therefore adds an additional energy barrier for the phase transformation to proceed.[72,73] The fractions of interstitial sites g_j and the embedded site energies $\Delta H_j^{0,\mathrm{e}}$ obtained by modeling as a function of compositions are plotted in Fig. 5.28. The fraction g_4 of $\mathrm{Mg_4}$ interstitial sites is the largest at all concentrations considered, but for Ti-rich compositions, a significant fraction of all other sites is also present.

It is counterintuitive that for a given temperature, the modeled and experimental plateau pressures *increase* with the Mg fraction y. Indeed, as seen in Fig. 5.29, the enthalpy of $\mathrm{Mg_4}$ sites decreases with increasing Mg fraction for any fixed H concentration in the hydride, and the plateau pressure should decrease accordingly. However, due to the changing amount of Ti, the minimum concentration $c_{\min} = 1 - g_4(y)$ at which the $\mathrm{Mg_4}$ site occupation starts is *not* constant. The $\mathrm{Mg_4}$ plateau pressure is thus essentially determined by the enthalpy of $\mathrm{Mg_4}$ sites $\Delta H_4(c_{\min})$ (*stars* in Fig. 5.29), and increases slightly with increasing Mg fraction. This weak dependence of the $\mathrm{Mg_4}$ site enthalpy on Mg fraction originates from the counteracting effect of the second and third terms in Eq. 5.27: Due to the small size of the Ti atom relatively to Mg, alloying makes the second term positive and reduces the stability of $\mathrm{Mg_4}$ sites towards hydrogen. However, adding Ti also increases $c_{\min}$, and therefore destabilizes the hydrogenation of $\mathrm{Mg_4}$ sites via a strengthening of the H-H interaction (third term). These theoretical considerations are consistent with our previous experimental work,[209] where we concluded from the temperature dependence of the $\mathrm{Mg_4}$ sites plateau pressure that the $\mathrm{Mg_4}$ enthalpy does not depend significantly on $\mathrm{Mg}_y\mathrm{Ti}_{1-y}$ composition.
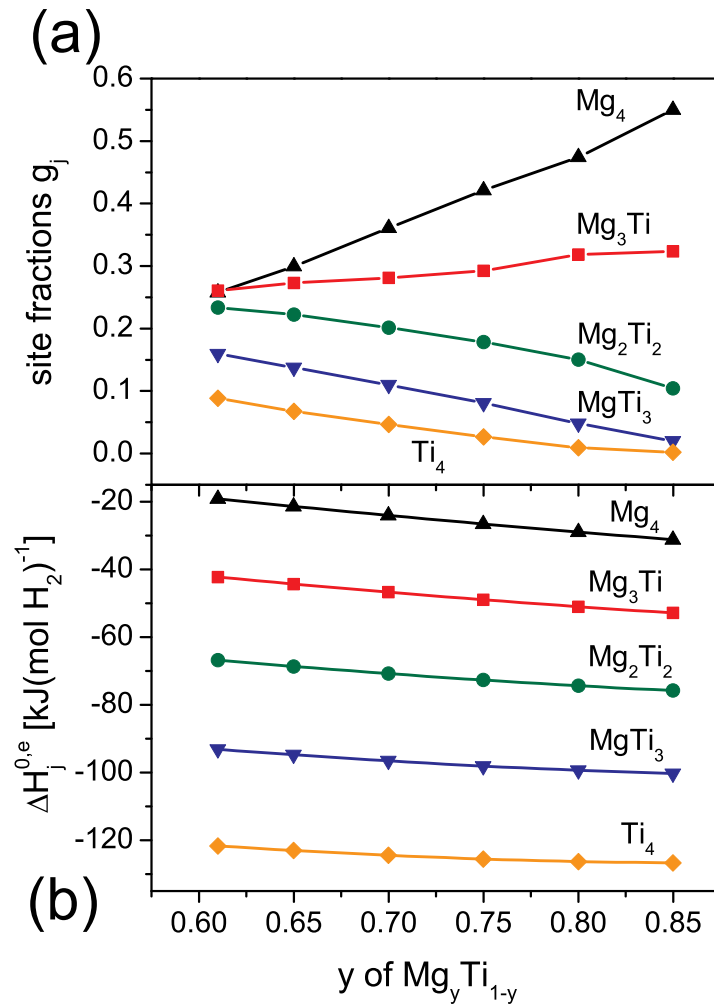
Figure 5.28: *Symbols*, (a) fractions g_j of Mg_jTi_{4-j} sites and (b), enthalpies of solution per site $\Delta H_j^{0,e}$ derived from the experimental PTIs using the multi-site model described in Sec. 5.5.1.
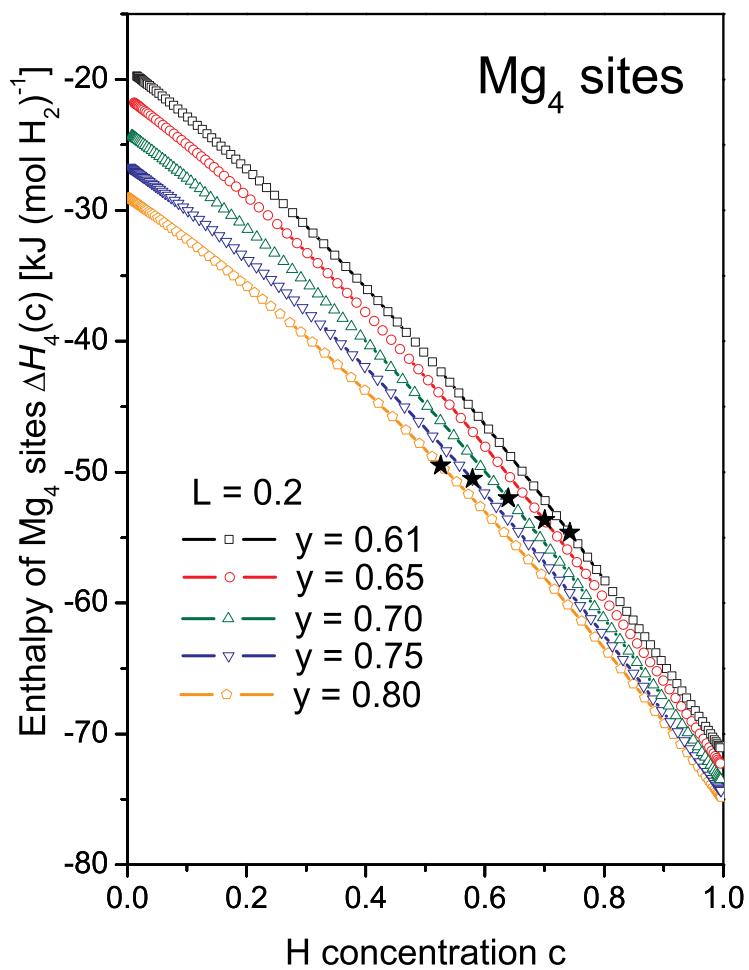
Figure 5.29: *Open symbols*, enthalpy of the Mg_4 sites $\Delta H_4(c)$ as a function of H concentration c for various Mg fractions y. *Filled Stars*, enthalpy $\Delta H_4(c_{min})$ of the Mg_4 sites at the minimum concentration for Mg_4 site occupation c_{min} as a function of Mg fraction.

5.5.3   Discussion

The input energies used in the modeling ($\Delta H^0_{Mg} = -36.6 \text{kJ}(\text{molH}_2)^{-1}$, $\Delta H^0_{Ti} = -85.6 \text{kJ}(\text{molH}_2)^{-1}$) are H solution enthalpies and seem at first sight not negative enough. To compare directly the energies used in the modeling with measured hydride (MgH_2 and TiH_2) enthalpies from literature, we need to calculate the enthalpy of an hypothetical material containing only Mg_4 (or Ti_4) sites at half the hydrogen filling ($c = 0.5$). For this we use equation Eq. 5.27 with $y = 1, j = 4$ (Mg_4 sites) and $y = 0, j = 0$ (Ti_4 sites). The obtained enthalpies are $\Delta H_4(0.5) = -52.2 \text{kJ}(\text{molH}_2)^{-1}$ and $\Delta H_0(0.5) = -108.6 \text{kJ}(\text{molH}_2)^{-1}$ for Mg_4 and Ti_4 sites respectively. These values are ~ 20 kJ$(\text{molH}_2)^{-1}$ less negative than those determined on bulk MgH_2 ($\Delta H = -76 \text{kJ}(\text{molH}_2)^{-1}$) and TiH_2 ($\Delta H = -130 \text{kJ}(\text{molH}_2)^{-1}$).[67] Such a discrepancy is not unusual for thin hydride films: Due to the hydrogen-induced lattice expansion, films, that are clamped to the substrate, get strained. Although at high H concentrations dislocations and a complex rearrangement of nanograins reduce clamping effects, [75] the remaining compressive strain reduces the hydride stability in a similar way as alloying does in Eq. 5.16. For example, experiments on pure Mg thin films report an enthalpy for hydrogen absorption of $\Delta H = -60.7 \text{kJ}(\text{molH}_2)^{-1}$. [101] Additionally to the clamping to the substrate, the nanostructure of the films can also influence the enthalpy.[247]

To show the sensitivity of the model to the L and s parameters, the isotherms of $Mg_{0.61}Ti_{0.39}$ and $Mg_{0.75}Ti_{0.25}$ at temperature $\mathcal{T} = 333$ K are compared with simulations in Fig. 5.30 with the optimal s parameter and varying L values from completely "soft" ($L = 0$) to completely "rigid" clusters ($L = 1$) (Fig. 5.30(a) and (c)) and with a $L = 0.2$, for varying s parameters, from random ($s = 0$) to completely segregated Mg_4H_x and Ti_4H_x sites ($s = 1$) (Fig. 5.30(b) and (d)).

- For constant s and low L values ($L < 0.4$), the multi-site modeling reproduces the PTIs' shape reasonably well.

- For constant s and high L values, the cluster volume goes towards that of free clusters (See Eq. (5.9)), and the second alloying term in eq. 5.27, that effectively separate the site enthalpies $\Delta H^{0,e}_j$ from each other, goes to zero. Consequently, the $\Delta H^{0,e}_j$ values are too close from each other to be discriminated in the isotherms, which therefore exhibit only one large plateau. The gradual increase of pressure with optical transmission observed experimentally is therefore also not reproduced.

- For constant L and a fully random alloy ($s = 0$), the Mg_3Ti fraction becomes preponderant and, besides the Mg_4 plateau, a second plateau at lower pressures should be seen in the isotherms. This is not the case in the $Mg_{0.75}Ti_{0.25}$ isotherm and indicates that some local chemical separation occurs in Mg-Ti.
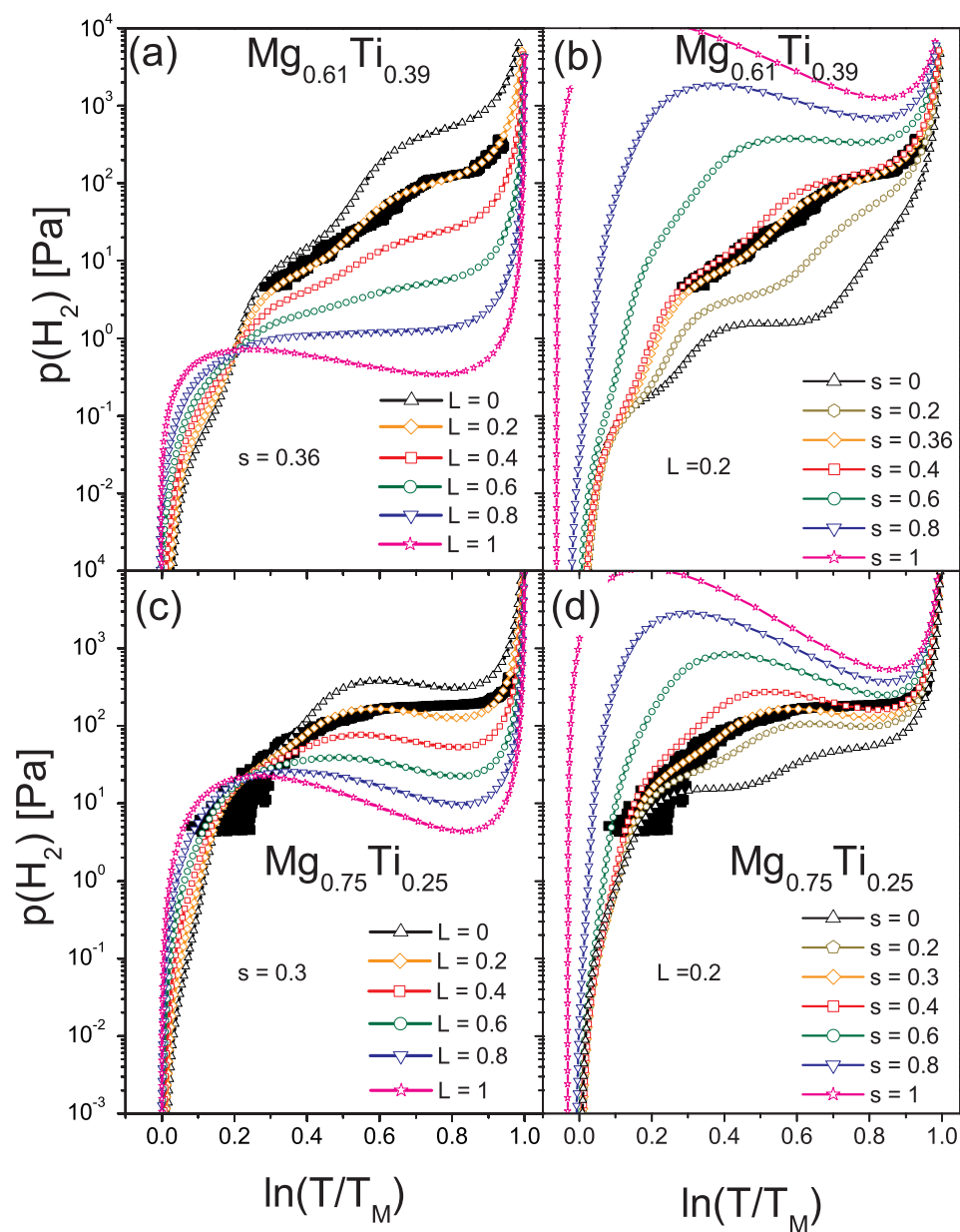
Figure 5.30: *Empty symbols*, PTI simulations for $Mg_{0.61}Ti_{0.39}$ with (a) varying L and $s = 0.36$, (b) $L = 0.2$ and varying s, and for $Mg_{0.75}Ti_{0.25}$ with (c) varying L and $s = 0.36$ and (d) $L = 0.2$ and varying s. *Filled squares*, corresponding experimental pressure–optical-transmission–isotherms at temperature $\mathcal{T} = 333$ K. The *orange diamond symbols* are the best simulations as shown in Fig. 5.27.

- For constant L and a fully segregated phases ($s = 1$), in this case, only two types of sites exist: Mg_4 and Ti_4. The calculated Mg_4 plateau is the only one in the vicinity of the experimental isotherm and cannot reproduce its sloping behavior.

These examples show that modeling PTIs with a simple multi-site lattice gas model is powerful enough to determine s and L parameters and therefore discriminate between different possible microstructures in Mg-Ti-H. A certain degree of chemical segregation ($s > 0$) must be introduced in the simulated isotherms to reproduce the experimental data properly. Moreover, while the material remains X-ray coherent, the non-zero L parameter shows that the volume of interstitial sites still depends on the local chemical composition, and therefore indicates the presence of local lattice size modulations. This is consistent with Michaelsen,[216] who showed that coherent inhomogeneities must be larger than several nanometers before they can be detected by conventional XRD.

According to the model, the successive filling of sites with increasing pressure should result in a modulated isotherm slope (See Fig. 5.26b), and not in a gradual decrease of the isotherm slope as observed in the experiments (See all panels of Fig. 5.27). Within the measured pressure range, two interstitial sites, Mg_3Ti and Mg_4, contribute to the isotherms (See arrows in Fig. 5.27a). Due to stress and/or microstructural defects, these two interstitial sites most probably have a certain energy distribution for H occupation. This leads to a smearing of the isotherms and consequently to a monotonously decreasing isotherm slope.

The values of the CSRO parameter s as a function of composition are summarized in Fig. 5.31, together with s values obtained from Ti K-edge EXAFS measurements.[44] It is remarkable that the values derived from PTI modeling are in such good agreement with those calculated from the first coordination number around Ti atoms determined by EXAFS. In both cases, s is around 0.2 to 0.4 for Mg fraction $0.6 < y < 0.8$, with little variation upon composition. This confirms that a certain degree of chemical segregation does occur in systems with a positive enthalpy of mixing, even if a rapid quenching technique such as sputtering is used.

5.6　Summary and conclusions

Hydrogenation of Mg_yTi_{1-y} thin films prepared by co-sputtering of Mg and Ti is monitored continuously by Hydrogenography, electrically, with X-ray diffraction and EXAFS. All the properties are found to depend on the metal ratio in the parent alloy. Structurally, as-prepared films show only one crystalline phase over a wide composition range ($0.55 < y < 0.95$) that corresponds to a hexagonal Mg-Ti alloy. Hydrogenation induces a reversible phase transformation. The structure of the hydride depends on the metal ratio in the parent
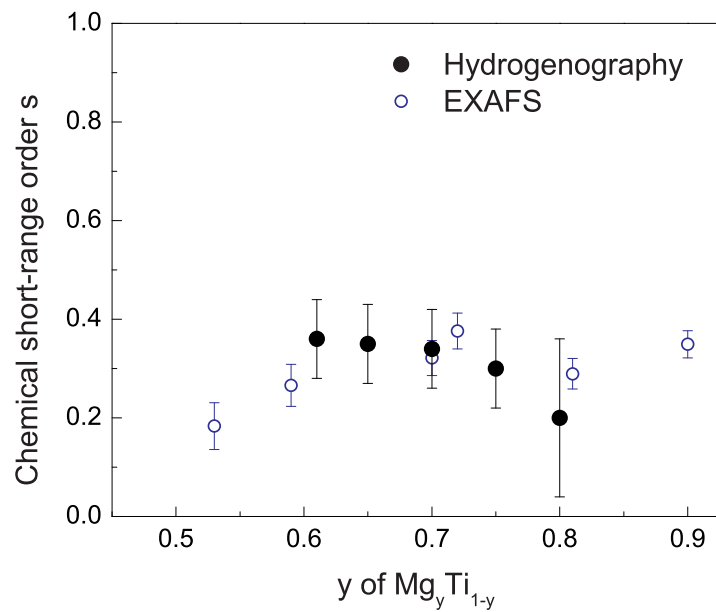
Figure 5.31: *Filled circles*, Chemical short-range order (CSRO) parameter s for various Mg_yTi_{1-y} compositions derived from hydrogenography data by means of the multi-site model described in Sec. 5.5.1. The increased error bar at $y = 0.80$ originates from a larger error in the metallic state transmission T_M at this composition. *Empty circles*, CSRO parameters from EXAFS measurements (as-deposited state, data from Baldi et al. [44]).

alloy. From XRD, the average structure resembles the rutile MgH_2 phase for high Mg content samples (y>0.87) and is fluorite otherwise ($y < 0.87$). At intermediate composition, coexistence of both phases is found. Highly reflective in the metallic state, the films are highly absorbing in the fully hydrogenated state. Such a highly absorbing state hints at the coexistence of a metallic and a semiconducting phase. It is however, not simply a composite material consisting of independent MgH_2 and TiH_2 grains. By means of EXAFS we show that in Mg_yTi_{1-y} thin films the microstructure cannot be interpreted as a random distribution of Mg and Ti atoms either, but that a certain level of local chemical segregation occurs, without affecting the long-range structural coherency of the film. The amount of segregation does not depend strongly on composition and is reversible upon cycling with hydrogen. The complete reversibility of the system and the structural coherence are probably related to the similarity of the molar volumes of TiH_2 and Mg. From a fundamental point of view, such a microstructure can explain the origin of the optical properties of Mg-Ti-H thin films.[194]

The contribution of Hydrogenography to this chapter is twofold: First, we show that pressure–optical-transmission–isotherms, the enthalpy and entropy of hydride formation can be measured optically and simultaneously on a large number of samples under exactly the same external parameters of pressure and temperatures. The two hydride phases (rutile and fluorite MgH_2-like) found by XRD depending on composition are seen in the isotherms as two distinct plateaus that are coexisting in the $0.85 < y < 0.89$ range. The very small pressure difference between these two plateaus confirms that the local geometry around a hydrogen atom (rutile or fcc) has little influence on the site energy in MgH_2. Finally, the unprecedent range of temperatures measured confirms the stability of the metastable $Mg_yTi_{1-y}H_x$ microstructure and opens up the systematic investigation of enthalpy-entropy compensation effects in metalhydrides.

Secondly, we show that optical isotherms recorded by Hydrogenography also contain information about the microstructure of $Mg_yTi_{1-y}H_x$ alloys. By modeling of the pressure–optical-transmission–isotherms with a multi-site lattice gas model including chemical short range order, we effectively use hydrogen as a probe for tracking the degree of chemical segregation in the immiscible $Mg_yTi_{1-y}H_x$ alloy system. The unusual shape of the experimental PTIs and the plateau pressures at various Mg atomic fractions y and temperatures are well reproduced by the multi-site lattice gas model, assuming the chemical short-range order parameter s as only free varying parameter. We find that the sloping behavior in the isotherms is reproduced assuming the gradual filling with pressure of Ti-containing tetrahedral sites (mainly Mg_3Ti sites in the pressure range measured), while the plateaus are due to the hydrogenation of Mg_4 sites. The CSRO s values derived from the multi-site modeling of Hydrogenography data agree well with s values determined from EXAFS mea-

surements. The non-zero L parameter shows that the volume of interstitial sites depends on the local chemical composition, and therefore indicates the presence of local modulations of the crystal lattice size.

The ability to model optical isotherms is a significant step in understanding the Hydrogenography results from the microstructural point of view and adds a valuable tool in the combinatorial search for new light-weight hydrogen storage materials. Its applicability is not limited to structurally coherent systems such as Mg-Ti-H that are only chemically segregated on the short-range, but also to hydride systems such as Mg-V-H that completely phase segregate on the long-range upon hydrogen cycling.[248] More generally, this multi-site lattice-gas model, by determining two essential characteristics of an alloy microstructure that are the CSRO parameter s and the lattice modulation parameter L, is complementary to experimental local-environment probes such as EXAFS or more elaborate modeling approaches using Reverse Monte Carlo simulation and Molecular Dynamics[204] to characterize alloys created between immiscible elements.

5.7 Appendix

5.7.1 Automatic fitting procedure for the equilibrium pressure determination

We developed an automatic MATLAB fitting procedure to handle the large number of PTIs (~ 500) generated by each Hydrogenography experiment on the Mg_yTi_{1-y} gradient thin films. The procedure chosen to routinely find the equilibrium pressure is to fit the isotherms. The equilibrium pressure is then calculated from the output parameters of the fit. Generally the isotherms consist in a gradual increase in optical transmission followed by a sloping plateau. We therefore approximate the gradual increase by a linear background, on top of which a Boltzmann function is added to simulate the plateau in optical transmission. The Boltzmann function is represented by the following equation:

$$\ln \frac{T}{T_\mathrm{M}} = \ln \frac{T_\mathrm{MH}}{T_\mathrm{M}} \left[1 - \frac{1}{1 + \exp\left(\frac{p - p_c}{\Delta p} \right)} \right] \tag{5.35}$$

with the final transmission T_MH, the center of plateau p_c and Δp, which is proportional to the plateau width, as fit parameters.

Figure 5.32 shows an example of the Boltzmann function used together with its first and second derivatives with respect to p. Depending on the type of experiment carried out, the equilibrium pressure can be chosen as the pressure at the center of the plateau (*vertical dotted line* in Fig. 5.32), which is directly the parameter p_c from the fit, or another function of p_c and Δp. As discussed

in Sec. 5.4.3, we take the equilibrium pressure for Mg$_y$Ti$_{1-y}$ films at the onset of plateaus in the isotherms, which we define here as $p_{\text{eq}} = p_c - 2\Delta p$ (*vertical full line* in the figure). Another option, used later in the numerical equilibrium pressure determination of Mg-Ni-Ti-H isotherms (See Chapter 6), would be to take the pressure at the maximum of the second derivative: within this fit procedure, it would be at $p_c + \ln(2 - \sqrt{3})\Delta p$ (*vertical dashed line*).

Practically, the fitting procedure works as follows: the user defines the interval taken for the linear background substraction, both in pressure and composition. The program then fits the background subtracted isotherms with a Boltzmann function, shows the graphical result and calculates the equilibrium pressure. This procedure is repeated until a satisfactory fit is obtained for all compositions. We show the graphical output of the fitting procedure for two very different examples in Fig. 5.33. In (a), the isotherm has a clear plateau and the background is almost horizontal. In (b), at the contrary, the determination of the onset of the very short, sloping plateau is only made possible by the *a priori* subtraction of a linear background.
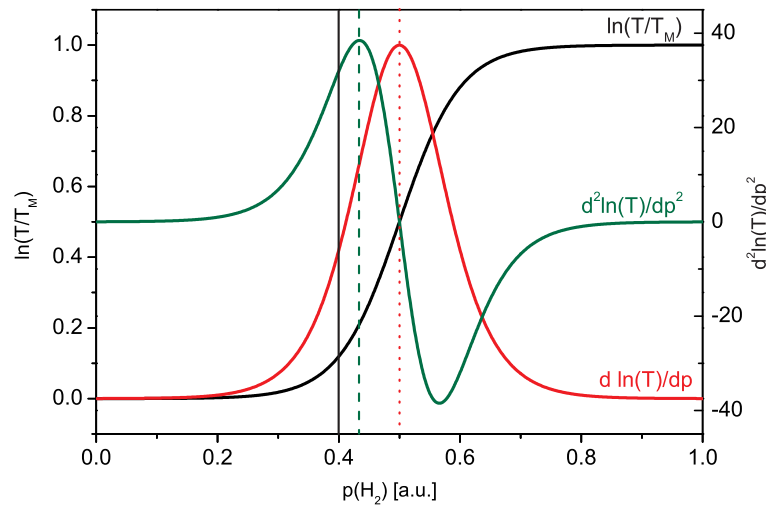
Figure 5.32: Example of a Boltzmann function (Eq. 5.35) used to extract automatically the equilibrium pressure from the Hydrogenography PTIs, together with its first and second derivatives. The chosen set of parameters for this example is: $\ln(T_{\text{MH}}/T_{\text{M}}) = 1$; $p_c = 0.5$ and $\Delta p = 0.05$. *Vertical lines*: the *dotted line* shows the position of the maximum of the first derivative p_c, the *dashed line* the position of the maximum of the second derivative $p_c + \ln(2 - \sqrt{3})\Delta p$, and the full line the equilibrium pressure $p_c - 2\Delta p$ as taken for the Mg$_y$Ti$_{1-y}$ experiments
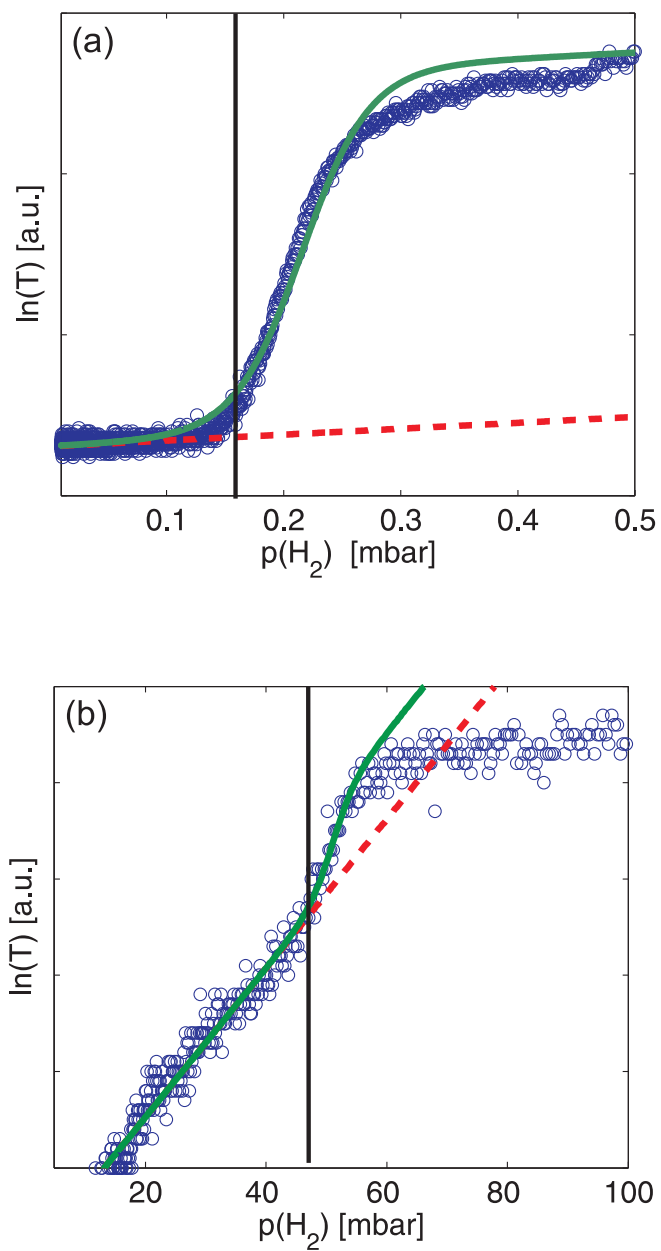
Figure 5.33: Two very different examples of automatic fitting of $Mg_yTi_{1-y}H_x$ PTIs. (a) $y = 0.80$, Temperature 297 K, (b) $y = 0.65$, Temperature 393 K. *Symbols*, data, *dashed line*, linear background, *full line*, Boltzmann fit. The vertical line indicates the position of the equilibrium pressure.

Chapter 6

The quaternary $\mathrm{Mg}_y\mathrm{Ni}_z\mathrm{Ti}_{1-y-z}\mathrm{H}_x$ system

6.1 Introduction

There have been many efforts to destabilize MgH_2 by alloying Mg with first-row transition metal (TM) elements.[102,249–251] For example, thin $\mathrm{Mg}_y\mathrm{Ti}_{1-y}\mathrm{H}_x$ films have remarkable optical, electrical and hydrogenation kinetics properties.[65,100,209] However, the addition of Ti does not destabilize MgH_2 significantly. Perhaps the most promising Mg-TM compound so far is the ternary hydride $\mathrm{Mg}_2\mathrm{NiH}_4$. This material has been studied extensively by experimentalists[66,66,102,117,252] and theorists.[253–255] $\mathrm{Mg}_2\mathrm{NiH}_4$ can theoretically store 3.6 wt. % of hydrogen reversibly. The hydride formation kinetics is also significantly improved compared to MgH_2, but the enthalpy of formation $\Delta H = -64$ kJ (mol H_2)$^{-1}$ of this hydride is still too large. In order to destabilize $\mathrm{Mg}_2\mathrm{NiH}_4$ it has been alloyed with other transition metals (Ti, Cr, Mn, Fe, Co, Ni, Cu and Zn).[45,256] Yang et al.[45] show in a comparative experimental study that Ti is perhaps the most promising candidate as a dopant to destabilize $\mathrm{Mg}_2\mathrm{NiH}_4$. The remarkable properties of the $\mathrm{Mg}_y\mathrm{Ti}_{1-y}\mathrm{H}_x$ and the $\mathrm{Mg}_y\mathrm{Ni}_{1-y}\mathrm{H}_x$ systems in addition to the work of Yang et al.[45] motivated us to explore[209,247] the $\mathrm{Mg}_y\mathrm{Ni}_z\mathrm{Ti}_{1-y-z}\mathrm{H}_x$ system using Hydrogenography.

6.2 Experimental

6.2.1 Sample preparation and analysis

Thin metallic $\mathrm{Mg}_y\mathrm{Ni}_z\mathrm{Ti}_{1-y-z}$ films are prepared in a AJA 7-gun ultra-high vacuum dc/rf magnetron co-sputtering system with a base pressure of 10^{-7} Pa. The film is deposited on a 7.6 cm diameter circular sapphire substrate at room temperature. By co-sputtering with 3 off-axis targets positioned every 120° on a circle we deposit a $\mathrm{Mg}_y\mathrm{Ni}_z\mathrm{Ti}_{1-y-z}$ thin film with a compositional gradient. Each position on the sample has a different Mg:Ti:Ni ratio. The gradient and the relative amount deposited of each element is controlled by
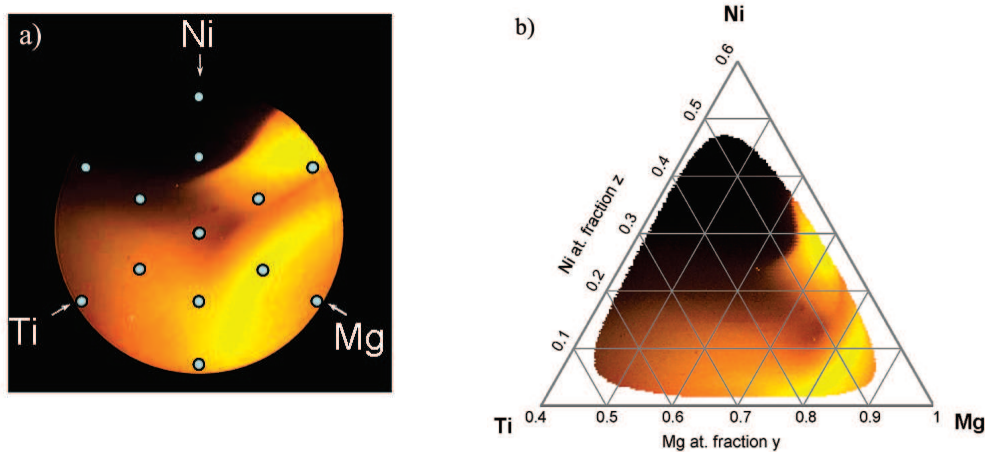
Figure 6.1: (a) A photograph of a partially loaded ($p(H_2) = 3 \times 10^3$ Pa and $\mathcal{T} = $ 333 K) $Mg_yNi_zTi_{1-y-z}H_x$ compositional gradient sample, which is illuminated from below with white light. We also indicate the triangular pattern of the 13 carbon substrates that we use for the RBS composition determination. (b) Ternary composition diagram representation of the optical transmission shown in (a).

the tilt angle and the power applied to the targets. These parameters thus determine the compositional range of the sample. As an unwanted side effect of the deposition technique the thickness in the film varies from 30 nm on the Mg-poor side to 100 nm on the Mg-rich side. The films are covered in-situ with a 20 nm Pd caplayer to promote H_2 dissociation and to prevent oxidation of the underlying film. The film is not heated above 363 K to prevent the formation of a Mg_6Pd alloy at the Pd-film interface.

The composition and thickness gradients are determined by Rutherford Backscattering Spectrometry (RBS) using 2 MeV He$^+$ ions with a 1 mm^2 spot size on films deposited on 13 glassy carbon substrates placed in a triangular radial pattern(see figure 6.1 a)). This deposition is done under the same sputtering conditions as the Hydrogenography wafers. The carbon substrates do not contribute to the background for energies above approximately 0.5 MeV. The Mg, Ni and Ti RBS peaks, measured at energies between 0.9 and 1.4 MeV, are well separated. This allows a precise (1-2 % accuracy) determination of the amount of each element deposited on the carbon substrates. The composition of each point on a Hydrogenography wafer is then interpolated from the RBS results. The relative composition accuracy is estimated to be between 2 % and 5 %, the closer to the six axis probed by RBS the better.

Figure 6.1a shows a photograph of partially loaded $Mg_yNi_zTi_{1-y-z}H_x$ gradient sample illuminated from below with white light. The transparent regions indicate hydrogen absorption. Each position on the sample represents a different ternary alloy composition, which is determined by RBS as described above.

The information in figure 6.1a can be transformed into a ternary composition diagram, which is shown in figure 6.1b. This figure indicates the composition range of the $Mg_yNi_zTi_{1-y-z}$ system probed in this study.

6.2.2   Experimental procedure and setup

After deposition the metallic films are transferred into an optical cell to monitor their transmission during hydrogenation. The whole cell is placed in an oven, which can control temperature from 305 K to 573 K. The complete thermal equilibration of the setup is verified by comparing the output of two PT-100 resistors placed at different locations in the oven, one of them being in contact with the sample holder. A 150 W diffuse white light source (the projector) illuminates the sample from the substrate side, and a 3-channel (RGB) SONY XC-003 Charged-Coupled Device (CCD) camera continuously monitors the transmitted light as a function of hydrogen pressure. The gas pressure increase is controlled by a MKS 248/250 forward Proportional-Integral-Differential (PID) system that regulates both inlet and outlet gas flows using electronic valves. 0.1 % and 4 % hydrogen in argon gas mixtures and pure H_2 gas are used to achieve hydrogen (partial) pressures between 10^{-1} Pa $<$ p(H_2) $< 10^6$ Pa.

The samples are hydrogenated and dehydrogenated twice before starting the pressure sweep measurements to relax the initial stress due to deposition. Hydrogen desorption is performed in a gas flow under 10^5 Pa of a 10 % oxygen in argon mixture. Typical pressure sweeps, in which we increase the pressure linearly in time, have a duration of 8.6×10^4 s. This large time is taken to ensure thermodynamic equilibrium throughout the experiment.

6.2.3   Data analysis

In total we measure 0.8×10^4 isotherms. Figure 6.2 shows several representative pressure–optical-transmission–isotherms (PTI). These are obtained by averaging the optical transmission during a pressure sweep experiment over 4×4 pixels to decrease noise. This figure demonstrates the variation in the shape of the PTI as a function of composition. The shape of the isotherms is discussed in more detail in subsection 6.3.2.

The equilibrium pressures determined by eye are indicated with dashed horizontal lines in figure 6.2. The equilibrium pressures for all compositions on the sample need to be determined automatically, since we measure $\sim 10^4$ isotherms in a single experiment. The numerical procedure used to determine the equilibrium pressure works as follows. First the PTI is smoothed using an adjacent averaging filter. The smoothed isotherm is then differentiated numerically. In Figs. 6.3 and 6.4 the numerical first derivatives are shown in dark grey together with the isotherms from figure 6.2. Note that the left axis only applies to the PTI. The maximum of the first derivative is located in the middle of the plateau and thus should indicate the equilibrium pressure.
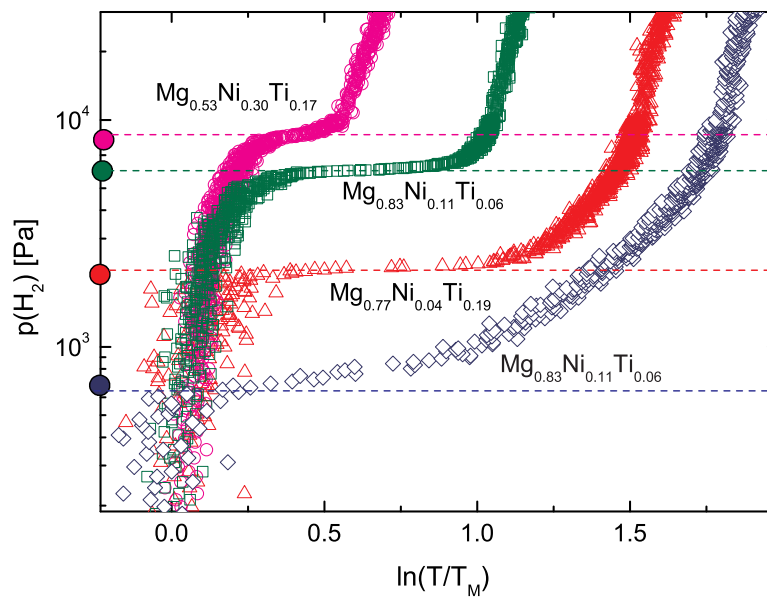
Figure 6.2: Selected pressure–optical-transmission–isotherms measured at
363 K. We also indicate the equilibrium pressure determined by eye (dashed
horizontal line) and the equilibrium pressure determined using a numerical
procedure (circles on the vertical axis).

However, many plateaus in the measured isotherms have a non-zero slope. Although a slope in the plateau can be an inherent material property (for example in Pd-Ag alloys[257]), in these isotherms it is mainly caused by a kinetic effect because the slope is reduced when the pressure increase rate is lowered. We expect that the true equilibrium pressure lies at the onset of the plateau in the PTI. The onset of the plateau can be determined in the following way. First we numerically differentiate the smoothed first derivative. The second derivative is shown in light grey in Figs. 6.3 and 6.4. This figure demonstrates that the position of the maximum in the second derivative indicates the onset of the plateau and is thus a good estimate of the equilibrium pressure.

The numerical procedure is optimized by choosing appropriate smoothing filters. We indicate the equilibrium pressures determined by an optimized numerical procedure in figure 6.2 with circles on the vertical axis. The numerical procedure leads to values for ΔH and ΔS typically within 1 kJ (mol H_2)$^{-1}$ and 4 J K^{-1} (mol H_2)$^{-1}$ respectively of manually determined values.

6.3 Results and discussion

6.3.1 Hydrogen induced change in optical transmission

Figure 6.5 shows the hydrogen induced change in optical transmission of a $Mg_yNi_zTi_{1-y-z}H_x$ gradient sample at several pressures during a pressure sweep experiment at $T = 333$ K. The change in transmission is dramatic and both the pressure at which this change occurs and the magnitude of the change depend strongly on composition. Although the composition of the as-deposited $Mg_yNi_zTi_{1-y-z}$ film varies continuously over the entire wafer, the photographs of the hydrogenated sample indicate clearly well-defined regions. There are several well known phases in the $Mg_yNi_zTi_{1-y-z}H_x$ system, namely TiH_2, MgH_2 and Mg_2NiH_4 in order of decreasing stability. In this subsection we aim to relate the observed regions, that differ in hydrogen absorption pressure, to the known phases in the system. This discussion is qualitative and the results must be confirmed by a quantitative analysis of the thermodynamics.

At low hydrogen pressures the Ti-rich side of the sample becomes slightly transparent (see figure 6.5b). Ti forms the metallic hydride TiH_2 with a bulk enthalpy of formation $\Delta H = -130$ kJ (mol H_2)$^{-1}$.[67] The small increase in optical transmission may be attributed to the absorption of hydrogen by Ti-rich sites.[258] As the pressure increases the Mg-rich side of the wafer becomes transparent (see figure 6.5c) due to the formation of MgH_2 ($\Delta H = -76$ kJ (mol H_2)$^{-1}$). At even higher pressures a change in transmission is observed in a region between the Mg and Ni targets (see figure 6.5d), which may be attributed to the formation of Mg_2NiH_4 ($\Delta H = -64$ kJ (mol H_2)$^{-1}$). Figures 6.5c-d also show transparent behavior for Mg-rich alloys. Recently Borsa et al.[65] found that in thin films Mg_yTi_{1-y} $(0.55 < y < 0.87)$ form hy-
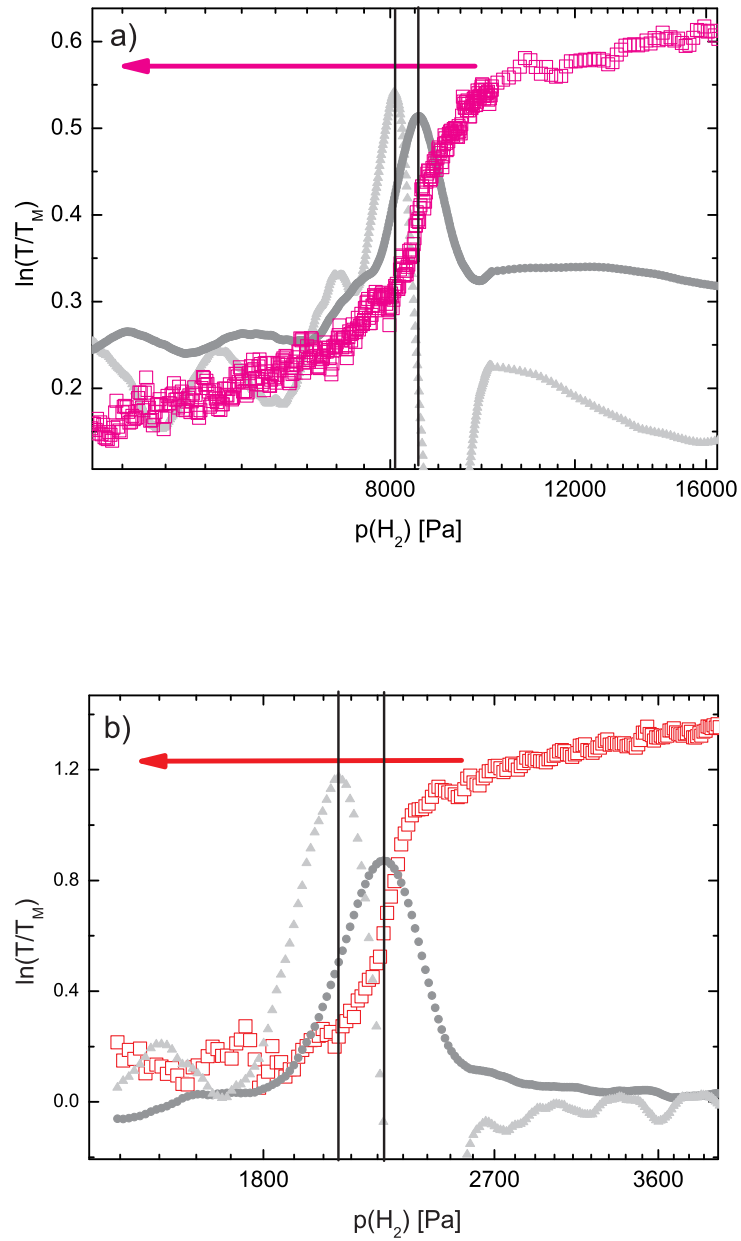
Figure 6.3: Demonstration of the numerical equilibrium pressure determination for the pressure–optical-transmission–isotherms shown in figure 6.2. The first and second derivatives are shown in light and dark grey respectively. Note that the vertical axis applies only to the pressure–optical-transmission–isotherm.
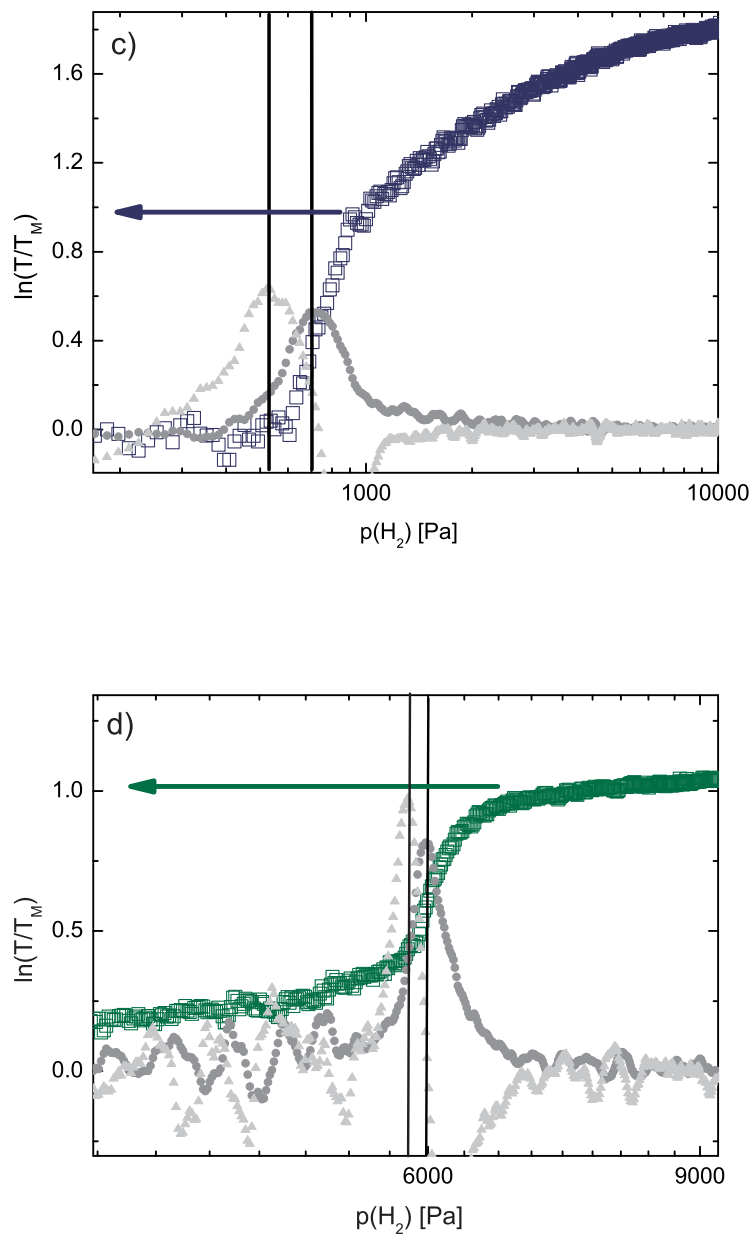
Figure 6.4: Demonstration of the numerical equilibrium pressure determination for the pressure–optical-transmission–isotherms shown in figure 6.2 (Continuation). The first and second derivatives are shown in light and dark grey respectively. Note that the vertical axis applies only to the pressure–optical-transmission–isotherm.
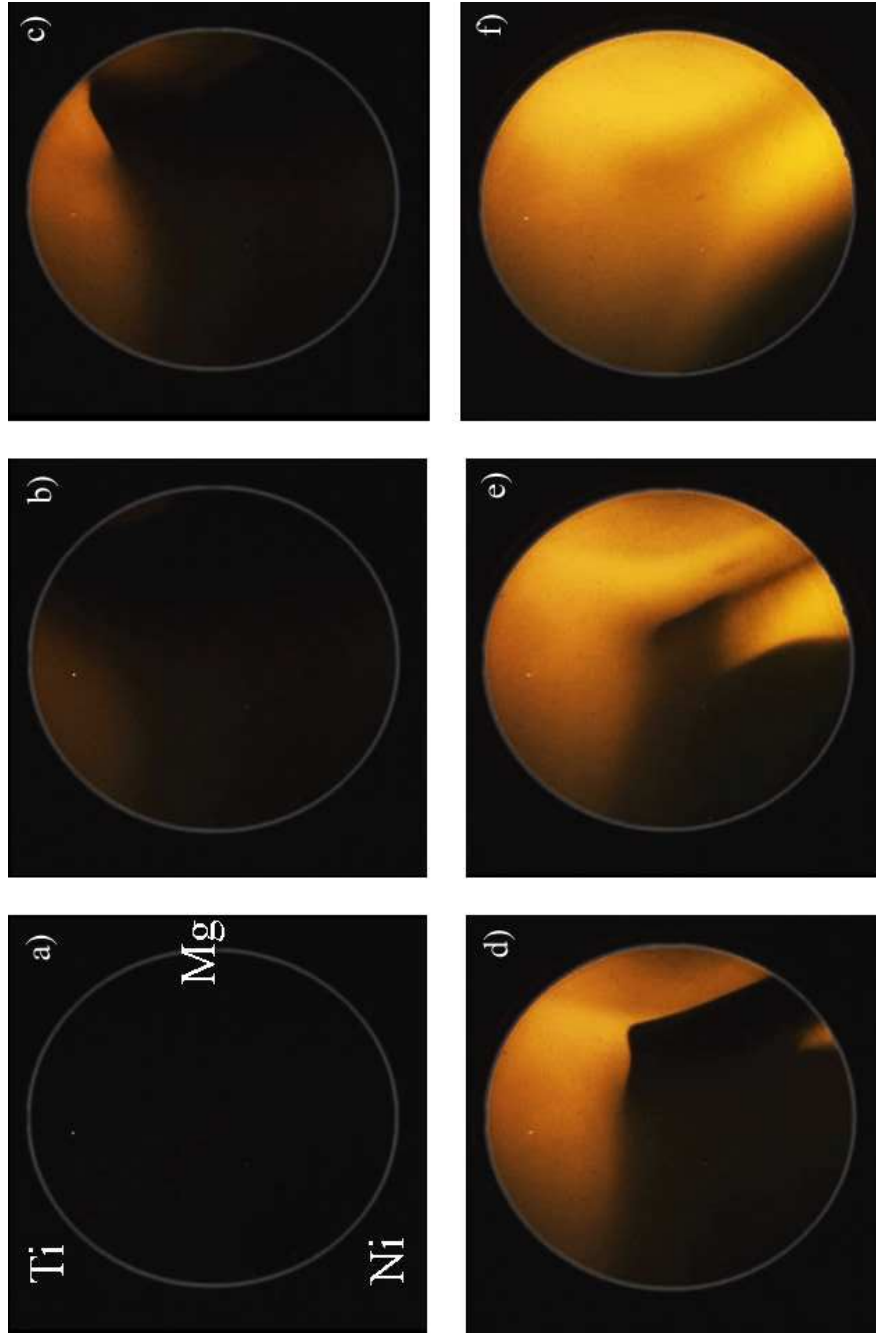
Figure 6.5: Evolution of the optical transmission of a $Mg_yNi_zTi_{1-y-z}H_x$ compositional gradient thin film illuminated from below during a hydrogen pressure sweep experiment at 333 K. The absorbed hydrogen induces a dramatic change in optical transmission. Although the composition of the as-deposited $Mg_yNi_zTi_{1-y-z}$ film varies continuously over the entire wafer, the photographs of the hydrogenated sample indicates clearly well-defined regions. We normalize the optical transmission to the transmission of the as-deposited state to remove optical effects due to the thickness gradient. a) The as-deposited state b) $p(H_2)=1.5\times10^2$ Pa c) $p(H_2)=6.5\times10^2$ Pa d) $p(H_2)=1.2\times10^3$ Pa e) $p(H_2)=1.8\times10^3$ Pa f) $p(H_2)=2.0\times10^3$ Pa.

drides with a fluorite structure. Although the kinetics of hydride formation of these $Mg_yTi_{1-y}H_x$ alloys is fast compared to rutile MgH_2, the thermodynamics of the two systems is surprisingly similar[209] despite the differences in structure and the presence of Ti.

In summary, a single pressure sweep experiment allows us to identify four hydride phases in the $Mg_yNi_zTi_{1-y-z}H_x$ system, namely fcc TiH_2, rutile MgH_2, fcc (fluorite) $Mg_yTi_{1-y}H_x$ ($0.55 < y < 0.87$) and monoclinic Mg_2NiH_4. Using Hydrogenography we can study efficiently how the thermodynamics of these phases is affected by doping. The qualitative analysis presented above, however, does not allow us to identify new quaternary hydride phases.

6.3.2 Pressure–optical-transmission–isotherms

To further demonstrate (see also figure 6.2) the variation in the shape of the isotherm as a function of composition we show PTIs of several $Mg_yNi_zTi_{1-y-z}H_x$ compositions in figure 6.6. These isotherms are smoothed using an adjacent averaging filter to remove the noise. In this subsection we discuss the shape of the isotherm in more detail.

The green curve exhibits a well-defined plateau and is representative for the majority of the isotherms we measured. The magenta curve has a similar shape, although this plateau has a non-zero slope. This slope is most likely caused by a slow kinetics. In contrast, the black curve exhibits an extremely flat and wide plateau. This curve represents compositions where the fluorite $Mg_yTi_{1-y}H_x$ phase is observed, which is known to have a fast kinetics and a hydrogen capacity comparable to MgH_2.[65] It is tempting to conclude that the later property is demonstrated in figure 6.6 because the optical transmission of the hydrogenated state of the black curve is comparable to that of Mg-rich compositions (red curve).

Very interesting behavior is observed in the red curve, which corresponds to a Mg-rich composition. The shape of this isotherm can be understood qualitatively as follows. The formation of MgH_2 has a very slow kinetics, which is limited by the hydrogen diffusion through the film. At the equilibrium pressure a thin shell of MgH_2 is formed on the Mg-grains, which results in a significant increase in optical transmission of the film. The hydrogenated layer grows inwards with a velocity $\sim \frac{1}{\sqrt{t}}$ and, consequently, the rate at which the sample becomes transparent decreases in time. This behavior is observed in the PTIs. Note that the pressure axis may also be read as a time axis, since the pressure is increased linearly in time.

The purple curve, which represents a Ti-rich composition, exhibits a gradual increase in transmission as a function of hydrogen pressure, but lacks a well defined plateau. Therefore, we can not assign an equilibrium pressure to these compositions. This also applies for Ni-rich alloys (not shown), although for these materials the increase in optical transmission is relatively small.

The blue curve exhibits a remarkable feature. This isotherm contains two plateaus, which suggests either a two-step hydrogenation reaction or the presence of coexisting hydride phases. Structural data, which is measured using X-Ray Diffraction (XRD) supports the latter scenario.[65] The plateau at a lower pressure is attributed to the rutile MgH_2 phase since it becomes more pronounced for increasing Mg content, and the second plateau is due to the fluorite $Mg_yTi_{1-y}H_x$ phase. Because of the coexistence of two plateaus we are not able to assign a single equilibrium pressure to these compositions. The region of coexistence of two plateaus extends to Mg-Ni-rich compositions. For these alloys a coexistence of Mg_2NiH_4 and MgH_2 is likely. A coexistence between these hydrides is also found by Lohstroh et al.[108] in this composition range in a study of the optical properties of Mg_yNiH_x ($2 \leq y \leq 10$) films.

6.3.3 Equilibrium pressure map at 313 K

By continuously recording the optical transmission as a function of the applied H_2 pressure, we construct the isotherms for each position (4×4 pixels) on the sample. From these isotherms we determine the equilibrium pressures for all positions on the sample using the numerical procedure described in subsection 6.2.2. Figure 6.7 shows a mapping of the equilibrium pressure of the $Mg_yNi_zTi_{1-y-z}H_x$ system at 313 K. The equilibrium pressure ranges over 2 orders of magnitude from 3×10^1 Pa to 1.5×10^3 Pa. In the black regions, the isotherms do not exhibit a plateau or have two plateaus in the pressure–optical-transmission–isotherms and this prevents us to a assign a (single) plateau pressure. The global structure of the pressure map is similar for all temperatures.

6.3.4 Enthalpy and entropy map

From pressure sweep experiments at 313 K, 323 K, 333 K, 353 K and 363 K we gather all the data necessary for the construction of Van 't Hoff plots for all compositions on the Hydrogenography wafer. An example of such a Van 't Hoff plot is given in figure 6.8b with the corresponding isotherms in figure 6.8a. From the Van 't Hoff plots at each position on the sample we obtain a ΔH and a ΔS map over the full range of compositions as shown in figure 6.9. The enthalpy and entropy plot show a striking and unexpected resemblance. We discuss this in more detail in subsection 6.3.5. We distinguish 4 main regions in the enthalpy map.

The first region is positioned in the lower right of the triangle at high ($y \geq 0.8$) Mg fractions. The red curve in figure 6.6 is representative for the PTIs in this region. As the Mg fraction increases from 0.84 to 0.88 the ΔH decreases from ≈ -50 kJ (mol H_2)$^{-1}$ to ≈ -60 kJ (mol H_2)$^{-1}$ and ΔS varies from ≈ -90 J K^{-1} (mol H_2)$^{-1}$ to ≈ -120 J K^{-1} (mol H_2)$^{-1}$ for increasing Mg fraction. The enthalpy of formation determined for the highest Mg fractions
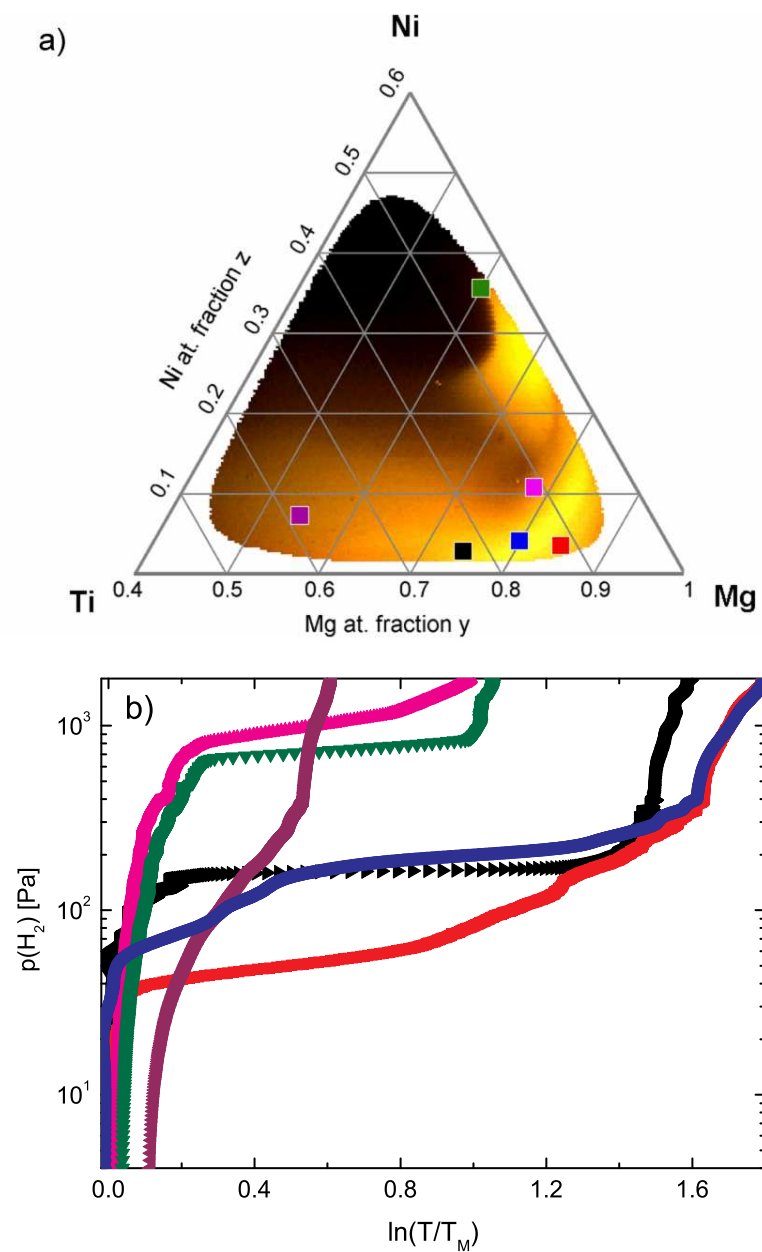
Figure 6.6: a) Ternary composition diagram representation of the optical transmission at 313 K of a partially loaded $Mg_yNi_zTi_{1-y-z}H_x$ compositional gradient sample, which is illuminated from below with white light. This diagram also indicates the compositions of several pressure–optical-transmission–isotherms shown in b). The noise in the optical transmission is removed using an adjacent neighbor averaging filter. The kink in the isotherms at 4×10^2 Pa is due to an increase in the pressure ramping speed.
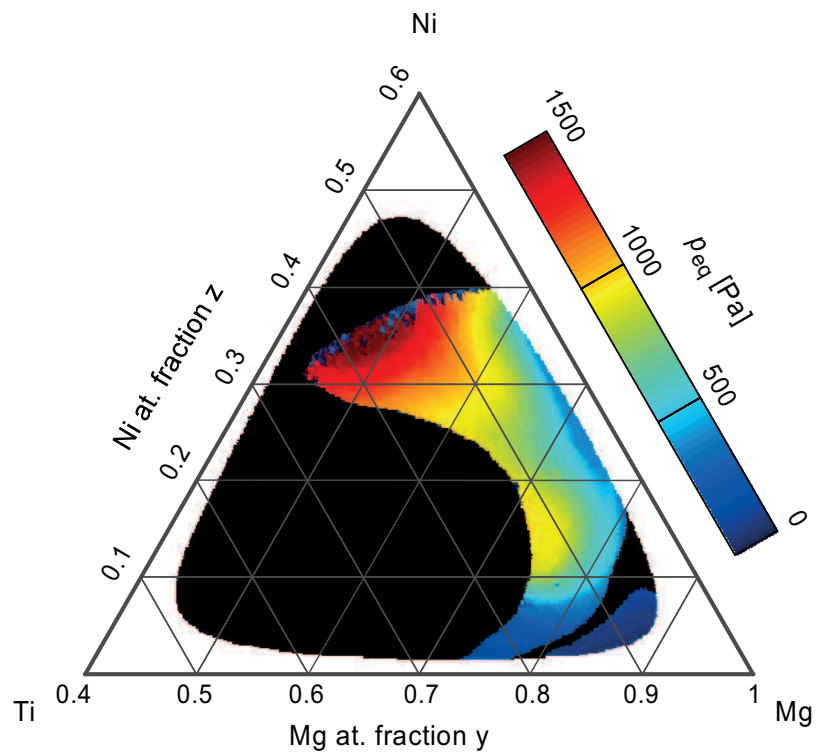
Figure 6.7: Ternary composition diagram showing the equilibrium pressure at 313 K of the $Mg_yNi_zTi_{1-y-z}H_x$ system in false colors. The regions in black correspond to compositions with an isotherm that does not have a well defined plateau (Mg-poor region) or with two plateaus (Mg-rich region).
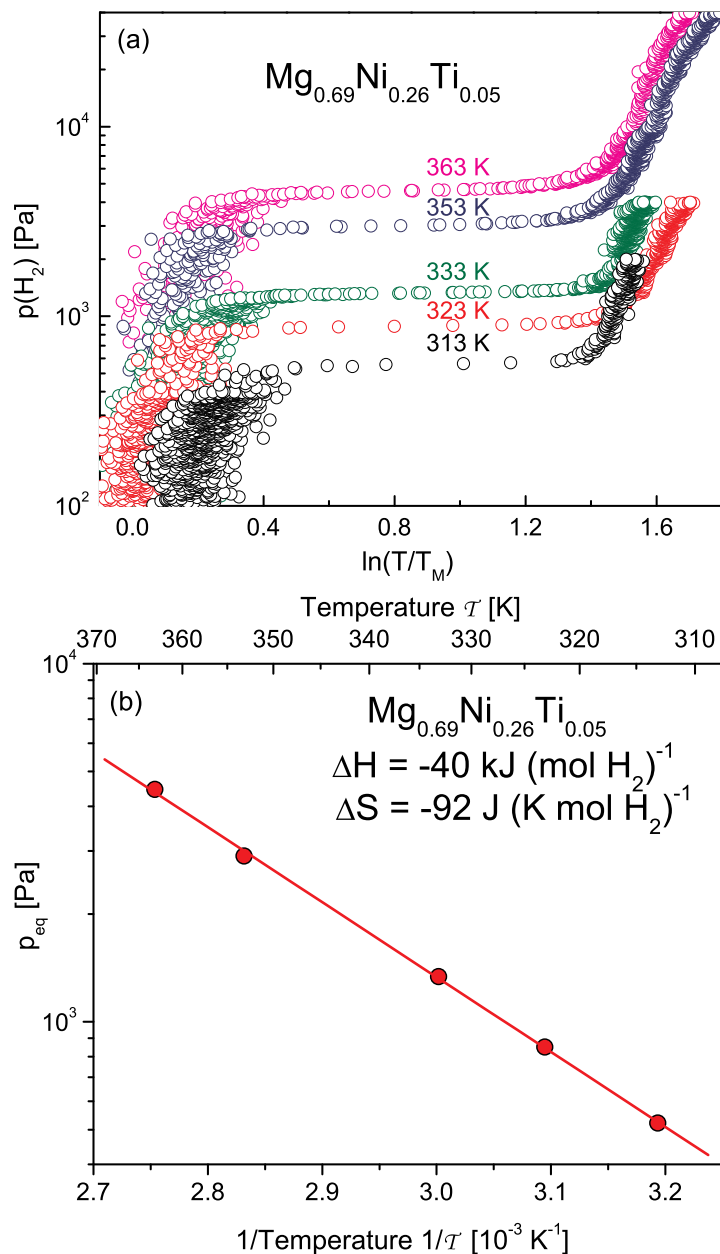
Figure 6.8: Pressure–optical-transmission–isotherms for five different temperatures (a) and the corresponding Van t Hoff plot (b) for $Mg_{0.69}Ni_{0.26}Ti_{0.05}$. The enthalpy of formation is ΔH=-40 kJ $(mol\ H_2)^{-1}$, which is significantly smaller than ΔH=-64 kJ $(mol\ H_2)^{-1}$ the bulk value of Mg_2NiH_4. However, the entropy change ΔS_0=-92 J K^{-1} $(mol\ H_2)^{-1}$ is significantly smaller than the entropy loss of H_2 gas, $-S^0_{H_2}$=-131 J K^{-1} $(mol\ H_2)^{-1}$, as in the case of the Pd-H system, which is discussed in chapter 3. This has the undesired effect of lowering the equilibrium pressure of the hydride.

is still considerably lower than the bulk value $\Delta H = -76$ kJ (mol H_2)$^{-1}$ of MgH_2. We would like to stress that in thin films the enthalpy of formation is often smaller than in the bulk due to the nano-grain microstructure of the film and due to partial clamping to the substrate, which inhibits the film from fully expanding upon hydrogenation.[36,75,101,259] An underestimation of the magnitude of ΔH may also be an experimental artifact. If the pressure sweep is carried out too fast the equilibrium pressure will be overestimated. At lower temperatures this effect is larger because of the slower kinetics. This error tends to reduce the slope of Van 't Hoff plots and thus leads to a smaller ΔH. A simple linear extrapolation of the measured data does, however, give $\Delta H \approx -80$ kJ (mol H_2)$^{-1}$ for a Mg fraction 1, value which is close to the bulk MgH_2 enthalpy. Cycling of the film may reduce clamping effects, thus leading to enthalpies closer to bulk values.

The second region is located in the lower part of the diagram with a Ni fraction less than 0.1 and a Mg fraction less than ≈ 0.8. The black curve in figure 6.6 is representative for the PTIs in this region. For these composition we find values around $\Delta H \approx -50$ kJ (mol H_2)$^{-1}$ and $\Delta S = -110$ J K^{-1} (mol H_2)$^{-1}$, which show little variation in this region as a function of composition.

The third region is the dark red region with an enthalpy of formation $\Delta H \approx -70$ kJ (mol H_2)$^{-1}$. The magenta curve in figure 6.6 is representative for the PTIs in this region. Although this region has a very large ΔH, the strikingly large $\Delta S \approx -160$ J K^{-1} (mol H_2)$^{-1}$ leads to equilibrium pressures even higher than the Mg_2NiH_4 compounds. The cyclability of these compositions is poor as the plateau in the isotherm deteriorates during cycling. This may hinder an accurate determination of the plateau pressure.

Finally, we discuss the region with a Ni fraction roughly between 0.2 and 0.4 (Region in dark blue in Fig. 6.9). The green curve in figure 6.6 is representative for the PTIs in this region. These compositions are of special interest. This region in the enthalpy map corresponds to hydrides with enthalpies of formation significantly less negative than those of MgH_2, the $Mg_yTi_{1-y}H_x$ system and the $Mg_yNi_{1-y}H_x$ system, which makes these materials interesting for hydrogen storage applications. Remarkable is that a relatively small addition of Ti to $Mg_yNi_{1-y}H_x$ does not result in an enthalpy value intermediate between that of the $Mg_yTi_{1-y}H_x$ and $Mg_yNi_{1-y}H_x$ systems. Unfortunately the entropy change $\Delta S = -92$ J K^{-1} (mol H_2)$^{-1}$ is significantly smaller than the standard hydrogen gas value $S^0_{H_2} = 131$ J K^{-1} (mol H_2)$^{-1}$ as in the case of the Pd-H system, which is discussed in chapter 3. This has the undesired effect of lowering the equilibrium pressure of the hydride. Nevertheless, at room temperature the equilibrium pressure of $Mg_{0.69}Ni_{0.26}Ti_{0.05}H_x$ is an order of magnitude larger than that of Mg_2NiH_4 and two orders of magnitude larger than that of MgH_2. In addition, Ti doping of Mg_2NiH_4 (3.6 weight %) reduces the reversible hydrogen storage capacity only marginally. We determined elec-

trochemically that 3.2 weight % of hydrogen can be stored reversibly for a compound with the composition $Mg_{0.69}Ni_{0.26}Ti_{0.05}$.[209] See figure 6.8 for the isotherms and Van 't Hoff plot of this composition.

6.3.5 Enthalpy-entropy compensation effects

In this subsection we discuss the surprising correlation between the ΔH and ΔS values measured with Hydrogenography on the $Mg_y Ni_z Ti_{1-y-z} H_x$ system. In figure 6.10a we show a plot of ΔH as a function of ΔS. We use different colors to indicate various regimes in the ternary composition diagram, which is shown as a legend. This plot demonstrates a remarkable linear correlation between ΔH and ΔS. We indicate the slopes, which have the unit of temperature, for different regimes in the figure. For some regimes this slope is determined using a linear regression fit. In these cases we also give the standard error. The slope is called the compensation temperature $\mathcal{T}_{comp}$. $\mathcal{T}_{comp}$ differs between the various regimes and ranges from 205 K to 424 K. The behavior of the green and black data points partially deviates from the simple linear correlation shown by the other data. In figure 6.10b we show representative Van 't Hoff plots for the various regimes. The strong correlation between ΔH and ΔS is known as enthalpy-entropy compensation (see Chapter 5 for definitions and references). Possible mechanisms leading to compensation effects deserve to be investigated in future Hydrogenography experiments.

The harmonic mean temperature $\mathcal{T}_H = 1/\langle 1/\mathcal{T} \rangle$ of the $Mg_y Ni_z Ti_{1-y-z} H_x$ Hydrogenography experiment is 336 K. For the regime represented by the magenta points in figure 6.10 we find that $\mathcal{T}_{comp}$ agrees with $\mathcal{T}_H$ within 1.1 σ. We would like to remind the reader that for these compositions the quality of the plateau is poor which causes large errors in the determination of ΔH. It is thus likely that the data in this region provide an illustration of a fake compensation effect due to an error in the analysis. For all other regimes $\mathcal{T}_H$ deviates significantly from $\mathcal{T}_{comp}$, which points in the direction of genuine compensation effect.
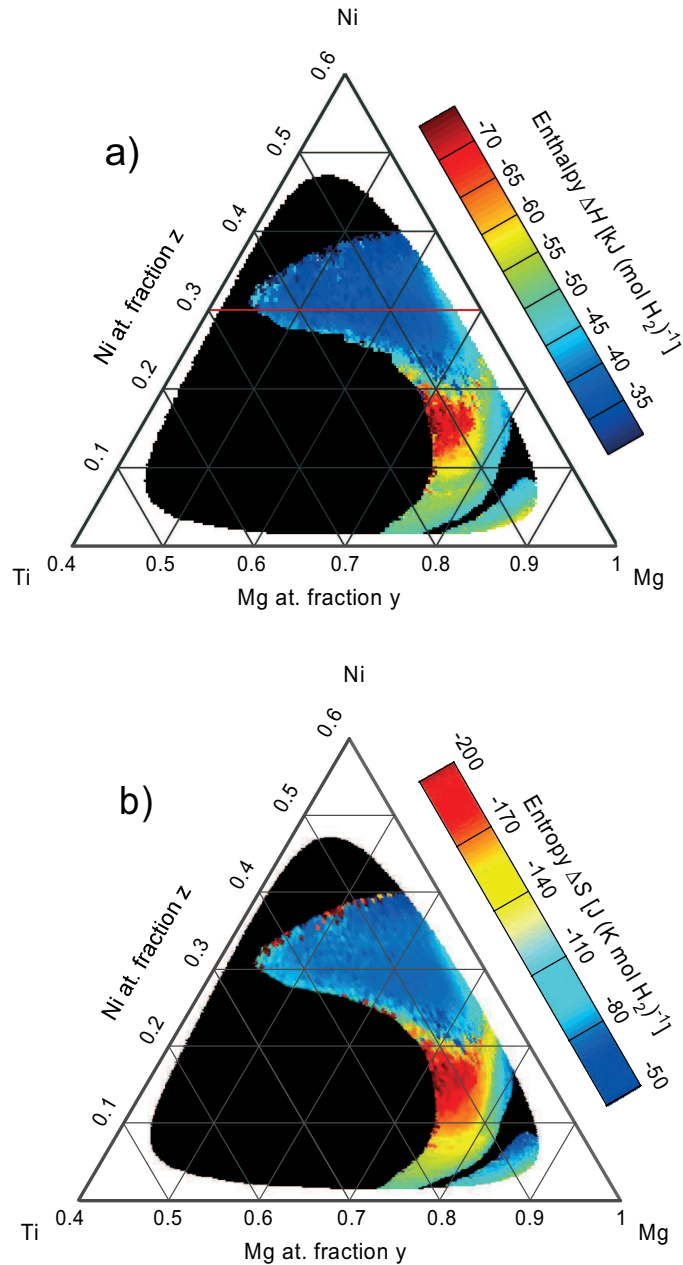
Figure 6.9: (a) Enthalpies ΔH and (b) entropies ΔS of hydride formation de-termined from the Van t Hoff plots for each pixel of the $Mg_yNi_zTi_{1-y-z}H_x$ gra-dient film. Regions in black corresponds to alloys that do not exhibit plateaus or for which two plateaus coexist. The region of interesting hydrogen storage materials is in dark blue.
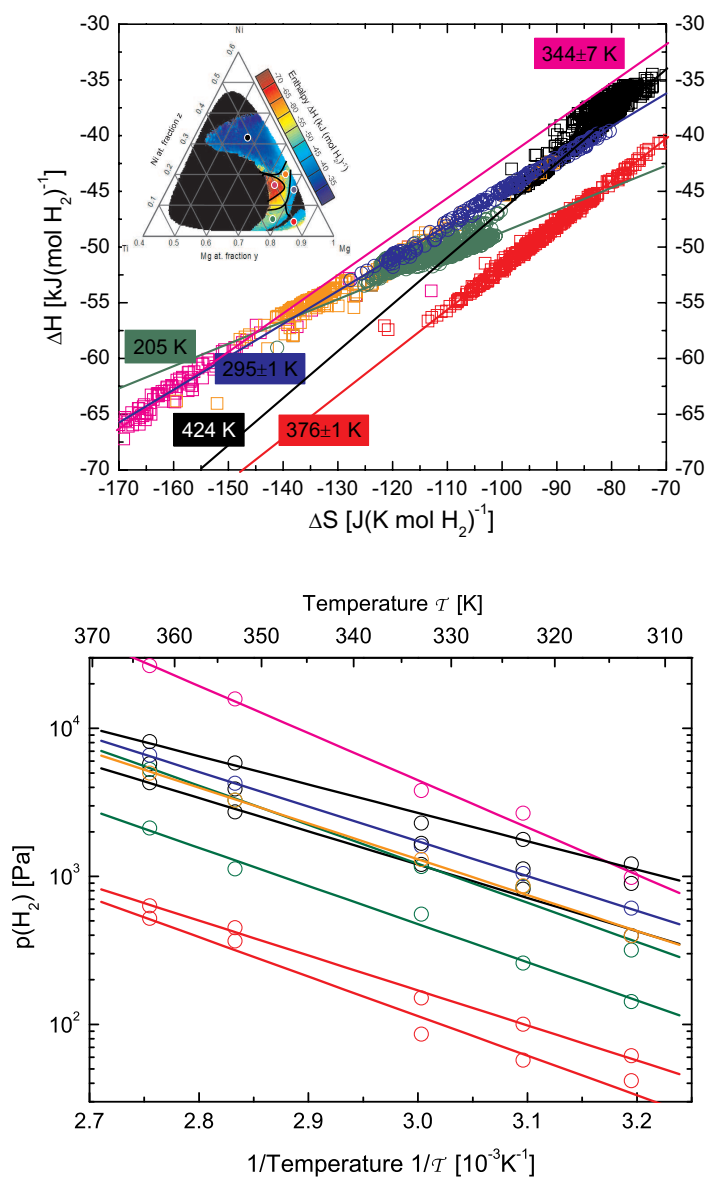
Figure 6.10: (a) Plot of the enthalpies ΔH of formation against the entropies of formation ΔS_0. The colors in this plot indicate several distinct regimes in the ternary composition diagram which is shown in the graph as a legend. We also indicate the slope of the lines for the various regions. In some cases the slope is determined with a linear regression fit and thus we also indicate the standard error. The orange points have a slope comparable to the blue points (b) Van 't Hoff plots for the different regimes shown in a) to demonstrate the linearity of the Van 't Hoff plots.

6.4 Conclusions and Outlook

In this chapter we demonstrated the combinatorial potential of Hydrogenography on the $Mg_yNi_zTi_{1-y-z}H_x$ system. We determined the enthalpy change ΔH and the entropy change ΔS of the hydrogenation reaction. These experiments allowed us to identify a narrow range of compositions with favorable thermodynamic properties. We found that doping a $Mg_yNi_{1-y}H_x$ alloy with small amounts of Ti lowers the heat of formation significantly to values around $\Delta H = -40$ kJ (mol H_2)$^{-1}$. Remarkably this doping does not result in an enthalpy value *intermediate* between that of the $Mg_yTi_{1-y}H_x$ and $Mg_yNi_{1-y}H_x$ systems, but in an enthalpy value less negative than both systems (See Fig. 6.11).
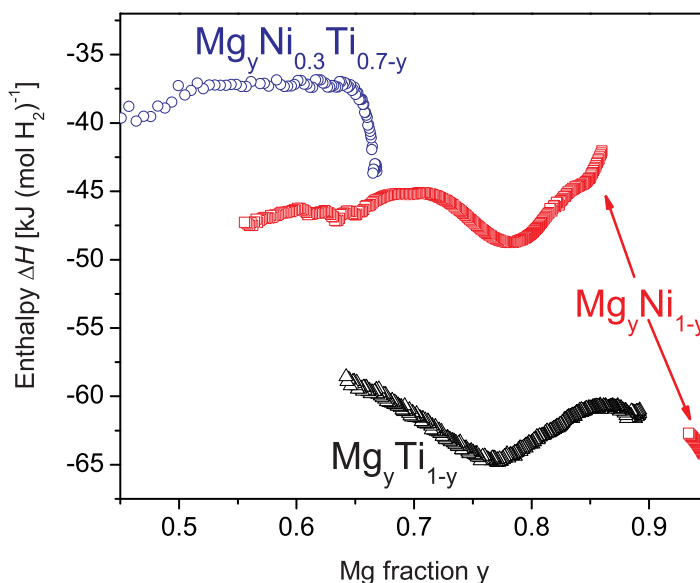
Figure 6.11: Compositional dependence of the hydride enthalpy of formation for Mg_yNi_{1-y}, Mg_yTi_{1-y} and $Mg_yNi_{0.3}Ti_{0.7-y}$ (this latest compositions correspond to the *red line* in Fig. 6.9a). Quite surprisingly this ternary alloy forms less stable hydrides than the other two binary alloys. Note that as expected the enthalpy value for $Mg_yNi_{0.3}Ti_{0.7-y}H_x$ tends to the $Mg_yNi_{1-y}H_x$ enthalpy for $y \to 0.7$.

We report that the composition $Mg_{0.69}Ni_{0.26}Ti_{0.05}$ optimally combines a favorable thermodynamics with a fast kinetics comparable to Mg_2NiH_4 and a reasonable hydrogen storage capacity (3.2 weight %). The entropy change $\Delta S_0 = -92$ J K^{-1} (mol H_2)$^{-1}$, however, is significantly smaller than the stan-

dard hydrogen gas value $S_{H_2}^0 = 131$ J K^{-1} (mol H$_2$)$^{-1}$, as in the case of the Pd-H system discussed in Sec. 3.3.1. This has the undesired effect of lowering the equilibrium pressure.

Although Hydrogenography is a powerful method, it is based on thin films that are very often X-ray amorphous. It is thus difficult to determine experimentally the phases that are formed in the as-deposited and hydride state of the system. The destabilization mechanism brought by Ti-doping has therefore been elusive. To elucidate this mechanism, C. P. Broedersz et al. presented a theoretical approach[260] in which likely hydrogenation scenarios in the Mg$_y$Ni$_z$Ti$_{1-y-z}$H$_x$ system are modeled with density functional theory (DFT). By calculating the formation enthalpy ΔH for each case and comparing these calculations with the experimental results they were able to single-out a scenario that is most likely responsible for the observed destabilization. They concluded that in the range of compositions interesting for application purposes (with a Ni fraction between 0.2 and 0.4), the energetically most favorable as-deposited state is a coexistence of Mg$_2$Ni and TiNi intermetallics, while the hydrided state consists of a single Ti-doped Mg$_2$NiH$_4$ phase. The destabilization mechanism by the Ti dopant occurs then probably as follows: Ti stabilizes the as-deposited state significantly by binding strongly to Ni atoms in a TiNi-like way. When the sample is hydrogenated the strongly bound Ti does not separate to form TiH$_2$. The Ti dopant is therefore embedded in the Mg$_2$NiH$_4$ structure and substitutes either Mg or Ni, without lowering the energy of the hydride significantly. This leads to the small (in absolute value) enthalpy of formation of Ti-doped Mg$_2$NiH$_4$.

The reversible and fast transformation from two phases to one phase upon hydrogenation at the moderate temperatures used in the Hydrogenography experiments (313 K$< T <$ 363 K) may be enabled by the small nm-sized grain microstructure of the system. This beneficial microstructure prohibits us, however, from measuring the phases using X-ray diffraction techniques. To gain information about the microstructure and test the DFT predictions, a local probe technique like EXAFS for which long-range order is not a prerequisite is ideal. We did some preliminary Ti K-edge EXAFS measurements on the as-deposited state for a Mg$_{0.67}$Ni$_{0.25}$Ti$_{0.13}$ composition, which is within the compositional region with favorable thermodynamics. The EXAFS magnitude and imaginary part of the phase-uncorrected Fourier transformed $\chi(k)$ is are shown in Fig. 6.12. The *dotted, dashed* and *full vertical lines* indicate the (phase uncorrected) distances between a Ti atom and a Mg, Ti or respectively Ni nearest neighbor in Mg$_y$Ti$_{1-y}$[44] or TiNi[261] films. The maximum amplitude of the EXAFS signal gives the first nearest neighbor (phase uncorrected) distance. For the Mg$_{0.67}$Ni$_{0.25}$Ti$_{0.13}$ thin film, we find a ~ 2.1 Å distance, which is in accordance with a Ti-Ni bond length. The fact that in the as-deposited state, Ti atoms are surrounded first by Ni atoms and obviously not by Mg or other Ti atoms pleads for the formation of a short-range ordered TiNi alloy

and agrees with the conclusions drawn by DFT calculations. More EXAFS measurements are planned on the Ti and Ni K-edges of these alloys to check whether the whole hydrogenation scenario predicted (Mg_2Ni + TiNi $\Leftrightarrow$ Ti-doped Mg_2NiH_4) is experimentally confirmed.
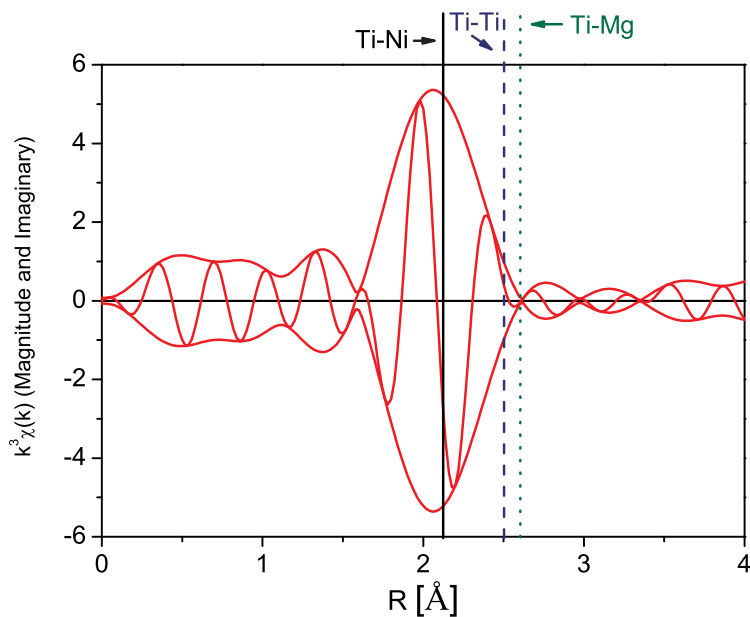
Figure 6.12: Magnitude and imaginary part of the phase-uncorrected Fourier transformed Ti K-edge k^3-weighted $\chi(k)$ EXAFS signal for $Mg_{0.67}Ni_{0.25}Ti_{0.13}$ in the metallic, as-deposited state. The *dotted, dashed* and *full vertical lines* indicate the (phase uncorrected) distance between a Ti atom and its Mg, Ti or respectively Ni nearest neighbor in Mg_yTi_{1-y}[44] or TiNi[261] films.

The Hydrogenography $Mg_yNi_zTi_{1-y-z}H_x$ experiments also reveal a remarkable linear correlation between the ΔH and ΔS_0 data. This phenomenon, which is not understood, is known as enthalpy-entropy compensation. Our combinatorial method has resulted in a demonstration of the compensation effect where all samples are produced and measured under exactly the same conditions, and thus Hydrogenography provides an excellent means to study this effect. A mixing process is a promising candidate to explain the observed compensation effect: If during hydrogenation two separated phases (Mg_2Ni + TiNi) transform into one (Ti-doped Mg_2NiH_4), it will affect the entropy change of the reaction. Since the entropy of the mixed state is higher than of the segregated state, ΔS increases (becomes more positive), which is consistent with the experimental data. In addition, the entropy and enthalpy correlate over a large range of compositions for a simple binary mixture model. In addition to

the the fundamental interest, compensation effects may be of crucial importance for hydrogen storage applications, since compensation constraints the tuning possibilities of the operating conditions of materials by doping.

Chapter 7

Towards alanates: $Mg_yAl_{1-y}H_x$ thin films

7.1 Introduction

The availability of a safe and effective way to store hydrogen reversibly is one of the major issues for its large scale use as an energy carrier.[5]

For this purpose, the ideal hydrogen storage material should have the following properties: high gravimetric and volumetric hydrogen density, fast kinetics of (de)hydrogenation near ambient temperature, long term stability and good thermal conductivity for removing the reaction heat. The availability and affordable price of the alloy constituents is also of importance.

As the understanding of hydride materials developed and their limitations for application in the automotive sector became clear, attention shifted away from simple binary or ternary hydride systems to compounds or composites consisting of multiple elements. However, the number of possible combinations grows factorially, and a nearly infinite parameter space opens. In the standard approach followed so far, the exploratory search for new light-weight hydrogen storage materials is very time consuming as a bulk sample is needed for each composition investigated. We present here a new combinatorial method that is capable of exploring typically 10^3 samples simultaneously. It is based on the use of large area thin film samples with controlled chemical composition gradients of two, three or more metal constituents.[57]

To monitor the hydrogen absorption, we exploit the fact that most complex metal-hydrogen systems undergo a metal-insulator transition upon hydrogen exposure.[50,66,103,262–266] By following the optical changes during hydrogenation, we are thus able to map simultaneously all the hydride-forming compositions of the gradient thin film. We use the term *Hydrogenography* for this direct mapping of the hydrides formed in a large compositional gradient sample, enabling the investigation of a full metal-hydrogen ternary phase diagram with one sample.

In this chapter, we exemplify this technique with $Mg_yAl_{1-y}H_x$ compositional gradient thin films and the hydrogenation properties thereof. Pure

magnesium reacts reversibly with hydrogen to form MgH_2. It is thus considered to be one of the most important candidates for the reversible storage of hydrogen due to its light weight, low cost and high hydrogen gravimetric density (7.6 wt%). However, its hydrogen ab/desorption kinetics is unsatisfactory due to the very low diffusion of hydrogen in MgH_2.[101] However, preparing nanocrystalline Mg[267] by ball milling and adding transition metals[256,268] or transition metal oxides[269] as catalysts improves the kinetics tremendously. This has initiated many studies on Mg-based hydrides, some of them with Al additions.[270–272] Another promising class of materials for hydrogen storage are the Al-based complex hydrides, since Bogdanovic and Schwickardi showed that the decomposition of sodium alanate, $NaAlH_4$, can be made reversible by the addition of Ti and Fe compounds as catalysts.[13] This stimulated the investigation of many other complex systems.[14–16,273] Among them, magnesium alanate, $Mg(AlH_4)_2$, with 9.3 wt% of hydrogen, is also a potential hydrogen storage material. It was recently synthesized in bulk form and its decomposition studied.[274,275] Furthermore, theoretical calculations predict $Mg(AlH_4)_2$ to be a large gap semiconductor.[264,265] The potential synthesis of magnesium alanate from the elements as well as the formation of MgH_2 as a function of the Al content triggered thus our interest for the $Mg_yAl_{1-y}H_x$ system in gradient thin films. Figure 7.1 is a summary of the hydrogenation properties of the Mg-Al-H system reported in the literature.[231] Various sample preparation methods (bulk, ball milled, microcrystalline) have been used. The atomic H content x in $MgAl_zH_x$ is displayed as a function of $z = [Al]/[Mg]$. For $z = 0$, the hydride formed is the rutile phase α-MgH_2. With increasing Al content, $x \le 2$ for $y < 2$. Given the uncertainty in the data, we conclude that $MgAl_zH_x$ segregates in MgH_2 and Al for $z < 2$. The only known Mg-Al-H hydride is the magnesium alanate, $Mg(AlH_4)_2$ (i.e. $z = 2$). This compound has been successfully synthesized by chemical reaction and its thermal desorption behavior has been studied.[274,276] However, to use magnesium alanate as an hydrogen storage material, it is important that it can be formed directly from the metallic elements Mg and Al at a moderate H_2 pressure.

In this chapter, we investigate the structural, optical and dc electrical properties of $Mg_yAl_{1-y}H_x$ ($0.2 \le y \le 0.9$) gradient thin films covered with Pd/Mg before and after exposure to hydrogen. We use Hydrogenography to map simultaneously all the hydride forming compositions and the kinetics thereof in the gradient thin film. Metallic Mg in the Mg_yAl_{1-y} layer undergoes a metal-to-semiconductor transition and MgH_2 is formed for all Mg fractions y investigated. The presence of an amorphous Mg-Al phase in the thin film phase diagram enhances strongly the kinetics of hydrogenation. In the Al-rich part of the film, a complex H-induced segregation of MgH_2 and Al occurs. This uncommon large-scale segregation is evidenced by metal and hydrogen profiling using Rutherford backscattering spectrometry and resonant nuclear analysis based on the reaction $^1H(^{15}N,\alpha\gamma)^{12}C$. Besides MgH_2, an additional semicon-
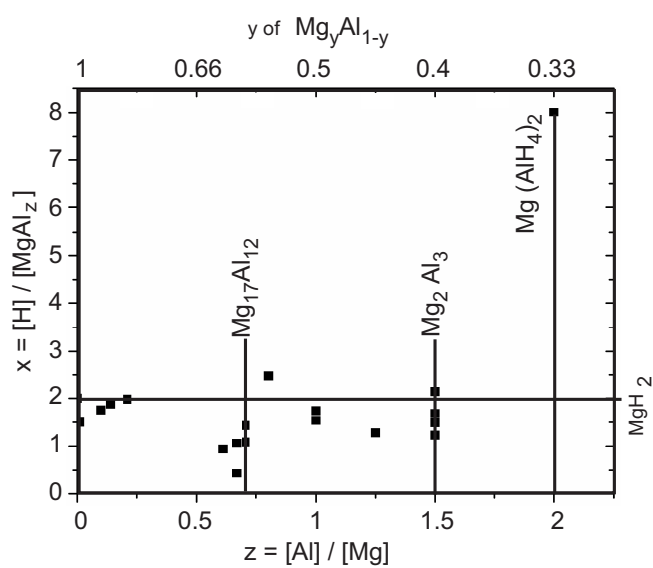
Figure 7.1: Summary of studies reporting on the hydriding of $MgAl_zH_x$.[231] The atomic hydrogen content x in $MgAl_zH_x$ is plotted as a function of z = [Al]/[Mg]. The top scale shows the Mg molar fraction y used throughout this chapter.

ducting phase is found by electrical conductivity measurements around an atomic [Al]/[Mg] ratio of 2 ($y = 0.33$). This suggests that the film is partially transformed into $Mg(AlH_4)_2$ at around this composition. We demonstrate that this approach sheds light on the complex hydrogenation process and thereby helps to optimize multi-component hydrogen storage systems.

7.2   Experimental

The samples consist of a Mg_yAl_{1-y} compositional gradient layer of typically 100 to 200 nm thickness covered with a 1 nm Mg layer to avoid an Al-terminated surface. The layers are capped with 10 nm of Pd to prevent oxidation and promote hydrogen dissociation and absorption. This stack of layers is sputtered at room temperature on 5 x 70 mm glass substrates by off-centered dc/rf magnetron sputtering sources. The argon pressure during deposition is $3 \cdot 10^{-3}$ mbar and the background pressure lower than 10^{-8} mbar. The chemical composition range is adjusted by varying the angle of both Mg and Al sources relative to the sample normal. Sputter rates in the center of the sample are determined *in situ* before deposition by a quartz crystal monitor. To study the influence of Ti as a catalyst/dopant on the hydride formation, we codeposit also "Ti doped" samples that consist of a Mg_yAl_{1-y} gradient layer doped with 3 at.% Ti. In "Ti covered" samples, a 5 nm Ti homogeneous buffer layer is deposited between the Mg_yAl_{1-y} and Pd layers.

The total thickness is measured every 5 mm by a DEKTAK[3] stylus profilometer. The dc electrical resistivity is recorded in a Van der Pauw configuration[121] on electrically separated zones every 3 mm. In the hydrogenated state, the metallic Pd overlayer shunts the semiconducting $Mg_yAl_{1-y}H_x$. To correct for this effect, the $Mg_yAl_{1-y}H_x$ and Pd layer are treated as two parallel resistors.[277]

The precise chemical compositions and in-depth homogeneity of the film are determined by Rutherford Backscattering Spectrometry (RBS) using 2 Mev He[+] ions on simultaneously deposited layers on glassy carbon substrates. These substrates do not contribute to the background for energies above approximately 0.5 MeV, allowing a precise determination of the amounts of each element in the sample as a function of depth. Besides the metals (Mg, Al, Pd), the oxygen content is obtained. Moreover, it is also possible to distinguish between oxygen adsorbed at the surface, absorbed in the film or adsorbed at the substrate-film interface. The measured RBS data are analyzed with the RUMP software.[278,279] As Mg and Al have nearly the same atomic number (12 and 13, respectively), RBS fits are used to deconvolute the Mg and Al contributions to the spectra. Further details about the RBS method can be found elsewhere.[280]

After deposition, metallic films are transferred into an optical cell to monitor their optical transmission during hydrogenation. The whole cell is placed

in a furnace to control temperature up to 300 °C. A 150 W diffuse light source illuminates the sample from the substrate side, and a 3-channel (RGB) SONY XC-003 charged-coupled device (CCD) camera monitors the transmitted light. Images during hydrogen ab/desorption processes are taken at different time intervals Δt (1 s $< \Delta t <$ 100 s) depending on the overall kinetics of the $Mg_yAl_{1-y}H_x$ composition under consideration.

Additional reflection and transmission measurements of the hydrogenated state are performed in a Perkin Elmer Lambda 900 diffraction grating spectrometer with an energy range from 0.495 to 6.19 eV (λ = 2500 - 200 nm). X-ray diffraction (XRD) measurements are performed in a BRUKER D8 spectrometer using Cu K_α radiation in a θ-2θ configuration.

The ^{15}N Nuclear Resonance Analysis (NRA) method is used for hydrogen depth profiling of the sample, and is performed at the Tandem accelerator in Uppsala. The technique is based on the $^1H(^{15}N,\alpha\gamma)^{12}C$ nuclear resonance reaction and provides the depth profile as well as the total amount of hydrogen per metallic atom.[281] For the profiling, the sample is bombarded with ^{15}N ions with an energy equal to or above the resonance energy (6.385 MeV). Upon penetration, the ions lose energy, and, at the depth where the ions have reached the resonance energy, the probability for the reaction is greatly enhanced. The depth resolution is typically 1 nm close to the surface but deteriorates with increasing depth due to energy straggling. The 4.43 MeV gamma rays are detected in a BGO detector placed at a distance of 3 cm from the sample at an angle of 0 degree with respect to the incident beam. The diameter of the beam at the surface of the sample is around 1 mm and the ion beam current (N^{2+}) is typically 10-40 nA. The detection limit is of some atomic ppm and the precision is determined by the counting statistics. The accuracy is governed by the quality of the calibration standard and the accuracy of the calculated stopping powers. The values used are from Ziegler[282] and the uncertainty is typically of a few percent. Bragg's rule[283] is used to calculate the stopping cross-sections of the compounds. Tantalum hydride ($TaH_{0.47}$) is used as a calibration sample for the absolute hydrogen concentration determination.[284]

7.3 As-deposited film

The hydrogenation of metal gradient thin films depends strongly on their (micro)structure and local composition. Therefore, an extensive characterization of the lateral gradient as well as of the composition as a function of depth after deposition is of primary importance.

In the as-deposited state, Mg_yAl_{1-y} samples are completely opaque and have shiny metallic surfaces, on the Pd side as well as on the substrate side. The results from RBS measurements are illustrated in Fig. 7.2. For each probed composition y on the gradient sample, the RBS spectrum is compared with the corresponding simulation of an homogeneous Pd/Mg-capped Mg_yAl_{1-y} layer.

Within the accuracy of the measurement, we conclude that the [Mg]/[Al] ratio is constant over the sample depth for each composition. We do, however, observe some inhomogeneously distributed oxygen. The enthalpies of formation of both magnesium and aluminium oxides (ΔH_f(MgO) = -601.6 kJ/(mol O), ΔH_f(Al$_2$O$_3$) = -558.6 kJ/(mol O)) are much larger than the ones of the corresponding hydrides (ΔH_f(MgH$_2$) = -37.7 kJ/(mol H), ΔH_f(AlH$_3$) = -2.8 kJ/(mol H)).[285,286] Therefore, the chemical purity of the sample is crucial to study the optical and electrical properties upon hydrogenation further. We find oxygen mainly at the substrate-film interface, with an elemental density of $3 \cdot 10^{16}$ at/cm^2 for all measured compositions. As a comparison, this value for as-received amorphous carbon substrates is also $3 \cdot 10^{16}$ at/cm^2. The oxygen amount at the film surface is less than $2 \cdot 10^{15}$ at/cm^2, while the interior of the film appears to be oxygen-free. This shows that the cap-layer provides an effective barrier against oxidation.

Measurements of dc resistivity as a function of hydrogen content or temperature proved to be highly valuable for the study of hydride thin films.[1,128,288] At present, our compositional gradient approach also enables us to measure the resistivity as a function of the metallic composition and thus to gain understanding in the related changes of structure for both the as-deposited and the hydrogenated state.

The resistivity ρ of the as-deposited film as a function of composition follows Nordheim's rule,[124] with a broad maximum centered at $y = 0.49$ and a maximum $\rho = 47$ $\mu\Omega$cm (Fig. 7.3(a)). The resistivity then decreases towards the respective pure metal values. On Mg and Al film deposited separately we found $\rho_{Mg} = 5.69$ $\mu\Omega$cm and $\rho_{Al} = 3.81$ $\mu\Omega$cm. In the dilute solution limit, ρ exhibits a linear behavior typical for independent scattering processes:[289]

$$\rho(T, y) = \rho_{Al}(T) + y \cdot \left(\frac{d\rho}{dy}\right)_{Mg} \qquad 0 < y < 0.21 \qquad (7.1)$$

and

$$\rho(T, y) = \rho_{Mg}(T) + (1 - y) \cdot \left(\frac{d\rho}{dy}\right)_{Al} \qquad 0.69 < y < 1 \qquad (7.2)$$

We find $\left(\frac{d\rho}{dy}\right)_{Mg} = 5.8 \pm 0.1$ $\mu\Omega$cm/at% and $\left(\frac{d\rho}{dy}\right)_{Al} = 9.2 \pm 0.1$ $\mu\Omega$cm/at% for Mg and Al impurities respectively. This linear behavior points to the presence of an extended solid solution of Mg in Al (or Al in Mg) compared to the bulk Mg-Al phase diagram. These extended solubility ranges are indeed supported by X-ray diffraction (XRD), which reveals the presence of an hcp Mg phase for Mg atomic fractions $y > 0.5$ and a fcc Al phase for $y < 0.35$ (see Fig. 7.3(b)).

In its central part, the parabolic shape of the resistivity is characteristic for an electron-impurity dominated conduction and reflects the disorder of the Mg-Al mixture. There is no indication of the formation of another alloy
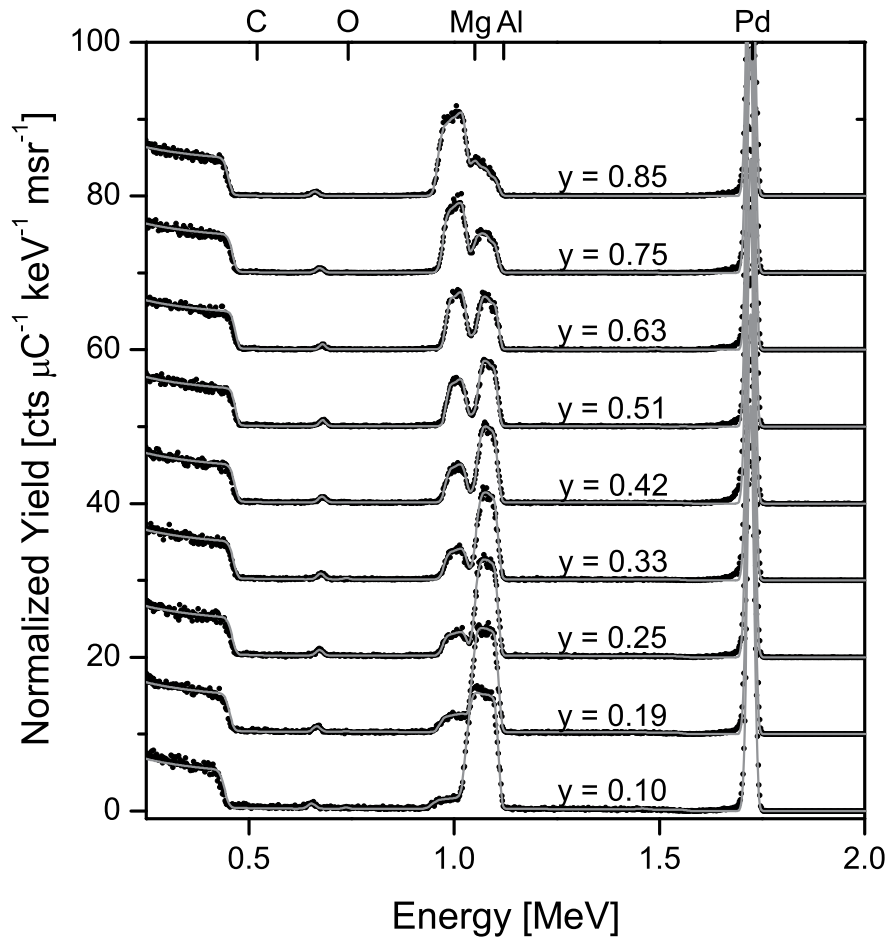
Figure 7.2: Solid circles: RBS spectra for various compositions of the as-deposited Pd-capped Mg_yAl_{1-y} gradient thin film on an amorphous C substrate. Top scale: edge (surface) energies for the elements present in the sample. Grey line: fits for (in-depth) homogeneous Mg_yAl_{1-y} layers. The obtained Mg fraction y is indicated on the graph.
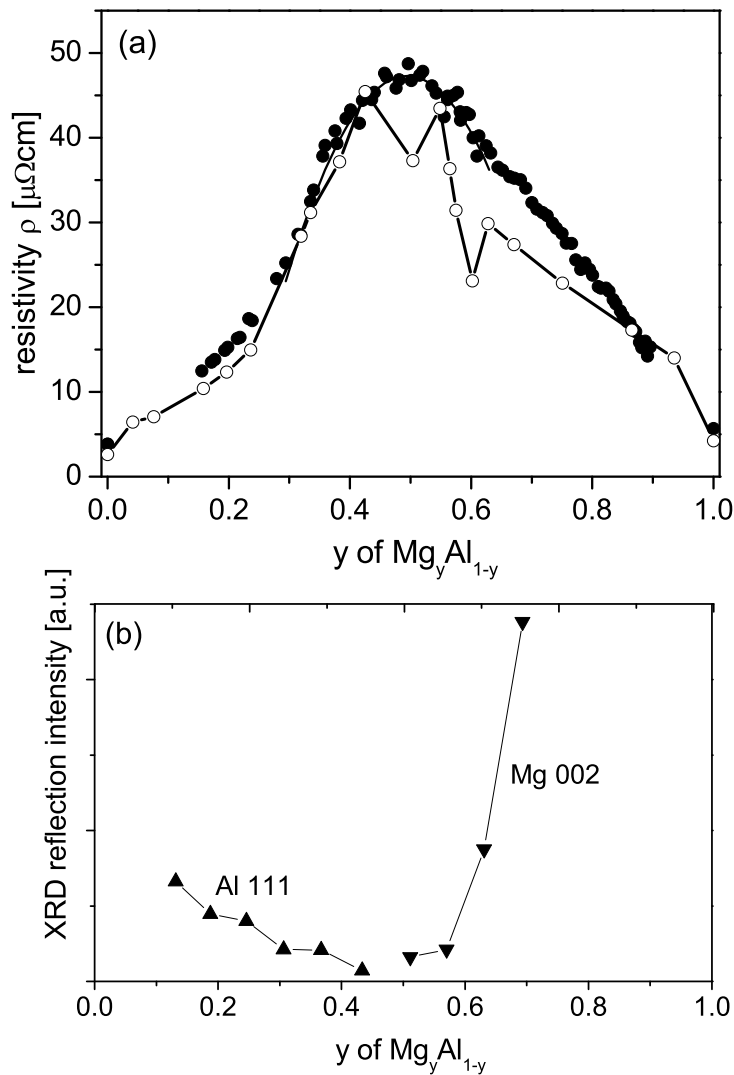
Figure 7.3: (a) *Filled circles*: resistivity ρ of the as-deposited Mg_yAl_{1-y} gradient layer. The *fitted parabola* centered on $y = 0.49$ reflects the effect of disorder scattering. Results are corrected for the 10 nm Pd cap-layer and normalized to a 200 nm Mg_yAl_{1-y} layer thickness. *Empty circles*: ρ of bulk Mg-Al alloys.[287] (b) Intensities of the out-of-plane Mg 002 (*down triangles*) and Al 111-reflections (*up triangles*) as a function of Mg content y.

phase at an intermediate composition, neither in the resistivity nor in the XRD measurements. In comparison, the bulk resistivity (Fig. 7.3(a)) clearly shows two dips at approximately $y = 0.5$ and $y = 0.6$. This reduced scattering is attributed to ordered MgAl and $Mg_{17}Al_{12}$ phases formed at these compositions [287]. The absence of these anomalies in the thin film resistivity supports our assumption that the Mg_yAl_{1-y} layer is mainly amorphous in the $0.5 < y < 0.6$ range.

In summary, the resistivity and XRD measurements of the as-deposited film reveal highly supersaturated single phase solid solutions of Al in Mg ($0.69 < y < 1$) and Mg in Al ($0 < xy < 0.21$) and an amorphous or nanocrystalline glassy metal for $0.5 < y < 0.6$. For the unspecified regions, we assume a coexistence of the limiting phases. This is consistent with other microstructural studies of Mg-Al coatings deposited by magnetron sputtering. [290]

7.4 Hydrided state

When the as-deposited Mg_yAl_{1-y} metallic gradient thin film is exposed to hydrogen gas, the hydrides which are likely to form are MgH_2 for the Mg-rich part of the gradient and magnesium alanate, $Mg(AlH_4)_2$, at around the composition $y = 0.33$. Indeed, we find indications of the formation of theses two phases. However, the distribution of these hydrides as a function of depth in the film, and hence the segregation occurring between them and the remaining metallic fraction of the film has also to be characterized. Nuclear Resonance Analysis (NRA) combined with spectral optical transmission measurements give a good understanding of the hydrided part of the active layer. Complementary to this, Rutherford Backscattering Spectrometry (RBS), X-Ray Diffraction (XRD) and conductivity measurements are used to study the metallic fraction after hydrogenation.

7.4.1 H-induced segregation

The as-sputtered samples consist of Mg and Al homogenously dissolved in Al and Mg, respectively. As already discussed in section 7.3, the solubility range is larger in thin films than in bulk samples due to the growth process. For most of the compositions, hydrogenation at $\mathcal{T} = 110\,°C$ and $p_{H_2} = 1$ bar forces the system to segregate into the thermodynamically most stable phases MgH_2 and Al. [271,272]

This process is investigated by X-ray diffraction. Figure 7.4 shows X-ray patterns of a $Mg_{0.2}Al_{0.8}$ film during hydrogenation. The initial spectrum is attributed to a single Al 111 reflection originating from a homogenous Al-phase with a slightly increased lattice parameter due to dissolved Mg. During *in situ* hydrogenation a second peak evolves, which quickly grows, while the original one disappears (see Fig. 7.5)). The corresponding lattice parameter

of the evolving peak is that of pure aluminium. Thus, we have followed the
decomposition of Al(Mg) into pure Al and probably MgH_2. X-ray peaks of
MgH_2 have not been detected, presumably due to too small a grain size of the
precipitates.

To measure the hydrogen content directly, the hydrogenated Mg_yAl_{1-y} gra-
dient film is probed by NRA. In fig. 7.6, the data have been compiled into a hy-
drogen depth profile as a function of the Mg atomic fraction y in $Mg_yAl_{1-y}H_x$.
It demonstrates that the hydrogen distribution in the film depends markedly
on the alloy composition y.
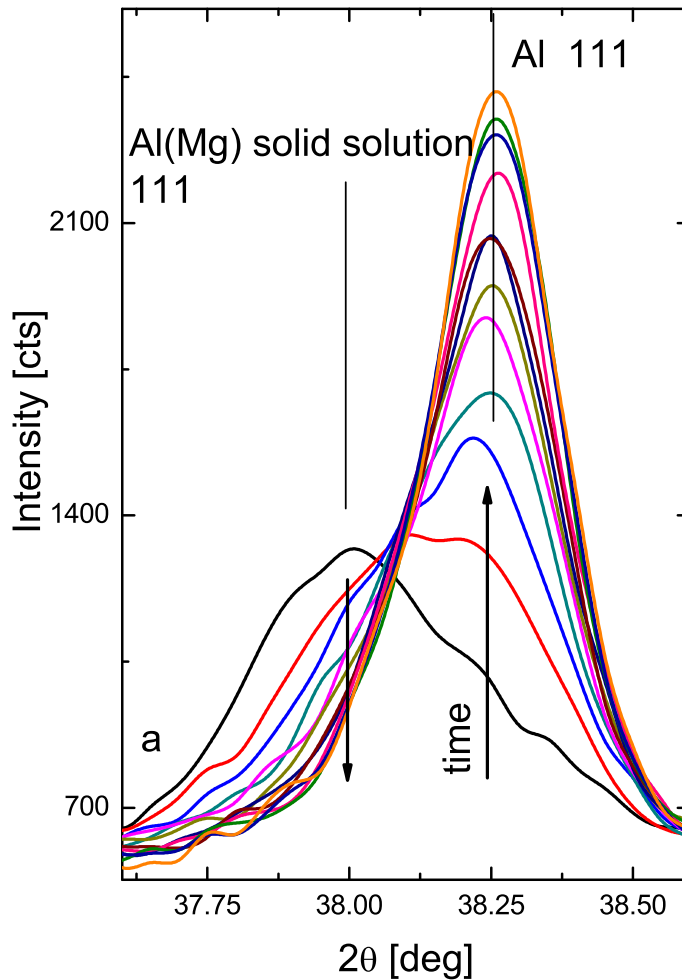
Figure 7.4: Grain growth of Al in $Mg_{0.2}Al_{0.8}$ during hydrogenation probed by
X-ray diffraction (I). **(a)** Raw X-ray spectra during H-exposure at $p = 1$ bar
and $\mathcal{T} = 110$ °C.

However, without the information of the metal distribution inside the film,
a distinct proof for the formation of a particular hydride is difficult. RBS
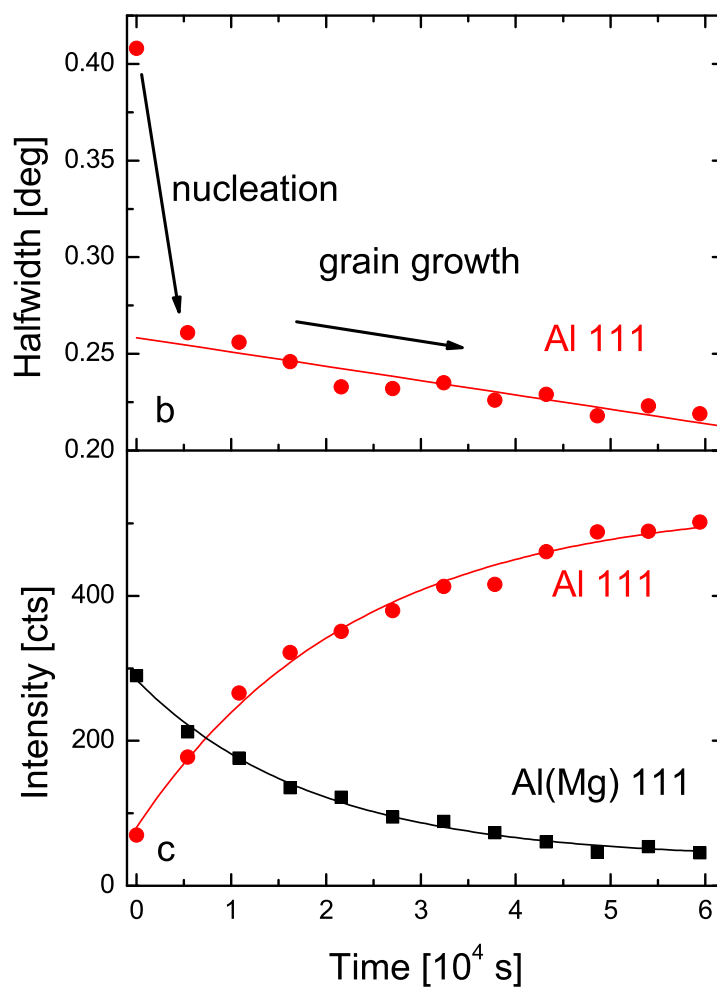
Figure 7.5: Grain growth of Al in $Mg_{0.2}Al_{0.8}$ during hydrogenation probed by X-ray diffraction (II). (b) Halfwidth of the Al 111 peak and (c) intensity of both peaks as a function of time.
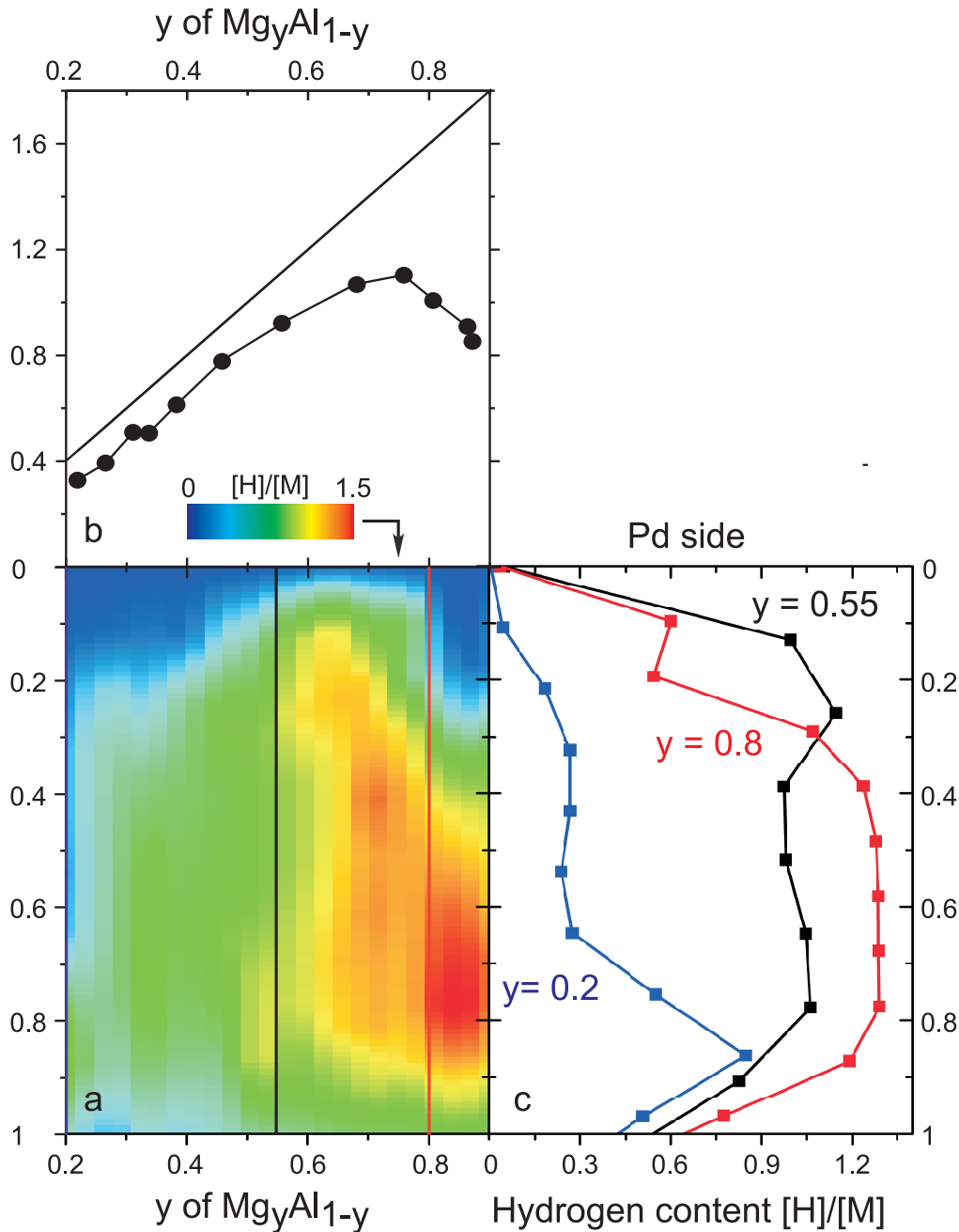
Figure 7.6: Nuclear Resonance Analysis (NRA) is used for hydrogen depth profiling of hydrided Pd-capped Mg_yAl_{1-y} films. (**a**) Contour plot of the hydrogen-to-metal ratio [H]/[M] as a function of film depth and magnesium fraction y of the Mg_yAl_{1-y} layer. The thickness of the film is normalized for all compositions. A depth of 0 corresponds to the (Pd-) surface, while 1 indicates the substrate interface. (**b**) Filled circles, [H]/[M] integrated over the film thickness, as a function of the Mg fraction y. The decrease of hydrogen content for Mg-rich compositions is due to unloading of the surface during the transfer of the sample in air. The full line indicates the theoretical maximum [H]/[M] for a mixture of MgH_2 and Al. (**c**) [H]/[M] depth profile for a mainly uniform hydrogen distribution (red, $y = 0.8$), a hydrogen enrichment at the surface (black, $y = 0.55$), and a hydrogen enrichment at the interface with the substrate (blue, $y = 0.2$), respectively.
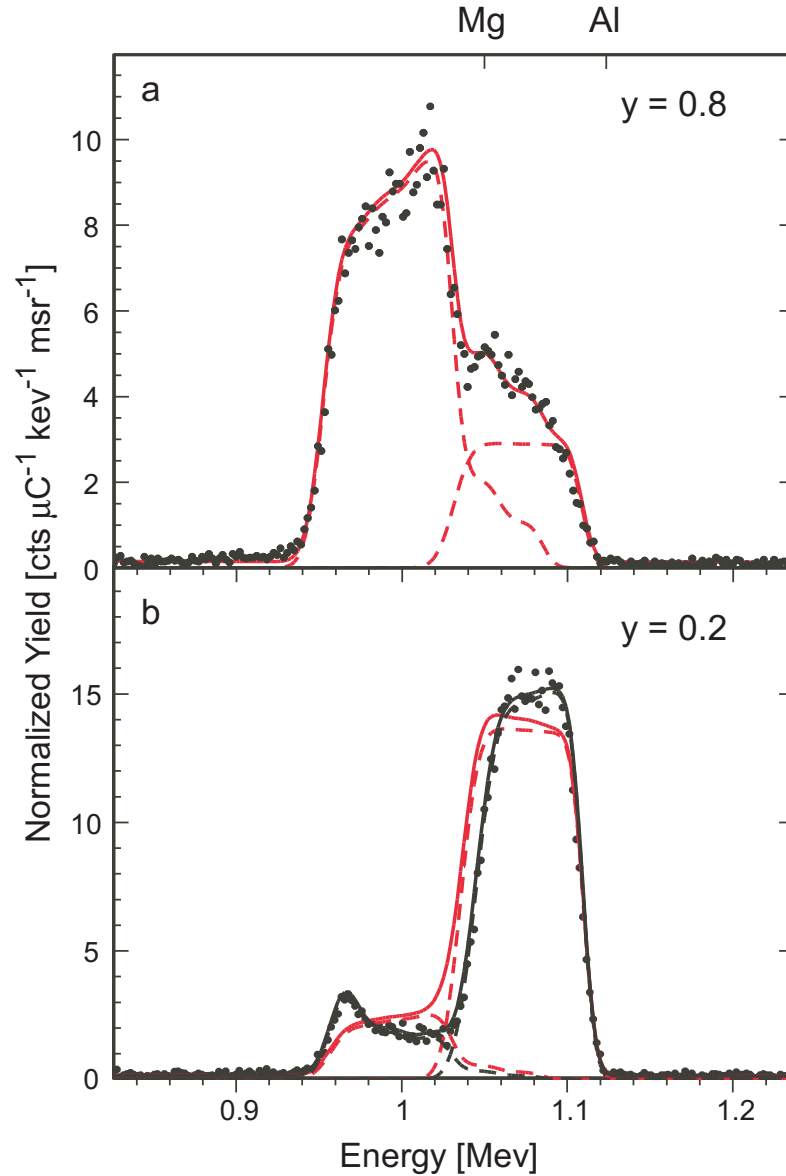
Figure 7.7: The Mg and Al contributions to RBS spectra of hydrogenated $Mg_yAl_{1-y}H_x$ layers. (**a**) $y = 0.8$, hydrogen-to-metal ratio $x = [H]/[M] = 0.5$. Full line, fit for an homogeneous layer. (**b**) $y = 0.2$, $x = 0.3$. Full line (gray), fit for an homogeneous layer, (black) fit for a segregation of Al towards the film surface and MgH_2 towards the interface (see Table 1). Dashed lines show the separate Mg and Al contribution. Top scale: Edge (surface) energies for Mg and Al.
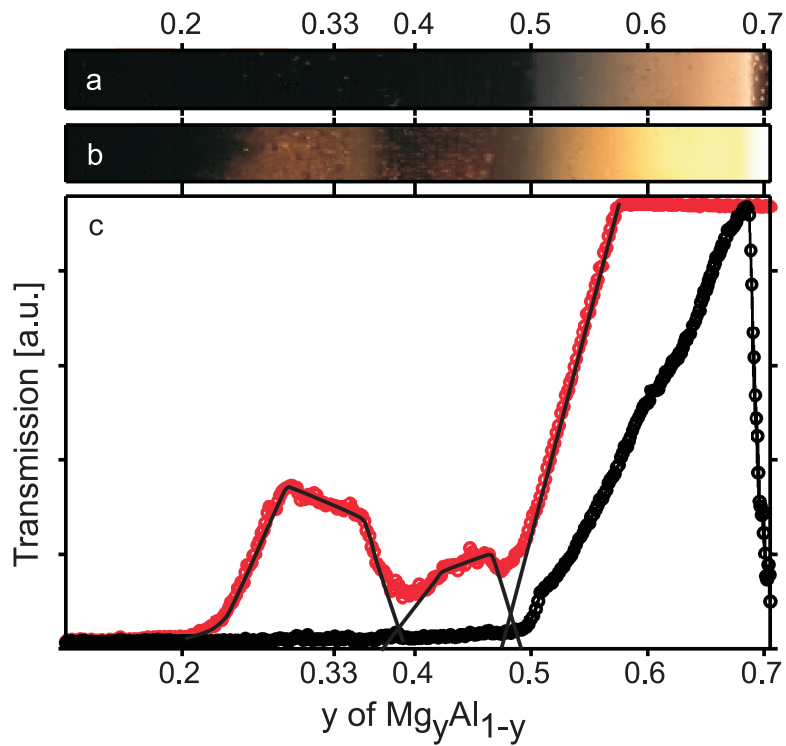
Figure 7.8: $Mg_yAl_{1-y}H_x$ gradient sample hydrogenated at $\mathcal{T}$ = 110°C and $p(H_2)$ = 1.1 bar. Transmission image after (**a**) 10^3 s, (**b**) 10^5 s hydrogen exposure time. (**c**) CCD red channel transmission as a function of composition. Black circles: after 10^3 s, red circles: after 10^5 s. Black lines indicate schematically the contributions of the various phases discussed in the text.

can deliver the elemental depth profile of a thin film. For this, we fitted the RBS spectrum of the hydrogenated film, keeping the total number of Mg and Al atoms as determined in the as-deposited state constant. Furthermore, we implement the hydrogen content determined by NRA in the fit to account for the reduction of the (planar) density after hydrogenation. The RBS spectra of a Mg-rich and an Al-rich $Mg_yAl_{1-y}H_x$ film after hydrogenation are shown in Fig. 7.7. Mg-rich films with $y > 0.5$ show a uniform distribution of Mg and Al, while it is clearly evident that Al-rich films ($y \leq 0.2$) are enriched in Mg at the interface.

With these two pieces of information we can draw a detailed description of the segregation phenomenon in $Mg_yAl_{1-y}H_x$ films during hydrogenation. Mg-rich films ($y > 0.5$) show a uniform distribution of hydrogen and metal atoms. Here, the hydrogen depletion at the surface is due to a partial unloading of the film during measurement. At these low Al-concentrations, Al is dissolved in the Mg-matrix. During magnesium hydride formation small Al-clusters are formed (see section 7.4.2), which are uniformly dispersed in the MgH_2-matrix. The small Al clusters impede the formation of a MgH_2-blocking layer, [113] and indeed, the kinetics of Al-doped Mg-films is enhanced compared to pure magnesium. This qualitative explanation is in agreement with the optical and kinetics measurements reported in the next section.

Layer	Elemental density $[10^{15}\text{at} \cdot \text{cm}^{-2}]$				Mg_yAl_{1-y}	[H]/[M]
	Pd	Mg	Al	H	y	x
1	68	-	-	-	-	-
2	1	28	275	41	0.09	0.14
3	1	36	250	54	0.13	0.19
4	-	22	110	30	0.17	0.23
5	-	61	36	73	0.63	0.75

Table 7.1: $Mg_{0.2}Al_{0.8}$ after hydrogenation: result of the RUMP modeling of the RBS measurement. Layer 1 represents the Pd cap-layer and 5 the layer closest to the substrate.

At higher Al-concentrations ($y < 0.5$), the transport of metal atoms becomes rate-limiting, and the rate constant of the kinetics is of the order of the diffusion constant of Al in Mg.[291] This explains the slower kinetics at these Al-contents, since for the nucleation and growth of the hydride more Al has to be (re)moved. Furthermore, as in similar fcc metals, hydrogen diffusion is very slow in Al.[292] This implies that the observed percolation (see section 7.4.4) of the top metallic layers hinders further hydrogenation. This would explain the hydrogen enrichment at the surface of $Mg_yAl_{1-y}H_x$ films for $0.4 < y < 0.5$ (Fig. 7.6).

However, this explanation does not hold anymore for Al-rich Mg_yAl_{1-y} films ($y < 0.25$). Here, a strong hydrogen enrichment at the interface is evident. RBS combined with NRA results clearly indicate a segregation of Al and MgH_2 followed by a migration of Al towards the surface and of MgH_2 towards the interface. Why these phases migrate to different interfaces is not clear yet.

It is worthwhile to note that the reported segregation is purely H-induced. Annealing the as-deposited samples in vacuum at 110 °C does not produce such compositional inhomogeneities.

Finally, no segregation, and a slightly higher hydrogen content is found around the [Mg]/[Al] = 2 ratio (Fig. 7.6b). This is also corroborated by optical and electrical measurements (Fig. 7.8 and 7.11). Interestingly, it is the right ratio to form $Mg(AlH_4))_2$, and probably a small amount of it is present in the film (see section 7.7).

7.4.2   Optical transmission

By applying 1.1 bar hydrogen pressure at 110°C, some regions of the sample become transmissive (Fig. 7.8). After 10^3 s of hydrogen exposure, Mg_yAl_{1-y} with $0.5 < y < 0.69$ displays a color neutral transmission (Fig. 7.8a). It is important to note that the segregation processes reported in section 7.4.1 have hardly started yet at this time (see Fig. 7.4). We assume therefore that the film is still homogeneous over its entire thickness. The intensity, which is highest at $y = 0.69$, decreases linearly with decreasing Mg content, and has a cutoff at $y = 0.5$ (Fig. 7.8c). We attribute this behavior to the formation of MgH_2, which is a colorless insulator with a band gap of 5.6 eV.[64] From NRA measurements, the in-depth integrated [H]/[Mg] ratio at these compositions is between 1.7 and 1.5. This means that 75% to 85% of the Mg is transformed into MgH_2. This is in good agreement with Johansson et al., who found similar unreacted Mg fractions in thin hydrogenated Mg-Ni wedged films.[293]

From the low transmission in fig. 7.8, we notice that our film is still incompletely hydrogenated for $0.69 < y < 1$. In this composition range, it exhibits a hydrogenation behavior similar to that in pure Mg films, whose hydrogen uptake is kinetically hindered by a dense surface layer of MgH_2.[294] This is not astonishing if we consider that in the as-deposited state, our film consists of an extended solid solution of Al in Mg in this range.

For $0.5 < y < 0.69$, hydrogenation occurs already within 10^3 s. There are two factors explaining a faster kinetics at these Al-richer compositions: Firstly, Mg crystallinity is decreased due to the presence of the Mg-Al amorphous phase.[295] Secondly, the presence of Al at the surface of Mg grains will speed up the hydrogen uptake, as it is the case for surface Ni[103,113,296] or MgO_x.[35]

Finally, Al-rich compositions ($y < 0.5$) have not absorbed enough hydrogen at $t = 10^3$ s to exhibit a significant transmission.

After 10^5 s of hydrogen exposure, Mg fractions above $y = 0.69$ have hydrided. Furthermore, an additional feature has appeared in transmission in the Al-rich region (Fig. 7.8b): a broad peak is present for $0.26 < y < 0.36$. This transmission is centered around an [Al]/[Mg] ratio of 2 ($y = 0.33$), suggesting the formation of $Mg(AlH_4)_2$.

7.4.3 Spectrophotometry

To clarify the nature of the optical features present in the Al-rich part of the sample after 10^5 s of hydrogen exposure, we measure the transmission of hydrogenated films from 0.5 to 6 eV photon-energy. To maximize the transmission, the Mg_yAl_{1-y} layer is only 40 nm thick, capped with 8 nm of Pd. The samples are deposited on quartz substrates. The measured spectra are compared with calculations based on two extreme cases :

1. Homogeneous mixture:

   For a given composition y, the $Mg_yAl_{1-y}H_x$ sample is an homogeneous mixture of MgH_2 and Al. Its dielectric function $\langle \tilde{\epsilon} \rangle$ is described by an effective medium theory if the grain size of the respective particles is smaller than the wavelength of light. We use Bruggeman's approximation for spherical particles. $\langle \tilde{\epsilon} \rangle$ is then implicitly given by:[297]

$$f_A \frac{\tilde{\epsilon}_A - \langle \tilde{\epsilon} \rangle}{\tilde{\epsilon}_A + 2\langle \tilde{\epsilon} \rangle} + f_B \frac{\tilde{\epsilon}_B - \langle \tilde{\epsilon} \rangle}{\tilde{\epsilon}_B + 2\langle \tilde{\epsilon} \rangle} = 0 \qquad (7.3)$$

   $f_{A,B}$ and $\tilde{\epsilon}_{A,B}$ are the volume fractions and the complex dielectric functions of the phase A (MgH_2) and B (Al), respectively. The transmission of the Pd-capped $Mg_yAl_{1-y}H_x$ layer is then calculated.

2. Layered segregation:

   The H-induced segregation is fully reached and the sample consists of a $Pd/MgH_2/Al$ stack.

Figure 7.9 displays the measured and calculated transmission for the compositions $y = 0.32$, 0.39 and 0.51. For $y = 0.51$ and 0.32, the measured spectrum fits reasonably well with the one calculated for an in-depth homogeneous $Mg_yAl_{1-y}H_x$ layer. Moreover, calculations of a segregated layer predict a broad peak around 4.5, or, respectively 5.5 eV, which is not observed experimentally. At an intermediate composition ($y = 0.39$), we do observe an additional peak at high energies (4.5 eV) which can be related to segregation. Note that the calculations for an homogeneous MgH_2-Al mixture yield always a larger transmission than the segregated ones in the visible range (from 1.2 to 3 eV), which we use for hydrogen mapping with our CCD. Partly segregated
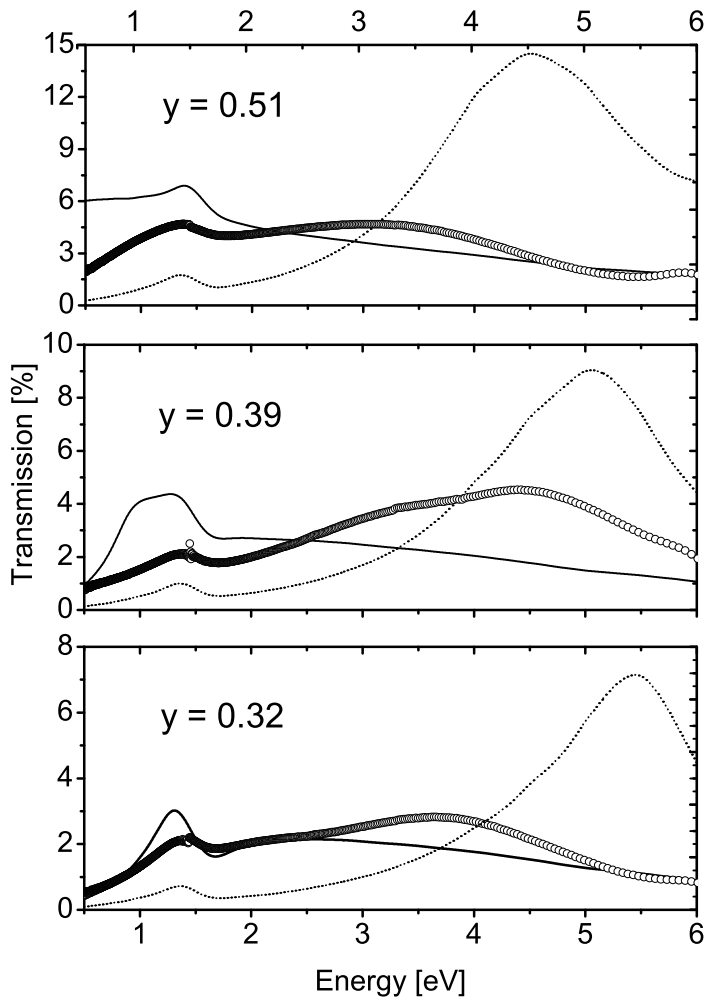
Figure 7.9: Comparison between experimental and theoretical optical transmission spectra for a 40 nm $Mg_yAl_{1-y}H_x$ film capped with 8 nm of Pd. (o) Measured spectra for $y = 0.32$, 0.39 and 0.51. Solid lines, calculations based on homogeneous mixtures of MgH_2 and Al by the Bruggeman approximation. Dashed line, calculations for fully segregated MgH_2 and Al bilayers.
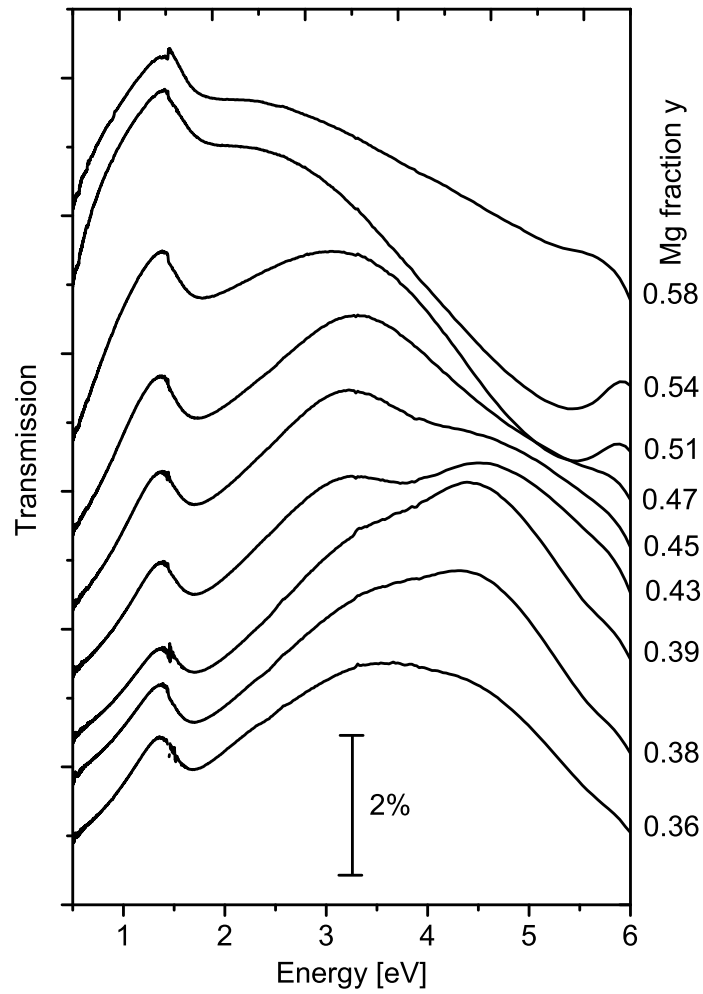
Figure 7.10: Optical transmission of a 40 nm $Mg_yAl_{1-y}H_x$ film capped with 8 nm Pd as a function of photon-energy. A shift of 0.8% in transmission intensity is added between two consecutive spectra for clarity.

MgH_2 could then account for the low intensity observed in the $0.39 < y < 0.5$ range (see Fig. 7.8), while the higher intensity observed around $y = 0.33$ is well fitted by an homogeneous mixture of MgH_2 and Al. For higher Al contents ($y \leq 0.2$), RBS and NRA measurements (see section 7.4.1) show that MgH_2 segregates strongly towards the quartz substrate. However, the intensity is too low ($< 1\%$) for an optical analysis.

As complex segregation phenomena occur while hydrogenating the $Mg_yAl_{1-y}H_x$ gradient, it is difficult to model the exact shape of a transmission spectrum at a given composition. However, the (non)-occurrence and respective position in energy of the different transmission peaks are characteristic for each composition. Moreover, for 40 nm films, the interference maxima due to the layer thickness are approximately 15 eV apart and do not contribute significantly to the shape of the transmission spectrum. Therefore, each spectrum becomes a "fingerprint" of the corresponding composition and gives a qualitative understanding of the process contributing most to the optics. To illustrate this, the transmission spectra in the range $0.36 \leq y \leq 0.58$ are displayed in Figure 7.10. They can be schematically assigned to three groups: from $x = 0.58$ to 0.51, the film is homogeneous over its thickness, the peak around 6 eV for $y = 0.51$ and 0.54 being the signature for the unreacted Mg fraction mixed with MgH_2 and Al. From $y = 0.47$ to 0.38, the peak around 4.5 eV accounts for the MgH_2/Al segregation in the sample. Finally the sample becomes homogeneous in-depth again for a composition $y = 0.36$.

7.4.4 Conductivity

For a characterization of the metallic fraction present in the gradient thin film, we study the dc conductivity σ as a function of composition. Figure 7.11 displays σ before and after hydrogenation for $3 \cdot 10^5$ s at $p = 1.1$ bar H_2 and $\mathcal{T} = 110$ °C. As previously mentioned, conductivity variations in the as-deposited state are small because of the metallic nature of the film. In the hydrogenated state, it changes drastically: The Mg-rich part becomes semiconducting, with a conductivity below 1 $(m \Omega cm)^{-1}$. A striking feature is the positive conductivity shift in the Al-rich part ($0.15 < y < 0.5$) after hydrogenation. An increase of the Al grain size would account for this effect by shortening the current paths and reducing the intergrain contact resistances. From XRD measurements we indeed find an increase of the Al 111 reflection and a shift of the lattice parameter toward the bulk value during hydrogenation (See Fig. 7.4).

For all Mg compositions $y < 0.61$, the overall behavior of σ is well described by a power law:

$$\sigma \propto (v - v_c)^\beta \propto (y_c - y)^\beta \tag{7.4}$$

with a critical volume fraction of Al metal $v_c = 0.25 \pm 0.01$ corresponding to an atomic Mg fraction $y_c = 0.61 \pm 0.01$ and a critical exponent $\beta = 1.5 \pm 0.1$.
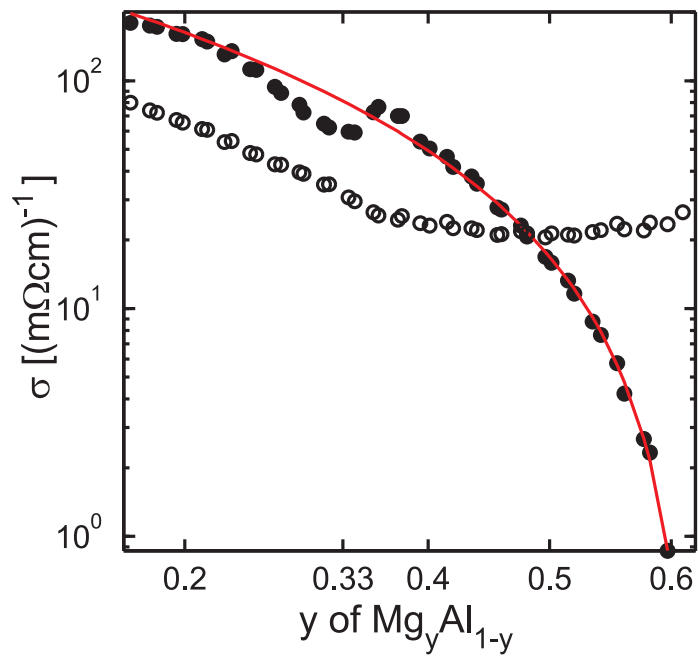
Figure 7.11: Conductivity σ of the Mg_yAl_{1-y} layer in the as-deposited state (empty circle) and in the hydrogenated state (filled circles). Data are corrected for the 10 nm Pd cap-layer and normalized to a 200 nm $Mg_yAl_{1-y}H_x$ layer thickness. The solid line is a fit of the data based on a simple cubic bond percolation model (critical Al volume fraction $v_c = 0.254$, critical exponent $\beta = 1.5$).

These values are in agreement with a simple cubic bond percolation model that predicts $v_c = 0.25$ and $\beta = 1.6 \pm 0.1$.[298,299] This is consistent with the conclusion that the sample consists of MgH_2 inclusions in Al.

However, the lower conductivity observed for $0.26 < y < 0.36$ is not reproduced by the model of Al percolation in MgH_2. The compositional range of the conductivity deviation corresponds well to that of the optical transmission feature observed in section 7.4.2. This indicates that less Al contributes to the conduction and may be involved in the formation of a small amount of insulating $Mg(AlH_4)_2$ phase. However, no deviation from the model is found for $0.4 < y < 0.5$. This suggests that the slightly higher, inhomogeneous transmission observed in this range (see Fig. 7.8) does not involve any $Mg_yAl_{1-y}H_x$ compound and is due to MgH_2 which is formed from the purely amorphous Mg-Al phase.[290]

Theoretical calculations predict $Mg(AlH_4)_2$ to be a large band gap semiconductor.[264,265] However, the deviation in conductivity measured for $0.25 < y < 0.35$ is small compared to the contribution of the MgH_2-Al mixture. From measurements of the film expansion after hydrogenation, we estimate that less than 5% of the film is transformed into $Mg(AlH_4)_2$.

7.5 Kinetics

Hydrogenography makes it also possible to follow in detail the kinetics of hydrogen uptake of Mg_yAl_{1-y}. Figure 7.12 (b) gives the temporal evolution of the transmission upon hydrogenation for $0.2 < y < 0.71$. Hydrogenation starts first at around a nominal composition of Mg_2Al after 10^2 s (Fig. 7.12c). The transmission extends gradually towards the MgAl nominal composition before 10^3 s. By comparison with Fig. 7.8c, we conclude that this transmission lobe is induced by MgH_2, with a loading time $\tau = 200$ s for the fastest composition at around $y = 0.67$ (Fig. 7.12c). Here τ is defined as the time where $\log T = 1/2 \log(T_{max})$, taking the final transmission level T_{max} as fully loaded. For Mg fractions higher than $y = 0.68$, the formation of a MgH_2 blocking layer reduces the hydrogenation kinetics substantially and increases τ to $1.5 \cdot 10^3$ s for $y = 0.7$. As this change in uptake rate is occurring at the limit of the Al solubility in Mg, we conclude that an admixture of the amorphous Mg-Al phase to the Mg(Al) phase improves the hydrogenation kinetics dramatically.

As discussed in section 7.4.1 previously, compositions between $y = 0.5$ and 0.38 still exhibit a low transmission after 10^3 s because of the H-induced segregation of Mg_yAl_{1-y} into MgH_2 and Al. For Al-richer compositions, a second transmission lobe develops at around a nominal composition of $MgAl_2$ ($y \simeq 0.33$) (Fig. 7.12b) with a loading time of 10^4 s.

We attribute this rise in transmission to an homogeneous mixture of MgH_2, Al and possibly $Mg(AlH_4)_2$ (at most 5%). Its slower kinetics is related to the slow diffusion of the metal atoms.
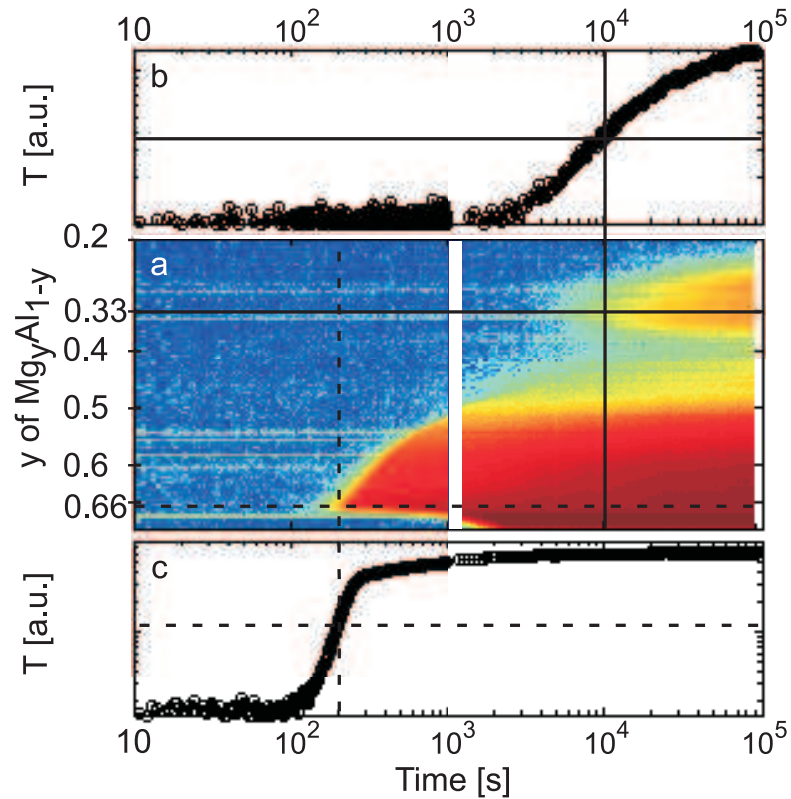
Figure 7.12: Evolution of the optical transmission (from the CCD, bandwidth from 1.1 to 3.3 eV) of a Mg_yAl_{1-y} gradient layer capped with 10 Pd during hydrogenation at 110 °C and $p(H_2) = 1.1$ bar. The composition y varies from $y = 0.2$ to $y = 0.71$. (**a**) Contour plot of the transmission as a function of Mg fraction y and time. Blue corresponds to low transmission and red to high transmission. (**b**) Transmission for $y = 0.32 \pm 0.01$ (**c**) Transmission for the fastest hydriding composition of $MgH_2 + Al$ in Mg_yAl_{1-y} with $y = 0.67 \pm 0.01$.

Finally, for composition of $y \leq 0.2$, no significant rise in transmission occurs. Although MgH_2 present in the sample segregates towards the substrate (see section 7.4.1), the thick Al layer on top prevents transmission.

7.6   Surface Ti vs Ti doping

An advantage of using thin films is that in contrast to bulk, they offer the opportunity to discriminate between the different roles of additives. Either as a destabilizing dopant, or as a catalyst on the surface. We follow the transmission of the Mg_yAl_{1-y}, Ti doped, and Ti covered gradients samples under a constant hydrogen pressure of 1.1 bar from room temperature up to 120 °C with a heating rate of 3°C/hr. After cooling down under hydrogen atmosphere, we dehydride the film in air with the same heating rate up to 200 °C. Figure 7.13 shows the temperature and composition dependence of the transmission of a $Mg_yAl_{1-y}H_x$ gradient sample (Fig. 7.13b) compared to that of a Ti doped $Mg_yAl_{1-y}H_x$ gradient sample (Fig. 7.13a). We observe the following features: (i) Both films start to hydride at the same composition of $y = 0.62$ around room temperature. (ii) For low temperatures ($\mathcal{T} < 80$°C) the region where MgH_2 forms is slightly smaller in the Ti doped sample than in the pure Mg-Al film. This can be seen in Fig. 7.13c) for a y = 0.5 composition. (iii) Ti doping lowers the hydriding temperature of the Mg-rich part (Fig. 7.13c), $y = 0.7$). (iv) However, the main difference comes from the Al-rich region. The Ti doped sample stays non transmittive for $y < 0.35$, and hence no formation of $Mg(AlH_4)_2$ is found (Fig. 7.13c), $y = 0.33$).

Figure 7.14 shows a comparison of the transmission of samples with and without a Ti buffer layer during hydrogen absorption at $p(H_2) = 1.1$ bar and desorption in air. Absorption is similar for both samples. However, the desorption temperature is lowered by about 100 °C if a 5 nm Ti layer is present between the Pd and the Mg_yAl_{1-y} layer. This suggests that Ti catalyzes the decomposition of $Mg(AlH_4)_2$ when it is located at the film surface.
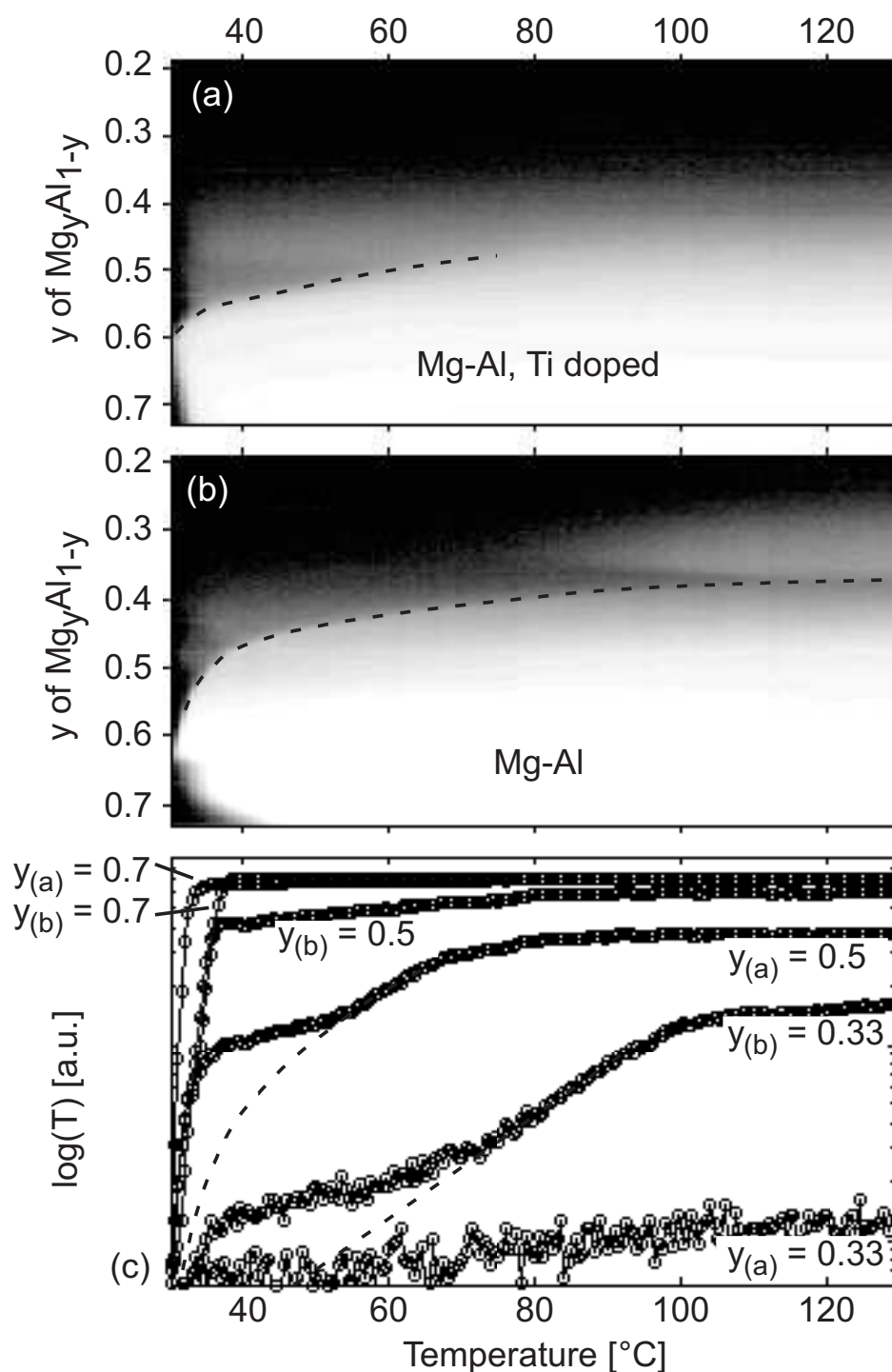
Figure 7.13: Contour plot of the transmission as a function of temperature and composition for (a) a $Mg_yAl_{1-y}H_x$ gradient doped with 3% of Ti and (b) a $Mg_yAl_{1-y}H_x$ gradient sample during hydriding ($p(H_2) = 1.1$ bar, heating rate: 3°C/hr). The dashed lines indicate the region in which MgH_2 is formed. In (c), the transmission for three compositions $y_{(i)}$ of samples (a) and (b) is given as a function of temperature. Dashed lines: corrected transmissions for internal reflections in the hydrogen cell.
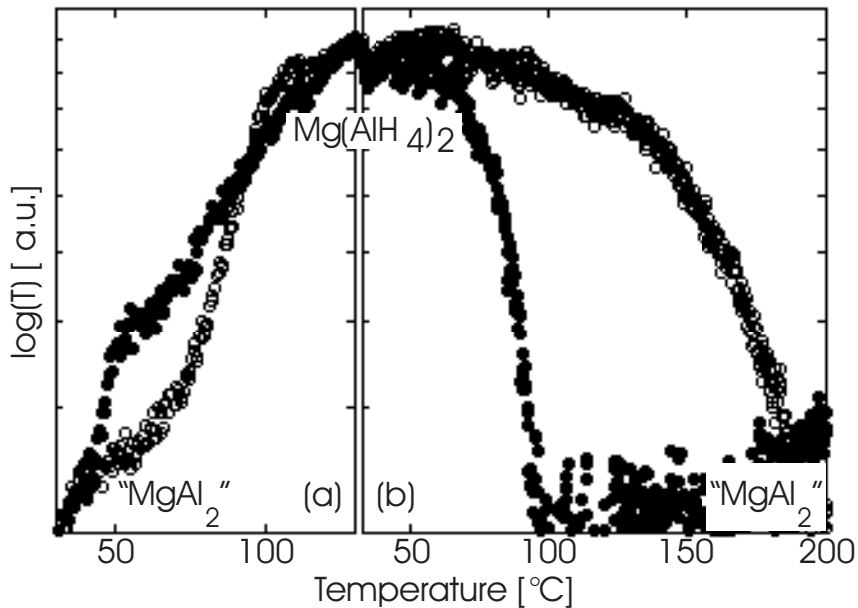
Figure 7.14: Transmission as a function of temperature at a nominal $MgAl_2$ composition during (a) hydrogen absorption at $p(H_2) = 1.1$ bar and (b) desorption in air. Open circles: without a 5 nm Ti buffer layer. Filled circles: with a 5 nm Ti buffer layer.

7.7   Conclusions

Hydrogenography, i.e. the thin film analysis techniques combined with the use of compositional gradient samples, enables us a detailed understanding of the hydrogenation of Mg_yAl_{1-y} alloys:

The first important result is that hydrogenation of Mg_yAl_{1-y} thin films occurs at much milder conditions $(p(H_2) = 1.1$ bar and $\mathcal{T} = 110°C)$ than in the corresponding bulk samples. Another advantage is that the mapping by optical transmission of the hydrides and the kinetics of the formation thereof is possible throughout the entire film simultaneously. Under these conditions, MgH_2 is found to form at all alloy compositions investigated $(0.2 \leq y \leq 0.9)$. An extrapolation of the integrated hydrogen content towards Al-richer compositions (see Fig. 7.6b) shows that MgH_2 would form even in Mg_yAl_{1-y} alloys containing a Mg fraction as low as 5%.

However, a comprehensive characterization of the as-deposited film, as well as the knowledge of the structural changes occurring during hydrogenation are essential for the analysis of the optical measurements. Resistivity and XRD measurements as a function of the Mg fraction y in the as-deposited metallic state show that Mg_yAl_{1-y} alloys in thin film form do not follow the bulk phase diagram. The extended metallic solubility ranges and the absence of ordered

phases in the as-deposited state determine the overall behavior of the kinetics. The ability to probe an almost continuous set of compositions shows that the best kinetics of hydrogen absorption is achieved for the Mg-richer composition containing the amorphous (or nanocrystalline) Mg-Al alloy. This also points out the importance of thin sputtered films as an alternative to ball-milling to obtain glassy metastable phases and therefore to optimize the hydrogenation kinetics. Moreover, thin film deposition techniques enable one to control the concentration and location of impurities or catalysts in the sample more easily than in the bulk.

Although the morphology of the as-deposited film clarifies the kinetics of the Mg-rich part of the sample, it does not explain the complex pattern behavior of the optical transmission observed for Al-rich compositions in the hydrogenated state. Joined NRA, RBS and optical spectra measurements provide complementary information on the large-scale hydrogen-induced segregation that occurs at these compositions. The occurrence and direction of the MgH_2 migration is found to depend strongly on the Mg fraction y. For Mg dissolved in the Al lattice ($y < 0.21$), RBS and NRA measurements show clearly that MgH_2 strongly segregates towards the substrate. It is as yet unclear which process triggers the direction of the MgH_2 (and Al) migration.

Unreacted Mg, as well as the degree of (in)homogeneity of the whole Mg_yAl_{1-y} layer are also detected by an optical transmission-energy spectrum, even for Mg fractions ($0.36 < y < 0.5$) for which the segregation is happening on a smaller scale, and thus is difficult to resolve by NRA. This shows the complementarity of optical transmission, that probes directly the full stack of layers, with depth sensitive ion beam techniques like NRA and RBS. The comparison between measured optical spectra and the simulated ones also explains the low transmission intensity observed during kinetics experiments for this compositional range. This time, the starting alloy is an amorphous Mg-Al alloy, and the MgH_2 forms preferentially towards the Pd surface.

The two above examples show the variety of possible segregation phenomena in a single metal-hydride system and the potential of thin film related techniques to study them in detail.

For Mg fractions $0.25 < y < 0.36$, the film is found to be homogeneous in depth for both NRA and optical measurements. The observed optical transmission would account for a mixture of MgH_2 and Al. However, the [Al]/[Mg] ratio of 2, together with the following experimental facts indicate that a fraction of the whole layer has transformed into $Mg(AlH_4)_2$:

1. The integrated hydrogen content is slightly higher than the normal linear increase as a function of Mg fraction.

2. An anomalous conductivity behavior points to the presence of an additional semiconducting phase in the layer around $y = 0.33$.

3. The loading time, although the layer remains homogeneous, correlates well to the characteristic diffusion time of Al in Mg under these conditions. Co-sputtering results in an homogeneous mixture of Mg and Al atoms in the ratio 1:2. This means that long-range diffusion is not necessary -and also not observed- for the formation of the alanate. However, a short range atomic rearrangement of metal atoms is needed to form the ordered, ionic structure of $Mg(AlH_4)_2$. This would explain the long diffusive hydriding time observed.

Doping with metallic Ti suppresses the formation of $Mg(AlH_4)_2$. However, it favors the formation of MgH_2 for all Mg molar fractions above the Al percolation threshold ($y > 0.61$). In contrast, reversible formation of $Mg(AlH_4)_2$ is possible from the metallic elements below 100°C when using a Ti buffer layer.

The formation of $Mg(AlH_4)_2$ at 110 °C and 10^5 Pa is a surprising result, as from thermodynamic calculations,[300] this compound is expected to form, starting from a mixture of β-Mg_3Al_2 and fcc Al, around 10^7 Pa at this temperature, and only if the formation of MgH_2 is inhibited. However, the existence of $Mg(AlH_4)_2$ in thin films under similar moderate pressure and temperature was recently confirmed by XRD.[301,302] Such a thermodynamic stabilization of the Mg alanate formation reaction in thin film might be related to the microstructure in the as-deposited state, which consists in our case of an nanocrystalline or amorphous Mg-Al phase coexisting with fcc Al.

This investigation of the $Mg_yAl_{1-y}H_x$ system demonstrates the great potential of our compositional thin film approach for the search for new light-weight metal hydride storage materials. The ability to investigate hundreds of alloy compositions in a single thin film, the characterization of their microstructure before and after hydrogen loading and the determination of the most favorable kinetics enables us to optimize efficiently complex metal-hydride systems whose hydrogenation depends on a subtle interplay of thermodynamic stability, atomic diffusion of all constituents and surface catalysis.

References

1. J. N. Huiberts, R. Griessen, J. H. Rector, R. J. Wijngaarden, J. P. Dekker, D. G. de Groot, and N. J. Koeman, Nature **380**, 231 (1996).

2. A. L. Peratt, Astrophysics and Space Science **244**, 89 (1996).

3. IPCC, *Climate Change 2007: The physical science basis*, http://www.ipcc.ch/, 2007.

4. A. Züttel, www.empa.ch/H2E.

5. L. Schlapbach and A. Züttel, Nature **414**, 353 (2001).

6. A. Züttel, Naturwissenschaften **91**, 157 (2004).

7. K. Yvon, *Solid transition metal complexes, in Encycl. Inorg. Chem*, volume 5, Pergamon Press, New York, 1984.

8. P. Vajeeston, P. Ravindran, R. Vidyak, H. Fjellvåg, and A. Kjekhus, Phys. Rev. B. **68**, 212101 (2003).

9. T. Graham, Philos. Trans. Roy. Soc. London **156**, 399 (1866).

10. R. H. Wiswall and J. J. Reilly, Science **158**, 1168 (1974).

11. R. Griessen and T. Riesterer, *Topics in Applied Physics: Heat of formation models, in Hydrogen in Intermetallic Compounds I*, volume 63, Springer Verlag, Berlin, Heidelberg, 1988.

12. B. Bogdanović and M. Schwickardi, J. Alloys. Compd. **253**, 1 (1997).

13. B. Bogdanović, R. A. Brand, A. Marjanović, M. Schwickardi, and J. Tölle, J. Alloys. Compd. **302**, 36 (2000).

14. A. Züttel, P. Wenger, S. Rentsch, P. Sudan, P. Mauron, and C. Emmenneger, J. Power Sources **118**, 1 (2003).

15. B. C. Hauback, H. W. Brinks, and H. Fjellvåg, J. Alloys. Compd. **346**, 184 (2002).

16. H. W. Brinks and B. C. Hauback, J. Alloys. Compd. **354**, 143 (2003).

17. P. Chen, Z. Xiong, J. Luo, J. Lin, and K. L. Tan, Nature **420**, 302 (2002).

18. G. Sandrock, J. Reilly, J. Graetz, W.-M. Zhou, J. Johnson, and J. Wegrzyn, Appl. Phys. A **80**, 687 (2007).

19. C. H. Christensen, T. Johannessen, R. Z. Sørensen, and J. K. Nørskov, Catal. Today **70**, 165105 (2004).

20. A. Steinfeld, Int. J. Hydrogen Energy **27**, 611 (2002).

21. R. Aiello, M. A. Matthews, D. L. Reger, and J. Collins, Int. J. Hydrogen Energy **23**, 1103 (1998).

22. J. J. Hanak, J. Mater. Sci. **5**, 964 (1970).

23. H. Koinuma and I. Takeuchi, Nature Mater. **3**, 429 (2004).

24. J. Zhao, Prog. Mater. Sci **51**, 557 (2006).

25. X.-D. Xiang, Science **268**, 1738 (1995).

26. T. Fukumura, M. Ohtani, M. Kawasaki, Y. Okimoto, T. Kageyama, T. Koida, T. Hasegawa, Y. Tokura, and H. Koinuma, Appl. Phys. Lett. **77**, 3426 (2000).

27. J. Wang, Y. Yoo, I. T. C. Gao, X. Sun, H. Chang, X. Xiang, and P. Schulz, Science **279**, 1712 (1998).

28. R. Potyrailo and W. G. Morris, Appl. Phys. Lett. **84**, 634 (1984).

29. R. Potyrailo, Angew. Chem. Int. Ed. **45**, 702 (2006).

30. A. Ludwig, J. Cao, and J. Brugger, Meas. Sci. Technol. **16**, 1116 (2005).

31. J. P. Lemmon, Presentation at the MH2006 conference on Metal Hydrides, Maui-Hawaii, 2006 (2007).

32. P. Notten, M. Outwerkerk, H. van Hal, D. Beelen, W. Keur, J. Zhou, and H. Feil, J. Power. Sources **129**, 45 (2004).

33. B. J. Kooi, E. Zoestbergen, J. de Hosson, J. Kerssemakers, B. Dam, and B. Ward, J. Appl. Phys. **91**, 1901 (2004).

34. M. Dornheim, A. Pundt, R. Kirchheim, S. van der Molen, E. Kooij, J. Kerssemakers, R. Griessen, H. Harms, and U. Geyer, J. Appl. Phys. **93**, 8958 (2003).

35. P. Hjort, A. Krozer, and B. Kasemo, J. Alloys. Compd. **234**, L11 (1996).

36. J. N. Huiberts, J. H. Rector, R. J. Wijngaarden, S. Jetten, D. de Groot, B. Dam, N. J. Koeman, R. Griessen, B. Hjörvarsson, S. Olafsson, and Y. S. Cho, J. Alloys. Compd. **239**, 158 (1996).

37. C. Rehm, H. Maletta, M. Fieber-Erdmann, E. Holub-Krappe, and F. Klose, Phys. Rev. B. **65**, 113404 (2002).

38. W. Kalisvaart, R. Niessen, and P. Notten, J. Alloys. Compd. **417**, 280 (2006).

39. C. Olk, G. Tibbetts, D. Simon, and J. Moleski, J. Appl. Phys. **94**, 720 (2003).

40. S. J. van der Molen, J. W. J. Kerssemakers, J. H. Rector, N. J. Koeman, B. Dam, and R. Griessen, J. Appl. Phys. **86**, 6107 (1999).

41. A. T. M. van Gogh, S. J. van der Molen, J. W. J. Kerssemakers, N. J. Koeman, and R. Griessen, Appl. Phys. Lett. **77**, 815 (2000).

42. A. Borgschulte, W. Lohstroh, R. J. Westerwaal, H. Schreuders, J. H. Rector, B. Dam, and R. Griessen, J. Alloys Compd. **404-406**, 699 (2005).

43. S. Guerin, B. E. Hayden, and D. C. A. Smith, J. Comb. Chem. **10**, 37 (2008).

44. A. Baldi, R. Gremaud, C. P. Baldé, A. van der Eerden, P. de Jongh, H. Schreuders, J. H. Rector, B. Dam, and R. Griessen, Submitted to Phys. Rev. B (2008).

45. H. Yang, H. Yuan, J. Ji, H. Sun, Z. Zhou, and Y. Zhang, J. Alloys. Compd. **330-332**, 640 (2002).

46. E. M. Lifshitz and L. D. Landau, *Statistical Physics (Course of Theoretical Physics)*, Pergamon press, Oxford, 3rd edition, 1980.

47. A. Züttel, Mat. Today **6**, 24 (2003).

48. B. N. Chapman, *Glow discharge processes: sputtering and plasma etching*, Wiley-Interscience, New York, 1980.

49. E. D. Palik, *Handbook of Optical Constants of Solids*, Academic Press, San Diego, 1998.

50. M. J. van Setten, G. A. de Wijs, V. A. Popa, and G. Brocks, Phys. Rev. B. **75**, 035204 (2007).

51. E. Hurtós and J. Rodríguez-Viejo, J. Appl. Phys. **87**, 1748 (2000).

52. J. J. Vajo, F. Mertens, C. C. Ahn, R. C. Bowman, and B. Fultz, J. Phys. Chem. B **108**, 13977 (2004).

53. J. Chen, N. Kuriyama, Q. Xu, H. T. Takeshita, and T. Sakai, J. Phys. Chem. B **105**, 11214 (2001).

54. U. Bösenberg, S. Doppiu, L. Mosegaard, G. Barkhordarian, N. Eigen, A. Borgschulte, T. R. Jensen, Y. Cerenius, O. Gutfleisch, T. Klassen, M. Dornheim, and R. Bormann, Acta Mater. **55**, 3951 (2007).

55. A. Borgschulte, J. Rector, B. Dam, R. Griessen, and A. Züttel, J. of Catal. **235**, 353 (2005).

56. A. Borgschulte, R. J. Westerwaal, J. H. Rector, B. Dam, R. Griessen, and J. Schoenes, Phys. Rev. B **70**, 155414 (2004).

57. R. Gremaud, A. Borgschulte, W. Lohstroh, H. Schreuders, A. Züttel, B. Dam, and R. Griessen, J. Alloys. Compd. **404-406**, 775 (2005).

58. R. Lässer and K.-H. Klatt, Phys. Rev. B. **28**, 748 (1983).

59. E. Wicke and H. Brodowsky, *Hydrogen in Metals II*, Springer, Berlin, 1978.

60. C. Nützenadel, A. Züttel, D. Chartoumi, G. Schmid, and L. Schlapbach, Eur. Phys. J. D **8**, 245 (2000).

61. C. Sachs, A. Pundt, R. Kirchheim, M. Winter, M. T. Reetz, and D. Fritsch, Phys. Rev. B. **64**, 075408 (2001).

62. M.-W. Lee and R. Glosser, J. Appl. Phys. **57**, 5236 (1985).

63. R. Feenstra, D. G. de Groot, J. H. Rector, E. Salomons, and R. Griessen, J. Phys. F: Met. Phys. **16**, 1953 (1986).

64. J. Isidorsson, I. A. M. E. Giebels, H. Arwin, and R. Griessen, Phys. Rev. B. **68**, 115112 (2003).

65. D. M. Borsa, R. Gremaud, A. Baldi, H. Schreuders, J. H. Rector, B. Kooi, P. Vermeulen, P. H. L. Notten, B. Dam, and R. Griessen, Phys. Rev. B. **75**, 205408 (2007).

66. W. Lohstroh, R. J. Westerwaal, J. L. M. van Mechelen, C. Chacon, E. Johansson, B. Dam, and R. Griessen, Phys. Rev. B. **70**, 165411 (2004).

67. F. D. Manchester, editor, *Phase diagrams of binary hydrogen alloys*, ASM International, Materials Park, 2000.

68. T. P. L. Pedersen, C. Liesch, C. Salinga, T. Eleftheriadis, H. Weis, and M. Wuttig, Thin Solid Films **458**, 299 (2004).

69. A. Pundt and R. Kirchheim, Annu. Rev. Mater. Sci. **36**, 555 (2006).

70. J. Weissmüller and C. Lemier, Philos. Mag. Lett **80**, 411 (2006).

71. D. Richter, R. Hempelmann, and R. C. Bowman, *Hydrogen in intermetallic compounds*, Springer, Berlin, 1992.

72. R. B. Schwarz and A. G. Khachaturyan, Acta Mater. **54**, 313 (2006).

73. R. B. Schwarz and A. G. Khachaturyan, Phys. Rev. Lett. **74**, 2523 (1995).

74. H. Wagner and H. Horner, Adv. Phys. **23**, 587 (1974).

75. G. Song, M. Geitz, A. Abromeit, and H. Zabel, Phys. Rev. B. **54**, 14093 (1996).

76. A. Pundt, Adv. Eng. Mater. **6**, 11 (2004).

77. A. Pundt, *Nanoskalige Metall-Wasserstoff-Systeme*, Universitätverlag, Göttingen, 2005.

78. R. Nowakowski and R. Duś, Langmuir **19**, 6750 (2003).

79. A. Pundt, E. Nikitin, P. Pekarski, and R. Kirchheim, Acta Mater. **52**, 1579 (2004).

80. I. Kraus and N. Ganev, *Residual stress and stress gradients, in Industrial applications of X-ray diffraction*, Marcel Dekker, New York, Basel, 2000.

81. A. Pundt, C. Sachs, M. Winter, M. Reetz, D. Fritsch, and R. Kirchheim, J. Alloys. Compd. **293-295**, 480 (1999).

82. H. Frieske and E. Wicke, Berichte der Bunsen-Gesellschaft **77**, 48 (1973).

83. C. P. Broedersz, Master's thesis, VU University Amsterdam, 2007.

84. T. Tanaka, M. Keita, and D. E. Azofeifa, Phys. Rev. B. **24**, 1771 (1981).

85. L. Gillespie and L. Galstaun, J. Amer. Chem. Soc. **51**, 2565 (1936).

86. E. Wicke and J. Blaurock, J. Less-Common Met. **130**, 351 (1987).

87. J. Pryde and C. G. Titcomb, Trans. Farad. Soc. **65**, 2758 (1969).

88. T. Kuji and W. A. Oates, J. Less-Common Met. **102**, 251 (1984).

89. T. Schober and H. Wenzl, *Hydrogen in Metals II*, Springer-Verlag, Berlin, 1978.

90. E. Fromm and H. Uchida, J. Less-Common Met. **131**, 1 (1987).

91. F. Schweppe, M. Martin, and E. Fromm, J. Alloys. Compd. **261**, 254 (1997).

92. A. Krozer and B. Kasemo, J. Phys.: Condens. Matter **81**, 1533 (1989).

93. J. I. Langford, J. Appl. Cryst. **11**, 10 (1978).

94. T. de Keijser, E. J. Mittemeijer, and H. C. F. Rozendaal, J. Appl. Cryst. **16**, 309 (1983).

95. Y. Pivak, R. Gremaud, H. Schreuders, B. Dam, and R. Griessen, in preparation (2008).

96. H. Wagner and A. Pundt, Appl. Phys. Lett. **92**, 051914 (2008).

97. D. Nanu and A. Böttger, J. Alloys. Compd. **446**, 571 (2007).

98. M. Slaman, B. Dam, M. Pasturel, D. Borsa, H. Schreuders, J. H. Rector, and R. Griessen, Sensors and Actuat. B-Chem. **123**, 538 (2007).

99. R. A. H. Niessen and P. H. L. Notten, Electrochem. Solid-State Lett. **10** (2005).

100. D. M. Borsa, A. Baldi, M. Pasturel, H. Schreuders, B. Dam, R. Griessen, P. Vermeulen, and P. H. L. Notten, Appl. Phys. Lett. **88**, 241910 (2006).

101. A. Krozer and B. Kasemo, J. Less-Common Met. **160**, 323 (1990).

102. J. J. Reilly and R. H. Wiswall, Inorg. Chem. **7**, 2254 (1968).

103. T. J. Richardson, J. L. Slack, R. D. Armitage, R. Kostecki, B. Farangis, and M. D. Rubin, Appl. Phys. Lett. **78**, 3047 (2001).

104. J. Isidorsson, I. A. M. E. Giebels, M. D. Vece, and R. Griessen, Proc. SPIE **4458**, 128 (2001).

105. M. Pasturel, M. Slaman, D. Borsa, H. Schreuders, B. Dam, R. Griessen, W. Lohstroh, and A. Borgschulte, Appl. Phys. Lett. **89**, 021913 (2006).

106. K. Yoshimura, Y. Yamada, and M. Okada, Appl. Phys. Lett. **81**, 4709 (2002).

107. D. Lupu, R. Sârbu, and A. Biriş, Int. J. Hydrogen Energy **12**, 425 (1987).

108. W. Lohstroh, R. J. Westerwaal, J. L. M. van Mechelen, H. Schreuders, B. Dam, and R. Griessen, J. Alloys Compd. **13**, 430 (2007).

109. G. Liang, S. Boily, J. Huot, A. V. Neste, and R. Schulz, J. Alloys. Compd. **267**, 302 (1998).

110. K. Zeng, T. Klassen, W. Oelerich, and R. Bormann, J. Alloys. Compd. **283**, 213 (1999).

111. L. Schlapbach, D. Shaltiel, and P. Oelhafen, Mater. Res. Bull. **14**, 1235 (1979).

112. E. Akiba, K. Nomura, S. Ono, and S. Suda, Int. J. Hydrogen Energy **7**, 787 (1982).

113. G. Friedlmeier, M. Arakawa, T. Hirai, and E. Akiba, J. Alloys. Compd. **292**, 107 (1999).

114. W. Ha, H.-S. Lee, J.-I. Youn, T.-W. Hong, and Y.-J. Kim, Int. J. Hydrogen Energy **32**, 1885 (2007).

115. L. Z. Ouyang, S. Y. Ye, H. W. Dong, and M. Zhua, Appl. Phys. Lett. **90**, 021917 (2007).

116. A. A. Nayeb-Hashemi and J. B. Clark, editors, *Phase diagrams of binary magnesium alloys*, ASM international, Metals Park, 2001.

117. S. Orimo and H. Fujii, Appl. Phys. A **78** (2001).

118. H. Watanabe, Y. Goto, H. Kakuta, H. T. A. Kamegawa, and M. Okada, Mat. Trans. **45**, 1350 (2004).

119. J. Ell, A. Georg, M. Arntzen, A. Gombert, W. Graf, and V. Wittwer, Sol. Energy Mater. Sol. Cells **91**, 503 (2007).

120. S. Bao, Y. Yamada, K. Tajima, M. Okada, and K. Yoshimura, Vacuum, in press (2008).

121. L. J. van der Pauw, Philips Res. Repts. **13**, 1 (1958).

122. J. L. M. van Mechelen, Master thesis, Vrije Universiteit Amsterdam (2004).

123. D. M. Borsa, W. Lohstroh, R. Gremaud, J. H. Rector, R. J. Wijngaarden, and R. Griessen, J. Alloys. Compd. **428**, 34 (2006).

124. L. Nordheim, Ann. Phys **9**, 641 (1931).

125. K. Schröder, editor, *Handbook of Electrical Resistivities of Binary Metallic Alloys*, CRC Press Inc., Florida, 1983.

126. N. Huang, H. Yamauchi, J.Wu, and Q.Wang, Z. Phys. Chem. **163**, 225 (1989).

127. T. Massalski, P. S. H. Okamoto, and L. Kacprzak, *Binary Alloy Phase Diagrams*, American Society for Metals, Metals Park OH, 1990.

128. I. A. M. E. Giebels, J. Isidorsson, and R. Griessen, Phys. Rev. B. **69**, 205111 (2004).

129. B. E. Sernelius, K.-F.Berggren, Z.-C. Jin, I. Hamberg, and C. G. Granqvist, Phys. Rev. B. **37**, 10244 (1988).

130. I. Hauberg, C. G. Granqvist, K.-F. Berggren, B. E. Sernelius, and L. Engström, Phys. Rev. B. **30**, 3240 (1984).

131. I. Hauberg and C. G. Granqvist, J. Appl. Phys. **60**, 123 (1986).

132. K.-F. Berggren and B. E. Sernelius, Phys. Rev. B. **24**, 001971 (1981).

133. A. Borgschulte, R. Gremaud, S. de Man, R. J. Westerwaal, J. H. Rector, B. Dam, and R. Griessen, Appl. Surf. Sci. **253**, 1417 (2006).

134. K. von Rottkay, M. Rubin, F. Michalak, R. Armitage, T. J. Richardson, J. Slack, and P. Duine, Electrochimica Acta **44**, 3093 (1999).

135. J. V. Dobson and M. J. Taylor, Electrochim. Acta **31**, 235 (1986).

136. H. Amandusson, L.-G. Ekedahl, and H. Dannetun, J. Membr. Sci. **193**, 35 (2001).

137. L.-G. Petersson, H. M. Dannetun, and I. Lundström, Surf. Sci. **161**, 77 (1985).

138. G. W. Crabtree, M. Dresselhaus, and M. Buchanan, Physics Today **57**, 39 (2004).

139. O. J. Boser, J. Less-Common Met. **46**, 91 (1976).

140. M. J. Ron, J. Alloys. Compd. **283**, 178 (1999).

141. M. Miyamoto, K. Yamaji, and Y. J. Nakata, J. Less-Common Met. **89**, 111 (1983).

142. Z. Haberman, J. Bloch, M. H. Mintz, and I. J. Jakob, J. Alloys. Compd. **253-254**, 556 (1997).

143. A. Osovizky, J. Bloch, M. H. Mintz, and I. J. Jakob, J. Alloys. Compd. **245**, 168 (1996).

144. A. Borgschulte, R. J. Westerwaal, J. H. Rector, B. Dam, and R. Griessen, Appl. Phys. Lett. **85**, 4884 (2004).

145. T. Vegge, Phys. Rev. B **70**, 035412 (2004).

146. M. Tsuda, W. Dino, H. Kasai, H. Nakanishi, and H. Aikawa, Thin Solid Films **509**, 157 (2006).

147. B. Hammer and J. Nørskov, Nature **376**, 238 (1995).

148. K. Nobuhara, H. Kasai, W. Dino, and H. Nakanishi, Surf. Sci. **566**, 703 (2004).

149. A. Andreasen, T. Vegge, and A. S. Pedersen, J. Phys. Chem. B **109**, 3340 (2005).

150. F. H. Constable, Proc. R. Soc. A **355**, 108 (1925).

151. G. C. Bond, Appl. Catal. A: General **191**, 23 (2000).

152. T. Bligaard, K. Honkala, A. Logadottir, J. K. Nørskov, S. Dahl, and C. J. H. Jacobsen, J. Phys. Chem. B **107**, 9325 (2003).

153. W. J. Moore, *Physical Chemistry*, Addison Wesley Longman, Harlow England, 1972.

154. W. Wallace, R. Karlicek, and H. Imamura, J. Phys. Chem. **83**, 1708 (1979).

155. W. Göpel, Surf. Sci. **85**, 400 (1979).

156. B. Hammer and J. Nørskov, Surf. Sci. **343**, 211 (1995).

157. J. Greeley and M. Mavrikakis, J. Phys. Chem. B **109**, 3460 (2005).

158. A. Michaelides, P. Hu, and A. Alavi, J. Chem. Phys. **111**, 1343 (1999).

159. A. Borgschulte, R. J. Westerwaal, J. H. Rector, H. Schreuders, B. Dam, and R. Griessen, J. of Catalysis **239**, 263 (2006).

160. Y. Fukai, *The Metal-Hydrogen System, Basic Bulk Properties, in Springer Series in Materials Science*, volume 21, Springer, Berlin, 1993.

161. F. Faglioni and W. A. Goddard, J. Chem. Phys. **122**, 014704 (2005).

162. T. Mitsui, M. K. Rose, E. Fomin, D. F. Ogletree, and M. Salmeron, Nature **422**, 705 (2003).

163. D. Tomanek, S. Mukherjee, V. Kumar, and K. Bennemann, Surf. Sci. **114**, 11 (1982).

164. D. McLean, *Grain Boundaries in Metals*, Oxford University Press, 1957.

165. T. McMullen, M. J. Stott, and E. Zaremba, Phys. Rev. B. **35**, 1076 (1987).

166. N. Serdyuk and A. Chuprina, Russ. J. Phys. Chem. **54**, 1615 (1980).

167. J. Crank, *The Mathematics of Diffusion*, Clarendon, Oxford, 1975.

168. H. D. Baehr and K. Stephan, *Wärme- und Stoffübertragung*, Springer, Berlin, 2004.

169. J. Renner and H. J. Grabke, Z. Metallkd. **69**, 639 (1978).

170. M. Johansson, C. W. Ostenfeld, and I. Chorkendorff, Phys. Rev. B. **74**, 193408 (2006).

171. M. Pasturel, R. Wijngaarden, W. Lohstroh, H. Schreuders, M. Slaman, B. Dam, and R. Griessen, Chem. Mater. **19**, 624 (2007).

172. M. Martin, C. Gommel, C. Borkhart, and E. Fromm, J. Alloys. Compd. **238**, 193 (1996).

173. J. Bloch, J. Alloys. Compd. **312**, 135 (2000).

174. M. I. Temkin, Dokl. Akad. Nauk. SSSR **152**, 156 (1963).

175. M. I. Temkin, Int. Chem. Eng. **11**, 709 (1971).

176. P. W. Atkins, *Physical Chemistry*, Oxford University Press, Oxford, 1994.

177. A. Borgschulte, R. Gremaud, and R. Griessen, Submitted to Phys. Rev. B (2007).

178. G. Barkhordarian, T. Klassen, and R. Bormann, J. Alloys. Compd. **407**, 249 (2006).

179. G. Liang, J. Huot, S. Boily, A. V. Neste, and R. Schulz, J. Alloys. Compd. **291**, 295 (1999).

180. N. Lopez, Z. Lodziana, F. Illas, and M. Salmeron, Phys. Rev. Lett. **93**, 146103 (2004), The authors considered ideal surfaces, but the effect will be even enhanced on practical surfaces, i.e. with steps or impurities.

181. W. Lohstroh, R. J. Westerwaal, B. Noheda, S. Enache, I. A. M. E. Giebels, B. Dam, and R. Griessen, Phys. Rev. Lett. **93**, 197404 (2004).

182. R. Gremaud, M. Slaman, H. Schreuders, B. Dam, and R. Griessen, Appl. Phys. Lett. **91**, 231916 (2007).

183. M. Y. Song and H. R. Park, J. Alloys. Compd. **270**, 164 (1998).

184. S. Orimo, K. Ikeda, H. Fujii, Y. Fujikawa, Y. Kitano, and K. Yamamoto, Acta Mater. **45**, 2271 (1997).

185. M. J. van Setten, G. A. de Wijs, and G. Brocks, Phys. Rev. B. **76**, 075125 (2007).

186. M. J. van Setten, G. A. de Wijs, and G. Brocks, private communication (2007).

187. P. Zolliker, K. Yvon, J. D. Jørgensen, and F. J. Rotella, Inorg. Chem. **25**, 3590 (1986).

188. H. N. Murty, D. L. Biederman, and E. A. Heintz, J. Phys. Chem. **72**, 746 (1978).

189. P. S. Rudman, J. Appl. Phys. **50**, 7195 (1979).

190. A. Borgschulte, M. Bielmann, A. Züttel, G. Barkhordarian, M. Dornheim, and R. Bormann, Appl. Surf. Sci **254**, 2377 (2008).

191. P. Mauron, F. Buchter, O. Friedrichs, A. Remhof, M. Bielmann, C. N. Zwicky, and A. Züttel, **112**, 906 (2008).

192. W. Luo and K. Gross, J. Alloys. Compd. **385**, 224 (2004).

193. P. Vermeulen, R. A. H. Niessen, and P. H. L. Notten, El. Comm. **8**, 27 (2006).

194. M. van Setten, G. de Wijs, S. Er, and G. Brocks, in preparation, arXiv:0804.0376v1 (2008).

195. S. Shuxi and E. Wäckelård, Sol. Energy Mater. Sol. Cells **90**, 243 (2006).

196. A. Baldi, D. M. Borsa, H. Schreuders, J. H. Rector, T. Atmakidis, M. Bakker, H. Zondag, W. van Helden, B. Dam, and R. Griessen, Int. J. Hydrogen Energy **33**, 3188 (2008).

197. H. S. M. Slaman, B. Dam and R. Griessen, Int. J. Hydrogen Energy **33**, 1084 (2008).

198. F. R. de Boer, R. Boom, W. C. M. Mattens, A. R. Miedema, and A. K. Niessen, *Cohesion in Metals: Transition Metal Alloys*, North-Holland Physics, Amsterdam, 1988.

199. G. Liang and R. Schulz, J. Mater. Sci. **38**, 1179 (2003).

200. W.P.Kalisvaart, H. Wondergem, F. Bakker, and P. Notten, J. Mater. Res. **22**, 1640 (2007).

201. T. Mitchell, S. Diplas, P. Tsakiropoulos, J. F. Watts, and J. A. D. Matthew, Philos. Mag. A **82**, 841 (2002).

202. P. Vermeulen, R. A. H. Niessen, D. M. Borsa, B. Dam, R. Griessen, and P. H. L. Notten, Electrochem. Solid-State Lett. **9** (2006).

203. D. Kyoi, T. Sato, E. Rönnebro, N. Kitamura, A. Uedac, M. Ito, S. Katsuyama, S. Hara, D. Noreus, and T. Sakai, J. Alloys. Compd. **372**, 213 (2004).

204. E. Ma, Progress in Mat. Sci. **50**, 413 (2005).

205. J. H. He and E. Ma, Phys. Rev. B. **64**, 144206 (2001).

206. J. H. He, H. Sheng, P. J. Schilling, C.-L. Chien, and E. Ma, Phys. Rev. Lett. **86**, 2826 (2001).

207. J. H. He, H. Sheng, J. S. Lin, P. J. Schilling, R. C. Tittsworth, and E. Ma, Phys. Rev. Lett. **12**, 125507 (2002).

208. B. E. Warren, B. L. Averbach, and B. W. Robert, J. Appl. Phys. **22**, 1493 (1951).

209. R. Gremaud, C. P. Broedersz, D. M. Borsa, A. Borgschulte, P. Mauron, H. Schreuders, J. H. Rector, B. Dam, and R. Griessen, Adv. Mater. **19** (2007).

210. P. H. L. Notten, M. Kremers, and R. Griessen, **143**, 3348 (1996).

211. E. S. Kooij, A. T. M. van Gogh, and R. Griessen, **146**, 2990 (1999).

212. J. P. Bastide, B. Bonnetot, J. M. Letoffe, and P. Claudy, Mat. Res. Bull. **15**, 1779 (1980).

213. P. van der Sluis, M. Ouwerkerk, and P. A. Duine, Appl. Phys. Lett. **70**, 3356 (1997).

214. R. Gremaud, A. Borgschulte, C. Chacon, J. L. M. van Mechelen, H. Schreuders, A. Züttel, B. Hjörvarsson, B. Dam, and R. Griessen, Appl. Phys. A **84**, 77 (2006).

215. L. Vegard, Z. Phys. **5**, 17 (1921).

216. C. Michaelsen, Philos. Mag. A **72**, 813 (1995).

217. A. Pundt and C. Michaelsen, Appl. Surf. Sci **87**, 264 (1995).

218. P. Vajeeston, P. Ravindran, A. Kjekshus, and H. Fjellvåg, Phys. Rev. Lett. **89**, 175506 (2002).

219. P. Vajeeston, P. Ravindran, B. C. Hauback, H. F. g, A. Kjekhus, S. Furuseth, and M. Hanfland, Phys. Rev. B. **73**, 224102 (2006).

220. Y. Pivak, private communication (2008).

221. A. Remhof, J. W. J. Kerssemakers, S. J. van der Molen, R. Griessen, and E. S. Kooij, Phys. Rev. B. **65**, 054110 (2002).

222. H. J. Kreuzer and N. March, Theor. Chim. Acta. **74**, 339 (1988).

223. L. Liu and G. Guo, Chem. Rev. 101, 673 (2001) **101**, 673 (20031).

224. K. Sharp, Protein Sci. **10**, 661 (2001).

225. G. C. Bond, M. A. Keane, H. Kral, and J. A. Lercher, Catal. Rev. Sci. Eng. **42**, 323 (2000).

226. R. R. Krug, W. G. Hunter, and R. A. Grieger, J. Phys. Chem. **80**, 2341 (1976).

227. A. Cornish-Bowden, J. Biosci. **2**, 121 (2002).

228. R. R. Krug, W. G. Hunter, and R. A. Grieger, J. Phys. Chem. **80**, 2335 (1976).

229. S. T. Picraux and F. L. Vook, Phys. Rev. Lett. **33**, 1216 (1974).

230. G. Thomas, private communication (2007).

231. G. Thomas and G. Sandrock, *Hydrides database, http://hydpark.ca.sandia.gov*, Sandia National laboratories.

232. R. Lacher, Proc. R. Soc. London A **161**, 525 (1937).

233. R. Griessen, A. Driessen, and D. G. de Groot, J. Less-Common Met. **103**, 235 (1984).

234. H. Hemmes, E. Salomons, R. Griessen, P. Sänger, and A. Driessen, Phys. Rev. B. **39**, 10606 (1989).

235. R. C. Brouwer, J. Rector, N. Koeman, and R. Griessen, Phys. Rev. B. **40**, 003546 (1989).

236. R. C. Brouwer and R. Griessen, Phys. Rev. B. **40**, 001481 (1989).

237. S. Froyen and C. Herring, J. Appl. Phys. **52**, 7165 (1981).

238. R. Griessen and R. Feenstra, J. Phys. F **15**, 1013 (1985).

239. T. Flanagan and J. Oates, *Topics in Applied Physics: Hydrogen in Intermetallic Compounds I*, Springer-Verlag, Berlin, Heidelberg, 1988.

240. H. Peisl and H. Zabel, Phys. Rev. Lett. **42**, 511 (1979).

241. J. D. Eshelby, Proc. R. Soc. London A **241**, 376 (1957).

242. G. Alefeld, Phys. Stat. Sol. **32**, 67 (1969).

243. H. Wagner, *Topics in Applied Physics: Hydrogen Metals I*, Springer-Verlag, Berlin, Heidelberg, 1978.

244. K. A. Gschneider, Solid State Physics **16**, 308 (1964).

245. R. Yu and P. K. . Lam, Phys. Rev. B. **37**, 8730 (1988).

246. W. Wolf and P. Herzig, J. Phys.: Condens. Matter **12**, 4535 (2000).

247. B. Dam, R. Gremaud, C. P. Broedersz, and R. Griessen, Scripta Mater. **56**, 853 (2007).

248. M. Gonzalez-Silveira, R. Gremaud, H. Schreuders, B. Dam, and R. Griessen, in preparation (2008).

249. J.-J. Didisheim, P. Zolliker, K. Yvon, P. Fischer, J. Schefer, M. Gubelmann, and A. F. Williams, Inorg. Chem. **23**, 1953 (1984).

250. J. J. Reilly and R. H. Wiswall, Inorg. Chem. **6**, 2220 (1967).

251. P. Zolliker, K. Yvon, P. Fischer, and J. Schefer, Inorg. Chem. **24**, 4177 (1985).

252. T. J. Richardson, J. L. Slack, B. Farangis, and M. D. Rubin, Appl. Phys. Lett. **80**, 1341 (2002).

253. G. N. García, J. P. Abriata, and J. O. Sofo, Phys. Rev. B **59**, 11746 (1999).

254. W. R. Myers, L.-W. Wang, T. J. Richardson, and M. D. Rubin, J. Appl. Phys. **91**, 4879 (2002).

255. U. Häussermann, H. Blomqvist, and D. Noréus, Inorg. Chem **41**, 3684 (2002).

256. G. Liang, J. Huot, S. Boily, A. V. Neste, and R. Schulz, J. Alloys. Compd. **292**, 247 (1999).

257. H. Brodowsky and E. Poeschel, Z. Phys. Chem. **44**, 143 (1965).

258. R. Gremaud, A. Baldi, M. Gonzalez-Silveira, B. Dam, and R. Griessen, Phys. Rev. B. **77**, 144204 (2008).

259. C. R. Krenn, Modelling Simul. Mater. Sci. Eng **12**, S415 (2004).

260. C. P. Broedersz, R. Gremaud, H. Schreuders, B. Dam, O. M. Løvvik, and R. Griessen, Phys. Rev. B. **77**, 024204 (2008).

261. T. Girardeau, K. Bouslykhane, J. Mimault, J. P. Villain, and P. Chartier, Thin Solid Films **283**, 67 (1996).

262. A. Peles, J. A. Alford, Z. Ma, L. Yang, and M. Y. Chou, Phys. Rev. B. **70**, 165105 (2004).

263. J. L. M. van Mechelen, B. Noheda, W. Lohstroh, R. J. Westerwaal, J. H. Rector, B. Dam, and R. Griessen, Appl. Phys. Lett. **84**, 3651 (2004).

264. M. J. van Setten, G. A. de Wijs, V. A. Popa, and G. Brocks, Phys. Rev. B. **72**, 073107 (2005).

265. O. M. Løvvik and P. N. Nolin, Phys. Rev. B. **72**, 073201 (2005).

266. O. M. Løvvik, Phys. Rev. B. **71**, 144111 (2005).

267. A. Zaluska and L. Zaluski, J. Alloys Comp. **288**, 217 (1999).

268. J. F. Pelletier, J. Huot, R. S. M. Sutton, A. R. Sandy, L. B. Lurio, and S. G. J. Mochrie, Phys. Rev. B. **63**, 052103 (2001).

269. W. Oelerich, T. Klassen, and R. Bormann, J. Alloys. Compd. **315**, 237 (2001).

270. R. Y. Y. Song, X. Guo, Phys. Rev. B. **69**, 094205 (2004).

271. A. Zaluska, L. Zaluski, and J. O. Ström-Olsen, Appl. Phys. A **72**, 157 (2001).

272. S. Bouaricha, J. P. Dodelet, D. Guay, J. Huot, S. Boily, and R. Schulz, J. Alloys. Compd. **297**, 282 (2000).

273. H. Morioka, K. Kakizaki, S. Chung, and A. Yamada, J. Alloys. Compd. **353**, 310 (2003).

274. M. Fichtner and O. Fuhr, J. Alloys. Compd. **345**, 286 (2002).

275. M. Fichtner, J. Engel, O. Fuhr, O. R. A. Gloess, and R. Ahlrich, Inorg. Chem. **42**, 7060 (2003).

276. M. Fichtner, O. Fuhr, and O. Kircher, J. Alloys. Compd. **356-357**, 418 (2003).

277. A. T. M. van Gogh, D. G. Nagengast, E. S. Kooij, N. J. Koeman, J. H. Rector, R. Griessen, C. F. J. Flipse, and R. J. J. G. A. M. Smeets, Phys. Rev. B. **63** (2001).

278. L. R. Doolittle, Nucl. Instr. Meth. Phys. Res. **B15**, 227 (1985).

279. http://www.genplot.com.

280. L. C. Feldman and J. W. Mayer, *Fundamentals of surface and thin film analysis*, Elsevier, New York, 1986.

281. W. Lanford, H. Trautvetter, J. Ziegler, and J. Keller, Appl. Phys. Lett. **28**, 566 (1976).

282. J. F. Ziegler, *The stopping and ranges of ions in matter, in Handbook of Stopping Cross-Sections for Energetic Ions in all Elements*, volume 5, Pergamon Press, New York, 1980.

283. W. K. Chu, J. W. Mayers, and M. A. Nicolet, *Backscattering Spectrometry*, Academic Press, New York, 1978.

284. B. Hjörvarsson, H. Ryden, T. Ericsson, and E. Karlsson, Nucl. Instr. Meth. Phys. Res. **B42**, 257 (1989).

285. D. R. Lide, *CRC handbook of chemistry and physics*, CRC press, 2005.

286. P. Claudy, B. Bonnetot, and J. M. Letoffe, Thermochim. Acta **27**, 205 (1978).

287. R. W. Klaffky, N. S. Mohan, and D. H. Damon, J. Phys. Chem. Solids **36**, 1147 (1975).

288. S. Enache, W. Lohstroh, and R. Griessen, Phys. Rev. B **69**, 115326 (2004).

289. N. F. Mott and H. Jones, *The theory of the properties of metals and alloys*, Dover Pub, London, 1936.

290. R. D. Arnell and R. I. Bates, Vacuum **43**, 105 (1992).

291. C. J. Smithells, *Smithells Metals Reference Book (7th Ed.)*, Butterworth-Heinemann, Oxford, 1992.

292. Y. Adda and J. Philibert, *La diffusion dans les solides*, Presses universitaires de France, Paris, 1966.

293. E. Johansson, *Synthesis and characterization of potential hydrogen storage materials*, PhD thesis, Acta Universitatis Upsaliensis, Uppsala, 2004.

294. J. Rydén, B. Hjörvarsson, T. Ericsson, E. Karlsson, A. Krozer, and B. Kasemo, J. Less-Common Met. **152**, 295 (1989).

295. K. Higuchi, H. Kajioka, K. Toiyama, H. Fujii, S. Orimo, and Y. Kikuchi, J. Alloys. Compd. **293-295**, 484 (1996).

296. F. G. Heisenberg, D. A. Zagnoli, and J. J. Sheridan, J. Less-Common Met. **74**, 323 (1980).

297. G. A. Niklasson and C. G. Granqvist, J. Appl. Phys. **55**, 3382 (1984).

298. D. Stauffer and A. Aharony, *Introduction to percolation theory*, Taylor and Francis, London, 1994.

299. S. Kirkpatrick, Rev. Mod. Phys. **45**, 574 (1973).

300. M. Palumbo, F. Torres, J. Ares, C. Pisani, J. Fernandez, and M. Baricco, Calphad **31**, 457 (2007).

301. G. Garcia, R. Doménech-Ferrer, F. Pi, J. Santiso, and J. Rodríguez-Viejo, J. Comb. Chem **9**, 230 (2007).

302. R. Domènech-Ferrer, M. G. Sridharan, F. P. G. Garcia, and J. Rodríguez-Viejo, J. Power Sources **169**, 117 (2007).

Summary

Hydrogenography

The search for new lightweight metal hydride storage materials is essentially looking for a needle in a haystack. This thesis addresses this issue by the development of a new thin film optical combinatorial approach, Hydrogenography, that greatly facilitates the identification and characterization of new hydrogen storage materials. The fact that absorption of hydrogen in a metal leads to large optical changes is at the basis of the method. We produce thousands of samples at once by sputter-depositing thin films with a compositional gradient. With a a straightforward optical setup, Hydrogenography makes it possible to monitor hydrogen ab/desorption simultaneously on all the samples under exactly the same experimental conditions. We show that Hydrogenography is much more than a monitoring technique, as it provides also a high-throughput method to measure quantitatively the key thermodynamic properties (enthalpy and entropy) of hydride formation, as well as the kinetics of hydrogen sorption. We apply a large panel of complementary techniques and models to understand the nature, boundaries, structure and morphology of the metal and hydride phases formed in compositional gradient thin films.

Stress relaxation in PdH_x

As a proof of concept for the Hydrogenography method, we consider first the thin film PdH_x system (Chapter 3). Although both the Pd metal and its hydride are metallic, we demonstrate that the optical transmission change during hydrogen sorption is high enough to record pressure-*optical transmission*-isotherms (PTI). Similarly to what is done with conventional pressure-concentration-isotherms, this allows us to obtain the thermodynamic parameters (enthalpy and entropy) of the hydrogen sorption reactions.

The evolution with the number of hydrogenation cycles of the ab- and desorption isotherms, correlated with the film morphology and microstructure evolution, provides essential information on the stress relaxation processes active in thin hydride films initially clamped to a substrate. Buckling relaxes the H-induced stress build up in thin films effectively. However, buckling does not relax stress homogeneously in the film. It is only after the formation of

a buckle-and-crack network that the film surface is fractionalized enough to enable a more homogeneous stress relaxation. This is clearly seen upon cycling in the isotherms, as a flat section progressively appears to replace the initially sloping plateaus, which corresponds to the transition from inhomogeneous to homogeneous stress distribution in the film. The enthalpy and entropy values of hydride formation for homogeneously relaxed films are in very good agreement with bulk literature values.

$\mathbf{Mg}_y\mathbf{Ni}_{1-y}\mathbf{H}_x$: thermodynamic-kinetic interplay

In chapter 4, we expand the optical isotherm acquisition method to $Mg_yNi_{1-y}H_x$ thin films with a compositional gradient in the Mg fraction y. This system is particularly interesting, as two semiconducting hydrides, MgH_2 and the complex Mg_2NiH_4, are likely to coexist in the film. Additionally, we study the effect of Mg- or Ni-doping, as a well as of specific compositons (phase boundaries, eutectics) on the hydrogenation properties. We focus especially on the rate of hydrogen absorption, for which we develop a two-step model to describe the experimental results.

Phase identification
In the metallic state, Mg_2Ni is the only crystalline phase observed for Mg fractions y below the Mg-Mg_2Ni eutectics ($y < 0.89$). Conversely, above the eutectics, the rutile Mg 002-reflection is the only one detected. After hydrogenation, the hydride consists of Ni-doped Mg_2NiH_4 below the [Mg]:[Ni] = 2 ($y < 0.67$) stoichiometric composition, and Mg-doped Mg_2NiH_4 between the stoichiometric and eutectic compositions ($0.67 < y < 0.89$). For $y > 0.89$, the main hydride phase is MgH_x, although some traces of Mg_2NiH_4 are found close to the eutectic composition. Full hydrogenation of Mg is hampered by the slow diffusion of H in the MgH_2 phase, and a large amount of metallic Mg remains in the layer. It is remarkable that the Mg_2Ni-Mg eutectic composition, that only concerns the metallic phases, has such an impact on the hydrogenation properties.

Thermodynamics
Pressure–optical-transmission–isotherms are recorded for all Mg_yNi_{1-y} compositions *simultaneously*. We are thus able to compare the relative stability of the different hydrides forming in the $Mg_yNi_{1-y}H_x$ layer at different compositions. While MgH_2 forms first, at higher pressures the plateau corresponding to the Mg_2NiH_4 complex hydride formation is visible. Ni- and Mg-doping slightly increases the equilibrium pressure of Mg_2NiH_4, the lowest p_{eq} being found close to the stoichiometry ($y \simeq 0.7$). The enthalpy values, though approximately constant within most of the measured compositional range, diverge then strongly for compositions close to the eutectic ($0.8 < y < 0.88$). Although a destabiliza-

tion with increasing Mg content is predicted by density functional calculations, the sharp divergence close to a major microstructural change at the eutectic indicates that the interfacial energy stored in the Mg2Ni and Mg phases boundaries might contribute to the total hydrogenation enthalpy.

Kinetics: results and modeling
Thanks to the *in situ* deposition of a PTFE overlayer, it is possible to record reproducible rates during different hydrogenation cycles, on the same sample, under exactly the same conditions and for all compositions. The H_2 pressure dependence of the rate makes it possible to extrapolate the *true equilibrium* coexistence plateau pressure p_{eq} as a function of composition y.

Recent measurements of activation energies of various hydrogen storage materials posed intriguing questions about their physical meaning. In order to rationalize the experimental results, a one-dimensional model is set up to estimate the time-, temperature- and pressure dependence of sorption kinetics and the relevance of several materials parameters involved in the process. The model, which incorporates explicitly surface and diffusion processes, results in three main conclusions:

1. It is impossible to distinguish between dissociation- or diffusion processes on/in a thin cover layer via the time dependence of the total kinetics.

2. In most cases, a *single rate limiting step* does not exist.

3. The apparent activation energy and the pressure dependence of the rate are functions of the relative importance of the elementary processes involved in H-sorption and E_{AA} is thus not an intrinsic materials property.

The optical measurements of the H sorption rate as a function of composition y in $Mg_y Ni_{1-y} H_x$, hydrogen pressure and temperature serve to validate the two-step modeling of the kinetics. From the temperature dependence of the rate, we obtain the surface activation energy of the Pd-capped $Mg_y Ni_{1-y} H_x$ films.

This joint kinetics and thermodynamics study draws a comprehensive picture of the hydrogenation of $Mg_y Ni_{1-y} H_x$ gradient thin films. It furthermore shows that multi-phase hydride systems containing complex hydrides with low or no crystallinity can by effectively addressed, and their kinetics and thermodynamcis measured using the all-optical Hydrogenography approach.

Chemical short-range order in $Mg_y Ti_{1-y} H_x$

Contrary to Mg and Ni, Mg and Ti are immiscible, and no stable bulk compound is expected at any composition in the metallic phase diagram. However, one of the most surprising properties of the $Mg_y Ti_{1-y} H_x$ films studied in chapter 5 is their structural stability: the initial high degree of mixing is maintained

upon hydrogen cycling. This property is reflected in the optical isotherms, which show an unusual shape, incompatible with a sequential hydrogenation of Ti and Mg in the film.

The contribution of Hydrogenography to this chapter is twofold: First, we show that pressure–optical-transmission–isotherms, the enthalpy and entropy of hydride formation can be measured optically and simultaneously on a large number of samples. The two hydride phases (rutile and fluorite MgH_2-like) found by XRD depending on composition are seen in the isotherms as two distinct plateaus that are coexisting in the $0.85 < y < 0.89$ range. The very small pressure difference between these two plateaus confirms that the local geometry around a hydrogen atom (rutile or fcc) has little influence on the site energy in MgH_2. Finally, the unprecedent range of temperatures measured confirms the stability of the metastable $Mg_yTi_{1-y}H_x$ microstructure and opens up the systematic investigation of enthalpy-entropy compensation effects in metal-hydrides.

Secondly, we show that optical isotherms recorded by Hydrogenography also contain information about the microstructure of $Mg_yTi_{1-y}H_x$ alloys. By modeling of the pressure–optical-transmission–isotherms with a multi-site lattice gas model including chemical short-range order, we effectively use hydrogen as a probe for tracking the degree of chemical segregation in the immiscible $Mg_yTi_{1-y}H_x$ alloy system. The unusual shape of the experimental PTIs and the plateau pressures at various Mg atomic fractions y and temperatures are well reproduced by the multi-site lattice gas model, assuming the chemical short-range order parameter s as only free varying parameter. We find that the sloping behavior in the isotherms is reproduced assuming the hydrogen-sites surrounded by one or more Ti atoms fill first, while the plateaus are due to the hydrogenation of sites surrounded only by Mg atoms. The CSRO s values derived from the multi-site modeling of Hydrogenography data agree well with s values determined from EXAFS measurements. The non-zero L parameter shows that the volume of interstitial sites depends on the local chemical composition, and therefore indicates the presence of local modulations of the crystal lattice size.

This multi-site lattice-gas model, by determining two essential characteristics of an alloy microstructure that are the CSRO parameter s and the lattice modulation parameter L, is complementary to experimental local-environment probes such as EXAFS or more elaborate modeling approaches using Reverse Monte Carlo simulation and Molecular Dynamics to characterize alloys created between immiscible elements.

Optimization of $Mg_yNi_zTi_{1-y-z}H_x$

We show in chapter 6 that Hydrogenography is also a very valuable method for performing exploratory searches for new hydrogen storage materials. The

deposition of a large portion of the Mg-Ni-Ti phase diagram at once makes it possible to quickly identify the range of composition with favorable thermodynamics and kinetics properties. The composition $Mg_{0.69}Ni_{0.26}Ti_{0.05}$ optimally combines a favorable thermodynamics with a fast kinetics comparable to Mg_2NiH_4 and a reasonable hydrogen storage capacity (3.2 weight %). The entropy change $\Delta S_0 = -92$ J K^{-1} (mol H$_2$)$^{-1}$, however, is significantly smaller than the standard hydrogen gas value $S_{H_2}^0 = 131$ J K^{-1} (mol H$_2$)$^{-1}$. This has the undesired effect of lowering the equilibrium pressure.

The experiments also reveal a remarkable linear correlation between the ΔH and ΔS_0 data. This phenomenon, which is not understood, is known as enthalpy-entropy compensation. Hydrogenography provides excellent means to study this effect, as all samples are produced and measured under exactly the same conditions.

In addition to the the fundamental interest, compensation effects may be of crucial importance for hydrogen storage applications, since compensation constraints the tuning possibilities of the operating conditions of materials by doping.

Towards alanates with $Mg_yAl_{1-y}H_x$

Alkali alanates form a promising class of complex hydrides in view of hydrogen storage, and in chapter 7 we aim at the synthesis of the $Mg(AlH_4)_2$ alanate from the elements. We use Hydrogenography to map simultaneously all the hydride forming compositions and the kinetics thereof in $Mg_yAl_{1-y}H_x$ gradient thin films. Additionally, we combine dc resistivity, X-ray diffraction, visible/ultraviolet spectrophotometry, resonant nuclear analysis and Rutherford backscattering spectrometry to identify the metal and hydride phases formed. This complex approach is made necessary by the large-scale hydrogen-induced segregation of MgH_2 and Al that occurs in the Al-rich part of the film.

The first important result is that hydrogenation of Mg_yAl_{1-y} thin films occurs at much milder conditions than in the corresponding bulk samples. Under these conditions, MgH_2 is found to form at all alloy compositions investigated. $(0.2 \leq y \leq 0.9)$.

Resistivity and XRD measurements in the as-deposited metallic state as a function of the Mg fraction y show that in thin films Mg_yAl_{1-y} alloys do not follow the bulk phase diagram. Extended metallic solubility ranges and the absence of ordered phases in the as-deposited state determine the overall behavior of the kinetics. The best kinetics of hydrogen absorption is achieved for the Mg-richer composition containing the amorphous (or nanocrystalline) Mg-Al alloy. Although the morphology of the as-deposited film clarifies the kinetics of the Mg-rich part of the sample, it does not explain the complex pattern behavior of the optical transmission observed for Al-rich compositions in the hydrogenated state. Joined NRA, RBS and optical spectra measure-

ments provide complementary information on the large-scale hydrogen-induced segregation that occurs at these compositions.

The occurrence and direction of the MgH_2 migration is found to depend strongly on the Mg fraction y:

1. For Mg dissolved in the Al lattice ($y < 0.21$), MgH_2 strongly segregates towards the substrate. Unreacted Mg, as well as the degree of (in)homogeneity of the whole Mg_yAl_{1-y} layer are also detected by an optical transmission-energy spectrum. This shows the complementarity of optical transmission, that probes directly the full stack of layers, with depth sensitive ion beam techniques like NRA and RBS.

2. For Mg fractions $0.25 < y < 0.36$, the film is found to be homogeneous in depth. The observed optical transmission would account for a mixture of MgH_2 and Al. However, the [Al]/[Mg] ratio of 2, the higher hydrogen content and the anomalous conductivity all indicate that a fraction of the whole layer has transformed into $Mg(AlH_4)_2$.

3. For Mg fractions ($0.36 < y < 0.5$), the starting alloy is an amorphous Mg-Al alloy, and the MgH_2 forms preferentially towards the Pd interface.

With Hydrogenography, we are thus able to screen on a broad scale the phase transformation processes that occur upon hydrogenation. Hydrogenography is complementary to other thin film techniques, giving essential information about the kinetics and thermodynamics of hydrogenation. Thin films can therefore be used as model systems to find new, tailored metal-hydrides for hydrogen storage.

Samenvatting

Hydrogenography

De zoektocht naar nieuwe lichtgewicht metaalhydrides voor waterstofopslag lijkt op het zoeken naar de spreekwoordelijke naald in een hooiberg. Dit proefschrift laat zien dat de identificatie en karakterisatie van nieuwe materialen voor waterstofopslag enorm vergemakkelijkt wordt door het gebruik van een nieuw ontwikkelde, combinatorische methode genaamd 'Hydrogenography'. De verandering in optische eigenschappen die het gevolg is van de waterstofopname door het metaal, ligt aan de basis van deze methode. Door simpelweg de optische transmissie te meten, kan de waterstofopname in duizenden verschillende materialen tegelijk worden bestudeerd onder exact dezelfde omstandigheden. Hiertoe prepareren we door middel van sputterdepositie dunne films, waarbij we door gradiënten in de compositie duizenden samples tegelijk produceren. Van deze dunne films kunnen de optische eigenschappen eenvoudig onder gecontroleerde omstandigheden worden gemeten. Hydrogenography kan nog veel meer: ook de thermodynamische eigenschappen (enthalpie en entropie) en de kinetiek van de hydrogenatie kunnen kwantitatief bepaald worden.

Spanning-relaxatie in PdH$_x$

Als bewijs voor het concept van onze methode onderzoeken we eerst het welbekende Pd-H systeem. (Hoofdstuk 3). Hoewel zowel palladium als palladiumhydride metallisch zijn, is de verandering van optische transmissie gedurende waterstofabsorptie hoog genoeg om optisch de waterstofopname als functie van de waterstofdruk te kunnen volgen. Net als met de vergelijkbare, conventionele druk-concentratie-isothermen, kunnen we nu de thermodynamische parameters (enthalpie and entropie) van de hydrogenatie-reactie bepalen door de druk-optische transmissie-isothermen te meten.

De evolutie van de ab- en desorptie-isothermen als functie van het aantal hydrogenatie-cycli laat zien, hoe de binding van de dunne palladiumlaag aan het substraat de hydrogenatie beïnvloedt. De veranderingen in filmmorfologie en -microstructuur leveren essentiële informatie over hoe de spanning,

die ontstaat door de waterstofgeïnduceerde roosteruitzetting van het palladium, gerelaxeerd wordt. Het blijkt dat de film gedeeltelijk los komt van het substraat (buckling). Deze buckling blijkt te correleren met de vorming van vlakke stukken in de grotendeels hellende plateaus in de isothermen. De waarden die we van de temperaturafhankelijkheid van deze vlakke isothermen vinden voor de enthalpie en entropie van de waterstofdesorptie blijken in hoge mate overeen te stemmen met de literatuurwaarden voor bulk palladium.

$Mg_yNi_{1-y}H_x$: De wisselwerking tussen thermodynamica en kinetiek

In hoofdstuk 4, laten we zien hoe we tegelijkertijd honderden optische isothermen bepalen in een dunne film met een compositiegradiënt ($Mg_yNi_{1-y}H_x$). Dit is een interessant materiaalsysteem omdat het voor de hand ligt te veronderstellen dat de film altijd uit twee stoichiometrische halfgeleidende hydrides (MgH_2 en de complexe hydride Mg_2NiH_4) zal bestaan.

Identificatie van de fase
In the metallische toestand is Mg_2Ni de enige kristallijne fase die we met röntgendiffractie waar kunnen nemen voor Mg concentraties kleiner dan het Mg-Mg_2Ni eutecticum ($y < 0.89$). Bij hogere Mg concentraties vinden we alleen de 002-reflectie van de rutiel magnesium fase. Na hydrogenatie vinden we aanwijzingen voor het bestaan van Ni-gedoopt Mg_2NiH_4 (voor $y < 0.67$) en Mg-gedoopt Mg_2NiH_4 tussen de stoichiometrische en eutectische compositie ($0.67 < y < 0.89$). Als $y > 0.89$ vinden alleen MgH_x. De hydrogenatie van Mg is echter niet volledig en een grote fractie blijft in de metallische toestand. Het is opmerkelijk dat het eutecticum, dat alleen op de metallische fase betrekking heeft, zo'n grote invloed op de hydrogenatie blijkt te hebben.

Thermodynamica
Met Hydrogenography registreren we de druk-optische transmissie-isothermen voor alle Mg_yNi_{1-y} composities *tegelijkertijd*. We kunnen zo direct de verschillen in relatieve stabiliteit van de gevormde hydrides vergelijken. Terwijl MgH_2 als eerste vormt, vinden we bij hogere waterstofdrukken de vorming van Mg_2NiH_4; precies zoals we op basis van de bulk vormingsenthalpie zouden verwachten. De doping met Ni en Mg verhoogt de evenwichtsdruk van Mg_2NiH_4 slechts marginaal. De laagste p_{eq} wordt dicht bij de stoichiometrische compositie ($y \simeq 0.7$) gevonden. De gemeten enthalpie blijkt ongeveer constant te zijn en divergeert alleen voor composities dicht bij het eutecticum ($0.8 < y < 0.88$). Deze divergentie dicht bij een grote microstructurele verandering (het eutecticum) duidt erop dat de interface energie die opgeslagen ligt in de Mg_2Ni en de Mg fase-grenzen wellicht een bijdrage levert aan de hydrogenatie enthalpie.

Kinetiek: resultaten en modellering

Dankzij de *in situ* depositie van een PTFE deklaag is het mogelijk reproduceerbare hydrogenatie-cycli te meten onder verschillende condities. Uit een welbepaalde H_2 drukafhankelijkheid van de sorptie-kinetiek, is het mogelijk de waarde van de *reële* evenwichtsdruk p_{eq} te bepalen als functie van de compositie.

Recente metingen van de activeringsenergie van verschillende waterstofopslagmaterialen heeft intrigerende vragen opgeworpen over de fysische betekenis ervan. Om onze experimentele resultaten te begrijpen hebben we een 1-dimensionaal model gemaakt om de tijd-, temperatuur- en drukafhankelijkheid van de sorptiekinetiek te bepalen en de relevantie van de diverse parameters. Dit model, dat expliciet de oppervlakte- en diffusieprocessen incorporeert, leidt tot drie conclusies:

1. Het is onmogelijk om te onderscheiden tussen dissociatie- en diffusieprocessen op basis van de tijdsafhankelijkheid van de sorptiekinetiek.

2. Een *enkele snelheidsbepalende stap* zal in het algemeen niet te definiëren zijn.

3. De schijnbare activeringsenergie (E_{AA}) en de drukafhankelijkheid van de sorptiesnelheid zijn functies van de relatieve belang van de elementaire sorptie-processen. E_{AA} is dus niet een intrinsieke materiaaleigenschap.

De optische meeting van de waterstof sorptie-snelheid als een functie van de compositie y in $Mg_yNi_{1-y}H_x$, de waterstofdruk en de temperatuur, bevestigen de aanwezigheid van een 2-stapsproces. Uit de temperatuurafhankelijkheid van de sorptiesnelheid bepalen we de oppervlakte-activeringsenergie van Pd-bedekte $Mg_yNi_{1-y}H_x$ films.

De combinatie van kinetische en thermodynamische metingen geeft ons een samenhangend beeld van de hydrogenatie van $Mg_yNi_{1-y}H_x$ dunne films met een compositiegradiënt. Deze studie laat zien dat een meerfasig hydride systeem bestaande uit complexe hydrides met geen of geringe kristalliniteit effectief bestudeerd kan worden. Hydrogenography is in staat de samenhang in de kinetiek en thermodynamica in deze fase's weer te geven.

Lokale chemische orde in $Mg_yTi_{1-y}H_x$

In tegenstelling tot het Mg-Ni systeem, zijn Mg en Ti niet mengbaar. We verwachten dus geen stabiele metallische Mg-Ti verbinding te vinden, waar dan ook in het fasediagram. Echter, in chapter 5 laten we zien dat de menging die bij depositie ontstaat, gehandhaaft blijft bij het herhaaldelijk beladen en ontladen met waterstof. De optische isothermen van het Mg-Ti-H systeem

laten een ongebruikelijk gedrag zien, dat incompatibel is met een sequentiële hydrogenatie van Ti en Mg. Dit staat in scherp contrast met wat we in andere Mg-systemen, zoals Mg-V-H, vinden.

Hydrogenography heeft in dit hoofdstuk twee functies: In de eerste plaats tonen we hier aan dat de enthalpie en de entropie van de hydridevorming simultaan aan een groot aantal samples gemeten kan worden. Afhankelijk van de compositie vinden we met röntgendiffractie een MgH_2-achtige fase met een rutiel of een fluoriet symmetrie, die we als twee verschillende plateaus in de optische isothermen terugvinden. Het geringe drukverschil tussen de twee plateaus bevestigt dat de lokale geometrie rond een waterstofatoom (rutile of fcc) weinig effect heeft op de energie van dat atoom in MgH_2. We vinden hetzelfde fase-gedrag bij hogere beladingstemperaturen. Dit duidt op een grote stabiliteit van deze $Mg_yTi_{1-y}H_x$ microstructuur en biedt de mogelijkheid de relatie tussen enthalpie en entropie systematisch als functie van de temperatuur te bestuderen.

Ten tweede laten we zien dat de optische isothermen die we met Hydrogenography registreren ook informatie bevatten over de microstructuur van de $Mg_yTi_{1-y}H_x$ legeringen. Door de druk-optische transmissie–isothermen te beschrijven met een multi-site roostergas model waarin de lokale chemische ordening is opgenomen, kunnen we de hydrogenatie gebruiken als een probe om de mate van chemische ordening in het $Mg_yTi_{1-y}H_x$ systeem te bepalen. We vinden dat de vorm van de optische isothermen een goede indicator is voor het bestaan van een lokale ordening in het metaalrooster. De graduele stijging van de transmissie met de druk, wordt door het model gereproduceerd als we aannemen dat eerst die waterstofsites gevuld worden die een of meer Ti-atomen als eerste orde buur hebben. De plateaus zijn het gevolg van het vullen van de sites die alleen door 4 Mg atomen omringd worden. De chemische lokale orde parameter s die we uit dit model bepalen, komt goed overeen met wat in EXAFS metingen gevonden wordt.

Het feit dat we niet alleen s maar ook de rooster-modulatie parameter L kunnen bepalen, laat zien, dat hydrogenography complementair is aan locale probes zoals EXAFS en modellering met bijvoorbeeld Reverse Monte Carlo simulatie en Moleculaire Dynamica bij het karakteriseren van de lokale orde die in sommige, niet-mengbare legeringen optreedt.

Optimaliseren van $Mg_yNi_zTi_{1-y-z}H_x$

In het hoofdstuk 6 laten we zien dat Hydrogenography een geschikte methode is om een nieuw waterstofopslagsysteem te exploreren. We zijn in staat om met de depositie van drie gradiënten in de compositie een groot gedeelte van het Mg-Ni-Ti fasediagram te reproduceren en daarbinnen snel een aantal composities te identificeren met geschikte thermodynamische en kinetische eigenschappen. $Mg_{0.69}Ni_{0.26}Ti_{0.05}$ blijkt een optimale combinatie van thermo-

dynamische eigenschappen te hebben, waarbij de kinetiek snel genoeg is en de waterstofopslagcapaciteit 3.2 gewichts % bedraagt. De entropie van de reactie $\Delta S_0 = -92$ J K^{-1} (mol H$_2$)$^{-1}$, is echter significant kleiner dan verwacht als we aannemen dat deze volledig bepaald wordt door de standaard waarde van waterstofgas $S_{H_2}^0 = 131$ J K^{-1} (mol H$_2$)$^{-1}$. Hierdoor is ook de evenwichtsdruk lager dan verwacht. Dit laat zien dat ook de entropie een parameter is die gebruikt kan worden om de evenwichtsdruk van de reactie te optimaliseren. De experimenten laten ook een opmerkelijke, lineaire correlatie zien tussen ΔH en ΔS_0. Dit verschijnsel, dat in de thermodynamische literatuur bekend staat als het enthalpie-entropie compensatie effect, is tot op heden onbegrepen. Hydrogenography is een perfecte manier om dit fenomeen nader te bestuderen, aangezien alle samples onder exact dezelfde condities gemaakt en gemeten worden. Behalve het fundamentele belang van het compensatie-effect, laat het ook zien dat we de enthalpie en entropie niet willekeurig kunnen variëren om zo de optimale werkdruk van het waterstofopslag materiaal te realiseren.

De eerste stap naar de alanaten

Alkali-alanaten zijn voor waterstofopslag een veelbelovende klasse van complexe metaalhydrides. In hoofdstuk 7 beschrijven we de synthese van een dunne Mg(AlH$_4$)$_2$ alanaat film uit de elementen. Met Hydrogenography brengen we simultaan alle hydride vormende composities in kaart die in Mg$_y$Al$_{1-y}$H$_x$ gradient dunne films gevormd worden bij geschikte temperatuur en waterstofdruk. We combineren informatie verkregen uit DC-weerstandsmetingen, röntgendiffractie, uv/vis spectrofotometrie, resonante nucleaire analyse en Rutherford backscattering spectrometrie om de gevormde metaal en hydride fases te identificeren. Deze complexe aanpak is nodig door de waterstofgeïnduceerde segregatie van MgH$_2$ en Al die in het Al-rijke deel van de film op blijkt te treden.

Allereerst vinden we dat de hydrogenatie van Mg$_y$Al$_{1-y}$ dunne films onder veel mildere condities plaats vindt dan in de corresponderende bulk samples. We vinden dat MgH$_2$ gevormd wordt over het gehele compositie bereik ($0.2 \leq y \leq 0.9$).

Weerstands- en röntgenmetingen als een functie van de Mg fractie y in de onbewerkte metallische toestand laten zien dat de Mg$_y$Al$_{1-y}$ legeringen in dunne film vorm zich anders gedragen dan op grond van het bulk fasediagram verwacht zou worden. We vinden dat de metallische oplosbaarheid veel groter is en dat geordende fase's ontbreken. De beste waterstofabsorptie kinetiek vinden we in het Mg-rijke deel dat amorf (of nanokristallijn) Mg-Al bevat.

Voor de Al-rijke composities vinden we na beladen een complex patroon in de optische transmissie. Dit is het gevolg van een waterstofgeïnduceerde segregatie die bij deze composities optreedt. De migratie van MgH$_2$ die bij hydrogenatie optreedt blijkt sterk af te hangen van de Mg fractie y:

1. Voor $y < 0.21$, segregeert Mg sterk naar het substraat toe. We detecteren ongereageerd Mg, en kunnen de mate van (in-)homogeniteit van de Mg_yAl_{1-y} laag met optische transmissiemetingen kwantitatief in kaart brengen. Dit laat zien dat optische metingen complementair kunnen zijn aan diepte selectieve metingen zoals NRA en RBS.

2. Voor Mg fracties $0.25 < y < 0.36$, blijkt de film homogeen in de dikte te zijn, wat suggereert dat er bij deze composities geen fase-segregatie optreedt. De waargenomen optische transmissie kan met een mengsel van MgH_2 and Al beschreven worden. Echter, bij een [Al]/[Mg] ratio van 2, vinden we een hogere waterstofconcentratie en ook een anomaal gedrag van de geleidbaarheid, en dit doet vermoeden dat er in een gedeelte van de laag $Mg(AlH_4)_2$ gevormd wordt.

3. Voor hogere Mg fracties ($0.36 < y < 0.5$), is het uitgangsmateriaal een amorfe Mg-Al legering en MgH_2 segregeert preferentieel naar het Pd interface.

Met Hydrogenography zijn we dus in staat, het brede scala aan fase transformatie processen die bij hydrogenatie optreden, in kaart te brengen. Hydrogenography is complementair aan andere dunne film analyse technieken, maar geeft daarenboven essentiële informatie over de kinetische en thermodynamische aspecten van de hydrogenatie. Dunne films kunnen zo als modelsystemen worden gebruikt om nieuwe, geschikte metaalhydrides voor waterstofopslag te vinden.

List of publications

19. *Hydrogenography of PdH_x thin films: influence of H-induced stress relaxation processes*
R. Gremaud, M. Gonzalez-Silveira, Y. Pivak, S. de Man, M. Slaman, H. Schreuders, B. Dam and R. Griessen,
submitted to Acta Mater. (2008).

18. *Optical properties of sodium alanate, GW_0 BSE calculations and thin film measurements*
M. J. van Setten, G. A. de Wijs, R. Gremaud, B. Dam, R. Griessen and G. Kresse,
in preparation (2008).

17. *Effect of the substrate on the thermodynamic properties of PdH_x thin films studied by Hydrogenography*
Y. Pivak, R. Gremaud, M. Gonzalez-Silveira, K. Gross, A. Walton, H. Schreuders, B. Dam and R. Griessen,
submitted to Scripta Mater. (2008).

16. *Optical analysis of hydrogen-induced segregation in Mg-V-H thin films*
M. Gonzalez-Silveira, R. Gremaud, H. Schreuders, B. Dam and R. Griessen,
in preparation (2008).

15. *Interplay of diffusion and dissociation mechanisms during hydrogen absorption in metal*
A. Borgschulte, R. Gremaud and R. Griessen,
submitted to Phys. Rev. B (2008).

14. *EXAFS study of short range ordering in $Mg_y Ti_{1-y} H_x$ thin films*
A. Baldi, R. Gremaud, D. M. Borsa, C. P. Baldé, A. M. J. van der Eerden, G. L. Kruijtzer, P. E. de Jongh, B. Dam and R. Griessen,
submitted to Phys. Rev. B (2008).

13. *Chemical short-range order and lattice deformations in $Mg_y Ti_{1-y} H_x$ thin films probed by Hydrogenography*
R. Gremaud, A. Baldi, M. Gonzalez-Silveira, B. Dam and R. Griessen,
Phys. Rev. B **77**, 144204 (2008).

12. *Formation of $Ca(BH_4)_2$ by hydriding CaH_2-MgB_2 composites*
    G. Barkhordarian, T. Jensen, S. Doppiu, U. Bösenberg, A. Borgschulte,
    R. Gremaud, Y. Cerenius, M. Dornheim, T. Klassen and R. Bormann,
    J. Phys. Chem. C **112**, 2743 (2008).

11. *Tuning the electrical, structural and optical properties of in-situ grown*
    MgH_2 thin films by activated reactive evaporation
    R. J. Westerwaal, C. P. Broedersz, R. Gremaud, M. Slaman, A. Borgschulte,
    W. Lohstroh, K. G. Tschersich, H. P. Fleischhauer, B. Dam and R. Griessen,
    Thin Solid Films, **516**, 4351 (2008).

10. *The highly destabilized Mg-Ni-Ti-H system investigated by density func-*
    tional calculations and Hydrogenography experiments
    C. P. Broedersz, R. Gremaud, B. Dam, R. Griessen and O. M. Løvvik,
    Phys. Rev. B **77**, 024204 (2008).

 9. *An optical method to determine the thermodynamics and kinetics of H*
    absorption and desorption in metals
    R. Gremaud, M. Slaman, H. Schreuders, B. Dam and R. Griessen,
    Appl. Phys. Lett. **91**, 231916 (2007).

 8. *Hydrogenography: an optical combinatorial method to find new light-*
    weight hydrogen storage materials
    R. Gremaud, C. P. Broedersz, D. M. Borsa, A. Borgschulte, Ph. Mauron,
    H. Schreuders, J. H. Rector, B. Dam and R. Griessen,
    Adv. Mater. **19**, 2813 (2007).

 7. *Characterization of hydrogen storage properties of Mg-Ni composition*
    spreads using micro-machined Si cantilevers
    A. Ludwig, B. Dam, J. Cao and R. Gremaud,
    Appl. Surf. Sci. **254**, 682 (2007).

 6. *Structural, optical and electrical properties of Mg-Ti-H thin films*
    D. M. Borsa, R. Gremaud, A. Baldi, H. Schreuders, B. Kooi, P. Ver-
    meulen, P. H. L. Notten, B. Dam, and R. Griessen,
    Phys. Rev. B **75**, 205408 (2007).

 5. *Combinatorial thin film methods for the search of new light-weight metal-*
    hydrides
    B. Dam, R. Gremaud, C. P. Broedersz and R. Griessen,
    Scripta Mater. **56**, 853 (2007).

4. *Critical composition dependence of the hydrogenation of $Mg_{2\pm\delta}Ni$ thin films*
D. M. Borsa, W. Lohstroh, R. Gremaud, J. H. Rector, B. Dam, R.J. Wijngaarden and R. Griessen,
J. Alloys Compd. **428**, 34 (2007).

3. *High-throughput concept for tailoring switchable mirrors*
A. Borgschulte, R. Gremaud, S. de Man, R. J. Westerwaal, J. H. Rector, B. Dam, and R. Griessen,
Appl. Surf. Sci. **253**, 1417-1423 (2006).

2. *Structural and optical properties of $Mg_yAl_{1-y}H_x$ gradient thin films: a combinatorial approach*
R. Gremaud, A. Borgschulte, C. Chacon, J. L. M. van Mechelen, H. Schreuders, A. Züttel, B. Hjörvarsson, B. Dam and R. Griessen,
Appl. Phys. A **84**, 77 (2006).

1. *Ti-catalyzed $Mg(AlH_4)_2$: A reversible hydrogen storage material*
R. Gremaud, A. Borgschulte, W. Lohstroh, H. Schreuders, A. Züttel, B. Dam and R. Griessen,
J. Alloys Compd. **404-406**, 775 (2005).

Acknowledgement

When I joined the Condensed Matter group at the Vrije Universiteit almost five years ago, I encountered a very original and imaginative community. I quickly learnt a lot about physics and (Dutch) life at the contact of the great variety of people populating the labs. To mention everything I benefited from everybody who was around is probably impossible.

I would like to thank first Ronald and Bernard, who patiently guided me through the whole PhD. As complementary duettists in physics and materials science, your enthusiasm, insight, inspiration and experience helped me tremendously. You also showed me how a scientific community works and gave me the opportunity to present my work at several national and international workshop and conferences. Among these events, a particularly unique experience was the opportunity to give a lecture at the Gordon research conference on hydrogen-metal systems 2007 in Waterville, ME, USA.

The daily life in the lab would not have been enjoyable without Andreas. Your continuous blossoming of ideas and discussions about absolutely all subjects was always very inspiring. Your straight way of experimenting remains an example for me. Dook, you introduced me to all the subtleties of the experimental devices in the lab and the long measuring days often ended by trying another restaurant in Amsterdam. Now that you are almost Swiss, we will certainly see each other more again. Herman, you quickly solve all experimental problems while keeping a cool head. Running and chatting with you in the Amsterdamse Bos also helped to decompress, Thank you! Wiebke, Ingrid and Stănică were always ready to explain me all what the beginner I was had to learn about thin films and hydrides.

Chase, we were quite a complementary team. In a memorable week of hard work, we set the basis of Hydrogenography. Our very fruitful collaboration ended up in a nice publication in Advanced Materials. Furthermore, you contributed in no more than three chapters in this thesis: 2, 4 and 6. Thank you very much, and I wish you a lot of success for rounding up your own PhD! Martin, without you, I would probably still be trying to acquire data. Your commitment and skills in programming cannot be replaced. Jan, you were always here to do RBS measurements, and nothing probably is more measurement-intensive than gradient films. You designed for me in no-time a

perfectly working UHV spectrometer head, and saved me this way from serious experimental troubles. And I liked very much your descriptions of the good old times, as you are, together with Kier, the living memory of this group! No experiment would be possible without the mechanical workshop, and especially Johan Kos who designed and constructed various equipments. Saskia Kars from the Geology department did professional SEM measurements of the Pd surfaces and offered me delicious coffees.

I would like also to thank the "hard core" of the hydrogen group during these years: while looking for solutions to the same problems, we never forgot to also have a lot of fun besides. Mathieu, always encouraging, hearing your French was reminding me the south of France every morning. Dana, you disentangled the Mg-Ti mystery and that greatly facilitated the analysis in chapter 5. We also spent never-to-forget holidays together in Hawaii after MH2006. Marta, thanks for all the discussions and the meaningful XRD data, your strive for precision is an example. Ruud, you gave me the layout of this thesis and helped me a lot going trough the organizational hurdles of the last months of the PhD. Thank you! Andrea, our first EXAFS beamtime together in Hamburg was quite an adventure, with a good ending! Genya, you where always ready to discuss and run a confirmatory experiment when I was writing the Pd chapter and time was becoming short. Erdny, thanks for bravely continuing work on the UHV spectrometer. Sven, thanks you for the AFM measurements and your expertise in computer matters! Sonia, I appreciated your fresh look on life and physics. Thank you also for the careful reading of my manuscripts before submission. Philippe, your analysis program resulted in beautiful graphs in the Mg-Ni-Ti-H publication and chapter.

I want to thank of course the rest of the group for the enjoyable discussions during coffee breaks and "de goede sfeer": Davide, Ninke, Annemarie, Rinke, Marco, Mariella, Diana, Kinga, Marcel, Kirsten, Iris and Christijn.

I would like to thank particularly the reading committee for the time they spent going through the thesis and participating in the defense. In addition, Andreas Züttel gave me the opportunity to start in Amsterdam by supporting me during the first year.

Last but not least, I would like to say a big thank you to my beloved Nathalie, for her love and support during all these years and the difficult decision to join me for almost two years in Amsterdam. Et finalement, un tout grand Merci à Poly, Jean-Bernard, Yella, Arthur et Corentin qui m'ont toujours offert sans compter soutien, amour et confiance durant ces années passées dans la lointaine Hollande.

Curriculum Vitae

Robin Gremaud was born on October 3rd 1978 in Marly, Switzerland. From 1994 to 1998 he followed high school at the Collège Ste-Croix in Fribourg, Switzerland. He studied Experimental Physics from 1998 to 2003 in the same city and did his graduation work entitled "Heat and mass transfer in metal-hydrides" in the Solid State Physics group of Prof. Louis Schlapbach under the supervision of Prof. Andreas Züttel. From 2003 to 2008 he did his PhD in the Condensed Matter group of Prof. Ronald Griessen at the VU University in Amsterdam, The Netherlands. During this time, he started and developed Hydrogenography, an optical thin film combinatorial approach to search for new hydrogen storage materials. This thesis is the outcome of this work. Since May 2008, he is a Postdoc in the Hydrogen & Energy Laboratory of the EMPA, an interdisciplinary research institution for material sciences and technology development in Dübendorf, Switzerland.